

2014

# Experimental determination of the forming limits of DP600 and AA5182 sheets in electrohydraulic free forming

Christopher Joel Lyall Maris  
*University of Windsor*

Follow this and additional works at: <http://scholar.uwindsor.ca/etd>

---

## Recommended Citation

Maris, Christopher Joel Lyall, "Experimental determination of the forming limits of DP600 and AA5182 sheets in electrohydraulic free forming" (2014). *Electronic Theses and Dissertations*. Paper 5130.

This online database contains the full-text of PhD dissertations and Masters' theses of University of Windsor students from 1954 forward. These documents are made available for personal study and research purposes only, in accordance with the Canadian Copyright Act and the Creative Commons license—CC BY-NC-ND (Attribution, Non-Commercial, No Derivative Works). Under this license, works must always be attributed to the copyright holder (original author), cannot be used for any commercial purposes, and may not be altered. Any other use would require the permission of the copyright holder. Students may inquire about withdrawing their dissertation and/or thesis from this database. For additional inquiries, please contact the repository administrator via email ([scholarship@uwindsor.ca](mailto:scholarship@uwindsor.ca)) or by telephone at 519-253-3000ext. 3208.

Experimental determination of the forming limits of DP600 and AA5182 sheets in  
electrohydraulic free forming

By

Christopher Maris

A Thesis  
Submitted to the Faculty of Graduate Studies  
through the Department of Mechanical, Automotive & Materials Engineering  
in Partial Fulfillment of the Requirements for  
the Degree of Master of Applied Science  
at the University of Windsor

Windsor, Ontario, Canada

2014

© 2014 Christopher Maris

Experimental determination of the forming limits of DP600 and AA5182 sheets in  
electrohydraulic free forming

By

Christopher Maris

APPROVED BY:

---

Dr. A. Alpas  
Engineering Materials

---

Dr. W. Altenhof  
Mechanical Engineering

---

Dr. D. Green, Advisor  
Mechanical Engineering

May 1, 2014

## **Declaration of Originality**

I hereby certify that I am the sole author of this thesis and that no part of this thesis has been published or submitted for publication.

I certify that, to the best of my knowledge, my thesis does not infringe upon anyone's copyright nor violate any proprietary rights and that any ideas, techniques, quotations, or any other material from the work of other people included in my thesis, published or otherwise, are fully acknowledged in accordance with the standard referencing practices. Furthermore, to the extent that I have included copyrighted material that surpasses the bounds of fair dealing within the meaning of the Canada Copyright Act, I certify that I have obtained a written permission from the copyright owner(s) to include such material(s) in my thesis and have included copies of such copyright clearances to my appendix.

I declare that this is a true copy of my thesis, including any final revisions, as approved by my thesis committee and the Graduate Studies office, and that this thesis has not been submitted for a higher degree to any other University or Institution.



## **Abstract**

Electrohydraulic forming is a pulsed metal forming process that uses the discharge of electrical energy across a pair of electrodes submerged in fluid to form sheet metal. Pulsed metal forming processes, including electrohydraulic forming, have been shown to increase the formability of sheet metals, which is of significant industrial interest. An experimental procedure was developed to quantify the formability in electrohydraulic free forming (EHFF) that is consistent with the quasi-static formability assessment convention. Novel sheet metal specimen geometries were created to quantify the formability across the entire minor strain spectrum. The experimental EHFF forming limit curve (FLC) was determined for both AA5182-O and DP600 sheets. Compared to their respective quasi-static FLCs, DP600 shows no formability improvement in EHFF while AA5182-O shows formability improvement over the entire range of minor strains including an 11% engineering strain improvement at the plane strain intercept. Numerical modeling indicated that peak strain rates reach approximately 2500 to 10,000 s<sup>-1</sup>.

## **Acknowledgements**

I would like to acknowledge the substantial contributions that Amir Hassannejadasl has made to this work. It was Amir's idea to use modified EHF specimens, and Amir designed the modified EHF specimens. Amir taught me how to use both Abaqus and LS-DYNA. Numerical simulation software is notoriously difficult to learn, and problems often arise that are very difficult to troubleshoot. Despite having his own work to do, Amir always had time to help me. It was exhausting trying to keep up to Amir's amazing technical knowledge, ability, focus, efficiency, and drive, but it allowed me to exceed any expectations I had for my Masters studies. Amir is a true friend, and I am grateful that he was such an important part of my life during my graduate studies.

I would like to thank Andy Jenner for the care and expertise he demonstrated while making the many parts required for my experimental work. Andy helped me numerous times to formulate a plan to solve my problems and he spent a lot of time to make many products for me. The products Andy built were perfectly manufactured, which reflected positively on the University and me when I used them at the industrial partner's research facility. Andy always found a way to find time for my requests despite the many other projects that he was working on. The quick turn-around was appreciated because I was able to take advantage of the small windows of availability at the industrial partner's research facility. Andy's skills and personality make him a major asset to the University of Windsor.

I would like to thank Alan Gillard for his assistance with the EHF experiments. Alan is an expert in EHF, and he plays a vital role in the success of the metal forming research team at Ford. Although the academic component of the project may have sometimes had requirements that didn't directly benefit the industrial work, he always took the time to listen to my ideas, answer my questions, and try my ideas. Alan was very helpful during the design of the new EHF tooling. He was always quick to respond to my emails and tried to fit in my testing whenever he could into his own busy schedule. Alan made me feel comfortable during my visits to Melvindale, and his hospitality was appreciated.

I would like to thank Dr. Green for being my supervisor. Dr. Green has a well-earned reputation for being one of the nicest people in the entire Engineering department. Dr. Green treats his graduate students very well and gives them the flexibility to define their own path for success.

# Table of Contents

<b>Declaration of Originality .....</b>	<b>iii</b>
<b>Abstract.....</b>	<b>iv</b>
<b>Acknowledgements .....</b>	<b>v</b>
<b>List of Tables .....</b>	<b>x</b>
<b>List of Figures.....</b>	<b>xii</b>
<b>List of Abbreviations .....</b>	<b>xviii</b>
<b>Nomenclature .....</b>	<b>xix</b>
<b>1 Introduction.....</b>	<b>1</b>
1.1 Background .....	1
1.2 Motivation .....	2
1.3 Objectives.....	3
1.4 Summary of Subsequent Chapters .....	4
<b>2 Review of the Literature.....</b>	<b>5</b>
2.1 Sheet Materials for Auto-body Applications .....	5
2.2 Formability .....	7
2.3 High-velocity Forming Processes .....	13
2.4 Formability Improvement via High-velocity Forming.....	17
<b>3 Methodology .....</b>	<b>24</b>
3.1 Experimental Methodology.....	24
3.1.1 Pulse Unit.....	25
3.1.2 Process Efficiency and Chamber Design .....	28
3.1.3 Tool Selection and Design .....	37
3.1.4 Electrical Insulation and Water Control .....	41
3.1.5 Sheet Material Selection .....	43

3.1.6	Specimen Preparation .....	46
3.1.7	Experimental EHF Process and Conditions .....	47
3.1.8	Strain Measurement .....	51
3.1.9	Mini-die Forming.....	56
3.1.10	Quasi-static Formability Tests .....	59
3.1.11	Material Characterization.....	62
3.2	Numerical Model Methodology .....	63
3.2.1	Numerical Model Details .....	64
3.2.2	Specimen Geometry.....	71
<b>4</b>	<b>Results .....</b>	<b>75</b>
4.1	Material Characterization.....	75
4.2	Quasi-static Formability Tests .....	78
4.3	Experimental EHFF.....	87
4.3.1	Energy .....	87
4.3.2	Formability.....	91
4.3.3	Anisotropy and Asymmetry .....	102
4.4	Numerical Simulation of EHFF .....	106
4.5	Comparison of Experimental and Numerical Results .....	114
4.6	Mini-die Forming Experiments.....	119
<b>5</b>	<b>Discussion.....</b>	<b>127</b>
<b>6</b>	<b>Summary and Conclusions .....</b>	<b>134</b>
	<b>Bibliography .....</b>	<b>136</b>
	<b>Appendices.....</b>	<b>142</b>
	Appendix A: Engineering Drawings of Custom Tooling .....	142
	Appendix B: Engineering Drawings of Modified EHF Specimens.....	157

Appendix C: Experimental EHFF Results .....	162
Appendix D: Numerical Simulation of EHFF Results by Strain Path.....	170
Appendix E: Numerical Simulation of EHFF Time History .....	186
<b>Vita Auctoris.....</b>	<b>189</b>

## List of Tables

Table 3-1: Comparison of aluminum biaxial specimens before and after the arc occurred outside the chamber. ....	27
Table 3-2: Comparison of the input voltages required to cause a neck and the failure types in biaxial AA5182-O specimens in the original and new chambers. ....	31
Table 3-3: Comparison of the input voltages required to cause a small split and the failure types in biaxial AA5182-O specimens in the new chamber without and with the chamber ring. ....	33
Table 3-4: Comparison of the input voltages required to cause a neck and the failure types in biaxial DP600 specimens in the new chamber with and without the inductance choke.....	34
Table 3-5: Comparison of the effects of simultaneously circumventing the choke and adding the chamber ring for plane strain DP600 specimens.....	36
Table 3-6: Comparison of the input voltage to cause a neck in biaxial AA5182-O specimens in the new chamber before the arc, without the chamber ring, and with the choke, to the configuration after the arc, with the chamber ring, and without the choke.....	37
Table 3-7: Heat chemistry of DP600 steel in weight percentage.....	44
Table 3-8: Material model work hardening parameters.....	45
Table 3-9: Material model strain rate hardening parameters. ....	45
Table 3-10: The standard number of rows and columns for each specimen. ....	53
Table 3-11: Repeatability and reproducibility study results for a sharp radius at the apex of a biaxial specimen and for a flat blank. ....	55
Table 3-12: Water material parameters.....	68
Table 4-1: AA5182-O and DP600 material parameters determined from quasi-static uniaxial tensile tests. ....	78
Table 4-2: DP600 input voltages to cause a neck. ....	88
Table 4-3: AA5182-O input voltages to cause a neck. ....	88
Table 4-4: Total number of necked specimens used to generate the FLC.....	95
Table 4-5: Total number of necked specimens in the final forming conditions. ....	95

Table 4-6: Quantity of specimens used to generate AA5182-O data points.....	98
Table 4-7: Average height of necked specimens (mm). .....	99
Table 4-8: Numerical simulation acceleration multiplier ( $\text{mm/s}^2$ ) for AA5182-O and DP600.....	106
Table 4-9: Ratio of experimental energy measured at the chamber (kJ) to the nodal acceleration applied in the simulation ( $\text{mm/s}^2$ ).....	116



## List of Figures

Figure 1-1: Model year 2012-2025 passenger car fuel economy targets. Image from NHTSA (2012).....	1
Figure 2-1: A generic engineering stress vs. strain curve. ....	7
Figure 2-2: Schematic of the Nakazima (hemispherical dome) test. ....	9
Figure 2-3: Schematic of the Marciniak (double blank) test. ....	9
Figure 2-4: Schematic of electromagnetic forming. Image from Imbert et al. (2004). ....	14
Figure 2-5: Schematic of explosive forming. Image from Avitzur (1983).....	15
Figure 2-6: Schematic of electrohydraulic forming.....	16
Figure 2-7: Strain measurements for free forming, 40° conical die forming, and 45° conical die forming of 1.0mm AA5754. Image from Imbert et al. 2004.....	18
Figure 2-8: The high velocity and quasi-static failure strains for five steels. Image from Seth et al. (2005). ....	19
Figure 2-9: FLDs of AA6061-T6 and AISI 1045 generated from quasi-static, impact, and explosive forming methods. Image from Dariani et al. (2009).....	20
Figure 2-10: Experimental displacement, velocity, strain, and strain rate for an AA5182-O specimen formed with 7.5kV in free forming. Image from Rohatgi et al. (2011). ....	21
Figure 2-11: Combined LDH and EHF formability results for 1.0mm DP590. Image from Golovashchenko et al. (2013). ....	22
Figure 3-1: The experimental EHF setup.....	24
Figure 3-2: The peak amperage delivered before and after the arc outside the chamber.....	27
Figure 3-3: Half view of the new chamber. ....	29
Figure 3-4: Half view of the original chamber and the chamber ring. ....	29
Figure 3-5: The chamber ring that was added to the new chamber to increase the volume.....	32
Figure 3-6: Peak current measurements with and without the choke. ....	35
Figure 3-7: A uniaxial specimen formed into a 50 degree conical die had negative displacement due to water reflecting off of the forming tool. ....	38

Figure 3-8: Half view of an electrohydraulic free forming configuration. ....	38
Figure 3-9: Bottom view of the open window forming tool. ....	39
Figure 3-10: The die adapter and adapter ring custom manufactured forming tools attached to the pre-existing open window forming tool. ....	40
Figure 3-11: The bottom electrical insulation and related components. ....	42
Figure 3-12: The die adapter mounted to the top electrical insulation. ....	42
Figure 3-13: Bottom view of the top insulation, protector sheet, and pipe. ....	43
Figure 3-14: A uniaxial specimen in the machining fixture on the bed of the CNC mill. ....	47
Figure 3-15: Recordings from the oscilloscope for a 6.1kV discharge used to measure positive voltage (1-yellow), negative voltage (2-blue), the differential voltage (M-red), the current at the chamber (3-purple), and the current at the Magnepress (4-green). ....	49
Figure 3-16: A copper bridge wire installed between the two electrodes. ....	50
Figure 3-17: Original and deformed circle grids for strain measurement using circle grid analysis. ....	52
Figure 3-18: A biaxial specimen with the row and column numbering system. ....	53
Figure 3-19: Half view of an electrohydraulic mini-die forming configuration. ....	57
Figure 3-20: Spacer and mini-die attached to the die adapter for use with the open window forming tool. ....	58
Figure 3-21: Experimental FLC and Keeler-Brazier theoretical FLC for 1.4mm DP590. Image from Sriram et al. 2009. ....	60
Figure 3-22: DP600 theoretical forming limit curve predicted by the Keeler-Brazier relation (Equation 1). ....	61
Figure 3-23: AA5182-O 1.0mm experimental forming limit curve obtained from Wu et al. (2003). ....	62
Figure 3-24: Abaqus numerical model assembly. ....	64
Figure 3-25: The meshed shell element sheet metal blanks for all for specimen geometries. ....	65
Figure 3-26: Numerical simulation geometry of the open window forming tool. ....	66
Figure 3-27: Numerical simulation geometry of the chamber bowl. ....	67

Figure 3-28: Section cut of the single Eulerian part containing the air (void) above the chamber and the water in the chamber bowl.....	68
Figure 3-29: The water contained in the chamber and nodal acceleration boundary condition. ....	70
Figure 3-30: Unit acceleration curve applied to the nodes on the hemispherical partition. ....	71
Figure 3-31: Modified specimens used by Davies (2012) and Dariani et al. (2009) which cracked in the corners of the cutout. ....	72
Figure 3-32: Modified specimens used by Davies (2012) and Dariani et al. (2009) which had two gauge sections on one specimen.....	72
Figure 3-33: The four experimental specimen geometries. ....	73
Figure 3-34: Strain concentration in the center of the gauge section for each of the specimen geometries.....	73
Figure 3-35: Numerically predicted strain path for each specimen geometry.....	74
Figure 4-1: Engineering stress versus engineering strain curves for DP600 and AA5182-O.....	76
Figure 4-2: True stress versus true strain curves for DP600 and AA5182-O.....	76
Figure 4-3: The power law fit for DP600 and AA5182-O.....	77
Figure 4-4: DP600 quasi-static theoretical and experimental forming limit curves.....	79
Figure 4-5: AA5182-O quasi-static experimental forming limit curves.....	80
Figure 4-6: Experimental quasi-static forming limit curves for DP600 and AA5182-O.....	81
Figure 4-7: Strain measurements from a biaxial quasi-static Nakazima test specimen. ....	82
Figure 4-8: Comparison of necked points generated using Nakazima and Marciniak tooling for 1mm DP590. Image from Sriram et al. (2009). ....	83
Figure 4-9: Comparison between standard North American and European theoretical models for 1.4mm DP590. Image from Sriram et al. (2009). ....	84
Figure 4-10: The experimental FLCs for 1.5mm DP600 and 1.4mm DP590. ....	86
Figure 4-11: The power trace for a 6.3kV pulse as measured at the chamber and at the Magnepress. ....	90

Figure 4-12: Summation of discharged energy over time for a 6.3kV pulse as measured at the chamber and at the Magnepress.....	90
Figure 4-13: Comparison of theoretical energy and experimental energy measured at both the Magnepress and chamber over the range of input voltages.....	91
Figure 4-14: DP600 1.5mm thick EHFF necked strain measurements and the resulting EHFF FLC.....	92
Figure 4-15: AA5182-O 1.5mm thick EHFF necked strain measurements and the resulting EHFF FLC.....	93
Figure 4-16: Necked specimens in each strain path for AA5182-O (top row) and DP600 (bottom row).....	96
Figure 4-17: Three consecutive aluminum intermediate draw specimens formed at 6.3kV were safe, necked, and split.....	97
Figure 4-18: AA5182-O 1.5mm thick EHFF necked and proximity to split strain measurements and the EHFF FLC.....	98
Figure 4-19: Comparison of the experimental EHFF FLCs for DP600 and AA5182-O.....	99
Figure 4-20: Final displacement of the sheet measured radially from the sheet center for necked DP600 and AA5182-O uniaxial specimens.....	100
Figure 4-21: Major strain distribution measured radially from the sheet center for safe DP600 and AA5182-O uniaxial specimens.....	101
Figure 4-22: Minor strain distribution measured radially from the sheet center for safe DP600 and AA5182-O uniaxial specimens.....	102
Figure 4-23: Major strain measurements from a safe biaxial AA5182-O specimen in the rolling and transverse directions.....	103
Figure 4-24: Major strain measurements from a safe biaxial DP600 specimen in the rolling and transverse directions.....	104
Figure 4-25: Splitting in biaxial DP600 specimens.....	105
Figure 4-26: Splitting in biaxial AA5182-O specimens.....	105
Figure 4-27: Radial distance from the sheet center to locations for measurements on uniaxial specimens.....	107

Figure 4-28: Final displacement of the sheet measured radially from the sheet center for experimental and numerical DP600 uniaxial specimens.....	108
Figure 4-29: Evolution of the sheet displacement measured radially from the sheet center for DP600 uniaxial specimens. ....	109
Figure 4-30: Velocity at distances of 0, 15, and 30mm from the specimen center for DP600 uniaxial specimens.....	110
Figure 4-31: Major strain at distances of 0, 15, and 30mm from the specimen center for DP600 uniaxial specimens. ....	111
Figure 4-32: Predicted strain path at distances of 0, 15, and 30mm from the specimen center for each specimen geometry for DP600.....	112
Figure 4-33: Predicted strain path at distances of 0, 15, and 30mm from the specimen center for each specimen geometry for AA5182-O.....	112
Figure 4-34: Equivalent strain rate and the average equivalent strain rate at distances of 0, 15, and 30mm from the specimen center for DP600 uniaxial specimens. ....	114
Figure 4-35: Comparison of experimental energy measured at the chamber (kJ) to the nodal acceleration applied in the simulation (mm/s <sup>2</sup> ).....	116
Figure 4-36: Comparison of experimental and predicted major and minor strains measured radially from the center of the DP600 uniaxial specimens.....	117
Figure 4-37: Predicted strain paths and experimental safe strain distributions in necked DP600 specimens. ....	118
Figure 4-38: Predicted strain paths and experimental safe strain distributions in safe AA5182-O specimens. ....	118
Figure 4-39: Comparison of experimental and numerical specimens showing that actual failures occurred from the center of the gauge as predicted by the strain distribution. ....	119
Figure 4-40: Side view of a safe EHFF specimen. ....	120
Figure 4-41: Strain measurements from one safe specimen in free forming with input voltage equivalent to the critical voltage. ....	121

Figure 4-42: Major and minor strains measured radially from the center of one specimen formed in EHFF with input voltage equivalent to the critical voltage.....	121
Figure 4-43: Side profile of a mini-die forming specimen with the die lower than the free forming height.....	122
Figure 4-44: Strain measurements from one specimen in mini-die forming with the die lower than the free forming height.....	123
Figure 4-45: Comparison of the major and minor strains measured radially from the centers of an EHFF specimen and one specimen formed in electrohydraulic mini-die forming with the die lower than the free forming height.....	123
Figure 4-46: Side profile of a mini-die forming specimen with the die higher than the free forming height.....	124
Figure 4-47: Strain measurements in mini-die forming with increased die height.....	125
Figure 4-48: Comparison of the major and minor strains measured radially from the centers of an EHFF specimen and one specimen formed in electrohydraulic mini-die forming with the die higher than the free forming height.....	125
Figure 5-1: The equivalent strain rate versus equivalent strain for DP600 uniaxial specimens.....	129
Figure 5-2: Safe grids measured on split EHFF aluminum specimens in comparison to the EHFF FLC. ....	131
Figure 5-3: Strain path from biaxial specimens in incomplete die forming (left) and complete die forming (right). Image from Golovashchenko et al. (2013)....	132

## List of Abbreviations

The following table defines various abbreviations and acronyms used throughout the thesis.

<b>Abbreviation</b>	<b>Explanation</b>
EF	Explosive forming
EHF	Electrohydraulic forming
EHDF	Electrohydraulic die forming
EHFF	Electrohydraulic free forming
EMF	Electromagnetic forming
FEA	Finite element analysis
FLC	Forming limit curve
FLC <sub>0</sub>	The plane strain intercept of the forming limit curve
FLD	Forming limit diagram
J-C	The Johnson-Cook material model
QS	Quasi-static

## Nomenclature

The following table defines some of the more significant terms used throughout the thesis.

<b>Term</b>	<b>Meaning</b>
AA5182-O	A particular aluminum alloy selected for this study.
DP600	A particular grade of dual phase steel selected for this study.
Eulerian analysis	A type of numerical analysis where the material is able to flow within the boundaries of the fixed mesh.
Formability	The ability of a given metal workpiece to undergo plastic deformation without being damaged.
Forming limit curve	A curve in principal strain space, below which there is no risk that a combination of strains will exhibit evidence of necking.
Forming limit diagram	A plot of major strain versus minor strain, which typically contains at least one forming limit curve.
Lagrangian analysis	A type of numerical analysis where the material is coupled to the mesh.
Neck	A failure mechanism attributed to the reduction of thickness due to strain localization.
Numerical simulation	A computer model used to reproduce the processes of a system.
Quasi-static	A process which happens so slow that rate and inertial effects are negligible.





Manufacturers must consider all avenues in order to satisfy the ambitious regulations for fuel economy improvements, such as improvements to drivetrain technology, aerodynamics, and air conditioner efficiency. Further improvements can come from tires with lower rolling resistance and by reducing the vehicle weight.

One way that weight reduction can be achieved is by using high strength materials such as advanced high strength steels, which allow for the down-gauging of automotive body panels (Cheah and Heywood, 2011). The higher strength of the material means that thinner, lighter panels can be used, while maintaining the overall strength of the panel. Another way to reduce vehicle weight is to use lower density materials such as aluminum or magnesium alloys. One of the barriers to further implementation of both high strength and low density materials is their relatively low formability in sheet forming operations as compared to mild steels. Formability is the capacity of a material to be readily drawn, stretched, or otherwise shaped. The relatively low formability of high strength and low density materials limits the number of applications where these materials can be used because it is not possible to stretch the sheet material into the desired shape. In order to increase the number of applications where high strength or low density materials can be used, considerable research is being carried out to develop forming processes which can be used to increase the formability of sheet materials.

Electrohydraulic forming (EHF) is a non-traditional forming process that shows considerable promise in terms of both improved formability results and good practicality for industrial processes. Electrohydraulic forming is a pulsed forming process that uses the discharge of electrical energy across electrodes submerged in a fluid to generate a pressure pulse that forms the workpiece.

## **1.2 Motivation**

Electrohydraulic die forming (EHDF) has been shown to provide significant formability improvements relative to quasi-static forming processes (Golovashchenko, 2013). However, the formability improvement of materials in electrohydraulic free forming (EHFF) relative to the quasi-static formability is largely unknown. An EHFF forming

limit criterion is required to advance the EHF process design methodology for use in industrial applications. However, due to the difficulty of such a task, there has not been a clear identification of the amount of formability improvement that can be achieved.

It is difficult to assess the formability in pulsed forming processes for a variety of reasons. The primary obstacle to quantifying the formability is that the quasi-static forming limit curve (FLC) generation methods, such as Nakazima tests, cannot be conducted at the speeds observed in EHF. The inability to use the established quasi-static FLC tests requires that new methods, which incorporate the dynamic effects of EHF, must be developed.

### **1.3 Objectives**

In order to implement EHF technologies into part production, the forming limits of materials in high-velocity forming processes are required. In order to address this issue, the objectives of this research are to:

- Develop an experimental procedure to determine the forming limit in EHFF.
- Determine the forming limits of AA5182-O and DP600 sheets formed in EHFF.
- Compare the formability in EHFF to that in quasi-static forming.
- Numerically model EHFF to determine the in-process parameters.

The experimental FLC results for EHFF will fill a gap of information regarding the proper forming limit criterion for pulsed forming processes. In particular, the EHFF forming limits for DP600 and AA5182-O will demonstrate the ability to apply the experimental technique to two very different classes of materials that are of significant industrial interest. The evaluation of the change in formability in EHFF relative to quasi-static forming will enhance the process design methodology employed by engineers to properly select materials that can benefit from EHF technology and be used in vehicle body structures. The numerical model will provide information about the in-process parameters (ie. velocity, strain, and strain rate) to allow for the comparison to previous high strain rate experiments and simulations.

## **1.4 Summary of Subsequent Chapters**

The focus of this research is on quantifying the formability changes that are observed when using a relatively new sheet metal forming technology. This new sheet metal forming technology can aid in vehicle lightweighting, which is one avenue to help passenger car manufacturers meet the ambitious requirements of the CAFE regulations.

Chapter 2 consists of a review of the literature on the topics of sheet materials for auto-body applications, formability, high-velocity forming processes, and formability improvement in high-velocity forming processes.

Chapter 3 describes the procedures that were used to conduct the EHF experiments, quasi-static formability tests, material characterization tests, and numerical simulations.

Chapter 4 presents the experimental and numerical results that were obtained. The numerical predictions are also compared to the experimental results.

Chapter 5 compares the original findings to previously published works. The validity of both original and previously published results is assessed, and errors in previously reported results are identified. This chapter highlights the importance of the described procedure for the rigorous determination of a failure criterion in EHFF.

Chapter 6 is summary of the advances in EHF technology that have been made and contains an assessment of the ability to achieve the stated objectives. Future advancements to continue the quantification of forming limit criterion for pulsed forming processes are suggested.

## 2 Review of the Literature

### 2.1 Sheet Materials for Auto-body Applications

The materials selected to manufacture the body-in-white and closure panels of an automobile have a strong influence on a vehicle's performance terms of safety, fuel economy, noise and vibration, and durability. Traditionally, auto-body components have been made from materials with good strength and formability such as mild steel.

Automotive manufacturers are replacing traditional materials with materials that have higher strength-to-weight ratios, such as high strength steels and low density aluminum alloys, to reduce vehicle weight and increase fuel economy in light of the CAFE regulations.

Down-gauging, or reducing the thickness of a part, is one way to reduce the overall weight of a vehicle. High strength steels, and in particular dual phase steels, can be used in down-gauging applications while maintaining the strength of a part. Dual phase (DP) steels derive their name from their microstructure, which consists of martensite islands dispersed throughout a ferrite matrix. This combination of soft, formable ferrite and a harder martensite phase provides superior strength without the decrease in formability that is characteristic of high-strength low alloy steels. Dual phase steels are designated by a number which represents the minimum ultimate tensile strength. For example, DP600 signifies a minimum ultimate tensile strength of 600MPa. Dual phase steels are increasingly being used in automobile body structures to reduce vehicle weight through down-gauging while maintaining crash safety performance.

Lightweighting, or producing a part from a less dense material, is another way to reduce the overall weight of a vehicle. Low density materials, including aluminum alloys, can be used in lightweighting applications, but typically result in a decrease in part strength. In lightweighting applications, the thickness of the part is often increased to maintain the strength of the part while still achieving a net weight savings. Aluminum alloys are commonly used due to their low density, corrosion resistance, and weldability. In particular, AA5182 is used extensively in the automotive industry because of its good

formability relative to other aluminum alloys. Wrought aluminum alloys (AA) are designated by a 4-digit number, the first of which indicates the main alloying element. Five thousand series aluminum alloys (designated as AA5xxx) have a main alloying element of Magnesium (Mg), and do not age harden. The naming convention of an aluminum alloy has no indication of its minimum ultimate tensile strength. However, the temper of an aluminum grade is generally appended to the designation to indicate any treatments the material has undergone, such as strain hardening or heat treating. A material with O temper has been annealed to bring it to the lowest temper available, making it the lowest strength and highest ductility temper. A material with O temper is the most easily bent and has the least tendency to spring back of all of the tempers available.

The tensile test is commonly used to determine the mechanical properties of materials, including materials used for auto-body components. Analysis of the engineering stress-strain curve (Figure 2-1) provides several important characteristics of the material, including yield strength, ultimate tensile strength, uniform elongation, fracture stress, and the total elongation. The yield strength (Marker #1, Figure 2-1) is the upper bound of the elastic deformation region. Beyond the yield strength, for ductile materials such as steel and aluminum, deformation is plastic and cannot be recovered when the load is removed. After the yield point, ductile materials undergo a period of strain hardening, in which the stress increases with increasing strain but the increment of stress required to cause further strain gradually decreases. The ultimate tensile strength is the maximum stress that a material can withstand in tension before failing (Marker #2, Figure 2-1). The uniform elongation is the strain that corresponds to the ultimate tensile strength (Marker #3, Figure 2-1). Subsequent loading leads to non-uniform elongation due to strain localization, and the evolution of localized strain eventually leads to failure. The fracture stress is the stress value at which fracture occurs (Marker #4, Figure 2-1). The total elongation is the engineering strain at which fracture occurs and is normally expressed in engineering strain (Marker #5, Figure 2-1). The strain hardening exponent (n-value) determines the rate of work hardening when the metal is deformed and is normally expressed in terms of true strain. Materials that have higher n-values have better formability than those with low n-values. The strain hardening exponent is the slope of

the logarithm of true stress plotted against the log of true strain curve, and is approximately equal to the true strain at maximum load.

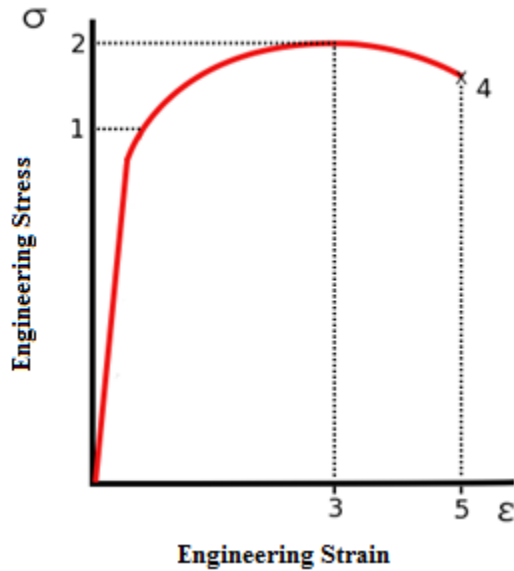


Figure 2-1: A generic engineering stress vs. strain curve.

## 2.2 Formability

The main challenge to implementing high strength steels and aluminum alloys is that these materials are typically less formable than the materials being replaced. Formability is the ability of a given sheet metal workpiece to undergo plastic deformation without failure. Forming limit curves have been used to visually display formability since the pioneering works of Keeler (1963), Goodwin (1968), and Hecker (1975) to quantify the ability of sheet materials to plastically deform without failure. The FLC is a curve in principal strain space that defines the limit of useful deformation in forming metallic sheet products, below which there is no risk of failure. The FLC is an effective quality assurance tool in the stamping industry for a range of forming conditions, such as deep drawing and stretching. Forming limit curves have been invaluable during die development, die try-out, and troubleshooting failures caused by localized necking during stamping. The ability of commercial Finite Element Analysis (FEA) to predict strain

states in virtual automotive parts has allowed FLCs to be used as failure criteria to evaluate forming feasibility during the early stages of product development.

The FLC is experimentally determined for a range of proportional strain paths where the ratio of major ( $\epsilon_1$ ) to minor ( $\epsilon_2$ ) strain remains constant to avoid non-linear strain path effects (Stoughton, 2001). Necking occurs as a result of plastic instability and the sheet metal visibly thins out in a narrow band as strain localizes in that area. The neck progresses as deformation continues until the weakened metal can no longer sustain the tensile forces across the neck and splitting eventually takes place. Necking is a failure mechanism that is characterized by plane strain deformation. The critical combination of strains was first observed to cause localized necking in the stretching of specimens using a hemispherical punch, a conical punch, and an elliptical punch by Keeler and Backofen (1963). The work of Keeler (1968) and Goodwin (1968) led to the construction of the modern forming limit diagram in strain space where any combination of strains above the curve presents some probability of failure.

An experimental forming limit curve can be constructed by plotting the critical combinations of strains on axes of major strain versus minor strain, for both negative and positive minor strains. There are several quasi-static experimental processes that can be used to determine the critical combinations of strains that create a neck. The hemispherical dome test, made popular by Nakazima (1968), uses fully clamped circular blanks with cut-outs of varying radii to obtain different load paths (Figure 2-2). The limiting dome height (LDH) test is a variant of the hemispherical dome test that uses strips of varying widths to generate different minor strains at failure. The double blank test, championed by Marciniak and Kuczynski (1973), is an improved version of the hemispherical dome test. The double blank test uses a carrier blank to eliminate the variability due to friction between the test piece and punch face (Figure 2-3). The flat bottom punch used in the double blank test eliminates the severe gradients normally found in the critical region of a workpiece formed in the hemispherical dome test and allows the neck to occur at the center of the specimen. The cross-section of the punch (rectangular, elliptic, or circular) can be altered to obtain different load paths.



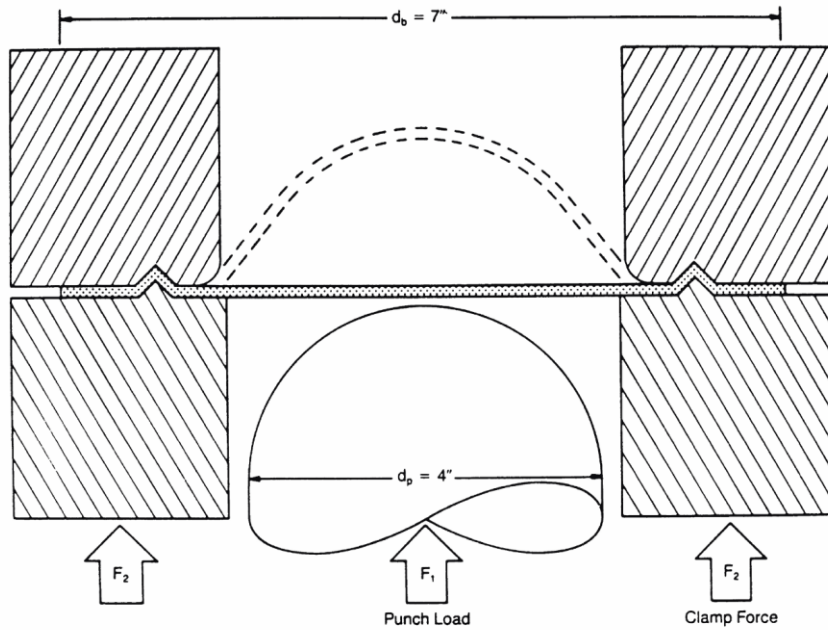


Figure 2-2: Schematic of the Nakazima (hemispherical dome) test.

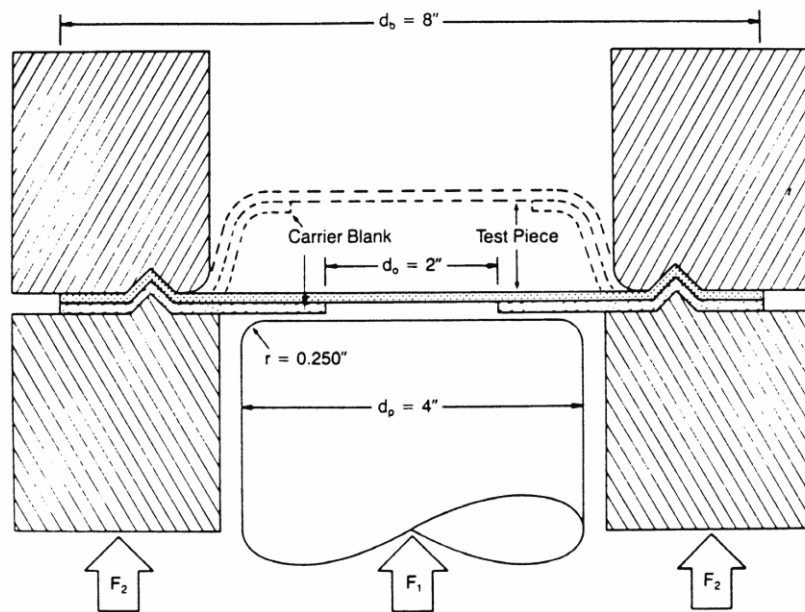


Figure 2-3: Schematic of the Marciniak (double blank) test.

The experimental determination of FLCs consists of forming samples until a failure point is reached. Around the world there are different techniques used to determine the FLC

which may potentially yield different results. The differences between the techniques lie in tooling, specimen geometry and in the method used to determine the critical strains.

Typically, in North America, necked grids for generating the experimental FLC are detected using the touch of a finger or visual observation (Green and Black, 2003). This tactile method is known in North America as the “Keeler” method, whereas Europeans refer to it as the “Hecker” method. The FLC is determined by plotting a curve that demarcates between safe and necked points in strain space (ASTM E2218, 2008).

Samples are formed until the strain sufficiently localizes in a region resulting in a neck. The subjective nature of distinguishing necked points from safe points requires that a large number of samples be formed and measured. The advantage with this method is that it is closest to the evaluation technique used in a press shop environment because limiting strains are recorded directly from incipient necks. However, the disadvantage lies in the fact that many samples and measurements are necessary to generate good quality FLCs using the sensory method. Further, it may be impossible to accumulate data points for certain regions of the FLC since there are many combinations of material and loading path that do not produce a neck before failure.

In Europe, the ISO 12004-2 standard procedure is used for the experimental determination of an FLC that is operator independent, does not rely on visible necking to generate data points, and requires less material and time than the Keeler method. Samples are formed until fracture and the strain distribution is measured across the fracture line. Limit strains are determined using an interpolation approach. Questions have been raised about the validity of the measured critical points because the determination of critical strains is based on curve fitting instead of physical measurement.

It was observed very early that the general shape of FLCs determined using the Keeler method do not vary significantly from one grade of low carbon steel to another, only the position of the FLC is shifted up or down in strain space to reflect differences in formability. As such, any difference in the plane strain formability ( $FLC_0$ ) of steels reflects a difference in the formability between the materials. Keeler and Brazier (1977) observed that, for low carbon steels, the amount of plane strain formability was primarily dependent on the strain hardening ability of the material (n-value) and sheet thickness.

The strain hardening exponent ( $n$ ) and sheet thickness ( $t_o$ ) (in millimeters) can be used to theoretically determine the forming limit in plane strain ( $FLC_0$ ), also known as the plane strain intercept (Equation 1). Despite the publication of other equations that more closely match the experimental data, Keeler and Brazier's equation for the plane strain intercept has been widely used across North America to predict the position of the FLC for low-carbon steel sheets due to its simplicity. To complete the theoretical FLC, the negative minor strain side of the FLC coincides with a constant thickness strain and can be plotted using the principle of constant volume. The positive minor strain side of the FLC is generally constructed using a 3<sup>rd</sup> or 4<sup>th</sup> order polynomial function obtained by fitting it to experimental data. Although this theoretical calculation was developed for low carbon steels, it is commonly used for DP steels with reasonable accuracy.

$$FLC_0 = \frac{(23.3 + 14.13t_o) * n}{0.21} \quad (\text{Equation 1})$$

Similarly, Raghavan et al. (1992) proposed a relation where the position of the FLC is dependent on the total elongation ( $e_f$ ) (in percent) in a tension test (Equation 2). The Raghavan equation was also intended for use with low carbon steels, but does not have the same popularity as the Keeler equation. The Raghavan equation is often not used because of the extra effort required to experimentally determine the total elongation and the variability of total elongation in successive uniaxial tension tests.

$$FLC_0 = 2.78 + 3.24t_o + 0.829e_f \quad (\text{Equation 2})$$

The observation of consistent FLC shape for low carbon steels, although it is often used for advanced high strength steels, does not apply to aluminum alloys. The complexity of both the shape and height of aluminum forming limit curves means that theoretical calculations of the FLC require using principles of plasticity, instability theory, and damage mechanics.

There are many factors, particularly during manufacturing, which can affect the formability of any sheet material. One should exercise caution when extrapolating an

experimental FLC generated from a particular batch of material and from a particular supplier to represent the formability for a particular grade of material. Changes to the shape and position of the FLC can occur from variations in chemistry and manufacturing processes, which vary from supplier to supplier and even from batch to batch.

Die engineers routinely use finite element analysis in the metal forming industry to assess the formability of sheet metal products long before the dies are built in order to save money in die build and tryout costs. One of the most important objectives in the numerical analysis of a production part is to avoid necking and fracture of the sheet metal. The engineer determines the forming severity by comparing the predictions of the FEA to a forming limit criterion, which is a function of the sheet metal properties and the forming history. Strains at different points across the surface of the part can be plotted on the forming limit diagram and the position of these strain points in relation to the forming limit curve provides an indication if failure (splitting, necking, or wrinkling) is expected. Obviously, a critical factor in the success of any numerical analysis is the reliability of this forming limit criterion.

The tremendous importance of FLCs in the sheet metal forming community has led to a considerable amount of research on FLCs of sheet metal involving many different aspects. The established empirical relations for many grades of automotive sheet steel must be independently validated for new materials and manufacturing processes. In general, research and development efforts on FLCs can be divided into three main categories: A) experimental determination B) empirical predictions based on experimental data C) theoretical calculations using principles of plasticity, instability theory, and damage mechanics. Recent high-velocity forming works have been focused on experimental determination of the FLC to provide a target for calibration of empirical and theoretical models. The formability observed in high-velocity forming is normally quantified by plotting experimental strain measurements on a forming limit diagram. This approach allows for an easy quantification of formability changes with respect to quasi-static limits.

### 2.3 High-velocity Forming Processes

High-velocity forming methods have been used for decades, but recently their potential to increase sheet metal formability beyond that of conventional forming processes has been gaining more interest in the automotive industry (Psyk et al., 2011, Mynors and Zhang, 2002). The increase in material formability from the use of high-velocity forming processes could allow manufacturers to use high strength steels or low density aluminum alloys for new applications or to increase the complexity of the geometry in existing applications. There are many factors that contribute to the selection of a particular high-velocity forming process such as capital investment, safety, the materials that can be formed with the process, and the ability to quickly conduct successive forming increments. The various methods of high-velocity forming can be grouped into three general categories based on the source of the forming energy and based on how that energy is transferred to the blank: electromagnetic forming (EMF), explosive forming (EF), and electrohydraulic forming (EHF).

Electromagnetic forming uses the release of stored electrical energy through a multi-turn coil to generate a magnetic force in the work piece that propels it into a single sided die (Figure 2-4). A capacitor bank is charged with high voltage electricity, on the order of several kilovolts. When a switch is closed to complete the circuit, the stored energy is discharged through a coil or electromagnetic actuator that is positioned in close proximity to the blank being formed. The rapid increase of current in the coil creates a strong transient magnetic field that induces Eddy currents in the conductive workpiece. The Eddy currents in the workpiece run in a direction opposite to the primary current in the coil and produce an associated secondary magnetic field around the workpiece. The opposite magnetic fields cause the coil and workpiece to repel each other by the Lorentz effect. The rapidly increasing magnetic force accelerates the workpiece away from the actuator. Electromagnetic forming is most easily practiced with workpiece materials of high electrical conductivity because Eddy currents are critical. Steel and magnesium sheets usually require low resistance drivers to be used with EMF because of their high electrical resistivities. The coil must be positioned within 5mm of the blank to generate sufficient magnetic forces, which does not lend itself to successive forming increments

since the blank is formed away from the coil. It is not possible to quickly conduct consecutive pulses with EMF without opening the tool because the coil must be repositioned to be in close proximity to the workpiece after each pulse. Moreover, the service life of a coil is greatly limited by fatigue resulting from the large magnetic forces generated in the coil.

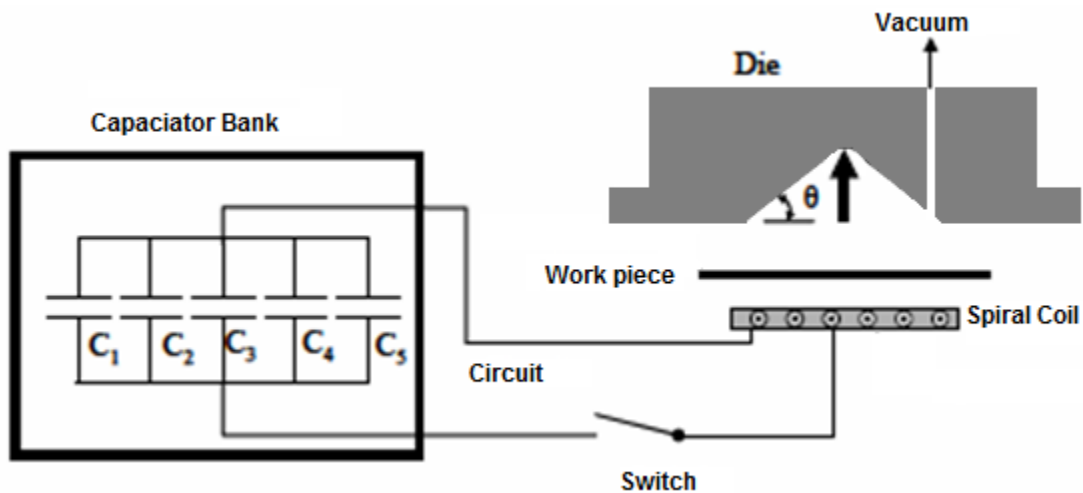


Figure 2-4: Schematic of electromagnetic forming. Image from Imbert et al. (2004).

Explosive forming uses the release of energy from an explosive charge to create a pressure pulse on the work piece (Figure 2-5). The charge is usually submerged in water to create a more uniform pressure distribution on the blank and increase the repeatability of the process. Explosive forming can be used with any workpiece material. It is not possible to quickly conduct consecutive pulses with EF without opening the tool because the explosive charge must be replaced after each pulse. The outcome of explosive forming processes is not consistent because small variations in the size and positioning of the charge can have a strong influence on the amount of energy that is released and on the rate of energy release. Explosive forming is not likely to be utilized for the high volume production of automotive panels because the use and storage of explosive materials in a manufacturing environment leads to obvious safety and security concerns.

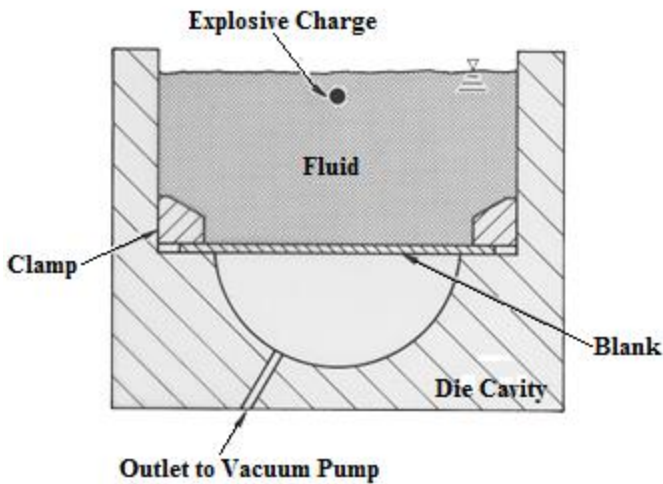


Figure 2-5: Schematic of explosive forming. Image from Avitzur (1983).

Electrohydraulic forming (EHF) is based upon a complex phenomenon related to the discharge of high voltage electrical current through a liquid (Figure 2-6). The first observations of strong mechanical forces generated during electric discharge in a liquid were reported by Lane (1767) and Priestly (1769). Additional historical perspectives, as well as early laboratory experiments and initial low volume industrial applications of the electrohydraulic effect for sheet metal forming, are described by Bruno (1968), Davies and Austin (1970) and Chachin (1978).

A bank of capacitors stores the high voltage electrical energy until the circuit is closed and the EHF process is initiated. The stored energy rapidly discharges across a pair of electrodes submerged in a fluid. The discharge of energy between the submerged electrodes creates a high pressure, high temperature plasma channel between the tips of the electrodes (Chachin, 1978). The resulting shockwave in the liquid, initiated by the expansion of the plasma channel, is propagated toward the blank at the acoustic velocity of the fluid. The water accelerated by the shock wave forms the sheet metal blank into a single sided die.

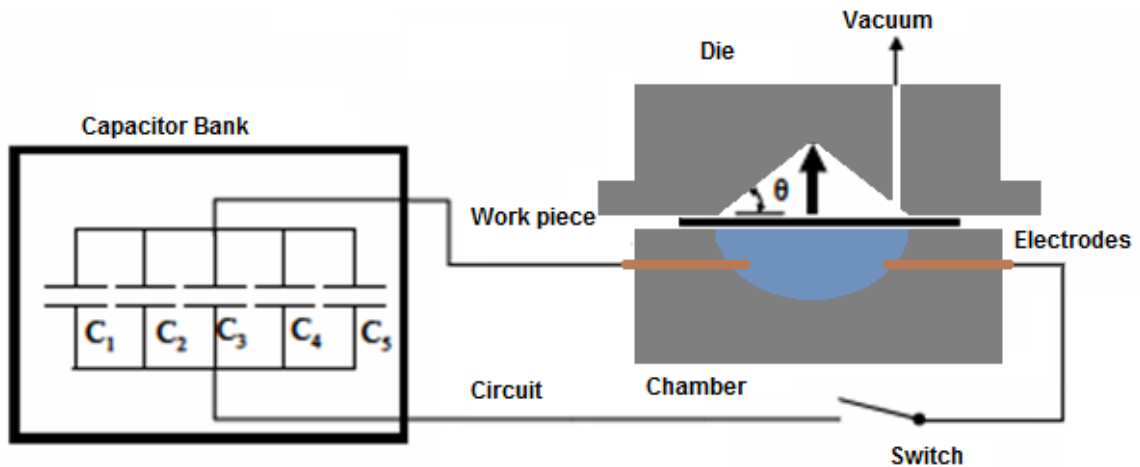


Figure 2-6: Schematic of electrohydraulic forming.

When considering the potential high volume production of automotive panels, EHF presents multiple advantages as compared to EMF. In contrast to EMF, EHF can be used with any workpiece material. In addition, the consumable electrodes in EHF are much cheaper and have a longer service life compared to the coil in EMF. The chief advantage of EHF is that, unlike EMF and EF, it is possible to quickly conduct successive EHF pulses to form a panel in a series of multiple forming increments because the water in the chamber can be refilled without opening the tool. In addition, the electrodes used in EHF do not need to be repositioned after each pulse because they can be located between 5 and 40cm away from the blank and still deliver a pressure pulse sufficient to plastically deform the blank.

Electrohydraulic forming is the most production ready of all the high-velocity forming processes. However, it is still not being implemented in large scale applications because the cycle time is slow compared to stamping, the electrodes must be in close proximity to the workpiece, and the results of the forming are not as repeatable as stamping. The production speed is limited by the time required to build-up the energy required for a discharge, the time required to fill the chamber with water, and the time required to vacuum the air from the die. The outcomes of EHF pulses are subject to significant variability because of the dynamic nature of the process, which makes achieving dimensional control challenging (Golovashchenko, 1999 and Woodward et al., 2011).



Despite some technical challenges, there are significant potential benefits of implementing EHF technology into vehicle production operations.

Aside from the recent interest in high-velocity forming processes (also referred to as pulsed forming processes or high strain rate forming processes) due to the potential to enhance material formability, there are a number of benefits that have historically made pulsed forming beneficial for certain applications. The significantly lower cost of one sided tools as compared to mating tools is one of the major advantages which has driven the initial implementation of pulsed forming technologies in low volume industrial and defense applications. The short duration of the applied forming pressure is a significant advantage compared to quasi-static one-sided forming processes, such as sheet hydroforming, because pulsed forming does not necessitate the large press sizes required for quasi-static hydroforming processes. The reduced press force required by pulsed forming processes allows extremely large parts to be formed with less capital investment and less technical challenges.

#### **2.4 Formability Improvement via High-velocity Forming**

Pulsed forming processes, including high-velocity forming processes, are capable of increasing the formability of sheet materials beyond their quasi-static forming limits. Perhaps the earliest experimental evidence showing the increased ductility of dynamically loaded tensile specimens was published by Clark and Wood (1950). A historical perspective of publications on the increase of material ductility in the dynamic tensile test was described by Hu and Daehn (1996). However, dynamic tensile tests are much less complex than pulsed metal forming processes and no clear correlation can be made between dynamic tensile tests and the formability observed in pulsed forming (Li et al., 2013). The significantly enhanced ductility observed in AA6061-T4, copper, and interstitial free iron sheets electrohydraulically formed into a conical die by Balanethiram and Daehn (1992, 1994) renewed interest in the dynamic deformation of metallic materials. Numerous authors have recently shown that high-velocity forming processes are capable of producing safe strains significantly above the quasi-static forming limit

curve for a variety of processes and materials. Research teams led by Worswick (2004, 2005), Daehn (2005), Dariani (2009), Rohatgi (2011, 2012), and Golovashchenko (1999, 2007, 2013) have made substantial contributions toward quantifying the formability improvements and identifying the mechanisms of formability improvement in high-velocity forming.

Imbert et al. (2004) conducted electromagnetic forming experiments of aluminum alloys AA5754 and AA6111 in both free forming and conical die forming. The free formed specimens did not show a formability increase, but the sheets formed into a conical die had necking strains above the quasi-static FLC (Figure 2-7). The disparity between the strain measurements for blanks formed into a 45 degree die compared to a 40 degree die indicates that there is some relation between the die geometry and the forming limit. Metallographic analysis indicated that damage is suppressed during the die forming process by the tool-sheet interaction. Accordingly, the magnitude of damage and the associated forming limit of the sheet vary with the die geometry because the effect of the tool-sheet interaction decreases as the die angle increases. The large compressive and shear forces that result from the blank contacting the die at high velocity suppress the nucleation and growth of voids within the sheet metal as it is deformed, thereby suppressing localization and failure (Samei et al., 2014). The high speed impact between the sheet and die causes phenomena such as through-thickness shear deformation and bending-unbending in the area of contact that suppress the damage mechanisms.

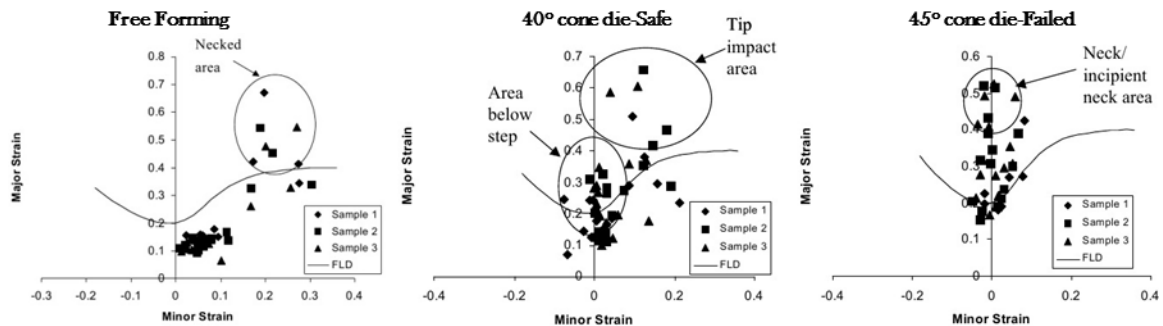


Figure 2-7: Strain measurements for free forming, 40° conical die forming, and 45° conical die forming of 1.0mm AA5754. Image from Imbert et al. 2004.

Seth et al. (2005) conducted electromagnetic forming experiments to study the impact of five grades of steel against curved male punches. The steels selected for the investigation were low cost, low carbon, and cold rolled steels with thicknesses between 0.15mm and 0.38mm thick. The sheets were accelerated towards axisymmetric and wedge shaped punches, each with three different cross section curvatures to achieve different strain paths. A scatter of high failure strains, on the order of 30–50% engineering strain were observed for all the steels tested. The high failure strains represent a significant improvement over the quasi-static formability, which was attributed to the instability strain due to high velocity deformation, through-thickness compressive stress due to impact, and the mechanical boundary conditions of the sheet. Although there are large differences in their quasi-static ductilities, the high velocity ductilities of these steels were approximately the same. Probably the most remarkable observation from this study is that all the steels studied, almost irrespective of their quasi-static ductility, showed very high formability in this deformation mode of high velocity impact (Figure 2-8). According to Seth et al. (2005), it appears that the quasi-static ductility of the material is not of primary importance to the material’s formability in high velocity impact. These observations highlight the possibility to take advantage of the dramatic improvement in formability to produce low cost components from high strength steels by using high-velocity forming operations.

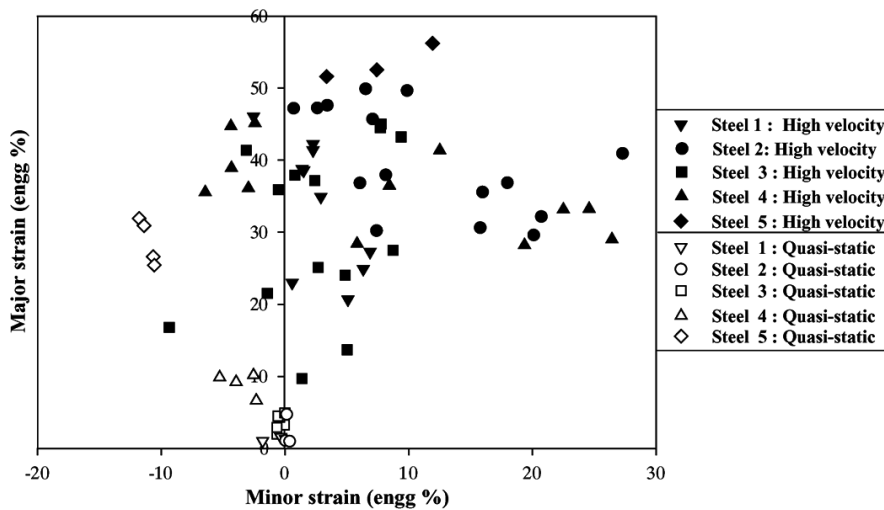


Figure 2-8: The high velocity and quasi-static failure strains for five steels. Image from Seth et al. (2005).

Dariani et al. (2009) conducted experiments to study the formability of AA6061-T6 aluminum and AISI 1045 steel. The formability of each sheet material was experimentally determined in quasi-static forming, impact forming, and explosive free forming operations. An investigation using notched specimens to generate data across the entire FLC showed substantial formability improvement in the explosive free forming of both materials (Figure 2-9). The formability improvements reported by Dariani et al. were much more moderate than the results reported by Seth et al. (2005). The low-velocity dynamic impact forming experiments showed a small formability improvement in the biaxial and plane strain regions of the FLD. The relative gain in FLC<sub>0</sub> of aluminum (2.4x) was much greater than steel (1.5x) in the explosive forming experiments.

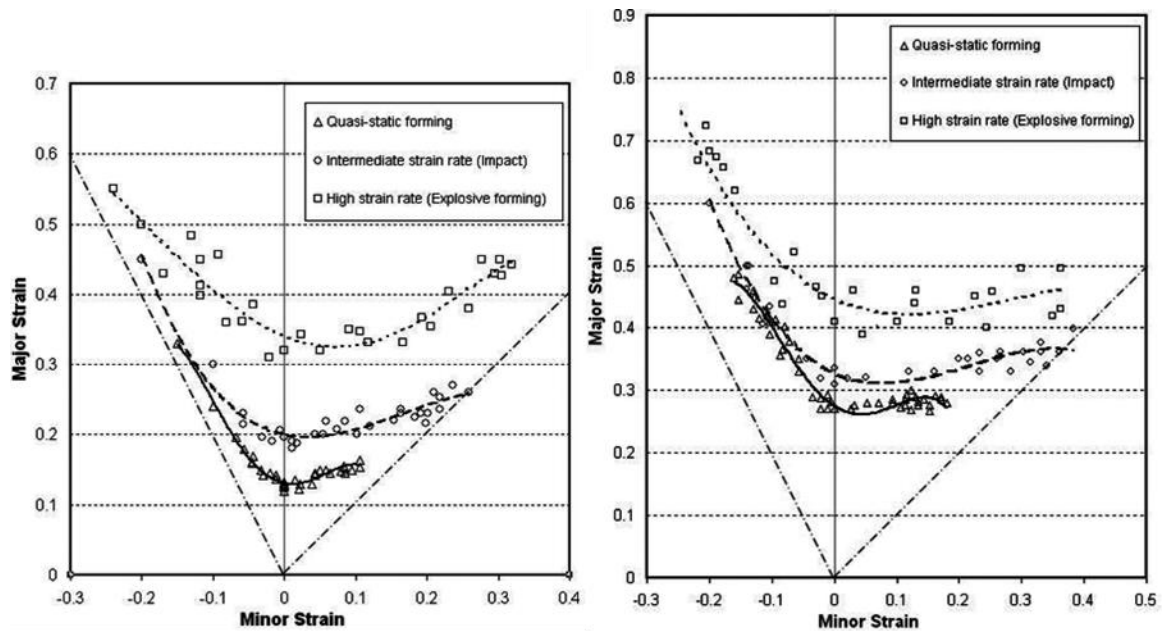


Figure 2-9: FLDs of AA6061-T6 and AISI 1045 generated from quasi-static, impact, and explosive forming methods. Image from Dariani et al. (2009).

Rohatgi et al. (2011) conducted electrohydraulic forming experiments of AA5182-O aluminum in free forming. The open window tool used in free forming allowed several in-process parameters to be quantified using high-speed digital image correlation. The experimental time evolution of sheet displacement, velocity, strain, and strain rate were quantified for three locations along the radial direction at distances of 0mm, 22.5mm, and

45mm from the center of the specimens (Figure 2-10). Prior research relied on the correlation between final strain measurements and numerical simulation to estimate strain rates and other in-process information. The experimental free forming results allow the opportunity to validate numerical models based on the time evolution of displacement, velocity, strain, and strain rate. However, the experiments lack energy measurements and detailed strain measurements, thus preventing other researchers from taking full advantage of the published results.

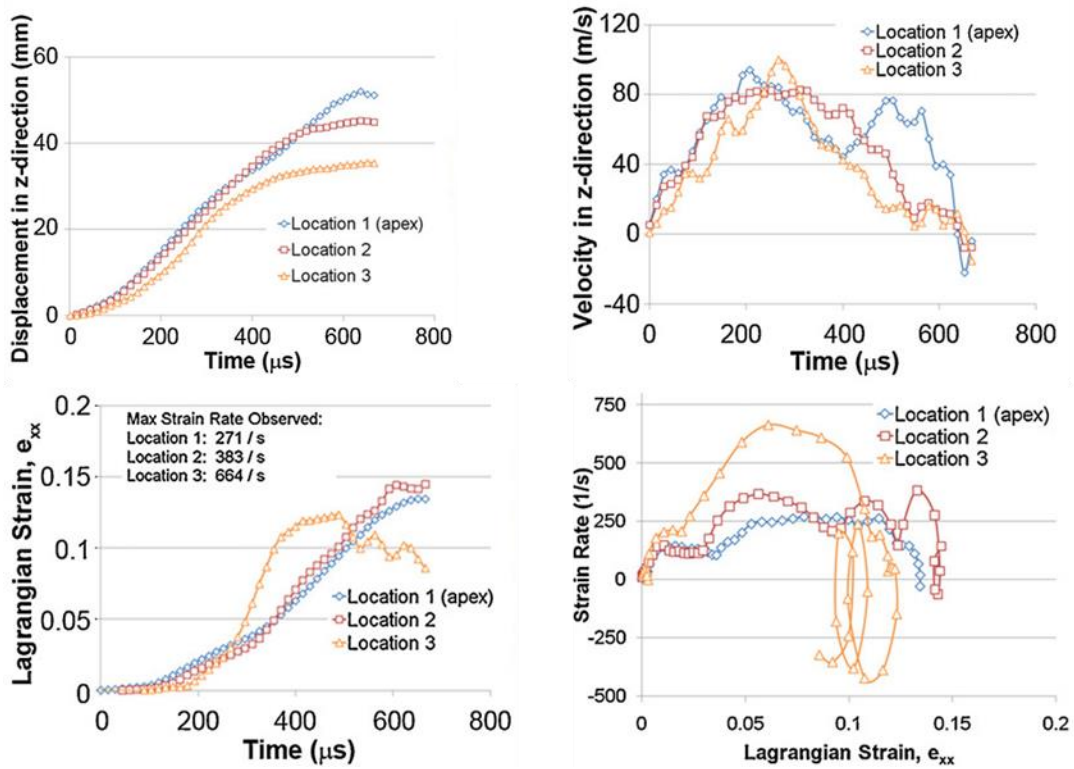


Figure 2-10: Experimental displacement, velocity, strain, and strain rate for an AA5182-O specimen formed with 7.5kV in free forming. Image from Rohatgi et al. (2011).

Golovashchenko et al. (2013) conducted electrohydraulic forming experiments on DP500, DP590, DP780, and DP980 dual phase steels into conical and V shaped dies, which induced strains in the biaxial and plane strain regions of the FLD, respectively. The maximum strains that were achieved were significantly greater than those which

were attained in Nakazima specimens formed over a hemispherical punch under quasi-static conditions. Increases in plane strain formability between 63%-190% were possible when the die was completely filled (Figure 2-11). However, when the die was unfilled, failure occurred near or below the theoretical quasi-static FLC. A numerical model predicted peak strain rates in the region of the apex of the conical specimens of approximately  $6000\text{s}^{-1}$  when the sheet fails to completely fill the die and approximately  $20,000\text{s}^{-1}$  when the sheet completely fills the die.

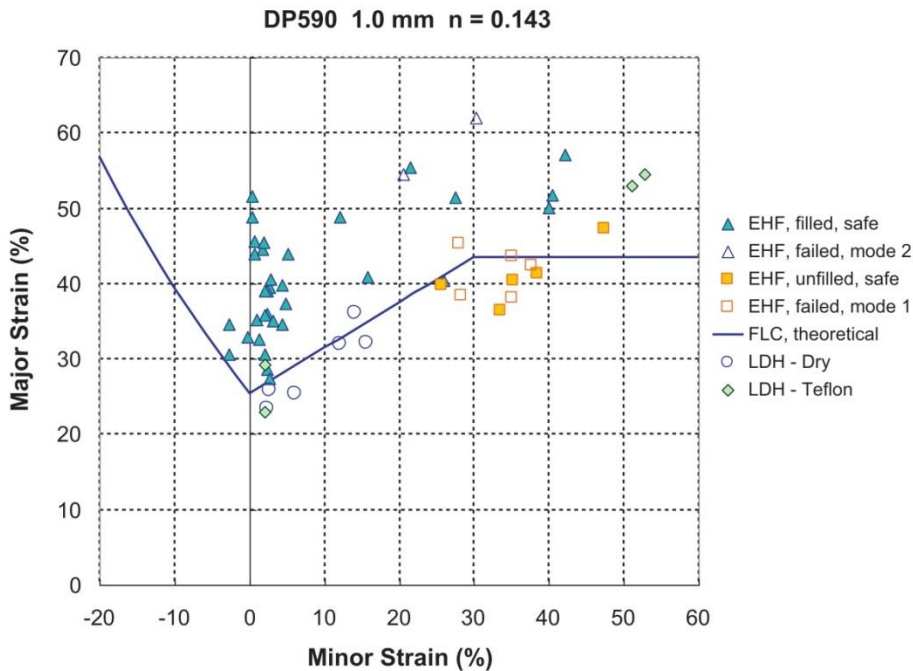


Figure 2-11: Combined LDH and EHF formability results for 1.0mm DP590. Image from Golovashchenko et al. (2013).

There is conflicting evidence about formability improvement in high-velocity forming. Golovashchenko et al. (2013) reported no formability increase in radially split biaxial DP590 blanks that failed to fill the die in EHF, and EMF experiments on aluminum alloys by Imbert et al. (2005), Oliveira et al. (2005), and Golovashchenko (2007) showed no formability improvement in free forming. In contrast, Dariani et al. (2009) showed moderate formability improvement in both AISI1045 steel and AA6061 aluminum using explosive free forming tests. Further complicating the evaluation of free forming formability is the fact that the majority of the previous high-velocity formability

investigations have reported only positive minor strains; this is because this strain state can be easily generated without modifying the blank geometry. To address this issue, Davies (2012) and Dariani et al. (2009) designed specimen geometries to generate strain states with negative and near zero minor strains in the gauge sections. However, in both attempts, the specimens were susceptible to cracking in the corners of the cut-outs prior to necking in the gauge section, so the gauge section results were unreliable. The specimens used by Dariani et al. (2009) and Golovashchenko et al. (2013) to generate different strain states required more than one experimental set-up, which could have an effect on the formability that is observed. In light of these issues, an experimental procedure to determine the formability across the entire minor strain spectrum in the same experimental set-up would substantially advance the ability to consistently quantify the formability of sheet materials in high-velocity forming.

### 3 Methodology

#### 3.1 Experimental Methodology

In EHF, electrical energy is stored by a bank of capacitors inside a pulse unit. The electrical energy is converted to the kinetic energy needed to form sheet metal by the rapid discharge of high voltage electrical current through a fluid. The discharge of electrical energy across a pair of electrodes in a fluid filled chamber creates a plasma channel between the electrode tips. As the plasma channel expands a pressure wave propagates toward the sheet metal blank at the acoustic velocity of the fluid. The main pieces of equipment required to conduct EHF experiments are a pulse unit, a chamber, a forming tool, and a press (Figure 3-1).

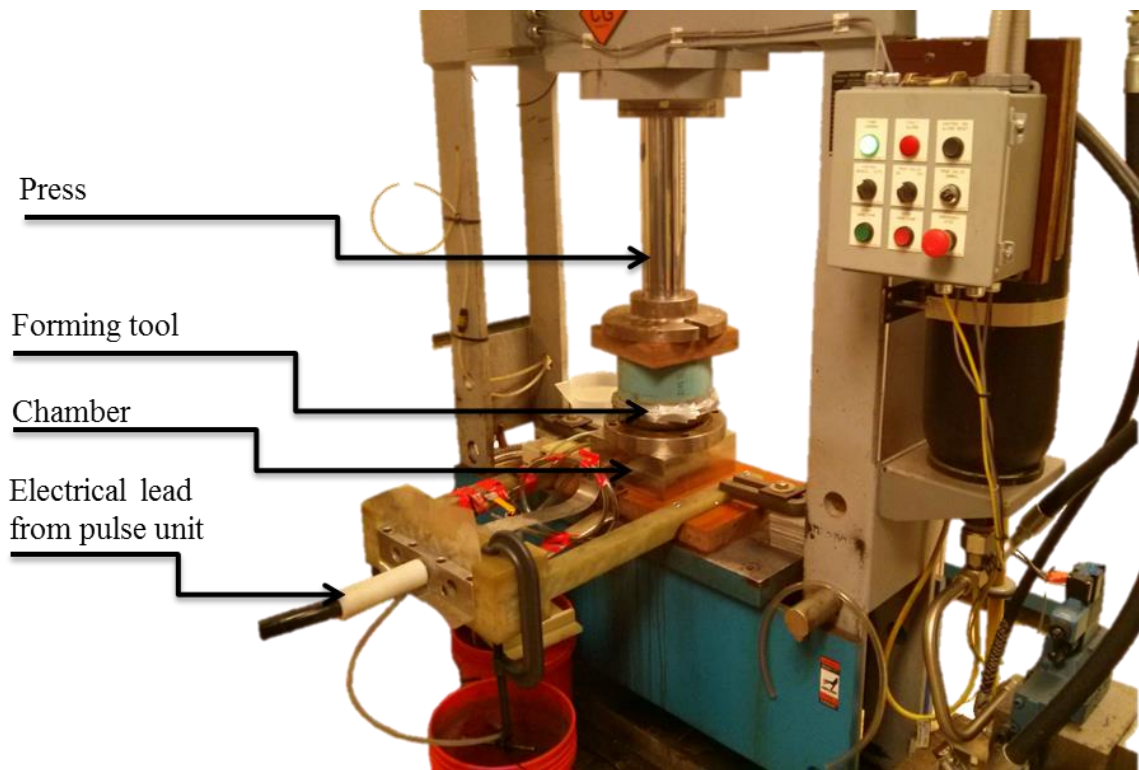


Figure 3-1: The experimental EHF setup.

New equipment was built and some existing tools were modified to facilitate the safe and effective operation of EHFF experiments. In order to quantify the forming limit of sheet materials in EHFF, experiments were conducted to determine the critical combinations of



strains which cause necking. The EHFF necking strains were obtained by deforming specimens along four different strain paths by following a detailed experimental procedure in order to ensure consistency between specimens. A measurement procedure was also established for consistent results and accurate strain measurements.

### 3.1.1 Pulse Unit

The Magnepress pulse unit was used to provide the electrical energy for the EHF experiments. The duration of the discharge and the actual energy delivered to the chamber are internal characteristics of the pulse unit, and could affect the outcome of the experiments. The sensitivity of the EHFF experiments to even small changes in the electrical pulse made it important to use only one pulse unit and thus avoid inconsistencies in the experimental data.

The operator can adjust the amount of energy discharged between the electrodes by specifying the input voltage. The Magnepress can deliver between 6kV and 15kV of input energy. The theoretical electrical energy ( $U$ ) stored in a charged capacitor can be expressed in terms of capacitance ( $C$ ) and voltage ( $V$ ) (Equation 3). The capacitance of the capacitor banks is an intrinsic property of a pulse generation machine and can only be adjusted by adding or removing capacitor banks. The Magnepress has four 50 $\mu$ F capacitor banks for a total capacitance of 200 $\mu$ F, and corresponding maximum energy storage of 22.5kJ. The pressure pulse generally lasts between 100  $\mu$ s and 200 $\mu$ s, with a peak magnitude on the order of 10MPa. The forming time for a sheet metal blank is on the order of 100-350 $\mu$ s. The Magnepress is paired with a hydraulic Dake press with a closing force of 100 tons to ensure that there is no drawing in of the blank.

$$U = \frac{1}{2} CV^2 \quad (\text{Equation 3})$$

The EHF chamber, die geometry, and workpiece material have the largest influence on the amount of energy required in an EHF discharge. The portion of the released electrical energy that is actually delivered to the sheet depends on factors related to the

experimental set-up and the electrical efficiency. The parameters which define the efficiency of the EHF process are the position of the electrodes, the shape and volume of the chamber, the distance between the discharge channel and the blank, the electrical properties of the liquid, the charged voltage, the capacitance of the circuit, and the inductance and resistance of the equipment and connecting cables.

It is important to note that the performance of the Magnepress pulse unit significantly changed during the EHF trials. Early in the experimental process, a strong arc occurred outside the chamber which resulted in a reduction in energy delivered to the forming chamber for the remainder of the experiments. The amount of current delivered with each pulse was significantly reduced after the arc (Figure 3-2). The evidence indicates that the arc caused some damage to the electrical system, resulting in a reduction of the amount of energy delivered to the chamber. Regrettably, the oscilloscope was not used to make voltage measurements before the arc, so it is not possible to quantify the amount of energy delivered with each pulse before the arc and therefore there is no baseline to directly quantify the reduction in energy. A comparison of biaxial AA5182-O specimens confirms that the arc caused damage to the Magnepress by reducing the amount of energy that is discharged with each pulse (Table 3-1). Before the arc, a specimen necked with an input voltage of 11.5kV (13.2kJ) and a second specimen split with an input voltage of 12.0kV (14.4kJ). After the arc, a specimen with an input voltage of 12.5kV (15.6kJ) was safe. Several changes were made to the experimental set-up to improve the process efficiency and overcome the energy lost from the damage caused by the arc, such that there would be sufficient energy to form a neck in all specimen geometries for both materials.

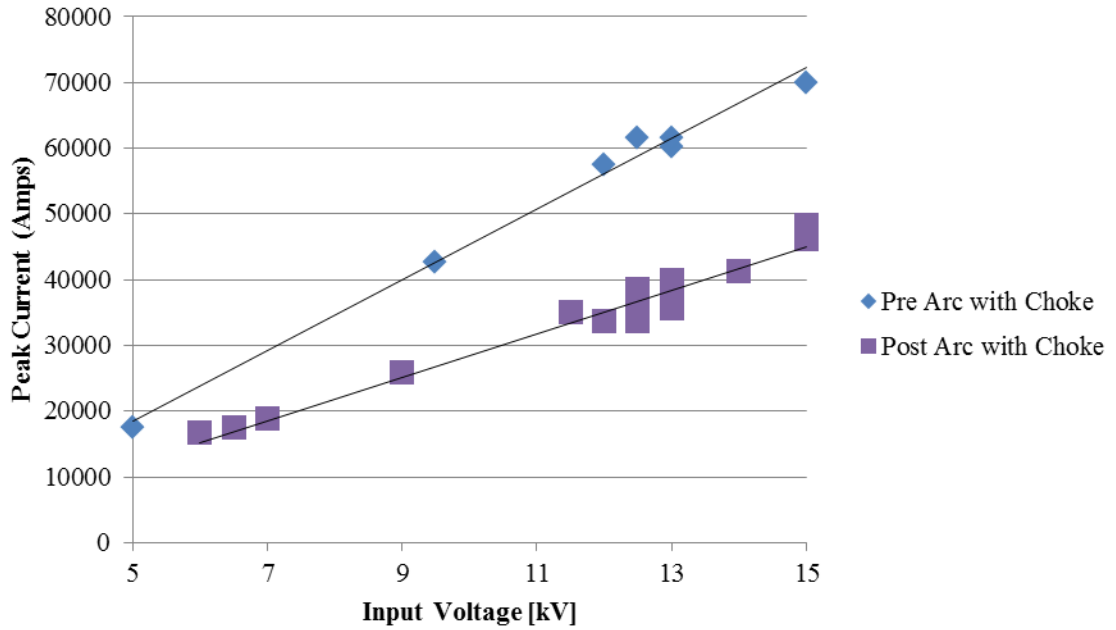


Figure 3-2: The peak amperage delivered before and after the arc outside the chamber.

Table 3-1: Comparison of aluminum biaxial specimens before and after the arc occurred outside the chamber.

Condition	Input Voltage (kV)	Result	Photo
Pre Arc	11.5	Neck	
	12.0	Split	
Post Arc	12.5	Safe	

### 3.1.2 Process Efficiency and Chamber Design

The maximum energy storage of the Magnepress pulse unit was insufficient to form all the specimen geometries with the original chamber. Several tooling modifications, including building a new chamber, were made to increase the efficiency of the EHF process and correspondingly lower the required energy to within the limits of the Magnepress.

A new chamber was built to improve the process efficiency by reducing the stand-off distance, decreasing the chamber bowl volume, and decreasing flow obstructions. The diameter and depth (120mm and 60mm, respectively) of the new chamber (Figure 3-3, Appendix A) were reduced to make a chamber bowl with 0.45L volume, more than seven times less than the 3.26L volume of the original chamber. The reduced volume of the new chamber makes it much more convenient to flush the water from the chamber after each pulse and refill it with fresh tap water. Flushing the chamber water after each pulse ensures that there are no dissolved metals in the water from the previous pulse which could change the electrical resistance of the water and affect the consistency of the EHF process. The flow obstructions in the original chamber occur because a steel ring is required to mate the large diameter chamber to the small diameter tooling (Figure 3-4). The change in diameter by the chamber ring restricts the flow of the water around the periphery of the chamber, and accordingly decreases the process efficiency. Flow restrictions such as the chamber ring affect the shape of the pressure wave that will impact the specimen (Hassannejadasl et al., 2014). Unlike the original chamber, the new chamber was built to match the existing tooling without any flow obstructions. The shape of a chamber is an important factor in the energy efficiency, so the new chamber bowl has a hemispherical shape to allow the pressure pulse to deflect off the chamber walls with as little energy loss as possible. Based on previous experience, an elliptical or square chamber bowl would lower the process efficiency by absorbing more of the energy from the shockwave when it impacts the chamber.

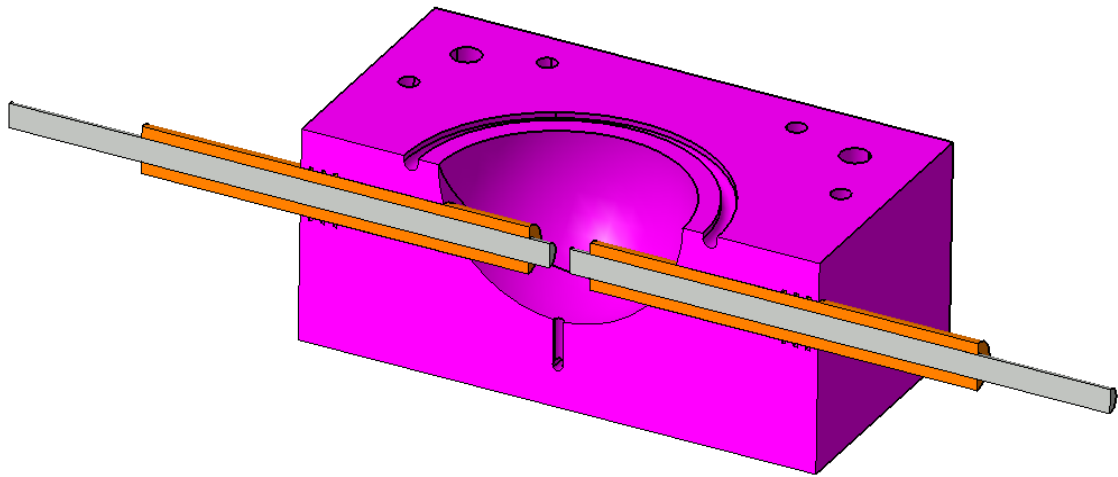


Figure 3-3: Half view of the new chamber.

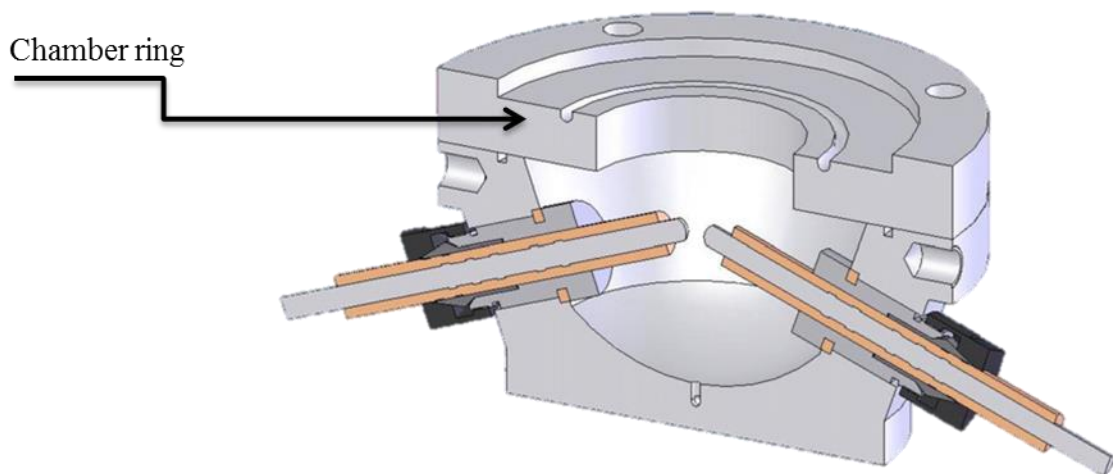


Figure 3-4: Half view of the original chamber and the chamber ring.



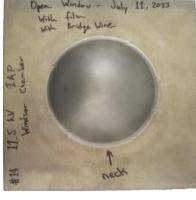

The new chamber has a flat top surface, unlike the stepped surface on the original chamber. The step in the original chamber allows for the manual alignment of forming tools, which all have the same circular shape and outer diameter. The new chamber uses removable dowels to align the dies. The dowel spacing was calculated such that square 200mmx200mm blanks can be used, which eliminates the extra steps required for the preparation of octagonal blanks. The flat surface of the new chamber allows for quicker

water clean-up after each pulse, which reduces cycle time. The largest benefit of the flat top surface is that it allows for chamber rings of different heights to be placed on top of the chamber in order to increase the volume of the chamber. In addition, the dowels can be easily removed to reveal a flat surface that allows for the easy attachment of dies of different sizes and shapes.

The electrodes in the new chamber were designed to sit horizontally to increase the longevity of the electrodes. The electrodes in the original chamber are installed at an angle from the horizontal, making them susceptible to bending forces which cause premature failure. The stand-off distance between the electrodes and blank in the new chamber was set to 30mm in an effort to reduce the energy loss as the pressure pulse propagates, compared to the original chamber which had a stand-off distance of 60mm.

The preliminary EHFF results obtained using the new chamber were significantly different than the results obtained in the original chamber (Table 3-2). The original chamber caused biaxial blanks to rupture radially, with the critical voltage for aluminum biaxial blanks between 6.8kV (4.6kJ) and 6.9kV (4.8kJ). The new chamber caused biaxial blanks to rupture circumferentially, with a critical voltage for aluminum biaxial blanks of 11.5kV (13.2kJ). The circumferential failure mode was different than the radial failure mode previously observed when forming biaxial specimens in the original chamber, but the biggest concern was that the process efficiency actually decreased with the new chamber because the critical input voltage range had increased compared to the original chamber.

Table 3-2: Comparison of the input voltages required to cause a neck and the failure types in biaxial AA5182-O specimens in the original and new chambers.

Condition	Input Voltage (kV)	Result	Photo
Original Chamber	6.8	Safe	
	6.9	Radial Split	
New Chamber	11.5	Neck	
	12	Circumferential Split	

The arc outside the chamber occurred before any further comparisons could be made. The amount of energy associated with a specified input voltage cannot be compared before and after the arc. However, the effects of changes made to the experimental setup to overcome the energy loss due to the arc can be compared.

The volume of water and the standoff distance between the electrodes and blank were thought to be the factors that lowered the process efficiency of the new chamber. A 30mm tall chamber ring (Figure 3-5) was added to increase the volume of water contained in the chamber by 340mL and to increase the standoff distance. With the addition of the chamber ring, the volume of the chamber bowl increased to a practical volume of 750mL with the electrodes installed. The chamber ring had the same opening

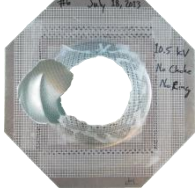
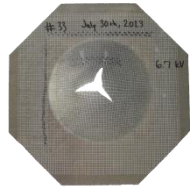
diameter as the new chamber, so no flow obstructions were introduced by adding the chamber ring. The failure mode in biaxial aluminum changed from circumferential splits to the expected radial splits with the addition of the chamber ring. The input voltage required to neck a biaxial aluminum sample reduced from 11.5kV (13.2kJ) without the chamber ring to 6.6kV (4.4kJ), which indicates the use of the chamber ring benefits the development of the pressure pulse before it contacts the blank. The improved process efficiency with the chamber ring shows that the volume of water contained in the new chamber without the chamber ring is much lower than the optimum amount and the stand-off distance was too small. The use of the new chamber with the chamber ring provided marginal process efficiency improvements over the original chamber.



Figure 3-5: The chamber ring that was added to the new chamber to increase the volume.



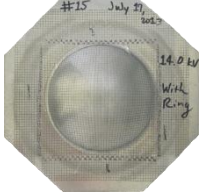
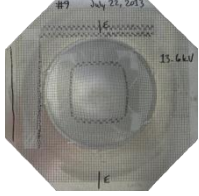
Table 3-3: Comparison of the input voltages required to cause a small split and the failure types in biaxial AA5182-O specimens in the new chamber without and with the chamber ring.

Condition	Input Voltage (kV)	Result	Photo
New Chamber -without chamber ring	10.5	Circumferential Split	
New Chamber -with chamber ring	6.7	Radial Split	

The Magnepress pulse unit has an optional electrical accessory called an inductance choke. The discharge circuit from the Magnepress can be wired through the choke and then from the choke into the busbars, rather than directly connecting the electrical leads from the Magnepress to the busbars. The choke helps to protect the Magnepress machine by preventing the current from exceeding the critical current limit. The choke delivers approximately the same energy to the chamber by lowering the current amplitude and increasing the time, essentially making the discharge less dynamic. During the troubleshooting process of trying to recover the energy lost by the arc outside the chamber, the choke was circumvented by wiring the Magnepress directly to the busbars. The oscilloscope and chamber ammeter were connected to observe the current-time traces with and without the choke. However, the voltage probes were not connected while the choke was being used, so it is not possible to provide quantitative values for the energy delivery in that configuration for comparison purposes. With the choke, a biaxial steel specimen necked with an input voltage of 14kV (19.6kJ). Without the choke, biaxial steel specimens necked with an input voltage of 13.6kV (18.5kJ). Bypassing the choke caused a small reduction in the input voltage and theoretical energy required to cause a neck in biaxial steel specimens (Table 3-4). The inductance choke was bypassed for the

remainder of the tests because it was not possible to form a necked uniaxial steel specimen when the choke was used. The peak current was nearly restored to pre-arc levels by removing the choke (Figure 3-6). Although the peak current was recovered, the total energy discharged was likely much less with the choke removed because the duration of the pulse was much shorter. Despite the likely net loss of energy delivered to the chamber from the pre-arc with choke condition to the post-arc without choke condition, the significantly reduced pulse time with the choke circumvented made the EHF discharge more dynamic and marginally reduced the input voltage required to form a neck.

Table 3-4: Comparison of the input voltages required to cause a neck and the failure types in biaxial DP600 specimens in the new chamber with and without the inductance choke.

<b>Condition</b>	<b>Input Voltage (kV)</b>	<b>Result</b>	<b>Photo</b>
New Chamber -with choke	14	Neck	
New Chamber -without choke	13.6	Neck	

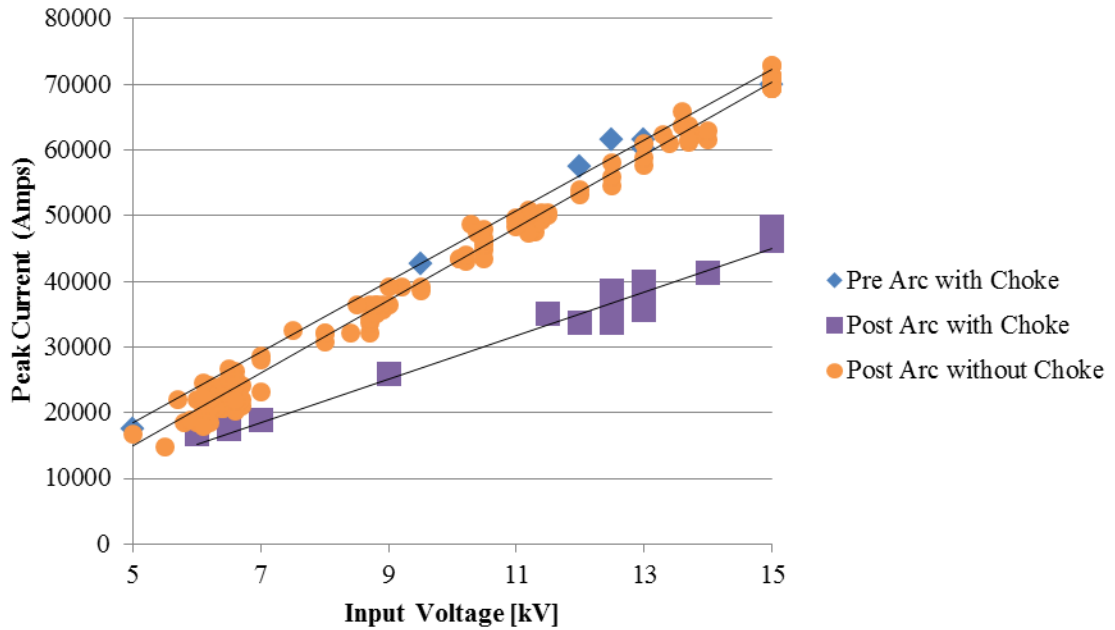

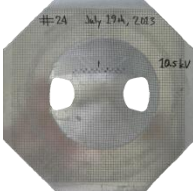


Figure 3-6: Peak current measurements with and without the choke.

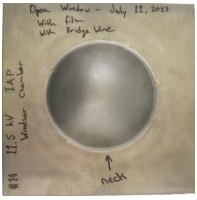
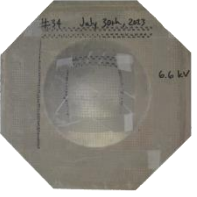
There is evidence to suggest that the input voltage required to form a necked specimen is reduced by either circumventing the choke or adding the chamber ring to the new chamber. However, because EHF is a dynamic process, it is important to ensure that simultaneously adding the chamber ring and circumventing the choke results in a reduction in the input voltage required to form necked specimens (Table 3-5). Two plane strain DP600 specimens were necked with an input voltage of 12.0kV (14.4kJ) when formed with the choke and without the chamber ring. When the choke was bypassed and the chamber ring was installed, the critical input voltage for plane strain DP600 specimen was 10.1kV (10.2kJ). It is evident that simultaneously bypassing the choke and using the chamber ring reduces the input voltage required to form a necked specimen.

Table 3-5: Comparison of the effects of simultaneously circumventing the choke and adding the chamber ring for plane strain DP600 specimens.

<b>Condition</b>	<b>Input Voltage (kV)</b>	<b>Result</b>	<b>Photo</b>
New Chamber -no chamber ring -with choke	12	Neck	
New Chamber -with chamber ring -without choke	10.1	Neck	

The simultaneous use of the chamber ring and circumventing the choke was shown to reduce the amount of input voltage required to form a necked specimen. However, it is also possible to determine if these changes were able to overcome the energy loss caused by the arc (Table 3-6). Prior to the arc, a biaxial AA5182-O specimen necked with an input voltage of 11.5kV (13.2kJ) without the chamber ring and with the inductance choke. After the arc, a biaxial AA5182-O specimen necked with an input voltage of 6.6kV (4.4kJ) with the chamber ring and without the inductance choke. The combination of using the chamber ring and circumventing the choke increased the overall process efficiency in excess of the energy loss caused by the arc.

Table 3-6: Comparison of the input voltage to cause a neck in biaxial AA5182-O specimens in the new chamber before the arc, without the chamber ring, and with the choke, to the configuration after the arc, with the chamber ring, and without the choke.

Condition	Input Voltage (kV)	Result	Photo
New Chamber -pre arc -no chamber ring -with choke	11.5	Neck	
New Chamber -post arc -with chamber ring -without choke	6.6	Neck	

The EHF set-up of the new chamber with the chamber ring and the choke circumvented is more efficient than the set-up using the original EHF chamber, as demonstrated by the reduction in input energy required to form non-safe specimens. Despite the increase in input voltage required to form a necked specimen after the damage caused by the arc, the process efficiency was sufficient to form at least one neck in each of the strain paths for both DP600 and AA5182-O. In order to be consistent, all the specimens used to generate the EHF FLC for both AA5182 and DP600 were formed on the Magnepress, with the new chamber, with the chamber ring, and without the inductance choke.

### 3.1.3 Tool Selection and Design

The EHF specimens used cut-outs of various size and shape to generate the desired strain path in the gauge section. The specimens were formed without driver sheets, which allowed water to pass through the holes in the blank. In a few test samples where the modified specimen geometries were formed in a closed die, the water that passed through the holes in the blank reflected off of the forming tool and on to the top side of the specimen and caused undesired deformation in the specimen. In extreme cases, the blank

actually formed in the opposite direction (Figure 3-7). The modified geometry specimens are better suited to open window (free forming) tools (Figure 3-8) because it is possible to prevent water from rebounding off the die and onto the top side of the specimens, thereby avoiding undesired deformation.

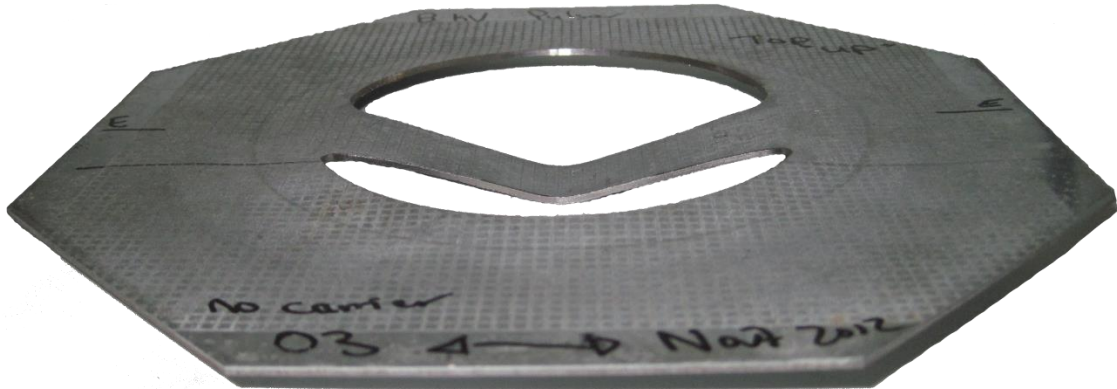


Figure 3-7: A uniaxial specimen formed into a 50 degree conical die had negative displacement due to water reflecting off of the forming tool.

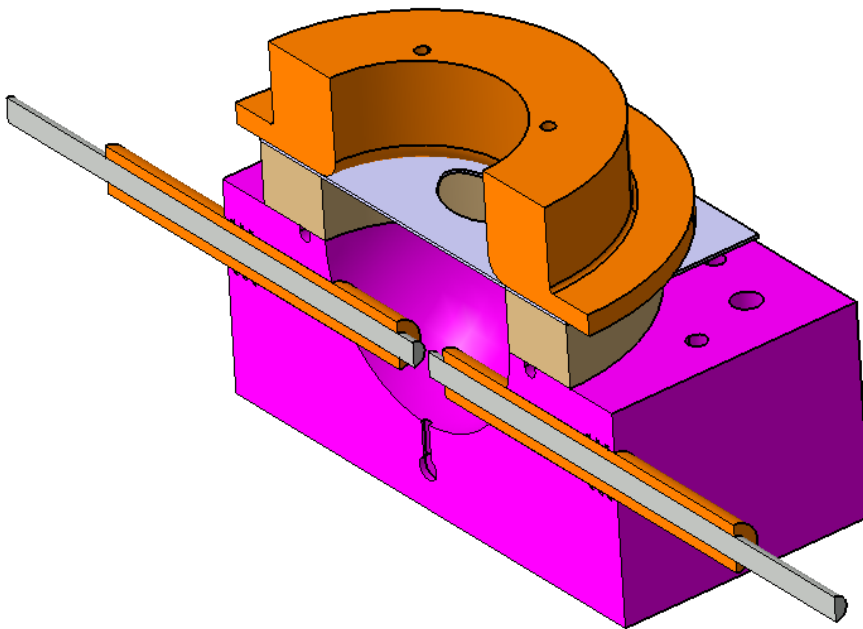


Figure 3-8: Half view of an electrohydraulic free forming configuration.

The open window tool was used to form modified specimens in the free forming condition. The open window tool has an inner diameter of 100mm, a clamping face of 230mm diameter, an entry radius of 10mm, and a height of 50mm (Figure 3-9). The existing open window tool was used in combination with several new custom made tools to prevent water from rebounding off the die or press onto the top surface of the blank.



Figure 3-9: Bottom view of the open window forming tool.

The open window tool was not tall enough on its own to prevent the water from hitting the press bed above the opening of the tool and rebounding back onto the blank, so custom made free forming tools were manufactured (Figure 3-10) to increase the distance between the blank and any surface that could rebound water back onto the blank. The die adapter tool allows the majority of the water to escape from the forming window because it has a taper that reduces to a 25.4mm wide flat section on the face closest to the blank. The flat section of the die adapter is 75mm away from the blank, sufficiently far that any water that does hit it cannot rebound onto the blank with enough energy to cause distortion. The custom made tools increase the distance between the blank and the upper press bed to 228mm. The custom made tools served many additional purposes including functionality, safety, and time efficiency.

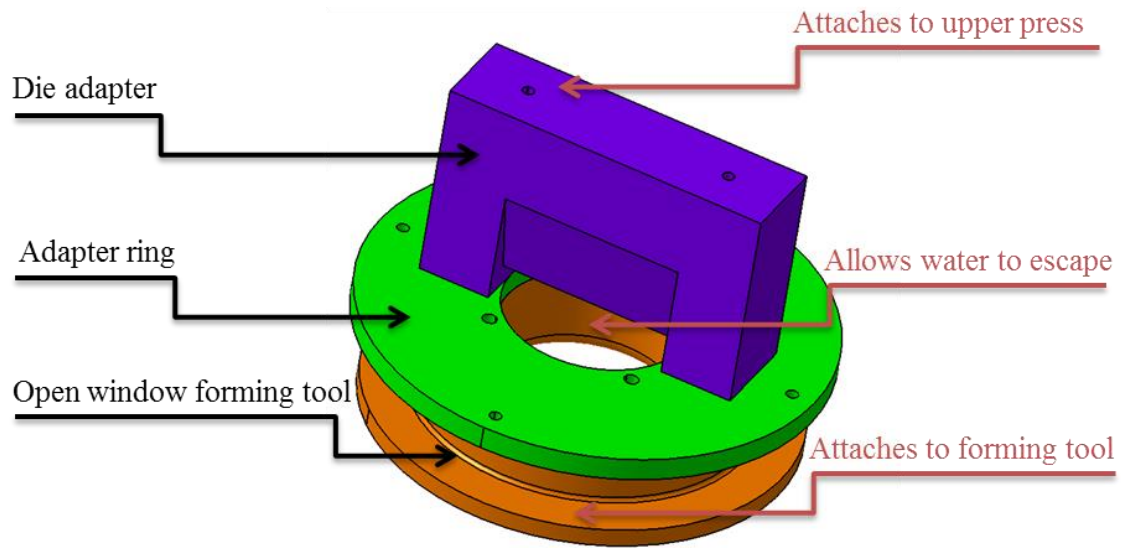


Figure 3-10: The die adapter and adapter ring custom manufactured forming tools attached to the pre-existing open window forming tool.

The adapter ring was bolted between the die adapter and the forming tool to allow the forming tool to rise when the press opens. The forming tool was previously manually added and removed from the forming chamber for each specimen to provide access to the specimen and chamber. A forming tool can weigh as much as 15.4kg (34lb) and the manual handling of the forming tool is an ergonomic issue because the operator can become fatigued after adding it and removing it from the chamber for approximately 30 specimens in one day. The previous methodology of manual handling of the forming tool could potentially cause the forming tool to fall when installing blanks and preparing the chamber between discharges. The adapter ring couples the forming tool to the opening of the press, which increases the operator's safety and decreases the cycle time required to form each blank. When installed, the adapter ring still maintains access to the bolts that attach the forming tool, thus allowing the forming tool to be changed without removing the entire top assembly from the press. The accessibility to conveniently change out the forming tool prevents the need for the time consuming alignment between the top and bottom tools when installing the upper assembly.



Electricity and water can degrade the integrity of the tools over time. The tools are susceptible to corrosion due to the frequent presence of water and electricity. To prevent corrosion, all of the metallic parts, including the chamber, adapter ring, and die adapter were manufactured from stainless steel. The ability of stainless steel to resist corrosion helps to maintain a smooth surface for attaching to other tools. In addition, corrosion on the interior chamber walls has the potential to dislodge, which would alter the resistivity of the water, thereby changing the pulse characteristics. Manufacturing the components from stainless steel extended the service life of the components and ensured that the performance of the components will be maintained for their entire service life.

#### **3.1.4 Electrical Insulation and Water Control**

The two most prevalent safety concerns of EHF are electricity and water. The high voltage electricity must be constrained to its desired path or else damage to equipment can occur. The water must also be contained or it can damage equipment, create slip hazards for the operator, and cause short circuits.

The tooling must be electrically insulated from the press bed to prevent short circuits that can occur if there is an electrical path with less resistance outside the chamber. Short circuits outside the chamber, commonly referred to as arcs, can damage equipment and reduce the energy discharged between the electrodes inside the chamber. If the press is insufficiently isolated from the electrical discharge, the electricity can travel through the grounded press which causes pitting in the ram and degradation of the hydraulic fluid. The press is insulated from the EHF equipment by garolite insulation, also referred to as G10. Two garolite insulation pieces were manufactured for the new chamber and upper tooling. The bottom garolite insulation had a special cut-out to allow the busbars to be positioned in an optimal configuration. The bottom insulation had tapped holes to mount the chamber, L brackets to secure the electrodes, and the busbar adapter (Figure 3-11). The top electrical insulation had four counterbore holes to attach the die adapter through the press side of the insulation (Figure 3-12). Although the die adapter only required two bolts, the additional holes were prepared so that any forming tool could be directly

attached to the top insulation in future experiments to allow the tool to be raised and lowered with the press. The bolt holes to attach the die adapter to the upper garolite were counter bored 12.7mm deeper than normal to allow custom made garolite plugs to thread into the garolite insulation. The threaded garolite plugs provided a minimum of 12.7mm garolite between the tooling and the upper press platen to electrically insulate the tools from the press.

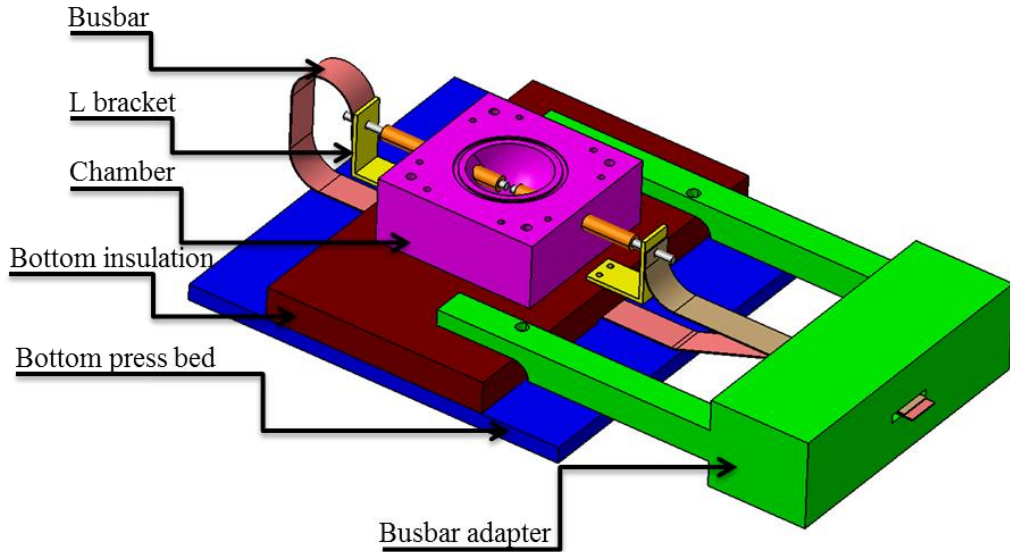


Figure 3-11: The bottom electrical insulation and related components.

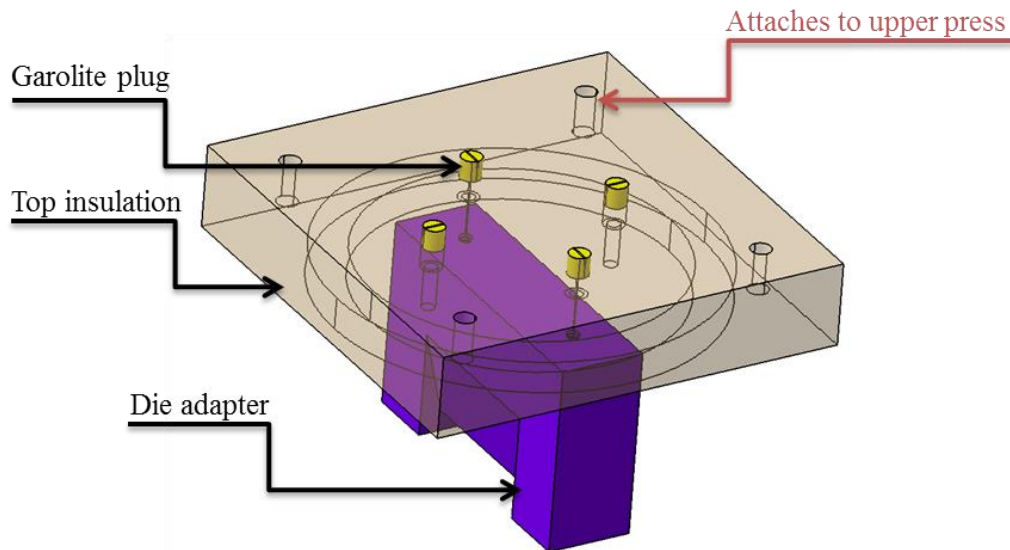


Figure 3-12: The die adapter mounted to the top electrical insulation.

A 230mm outer diameter plastic water main pipe was used to control the spray of water that exited the forming chamber through the holes cut in the test specimens. The top G10 insulation had a 19mm deep groove cut into it to allow the pipe to fit in and accordingly reduce the amount of water able to escape during each discharge (Figure 3-13). The seal between the insulator and pipe protected the surrounding equipment from water spray and reduced the cleanup time after forming each specimen. A 190mm outer diameter, 2mm thick circular stainless steel protector was inserted between the die adapter and the top garolite insulation to protect the insulation from the water pulse. Without protection, destruction of the garolite can occur in as little as 10 discharges due to the high energy of the water impacting the laminated garolite surface. The protector prevented the water from hitting the garolite insulation and extended its service life indefinitely.

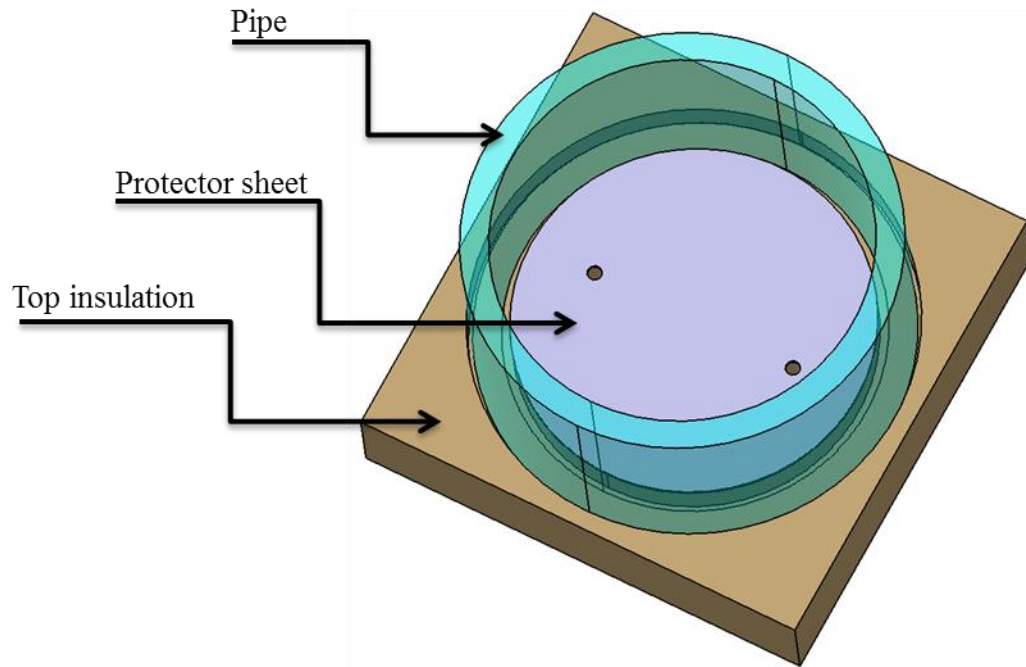


Figure 3-13: Bottom view of the top insulation, protector sheet, and pipe.

### 3.1.5 Sheet Material Selection

Two sheet materials of significant interest to the automotive industry, DP600 steel and AA5182-O aluminum, were selected for the study. Both materials were 1.5mm thick,

which allows the quasi-static and EHFF formability of the two materials to be compared without concern for material thickness effects. The heat chemistry of the DP600 steel used in this investigation is included in Table 3-7. AA5182 is composed of (in weight percentage) 95.2% Aluminum (Al), 0.35% Manganese (Mn), and 4.5% Magnesium (Mg).

Table 3-7: Heat chemistry of DP600 steel in weight percentage.

<b>C</b>	<b>Mn</b>	<b>P</b>	<b>S</b>	<b>Si</b>	<b>Al</b>	<b>Cu</b>	<b>Ni</b>	<b>Cr</b>	
0.107	1.497	0.011	0.001	0.175	0.038	0.057	0.015	0.181	
<b>Sn</b>	<b>Mo</b>	<b>V</b>	<b>Nb</b>	<b>Ti</b>	<b>B</b>	<b>Ca</b>	<b>N</b>	<b>W</b>	<b>Sb</b>
0.004	0.214	0.004	0.002	0.025	0.00022	0.0026	0.0061	0.0025	0.0013

The mechanical behaviour of the sheet metal blanks was represented using the Johnson-Cook (J-C) constitutive model (Johnson and Cook, 1983). The J-C model describes the flow stress ( $\bar{\sigma}$ ) as a function of strain, strain rate, and temperature effects (Equation 4), where  $A$  is the initial yield strength of the material at room temperature, and  $n$  is the strain hardening exponent. The equivalent plastic strain rate  $\dot{\bar{\epsilon}}$  is normalized with the reference strain rate  $\dot{\epsilon}_0$  at which  $A$ ,  $B$ , and  $n$  were determined. Parameter  $C$  represents the strain rate sensitivity of the material. The room temperature ( $T_R$ ) and melting temperature of the material ( $T_M$ ) are constants. The parameter  $m$  is the thermal softening exponent.

$$\bar{\sigma} = [A + B(\bar{\epsilon}_p)^n] \left( 1 + C \ln \frac{\dot{\bar{\epsilon}}_p}{\dot{\epsilon}_{p0}} \right) \left[ 1 - \left( \frac{T - T_R}{T_M - T_R} \right)^m \right] \quad (\text{Equation 4})$$

Although the strain hardening parameters of the J-C model are defined at a reference strain rate, the parameters are typically calibrated to more accurately capture the experimental results at the strain rates present in the simulation. The work hardening and rate dependent parameters used in the simulations (Table 3-8 and Table 3-9) were obtained by fitting high rate tensile test data (Rahmaan et al., 2014) to achieve the least

amount of error over the range of strain rates present in EHFF. The thermal effects from the electrohydraulic discharge, material deformation, and friction were assumed to have negligible influence on the forming process due to the very short deformation time, and therefore the thermal softening effects were omitted from the hardening model under the adiabatic assumption.

Table 3-8: Material model work hardening parameters.

<b>Parameter</b>	<b>AA5182-O</b>	<b>DP600</b>
Density (kg/m <sup>3</sup> )	2700	7800
Young's Modulus (GPa)	70	207
Poisson's Ratio	0.33	0.3
A (MPa)	98	228
B (MPa)	529	823
n	0.463	0.317

Table 3-9: Material model strain rate hardening parameters.

<b>Parameter</b>	<b>AA5182-O</b>	<b>DP600</b>
C	-	0.0165
$\dot{\epsilon}_0$	-	0.001

Aluminum has very small negative strain rate sensitivity (Rahmaan et al, 2014), so the strain rate hardening parameters were ignored from the J-C material model. Furthermore, the J-C material model does not fit the experimental aluminum uniaxial tension test data at low strain values. To improve the ability of the constitutive model to capture the actual material behaviour at low strain values, the experimental uniaxial tension test data was entered into the simulation using von Mises plasticity for AA5182-O.

### 3.1.6 Specimen Preparation

The large blanks received from the material suppliers were first cut into 200mmx200mm square sheets using a sheet metal shear. A 2.54mm (0.1in) square grid pattern was electro-etched onto one side of the blanks. The size of the grids was selected in accordance to the recommended size by ASTM E2218 (2008). To remove any surface contamination prior to gridding, the aluminum blanks were cleaned with Lectroetch brand #3 cleaner and the steel blanks were cleaned with Lectroetch brand #1 cleaner. The aluminum blanks were etched with LNC-5 electrolyte, and the steel blanks were etched with 112A electrolyte. In total, 390 specimens were prepared for the experiments, with the majority of the specimens etched with grids.

The circular shapes were initially cut into the sheet specimens with modified geometries using wire electrical discharge machining (wire EDM) to provide very smooth, non-hardened edges to avoid edge cracking. However, the wire EDM process stained the steel surface to the point where the grids were no longer readable, so a CNC mill was used to cut the specimen shapes. The coolant used in the CNC machining had minimal impact on the surface finish of the CNC machined blanks. Although new endmill bits were purchased to cut the specimens and a fixture was built to clamp the specimens, the CNC milling process was considerably more economical than wire EDM because wire EDM consumes expensive brass wire. The time required to cut the specimen geometries on the wire EDM machine was significantly longer than on the CNC mill because the wire EDM process is slow. For consistency, the specimens were machined with the rolling direction of the material parallel to the length of the gauge section such that the major strain was always parallel to the rolling direction.

An aluminum fixture (Figure 3-14) was built to secure the blanks, support the gauge section, and to reduce the vibration of the blanks during CNC milling. The fixture had discharge holes to drain the shavings and coolant. A 1mm deep 202mmx202mm square groove was cut in to the fixture to allow for consistent positioning of the blanks. The upper and lower halves of the fixture were held together with four bolts to clamp the blank firmly in position. The blanks were cut one at a time using a two pass cutting path. The first pass, or rough cut, used a 1/2inch bottom cutting carbide endmill. The second

pass, or finishing cut, used a 1/4inch bottom cutting carbide endmill. The feed rate and spindle speed for both cutting passes in aluminum were 1500mm/min and 5000RPM, respectively. The feed rate and spindle speed for both cutting passes in steel were 800mm/min and 3000RPM, respectively. The feed rate and spindle speed were set based on a balance of cutting time and quality. The complete cycle time for one blank varied between four and six minutes, depending on the geometry being cut.



Figure 3-14: A uniaxial specimen in the machining fixture on the bed of the CNC mill.

### **3.1.7 Experimental EHF Process and Conditions**

The main objective of the experimental work was to determine the forming limits of AA5182-O and DP600 sheets in EHFF. To this end, specimens must be deformed along specific strain paths until localized necking occurs. A necked specimen lies in the narrow transition between a safe specimen and a split specimen. To experimentally obtain necked specimens, a precise amount of energy must be delivered to the blank so that a local neck will be created without causing a split. The amount of energy required to form a sheet depends on a number of factors, including the material grade and thickness, the chamber geometry, and the specimen geometry. Although the orientation of the gauge section of the specimen relative to the electrodes was not shown to have much influence

on the amount of energy required to cause a neck, the length of the specimen gauge section was always aligned perpendicular to the electrodes for consistency.

The amount of energy delivered to the blank in the EHF process is controlled by specifying the input voltage of the discharge and is normally set in the range of 5-15kV. The critical input voltage where an incipient neck is formed in the specimen can be determined empirically. For a new geometry or material, an arbitrary input voltage is selected based on previous experience. If the EHF specimen is safe, then the input voltage is increased. If the EHF specimen is fractured, the input voltage is decreased. After several trials, it is possible to identify the range of input voltages between safe and split. It is usually possible to obtain a necked specimen by repeating several tests at input voltages in the transition range between safe and split. The input voltage range that makes up the transition region between safe and split specimens is unique to each material and specimen geometry. The process of finding the transition region is time consuming because there is often variation in the EHF process due to various types of energy losses.

The specified input energy and corresponding theoretical energy only provide a relative means of controlling the process from specimen to specimen. The voltage and current were measured to experimentally quantify the electrical energy delivered to the chamber: the voltage differential across the electrodes was measured using a voltage probe, the current was measured using a Rogowski coil that was coiled around the busbar leading in to the chamber, and a second current measurement was recorded from an internal Rogowski coil inside the Magnepress. The electrical signal was recorded at a frequency of 25GHz with an oscilloscope for one-hundred thousand intervals. Voltage and current waveform measurements (Figure 3-15) were used to calculate the power and energy at both the Magnepress and chamber.



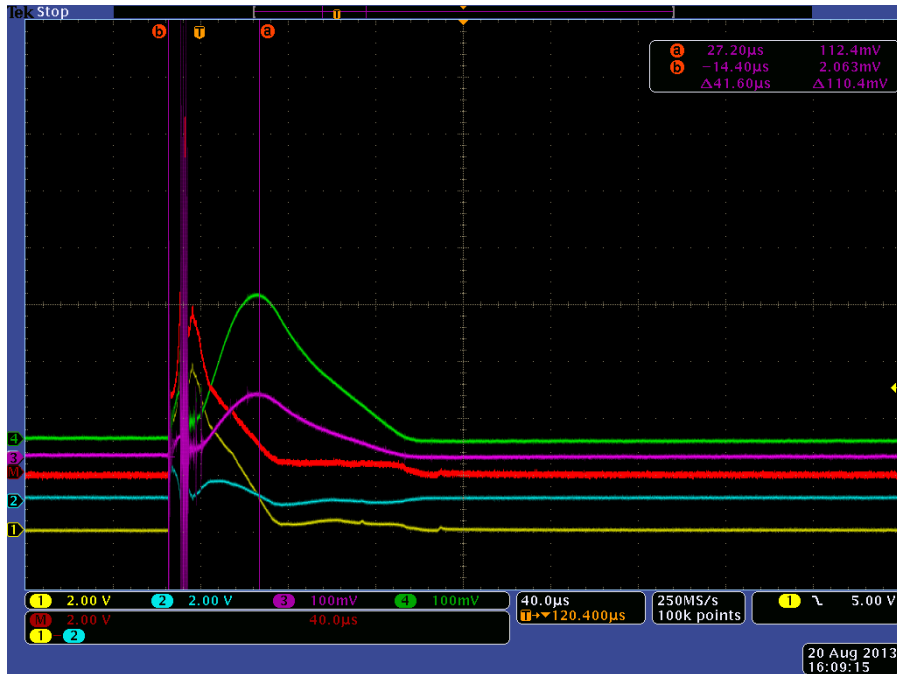


Figure 3-15: Recordings from the oscilloscope for a 6.1kV discharge used to measure positive voltage (1-yellow), negative voltage (2-blue), the differential voltage (M-red), the current at the chamber (3-purple), and the current at the Magnepress (4-green).

The experimental set-up used should not be changed for the duration of the experiments. Even when the experimental set-up is consistent, the trial and error process can be challenging because the outcome of the dynamic EHF process can vary based on the amount of energy lost to inefficiencies. The repeatability of the EHF process can be improved by experimental conditions such as the use of a bridge wire, draining the chamber water after each pulse, and not using carrier blanks.

A copper bridge wire can be installed between the electrodes to establish the flow of electrons and lower the voltage potential needed to complete the circuit (Figure 3-16). A bridge wire establishes a low resistance path for electrons to flow between the two electrodes, which can eliminate arcing in other areas, such as from the electrodes to the chamber bowl. The use of a bridge wire increases the likelihood of a repeatable discharge. Copper bridge wires, made from 28mm of 0.3mm diameter pure copper wire coiled around a 3.9mm rod, were used to increase the repeatability of the discharge and to avoid arcing.

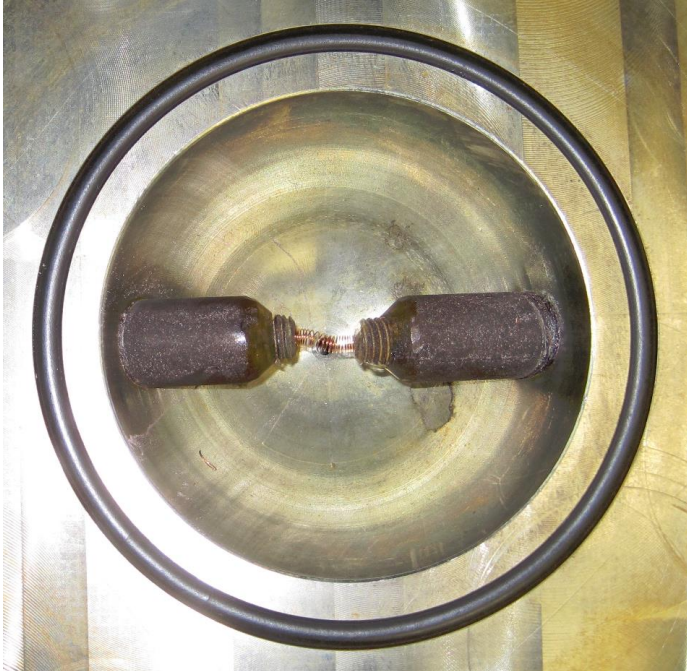


Figure 3-16: A copper bridge wire installed between the two electrodes.

An important parameter in the EHF process is the conductivity of the forming fluid. The high temperatures and high pressures in an EHF discharge can alter the dissolved oxygen and dissolved metal particulates in the water, thereby affecting its conductivity. The chamber and electrodes, particularly if they have surface oxidization, can dissolve metal particles into the water. The new chamber used in this work was manufactured from stainless steel to reduce the amount of rust that dissolves in the water. With each pulse the copper bridge wire is dissolved in the water and the colour of the water is much darker after even a single pulse, so it is obvious that some properties of the water have changed. An increase in the amount of dissolved particulates in the water would reduce the resistance of the water and increase the ability for the electricity to flow between the electrodes. The inconsistent electrical parameters would change the pulse time history and intensity of the plasma channel, and could potentially alter the deformation observed in the specimens. To ensure the conductivity of the water was consistent, the chamber was drained and refilled before each discharge.

Sheet drivers, or carrier blanks, were not used for the experiments. Carrier blanks would change the friction and loading conditions on the specimens, and would require more

material to be used in the experiments. However, carrier blanks would allow the modified specimens to be used in traditional die forming by preventing water from passing through the cut-outs in the specimens. New tooling was designed to prevent water from passing through the cut-outs in the blanks and therefore sheet drivers were not required. The tooling allowed the water to continue to travel freely without providing surfaces for the water to hit and reflect back on to the blank. In order to protect the operators and the equipment from a wet environment, safety measures were enacted to contain the water that passed through the holes in the blanks. There is some evidence to suggest that more energy is required to form the blanks without a driver because some useful energy escapes when the water passes through the holes in the specimen. Using carrier blanks could have prevented rebounding, would not have required tooling to be built, and could have reduced the amount of energy required to form a blank. Carrier blanks would have made the experiments, and the corresponding numerical simulations, significantly more complex in both the loading on the specimen and the friction interaction between the specimen and the carrier blank.

Despite the steps of using a copper bridge wire, refilling the chamber water, and not using carrier blanks, the EHF process still has significant variability. Even successive EHF pulses with the same conditions can produce different results due to a number of factors related to the dynamic nature of the process.

### **3.1.8 Strain Measurement**

The plastic deformation in metal forming processes is often measured using digital image correlation (DIC) or grid analysis. The specimens were electro-etched with grids prior to forming since it was too dangerous to use DIC equipment with the EHF experiments.

There are numerous grid patterns which can be used, however the two most popular are circle grids and square grids. Circle grids are historically the marking pattern that is used in industry because the strains can be read manually. Plastic deformation causes the circles to deform into ellipses, and while the major strain is always positive, the minor strain can be positive, negative, or zero (Figure 3-17). The amount of plastic strain at

each circle grid can be quickly and easily calculated by measuring the major and minor diameters of the ellipses using a ruler, or more commonly, a calibrated Mylar tape. Circle grids give direct visual indication of the principal directions of deformation, but the grids cannot be aligned with the rolling direction of the sheet and the deformation directions cannot be referred to in relation to the directionality of the material.

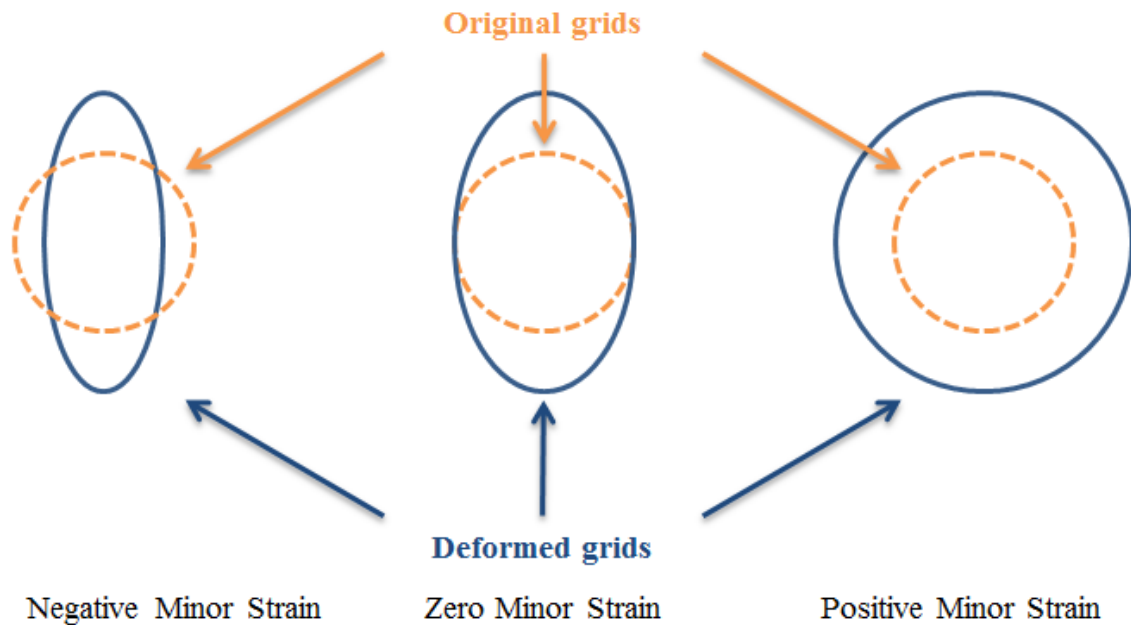


Figure 3-17: Original and deformed circle grids for strain measurement using circle grid analysis.

Square grid analysis is more accurate than circle grid analysis (Sklad and Verhaeghe, 2010), however square grids must be measured using a semi-automated or fully automated grid analysis system. Plastic deformation causes the square grids to deform into rectangles. Square grids lack the direct visual indication of the principal directions of deformation. Square grids can be aligned with the rolling direction of the sheet and the deformation directions can be referred to in relation to the directionality of the material.

The gauge sections of critical specimens were assigned row and column co-ordinates so that the strain measurements could be correlated to an exact location on a specimen (Figure 3-18). The quantity of rows and columns for each gauge section was standardized

to allow for the comparison of strain values based on location between specimens of the same geometry (Table 3-10).

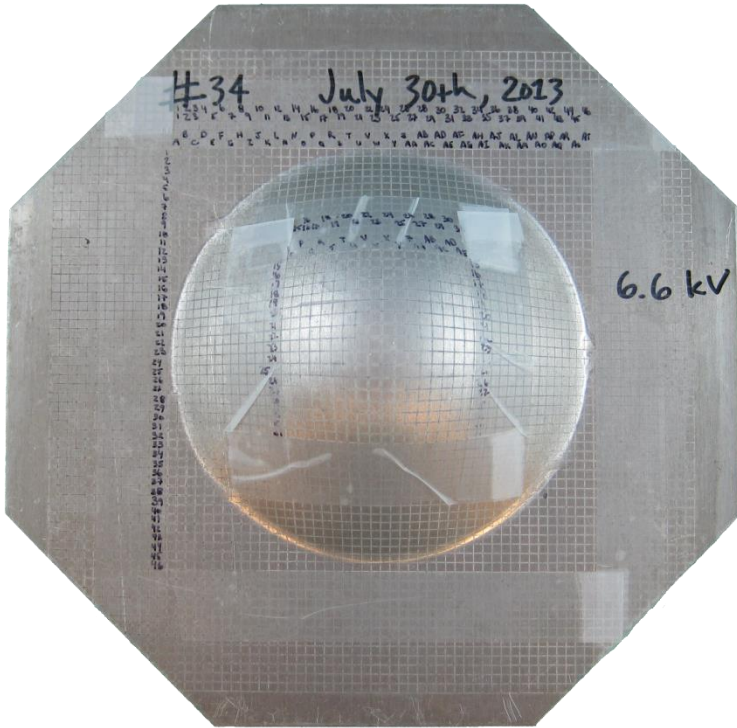


Figure 3-18: A biaxial specimen with the row and column numbering system.

Table 3-10: The standard number of rows and columns for each specimen.

Specimen	Rows	Columns
Biaxial	46	46
Plane Strain	13	20
Intermediate Draw	23	16
Uniaxial	37	7

On a necked specimen, each square grid that was measured was classified as either safe, marginal, or necked. A safe grid is one in which there is no evidence of a neck whatsoever. A marginal grid indicates that there was some probability that the neck was present in at least a portion of the grid. A marginal grid was either in close proximity to a neck or the neck passed through a corner of the grid. A necked grid was identified using

the Keeler tactile method, and the entire width of the neck passes through the bulk of the grid. Only the necked points were used to generate the FLC, all marginal points were omitted. In general, the marginal grids were slightly less strained than the grids that were clearly necked. By omitting the marginal points from the FLC, even though they generally contained some indication of necking, the FLCs are slightly higher than if the marginal points were included.

Major and minor strains were measured from the deformed grids on the EHFF specimens using the FMTI grid analyzer model 100U. The FMTI grid analyzer is a semi-automated system that incorporates a digital camera to form an image of a selected grid. The image is then processed by the accompanying software, which automatically locates the grid in the image and calculates the major and minor strain of the deformed grid. The FMTI strain measurement tool can be precise to  $\pm 0.5\%$  engineering strain (0.005 true strain) (FMTI Systems Inc., 2008). However, the practical accuracy of the strain measurement depends on the quality of the grid that is being measured, among other factors. In the case of a roller used during the electro-etching process with the silk screen, the stencil is stretched by about 2% in one direction. Stretching of the stencil affects the dimensions of the undeformed grid, and therefore the strain measurement of the deformed grid is less accurate. The FMTI grid analysis system performs strain measurements based on the digitization of the grid image projected onto the flat surface of the CCD sensor of a digital camera. The position of the grid in the camera's field of vision, the distance of the lens to the gridded surface, and the curvature of the gridded surface affect the shape and magnification of the image. A study was conducted to quantify each of these potential sources of error for strains measured on complex geometries (FMTI Systems Inc., 2008). In the case of a flat grid, the off center position of the grid has no effect on the measurement error. If the camera is held away from the surface of the sheet the error associated with the measurement increases linearly as the distance between the camera and grid plane increases. The error for a perpendicular offset between the camera and grid plane is on the order of 6% error for a 3mm gap. Similarly, tilting the camera so that it is not co-planar with the grid can affect the strain measurement. The surface curvature for relatively sharp radii can introduce moderate error on the order of about 3%, but the curvature effect is negligible for larger radii.

A study was conducted to evaluate the error associated with the repeatability (equipment variation) and reproducibility (appraiser variation) of the FMTI grid analysis strain measurement system. Three operators, one of which had never used the measuring system prior to this study, measured the major and minor strains of five square grids, three different times, at 15 minute intervals (SPC Reference Manual, 1992). The repeatability and reproducibility study was conducted at the apex of a biaxial specimen and on an undeformed specimen (Table 3-11). The sharpest radius of all the specimens occurs at the apex of a biaxial specimen thus is susceptible to the greatest curvature error when reading strains with the FMTI grid analyzer. The similarity between the errors at the apex of a biaxial specimen and on an undeformed sheet indicates that the curvature of the surface has little or no effect on the measurement error. The repeatability error of the undeformed grids is slightly higher than for the apex of a biaxial specimen because the strains being measured are close to the accuracy limit for the FMTI grid analysis system. In both regions, the error attributed to the combination of repeatability and reproducibility is approximately 4%, which equates to a negligible error of about  $\pm 1\%$  engineering strain for the majority of strain measurements. The results of the study indicate that the strain measurement system has excellent repeatability and reproducibility regardless of the region being measured.

Table 3-11: Repeatability and reproducibility study results for a sharp radius at the apex of a biaxial specimen and for a flat blank.

<b>Error Measurement</b>	<b>Apex of Biaxial</b>	<b>Undeformed</b>
Repeatability (%)	2.21	3.39
Reproducibility (%)	3.35	2.18
Repeatability and Reproducibility (%)	4.01	4.02

The generation of the forming limit curve from necked specimens can vary because the classification of grids as safe or necked depends on the experience of the operator and the sensitivity of his or her finger. The tactile method is widely used across North America and typically exhibits experimental scatter of only  $\pm 2\%$  (major strain) with high

reproducibility for experienced operators (Hecker, 1972). Including experimental error, the forming limit curve for a given material should be repeatable within  $\pm 5\%$  (ASTM E2218, 2008). To account for the variability of the FLC and other factors, design engineers normally implement a marginal zone of approximately 10% engineering strain below the FLC, depending on the material, to ensure the manufactured parts do not fail.

### **3.1.9 Mini-die Forming**

The forming limit curve for EHFF fills a critical void of information required by mechanical engineers to design forming tools for EHF applications when the contact stress with the die is non-existent or low. In addition to this novel free forming work, a new process for establishing the formability of materials deformed with electrohydraulic die forming (EHDF) was also developed.

The problem with traditional procedures for determining the formability in high contact stress applications is that a unique experimental setup, including a forming chamber and matching dies, is required for each strain path that is studied in traditional EHDF. For example, the research team led by Golovashchenko (2013) uses a conical chamber with a matching set of circular dies for biaxial stretching and a separate rectangular chamber with matching elongated V-shape dies for the plane-strain region of the FLC. The electrohydraulic discharge and the resulting pressure distribution on the blank are different between any two experimental set-ups, meaning that the dynamic forming processes experienced by the specimens for each strain path are not consistent. The comparison of pulsed pressure forming results from different experimental configurations, such as different chamber shapes, is not advisable because the formability enhancement mechanisms may not be equivalent from one configuration to the next. In addition to requiring a unique forming chamber for each strain path, several variations of the same forming tool at different angles are required for each chamber because the different formability of materials means that they can be stretched to different heights. Further, for a given sheet material, the amount of sheet-die contact affects the final height of a specimen and depends on both the energy supplied and the angle of the tool. The



dependence of the final forming height of a specimen on the intensity of sheet-tool contact means that the apex may never contact the die if the die wall is too steep. If the apex does not contact the die, failure may occur at the apex of the blank at the free forming limit despite the periphery of the blank experiencing significant contact with the die (Golovashchenko et al., 2013). Lastly, the biggest gap in the traditional die forming methodology is that there is no way to assess the formability limit on the negative minor strain side of the FLD.

A new die forming process, called mini-die forming, allows the modified specimen geometries to be formed without a sheet driver in high contact stress conditions. Rather than using the traditional conical or v-shaped dies, a mini-die could be inserted into the open window tool at a specified perpendicular offset distance from the gauge section of the blank (Figure 3-19). The gauge section of the blank would impact the die, but the mini-die is narrow enough to avoid reflecting the water that passes through the cut-outs in the specimens. In contrast to all the tooling required for each strain path in traditional die forming, mini-dies can be used with all four specimen geometries to conduct die-forming experiments that cover the entire spectrum of minor strains in the same chamber. Mini-die forming would allow for the determination of the EHDF formability on the negative minor strain side of the FLC which has never been accomplished.

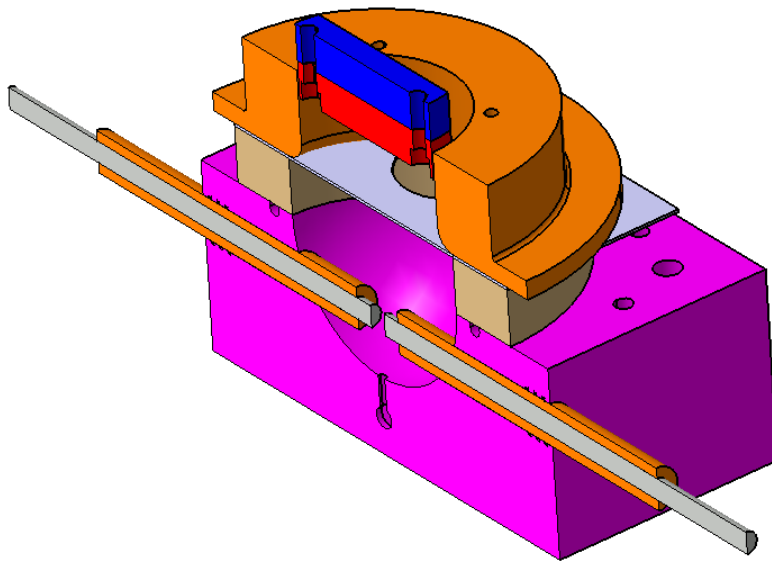


Figure 3-19: Half view of an electrohydraulic mini-die forming configuration.

The distance between the blank surface and the mini-die can be adjusted in 1mm increments using spacers, such that only the gauge section of the sheet contacts the tool. The gap can be set to a minimum of 1mm above the blank surface and to a maximum of 50mm above the blank surface, but the height of necked free formed specimens should provide a reference point for the initial mini-die offset distance. The amount of tool sheet interaction in mini-die forming can be controlled by adjusting either the input energy or the spacing between the blank and die, and thus does not require additional tooling. The die adapter tooling was designed to allow the operator to quickly adjust the gap between the blank and die or install a mini-die with different curvature without disassembling the entire upper tool (Figure 3-20). The mini-die can be accessed from the bottom through the open window tool, which allows the entire upper tool to remain attached to the upper press platen, in order to eliminate time consuming disassembly and assembly of the upper tools and to avoid the tedious alignment process between the upper tool and the chamber. Although only flat dies were manufactured for the proof concept experiments, new mini-dies with a different curvature profile are quick, easy, and affordable to manufacture.

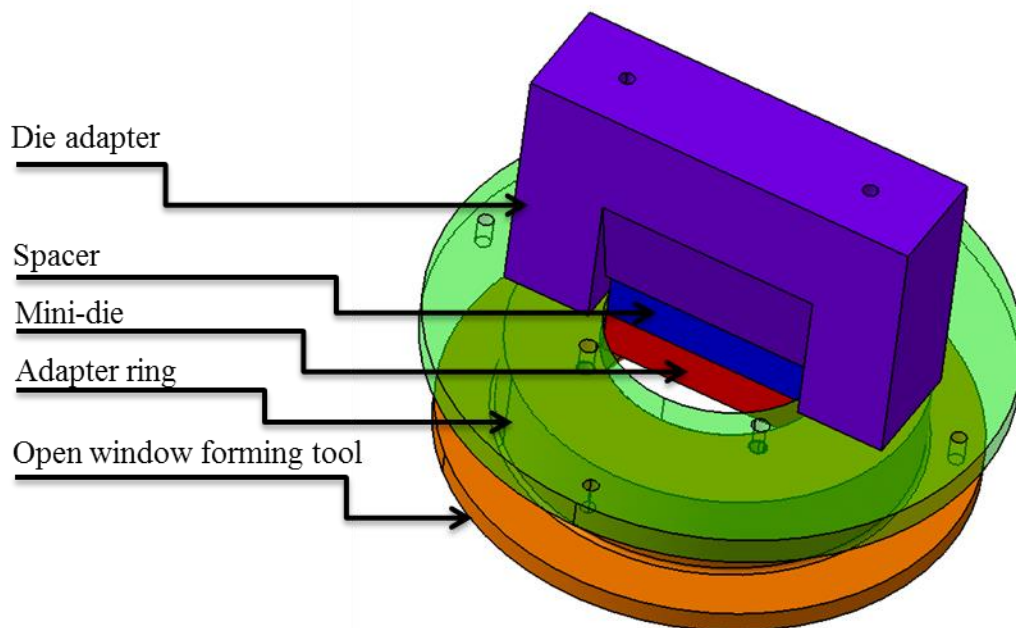


Figure 3-20: Spacer and mini-die attached to the die adapter for use with the open window forming tool.

### 3.1.10 Quasi-static Formability Tests

The quasi-static forming limits of the materials are required in order to evaluate any formability change resulting from using EHFF. The ideal quasi-static FLC for the comparison would be from the same batches of material and use the same FLC determination technique. Quasi-static FLCs were determined by personnel at an external research facility using the Marciniak test method for the same batches of material that were used for the EHFF experiments. However, the strains were measured using digital image correlation (DIC) and in-situ strain mapping. The forming limit curve for each material was created by using the ISO 12004-2 standard procedure for determining limiting strains. The methodology used for determining the limiting strains and subsequently creating the quasi-static FLC was different than the approach used for EHFF. The measurement of the quasi-static strains using DIC and generating the FLC using the ISO standard procedure, subsequent to the EHFF work, generated uncertainty about the validity of comparisons using the results from the two forming processes. Digital image correlation could not be used in conjunction with the EHFF experiments, so etched grids were used to record the strain. The Keeler method was used to identify necked grids on the EHFF samples because of its simplicity and familiarity.

Biaxial steel specimens were gridded and deformed using the Nakazima test (Hemispherical Dome test) for the purpose of metallography studies, but the macroscopic strain measurements are also useful here. A 75 ton Interlaken press was used to deform the specimens at a punch speed of 0.1mm/s. The limiting strains were measured according to the same procedure used for the EHFF specimens. The formability of the gridded specimens formed by the Nakazima test was compared to the forming limit curve established in accordance to the ISO 12004-2 standard using specimens formed by the Marciniak test to get an estimate of the difference between the two quasi-static forming limit curve methodologies.

The quasi-static FLC, like any other experimental measurement, is susceptible to error. The theoretical FLC for DP600 was calculated to provide a comparison for the experimental FLC. The theoretical forming limit curve for mild steels can be estimated using equations developed by Keeler and Brazier (1977). Although not originally

developed for high strength steels, the equations are generally known to provide a good estimate of the formability of dual phase steels. A detailed study on three different grades and different thicknesses of dual phase steels indicates that the theoretical curve matched the experimental data in at least two of the three regions of a FLD (Sriram et al., 2009). The results of Sriram et al. showed that the theoretical FLC perfectly matched the experimental FLC in the negative and zero minor strain regions of the curve, and had a slightly different slope on the positive minor strain side of the diagram (Figure 3-21). The DP600 manufacturer generally does not conduct internal formability experiments and instead provides its customers with the theoretical FLC because it is normally a good indicator of the formability of the material. The theoretical FLC was calculated using the Keeler-Brazier formula for DP600 based on an n-value of 0.184 and a thickness of 1.5mm (Figure 3-22), and has a plane strain intercept of 39% engineering strain. Although the grade and thickness of the materials are the same, the location of the FLC for the material used by Sriram et al. should not be compared because the n-values are drastically different, and the n-value is known to affect the height of the FLC.

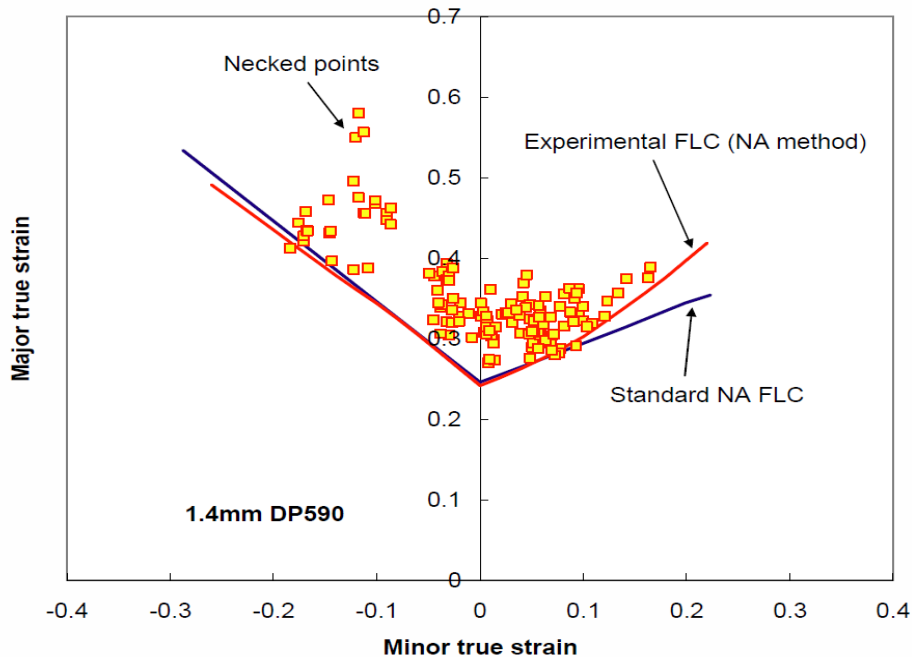


Figure 3-21: Experimental FLC and Keeler-Brazier theoretical FLC for 1.4mm DP590. Image from Sriram et al. 2009.

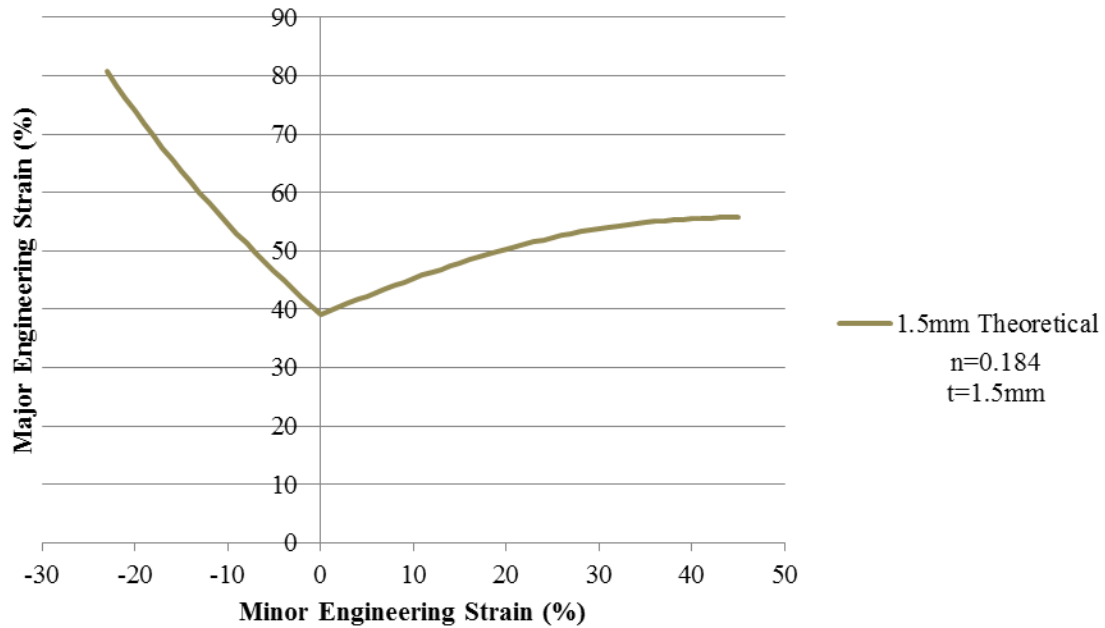


Figure 3-22: DP600 theoretical forming limit curve predicted by the Keeler-Brazier relation (Equation 1).

The theoretical calculation of an aluminum forming limit requires the use of principles of plasticity, instability theory, and damage mechanics. Instead, an experimental curve for 1.0 mm AA5182-O obtained from literature was used to assess the validity of the shape and position of the experimental quasi-static forming limit curve (Figure 3-23). If the height of the FLC for AA5182-O increases with thickness as it does with steel, the FLC for the 1.5mm aluminum used in this investigation should be above the experimental curve obtained from the literature. However, there are many variables that can affect the formability of any sheet material from supplier to supplier. The formability of the two materials should be similar despite the comparison of the two experimental FLCs for different thickness materials from different suppliers.

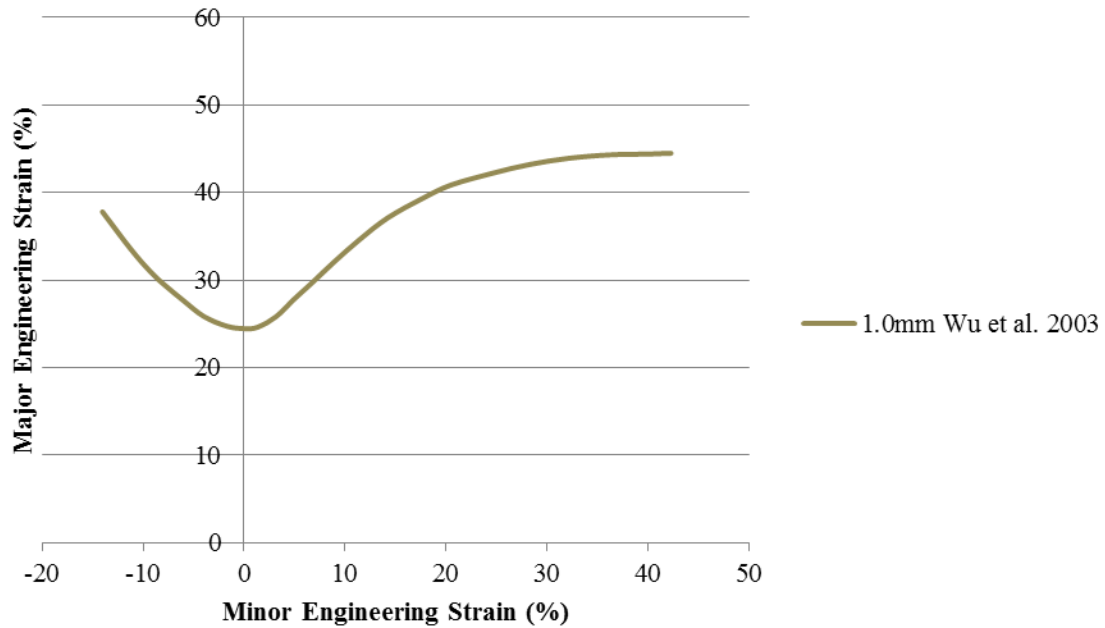


Figure 3-23: AA5182-O 1.0mm experimental forming limit curve obtained from Wu et al. (2003).

### 3.1.11 Material Characterization

Many different types of tests have been developed to evaluate the formability of sheet materials, but the simplest and most common is undoubtedly the uniaxial tensile test. The standard tensile test is perfectly suited for determining many intrinsic material properties. However, the ratio of major to minor strains is essentially constant throughout the duration of the test and therefore does not provide data for other modes of deformation.

Uniaxial tension tests were conducted to determine the quasi-static material properties for both AA5182-O and DP600. Tension test specimens were prepared from each of the 1.5mm thick as-received materials according to the ASTM E-8 (2011) standard with gauge section dimensions of 76.2mm (3 inch) length and 12.7mm (0.5 inch) width. An MTS Criterion model 45 load frame with a 150kN load cell was used to perform the tests. Flat shaped wedge grips for materials 0-9mm thick were used to secure the specimens. The tests were controlled with a constant crosshead speed of 2.5mm/min ( $8.3 \times 10^{-4} \text{s}^{-1}$ ).

The strains were measured with an MTS Advantage AVX Video Extensometer using a 16mm lens. The specimens were marked with five points along the length of the gauge section spaced at half-inch increments from the center and two points across the width of the gauge section at the middle of the gauge section. Major strains were measured between each of the five axial marks, and between the marks corresponding to 25.4mm (1inch) and 50.8 (2 inch) initial separation. Minor strain was measured between the two marks that lie across the width of the gauge.

### **3.2 Numerical Model Methodology**

To achieve the objectives of experimentally determining the EHFF necking strains for four different strain paths, original specimens were designed using numerical simulation that could generate negative, near zero, and positive minor strains so as to cover the entire forming limit curve. The geometries for the experimental specimens were optimized using numerical simulations of EHFF using the commercial finite element software Abaqus/Explicit to provide the desired strain path in the gauge section and to avoid stress concentrations that could cause failure outside of the gauge section. In-process information about the EHFF process was obtained from the numerical model after the model was calibrated to experimental data.

### 3.2.1 Numerical Model Details

The numerical model of the EHFF process consists of six different parts: the sheet metal blank, the open window forming tool, a single Eulerian part that contains air and water, the air-water initial partition, the chamber bowl, and an acceleration partition (Figure 3-24).

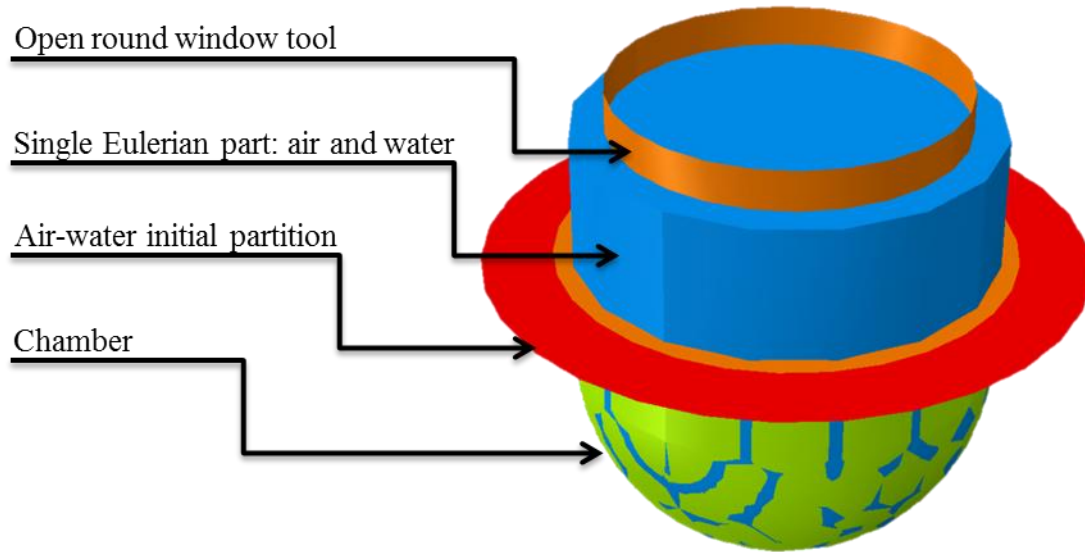


Figure 3-24: Abaqus numerical model assembly.

The sheet metal blank was modeled as a circular disk of 120mm diameter using shell elements. Although the experimental specimens were octagons cut from 200mm square sheets, the high press clamping forces were assumed to eliminate any strains beyond the 120mm diameter. Shell elements were selected due to the plane stress condition in free forming. In die forming, the stress state is three-dimensional and solid elements should be used to capture the significant through-thickness compression and shear forces that develop in EHDF. The small thickness dimension compared to the diameter of the blank would require a very small element size, and correspondingly a large number of elements, to maintain a reasonable aspect ratio for solid elements. Very small element sizes would increase the computational cost in two ways; by increasing the number of elements to be computed, and by reducing the stable time increment. In addition to the larger mesh size that can be used with shell elements, they also require less



computational time than solid elements. The shell section assignment specified 11 integration points through the thickness and the Simpson integration rule. The thickness for both AA5182-O aluminum and DP600 steel was set to 1.5mm to correspond to the experimental blanks. The specimens for uniaxial, intermediate draw, plane strain, and biaxial strain paths in the gauge section, were meshed with 2,200, 3,300, 4,400, and 6,220 1.5mm standard linear reduced integration quadrilateral elements respectively (Figure 3-25).

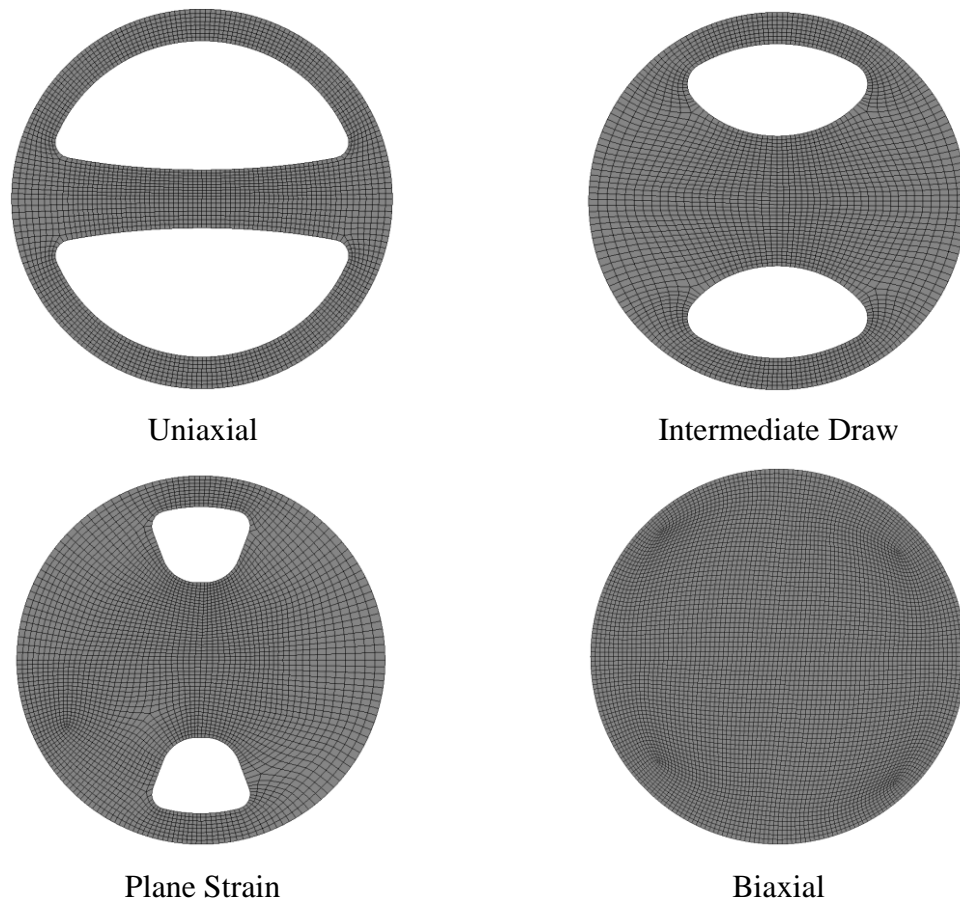


Figure 3-25: The meshed shell element sheet metal blanks for all for specimen geometries.

The open window forming tool was modeled as a discrete rigid shell based on the geometry of the actual tool that was used for the experiments (Figure 3-26). The inner diameter, entry radius, and height of the open window forming tool are the same as the experimental tool. However, the outer diameter of the clamping surface was reduced from 230mm on the actual tool to 130mm in the numerical model since the sheet is also

reduced in diameter based on the assumption of sufficient clamping force to prevent drawing of material. The tool was modeled as a discrete rigid part because analytical rigid parts are not able to interact with Eulerian materials (ie. the water would flow through an analytical rigid part). The open window tool was meshed with 5220, 2mm rigid quadrilateral shell elements. The open window tool was assigned an encastre boundary condition to prevent it from translating or rotating.

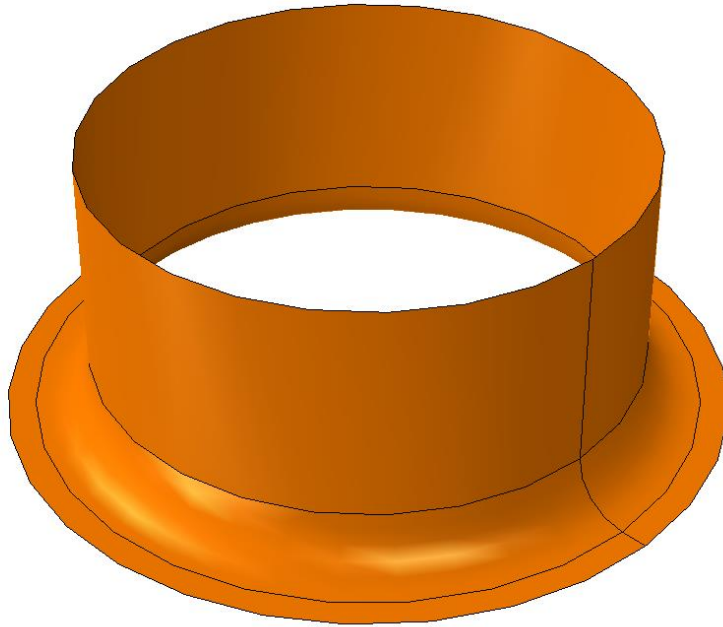


Figure 3-26: Numerical simulation geometry of the open window forming tool.

The inner bowl of the chamber was included in the simulation to prevent the inflow and outflow of material through the boundary of the Eulerian mesh (Figure 3-27). The bowl of the steel chamber used in the experiments was modeled to define the boundary for the Eulerian materials, since the boundary of the Eulerian mesh does not restrict inflow or outflow. The chamber bowl allows the simulations to capture the reflection of pressure waves off the chamber walls. The remaining details of the chamber were omitted to reduce the computational cost. The chamber was modelled as a discrete rigid part using 9352, 2mm rigid quadrilateral shell elements. The chamber was assigned an encastre boundary condition to prevent it from translating or rotating.

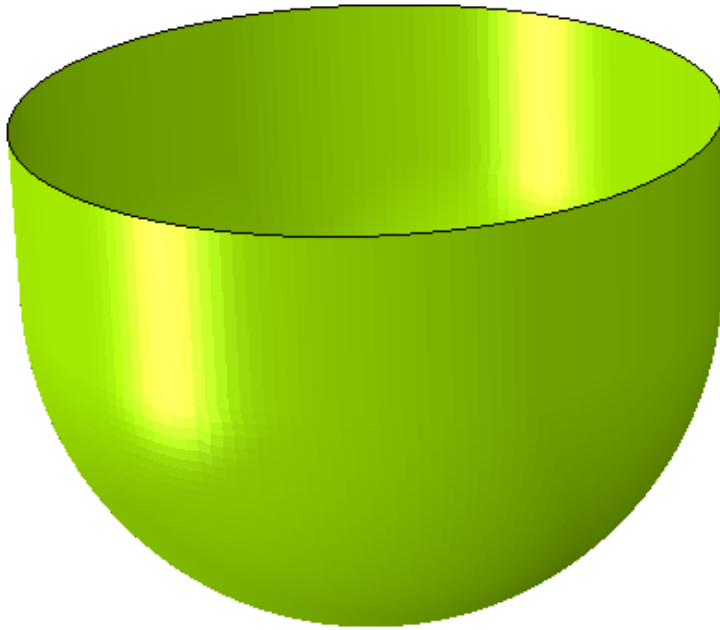


Figure 3-27: Numerical simulation geometry of the chamber bowl.

The air above the chamber and the water in the chamber were modeled as one solid part (Figure 3-28). The properties of water were assigned to the part using an Eulerian section definition and a Mie-Gruneisen (Us-Up) equation of state definition (Table 3-12). The water was assigned the 120mm diameter hemispherical geometry of the chamber bowl. A 30mm tall circular disk was added to represent the chamber ring which was added in the experiments. The air was modeled as a 400mm tall cylinder on top of the chamber water. The height of the air ensures that even the experimental specimens with the highest forming height do not exceed the region. The properties of the air were not assigned and the region that initially contained air was filled with a void material. The combined part was meshed with 199,456, 2mm explicit Eulerian elements with reduced integration and hourglass control.

Table 3-12: Water material parameters.

Parameter	Water
Density (kg/m <sup>3</sup> )	1000
Speed of Sound (m/s)	1450
Dynamic Viscosity (Pa×s)	0.001

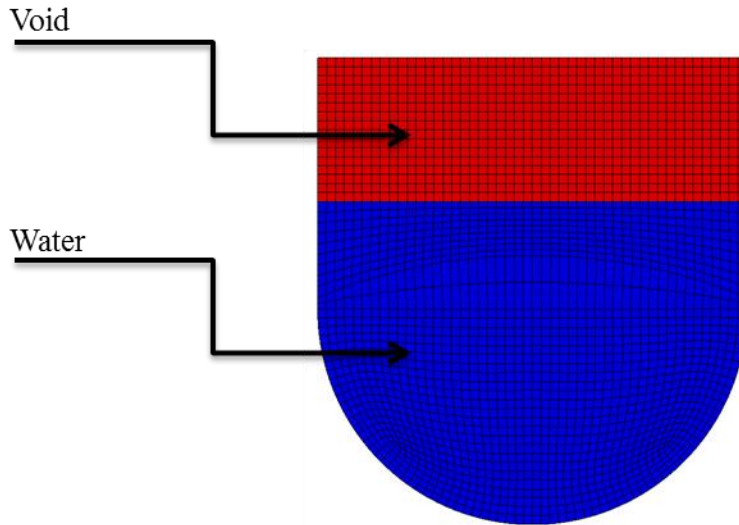


Figure 3-28: Section cut of the single Eulerian part containing the air (void) above the chamber and the water in the chamber bowl.

The initial partition between the air and water Eulerian materials was defined by a shell part positioned at the bottom of the blank and slightly larger in diameter than the chamber. The partition was used in the predefined field definition which set the initial conditions of water below the blank and air, or void, above it. The void above the chamber needed to be defined in the Eulerian volume to allow the water to travel into that space as the simulation progressed.

The 100 ton press closing force was assumed to be sufficient to ensure no material drawing, and was simulated by assigning an encastre boundary condition to the perimeter of the blank to prevent it from translating or rotating. Based on the assumption of no material drawing, the diameter of the blank was reduced to 120mm, which represents the inner diameter of the clamping area between the open window tool and the blank. The

clamping face of the open window tool was also reduced to 120mm. The diameter of the chamber bowl also corresponds to the inner diameter of the clamping area.

The discharge of the high voltage electrical current through a liquid creates a high temperature, high pressure plasma channel between the electrode tips. The expansion of the plasma channel creates a shockwave that propagates through a water filled chamber to the surface of the sheet at the speed of sound in the fluid. The mass and momentum of the shockwave accelerate the blank toward the die. Numerical analysis of this phenomenon takes the majority of the computation time required for the analysis of the EHF process. A very fine mesh in the small discharge channel between the electrodes and in the area around it requires an extremely small time step in an explicit integration procedure. As a result, most of the computation time is consumed before any pressure is applied to the workpiece. Although this approach provides full details on the pressure propagation mechanism, it is difficult to justify the high computational cost. The voltage and current measurements from the experiments were not used to generate the input loading in the numerical model because it is very difficult to incorporate experimental losses such as heat and noise into the numerical simulation. The main emphasis of the simulation was to understand the mechanics of the deformation occurring when the sheet is formed. Therefore, a simplified and computationally efficient approach that omitted the electrode geometry and the expansion of the plasma channel was used for the analysis of pressure pulse propagation through the chamber. A fully developed shockwave was simulated by applying nodal acceleration in the direction normal to the surface of a spherical partition in the Eulerian mesh. The method used to apply energy to the simulation still captured the correct deformation of the blank, but omitted the very computationally intensive initial stage of the EHF process before any sheet deformation takes place.

The spherical partition of nodes (acceleration partition) used to apply the acceleration was a hemispherical surface with a 160mm radius on the same axis as the circular Eulerian parts (Figure 3-29). The apex of the hemispherical partition was 75mm above the bottom of the chamber bowl, which corresponds to 45mm above the centerline of the electrodes in the chamber and a standoff distance of 15mm from the blank. The

magnitude of acceleration did not vary spatially across the hemispherical region. The intensity, duration, and distribution of the acceleration applied to the nodes were calibrated based on both the final forming height and strain throughout the gauge section of the blank.

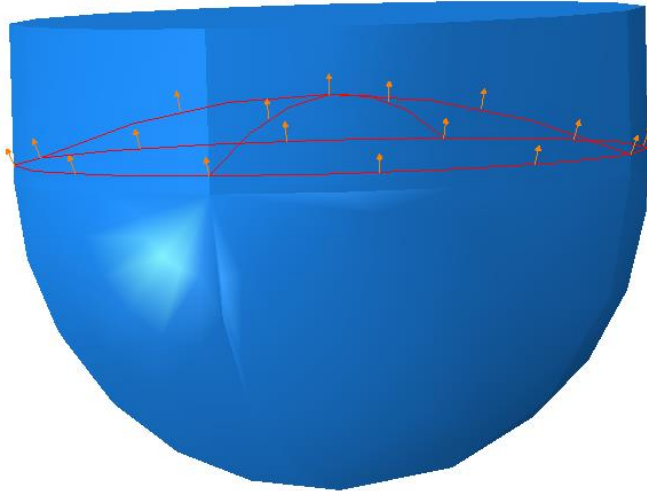


Figure 3-29: The water contained in the chamber and nodal acceleration boundary condition.

The nodal acceleration was given a similar duration and sinusoidal shape to the power trace observed in the experiments (Figure 3-30). The curvature of the specimens was used to calibrate the duration of the nodal acceleration applied in the numerical model to be  $200\mu\text{s}$ , while the experimental electrical discharge lasted for only  $120\mu\text{s}$ . The duration of the pressure pulse is estimated to be on the same order as the duration of the electrical discharge, since the experimental pressure pulse develops from the electrical discharge.

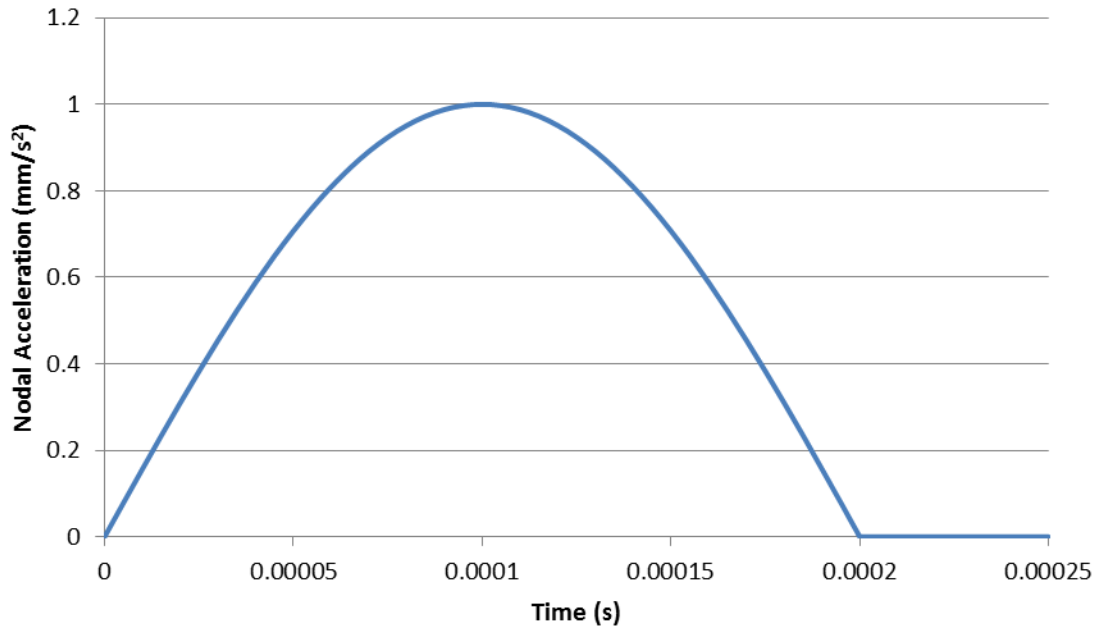


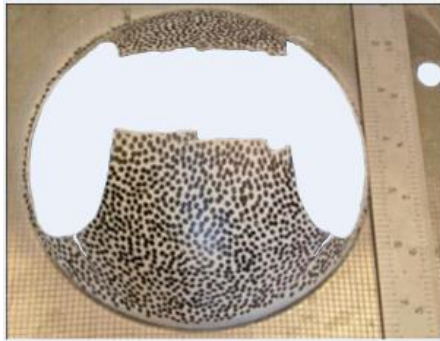
Figure 3-30: Unit acceleration curve applied to the nodes on the hemispherical partition.

Contact in the model, including Lagrangian-Lagrangian and Lagrangian-Eulerian interactions, was defined using the Abaqus All\* with self general contact definition (Dassault Systèmes, 2010). The contact between the sheet and die was given a separate definition, using the penalty friction formulation and a friction co-efficient of 0.05. The models were run for a time period of 0.0015s, and the output was requested for 1500 evenly spaced intervals (1MHz sampling frequency).

### 3.2.2 Specimen Geometry

Unique specimens were designed by Davies (2012) and Dariani et al. (2009) to achieve negative and zero minor strain when formed with EHF and EF, respectively. However, in both cases, significant stress concentrations in the corners of the cutouts caused cracking to initiate at these locations. The presence of cracks away from the gauge section could significantly alter the strain path in the gauge section, which would lead to questions about the validity of the tests (Figure 3-31). In addition, these researchers also employed specimen geometries with multiple gauge sections on a single specimen (Figure 3-32),

which could lead to conflicting results if there is a disparity in strain measurement or failure status between the two sides. The problems experienced with the specimen geometries of previous researchers led to the design of specimens that minimized stress concentrations in the corners of the cutouts and that had exactly one gauge section per specimen.

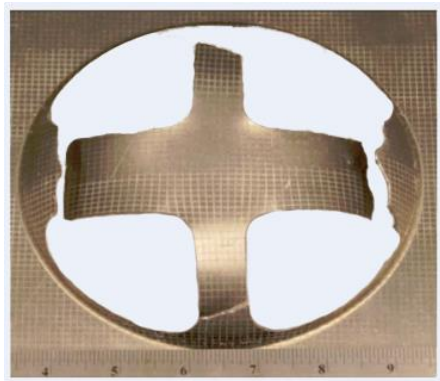


Davies



Dariani et al.

Figure 3-31: Modified specimens used by Davies (2012) and Dariani et al. (2009) which cracked in the corners of the cutout.



Davies



Dariani et al.

Figure 3-32: Modified specimens used by Davies (2012) and Dariani et al. (2009) which had two gauge sections on one specimen.

The numerical model described in Section 3.2.1 was used to design and optimize the geometry of the experimental EHF specimens. Four different specimen geometries were developed with holes of various shapes such that strains would develop in four critical



regions of the FLC. The final design for the four specimens shows a general trend of larger holes for specimens that generate negative minor strains in the gauge section (Figure 3-33, Appendix B). The larger cutouts in the negative minor strain specimens means that there is less material to resist the narrowing of the gauge section as the major strain increases. The inside forming area of the open window tool has a diameter of 100mm, which limited the size of the holes that could be cut in the specimens, and accordingly complicated the specimen design process.

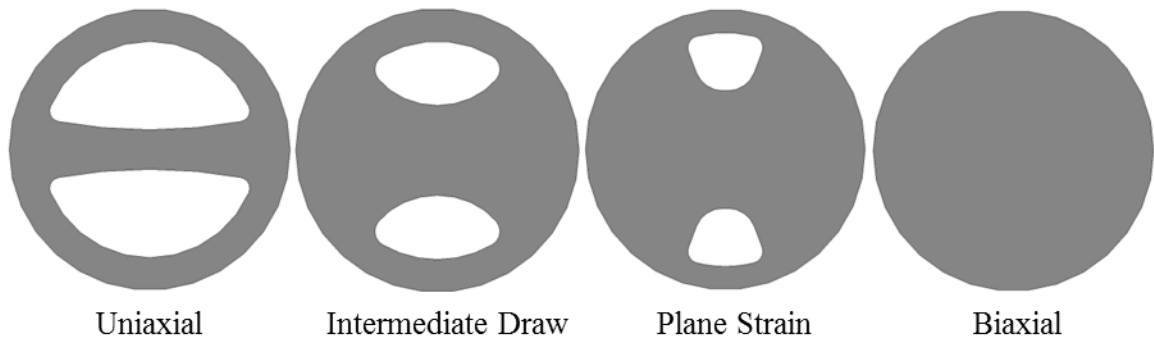


Figure 3-33: The four experimental specimen geometries.

The specimen geometries were designed such that the greatest major strain would be located in the geometrical center of the blank while minimizing stress concentrations in the corner radii of the cutouts (Figure 3-34). The four specimen geometries were designed to each generate a linear strain path in the gauge area of the blank and to generate strain data for four critical regions of the forming limit curve (Figure 3-35).

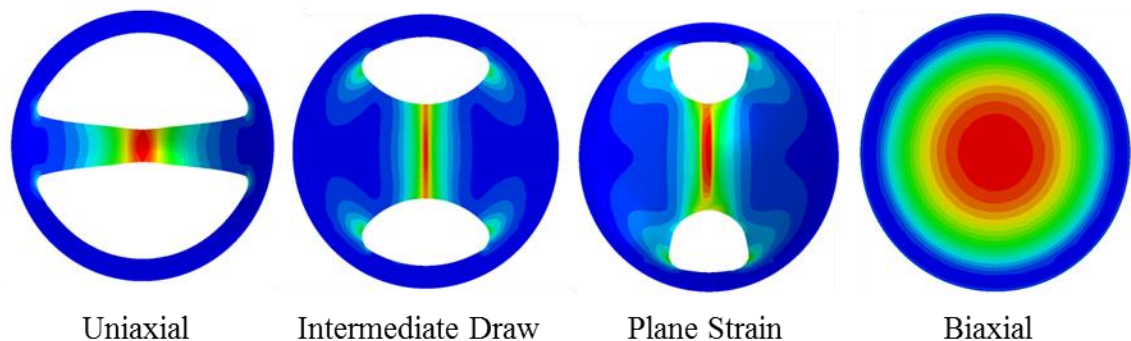


Figure 3-34: Strain concentration in the center of the gauge section for each of the specimen geometries.

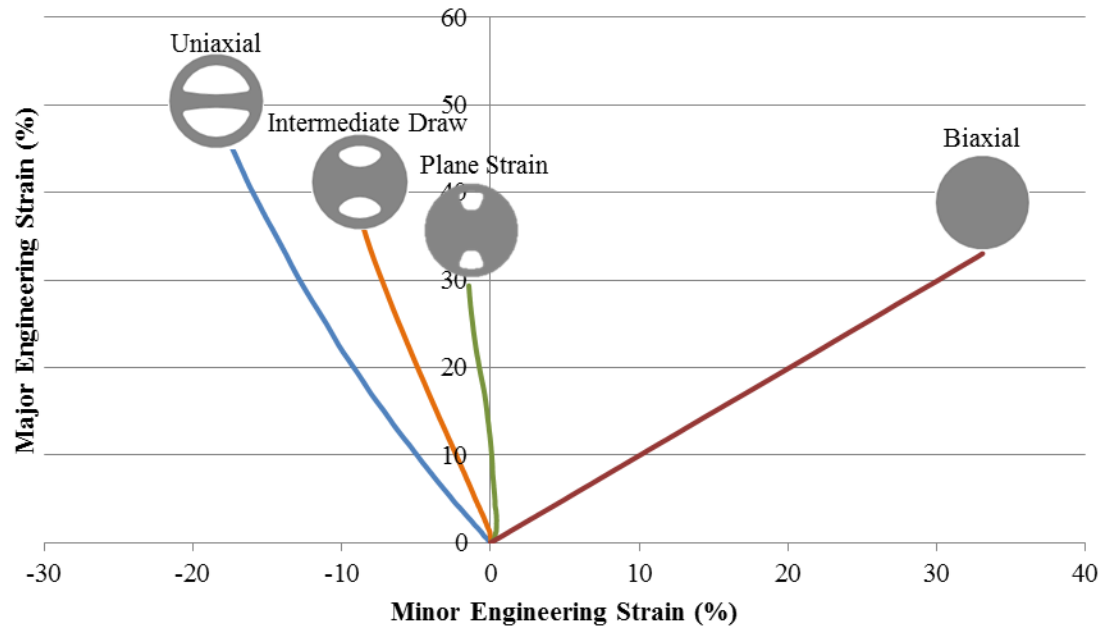


Figure 3-35: Numerically predicted strain path for each specimen geometry.

## 4 Results

### 4.1 Material Characterization

The results of the uniaxial tension tests ( $8.3 \times 10^{-4} \text{s}^{-1}$ ) were compiled for the 50.8mm (2inch) extensometer distance. The strain measurements for the 50.8mm extensometer were nearly identical to the measurements from the 25.4mm (1inch) extensometer until the severe localization occurred at failure, which indicates that the strains were nearly uniform along the length of the gauge section. The flow curves were used to determine the material parameters (Figure 4-1, Figure 4-2, Table 4-1). The yield strength for each material was determined by finding the intersection of the flow curve with a line having a slope equal to the elastic modulus and offset 0.002 true strain. The strain hardening exponent (n-value) was determined following the ASTM E646 (2007) method by finding the slope of the log of true stress versus log of true strain plot between 0.1 true strain and the strain at the ultimate tensile strength. The strength coefficient (K) was determined using Equation 5 (Leu, 1999). The power law was fit to the experimental data using the n-values and strength coefficients for both materials (Figure 4-3). The tensile tests were only conducted for the rolling direction of each material since the numerical constitutive model did not account for material anisotropy. Five specimens of each material were tested and the flow curves for both materials were remarkably consistent.

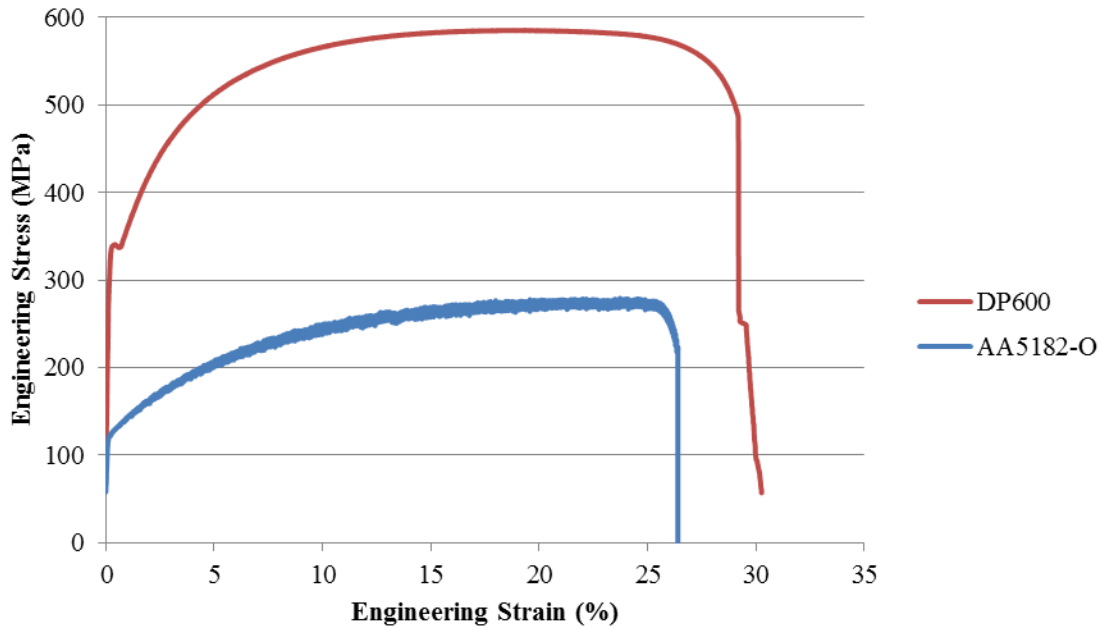


Figure 4-1: Engineering stress versus engineering strain curves for DP600 and AA5182-O.

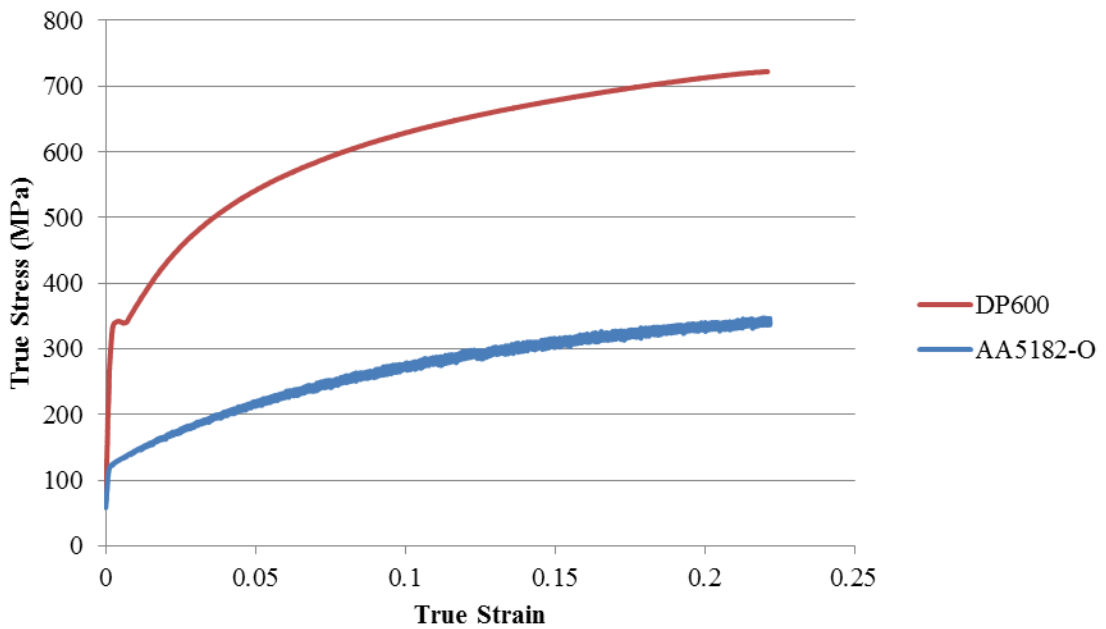


Figure 4-2: True stress versus true strain curves for DP600 and AA5182-O.

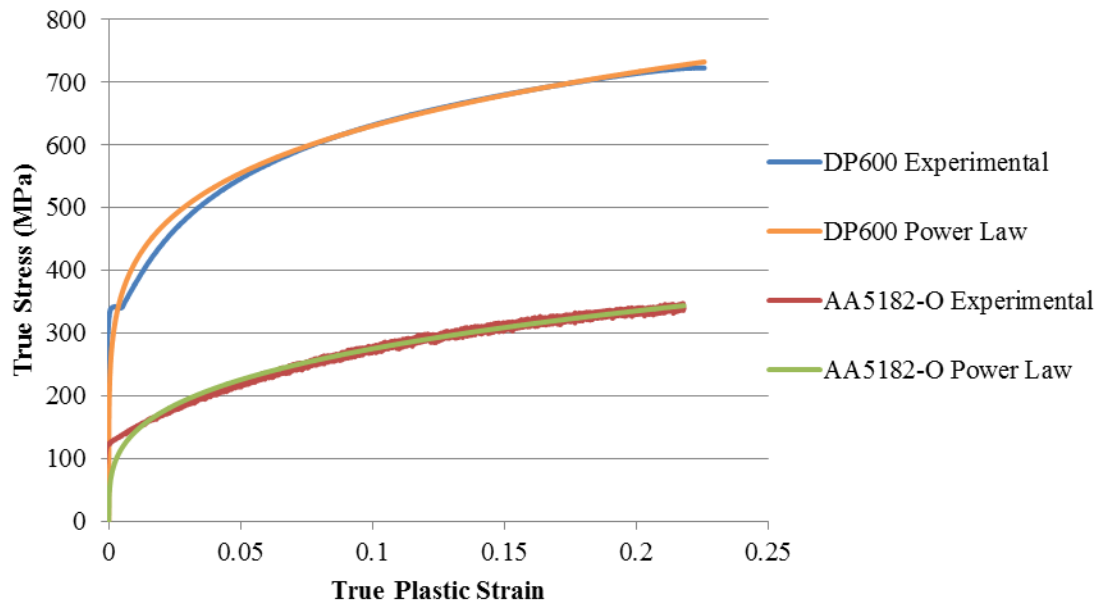


Figure 4-3: The power law fit for DP600 and AA5182-O.

$$K = UTS \left( \frac{e}{n} \right)^n \quad (\text{Equation 5})$$

Table 4-1: AA5182-O and DP600 material parameters determined from quasi-static uniaxial tensile tests.

<b>Material Parameter</b>	<b>AA5182-O</b>	<b>DP600</b>
Thickness (mm)	1.5	1.5
Elastic Modulus (MPa)	70	210
Yield Strength (MPa)	130	340
Ultimate Tensile Strength (MPa)	279	587
Strength Coefficient (K) (MPa)	531	963
Strain hardening exponent (n-value) (true strain)	0.286	0.184
Uniform elongation (engineering strain, %)	23.7	19.2
Total elongation (engineering strain, %)	26	29
Lankford coefficient ( $r_0$ )	0.727	0.687

The DP600 has significantly higher strength than the AA5182-O, but the aluminum has a significantly higher strain hardening exponent than the steel, an indication that it could have greater quasi-static formability. However, the steel has a larger failure strain, so it is difficult to predict which material will have a greater quasi-static formability. The aluminum has a 3% engineering strain difference between the end of uniform elongation and fracture, whereas the steel has a 10% engineering strain difference. The reduced post-uniform elongation is an indication that it may be challenging to form a neck in the aluminum EHF samples.

#### 4.2 Quasi-static Formability Tests

The quasi-static FLCs were obtained using Marciniak tests performed at an external research facility. The results for both materials are lower than anticipated, even accounting for the conservative nature of the ISO standard procedure.

The quasi-static experimental FLC for DP600 determined by an external research facility is significantly lower than the Keeler-Brazier theoretical curve (Figure 4-4). The DP600 quasi-static experimental forming limit curve is about 10% engineering strain lower than the theoretical curve in the uniaxial and biaxial regions. The quasi-static experimental plane strain intercept is remarkably 20% engineering strain lower than the theoretical curve. The significant difference in formability between the theoretical and experimental curves is not common for this grade of material. The shape of the experimental curve is quite similar to the standard shape for steels, and the absolute minimum of the curve lies on the zero minor strain axis.

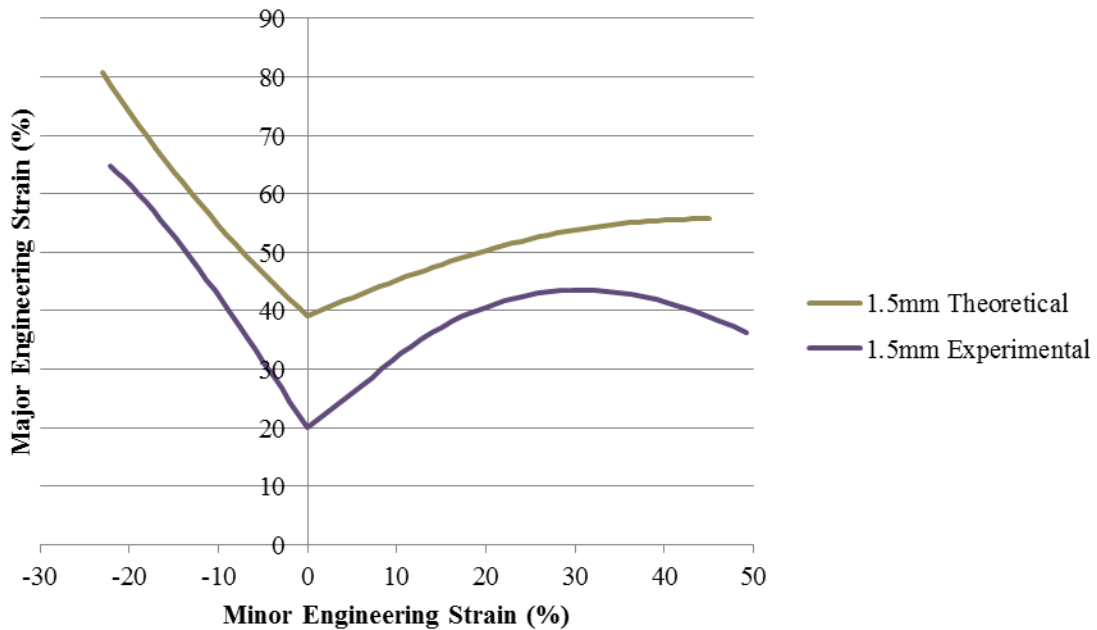


Figure 4-4: DP600 quasi-static theoretical and experimental forming limit curves.

The experimental quasi-static forming limit for AA5182-O determined by an external research facility has approximately the same shape and position as the experimental curve published by Wu et al. (2003) for the same material (Figure 4-5). In general, the FLC does not differ significantly from batch to batch of the same aluminum alloy. Wu et al. also used the Marciniak test to create necked grids and the Keeler method to plot the FLC. The Keeler method of determining the FLC (used for the 1.0mm sheet) would generally displace the FLC upward relative to the ISO standard procedure (used for the

1.5mm sheet), although Li et al. (2013) noted that the Keeler and ISO methods for FLD determination led to very similar results for AA5182-O. According to the general trend of a thicker sheet being more formable than a thinner gauge of the same sheet material, the 1.5mm material should be more formable than the 1.0mm material. Conservatively, the 1.5mm AA5182-O sheet material is expected to be at least as formable as the 1.0mm material by assuming the differences in strain measurement methodology and material thickness negate each other. The similarity between the two experimental AA5182-O FLCs provides some confidence that the 1.5mm experimental curve is accurate. However, the difference between the two FLCs, particularly in excess of 25% positive minor strain, is the likely due to the difference between the Keeler method and the ISO standard procedure for determining the onset of necking.

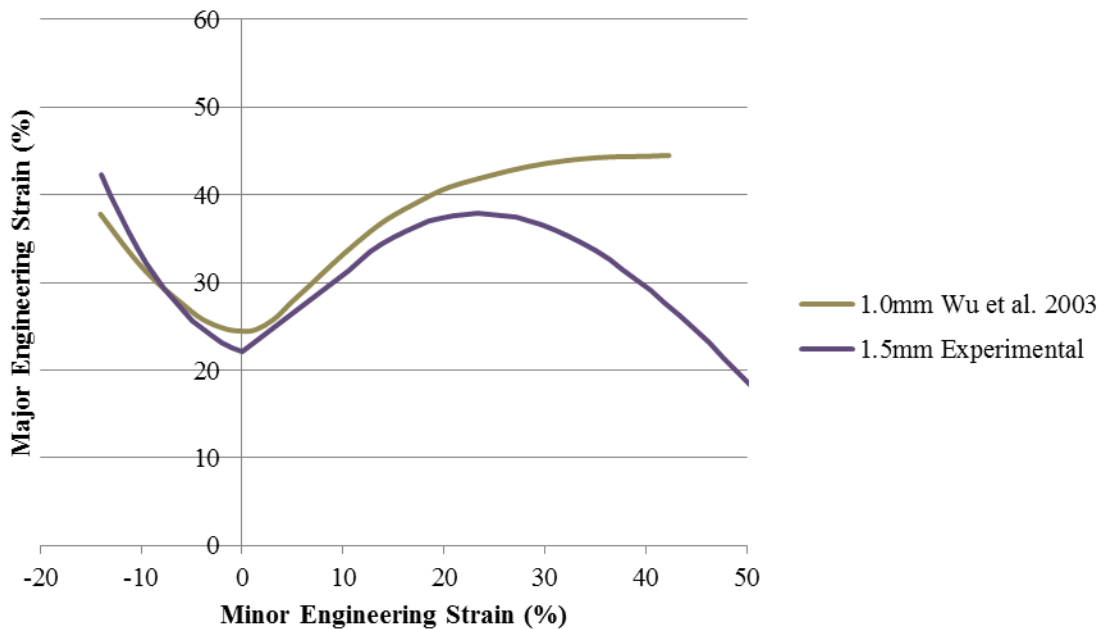


Figure 4-5: AA5182-O quasi-static experimental forming limit curves.

The position of the quasi-static forming limit curves for DP600 and AA5182-O are quite similar (Figure 4-6) as expected by comparing the n-values and total elongation values obtained from the uniaxial tension tests. The DP600 is marginally more formable than the AA5182-O in the uniaxial and biaxial regions of the FLD, but the plane strain intercepts are equivalent. The aluminum is only marginally less formable than the steel, so



formability should not be a major deterrent from using the lighter aluminum instead of the heavier steel for a particular application. The main factors that would dictate the selection of one material over another for a particular application are cost, weight, and strength.

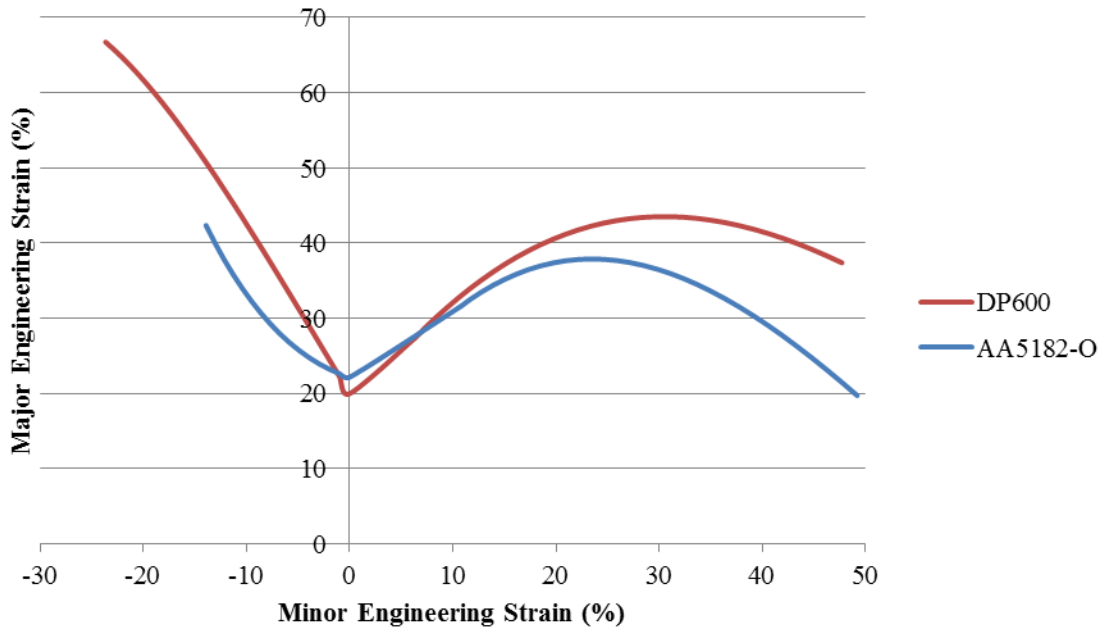


Figure 4-6: Experimental quasi-static forming limit curves for DP600 and AA5182-O.

The quasi-static Marciniak forming limit data that was obtained from the external research facility is not ideal for making comparisons with the EHFF forming limits because of the differences in procedures for determining the onset of necking. Instead of using DIC to measure the strains and determining the onset of necking using the ISO 12004-2 method, the FLC should have been generated using gridded specimens and the Keeler method. Fortunately, some gridded DP600 Nakazima test specimens were available for strain measurement using the Keeler method. The strains on the Nakazima specimens were measured using the same procedure as the EHFF specimens to provide a direct comparison of quasi-static formability. Unfortunately, only one necked specimen was obtained from the supply of gridded Nakazima samples, with the remaining specimens either safe or split. However, the necked grids obtained from the single necked sample strongly agree with the theoretical forming limit for the material (Figure 4-7). The

necked Nakazima points in the biaxial region suggest that the correct experimental FLC should be about 4% major engineering strain lower than the theoretical curve, but about 7% major engineering strain higher than the experimental FLC obtained from the external research facility. Although the sample size is small, the Nakazima data points obtained by measuring grids using the FMTI clearly indicate that the DP600 experimental quasi-static forming limit curve should be much closer to the theoretical curve. The questions raised about the reported quasi-static formability of the DP600 also apply to the reported quasi-static formability of the AA5182-O because the same procedure was used for both materials.

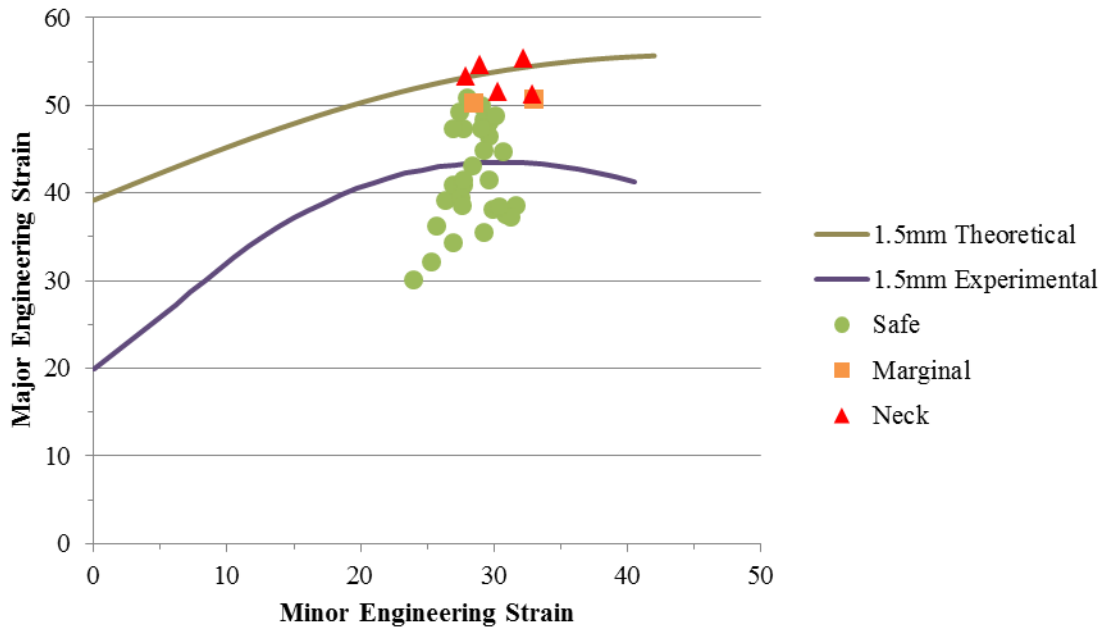


Figure 4-7: Strain measurements from a biaxial quasi-static Nakazima test specimen.

The formability of the DP600 observed using the Marciniak test coupled with the ISO standard procedure is much less than the formability reported by the Nakazima equipment coupled with the Keeler strain analysis method. Although the two quasi-static formability limits were generated using different experimental equipment, the results can still be compared. Experiments by Sriram et al. (2009), using the ISO 12004-2 standard procedure to define the limiting strains, found that the differences between the Nakazima and Marciniak tests caused by tooling geometry and friction effects are negligible for a

range of dual phase steels that included 1mm thick DP590 (Figure 4-8). The work of Sriram et al. (2009) indicates that the test methods are not responsible for the discrepancy observed in the DP600 quasi-static forming limit curve.

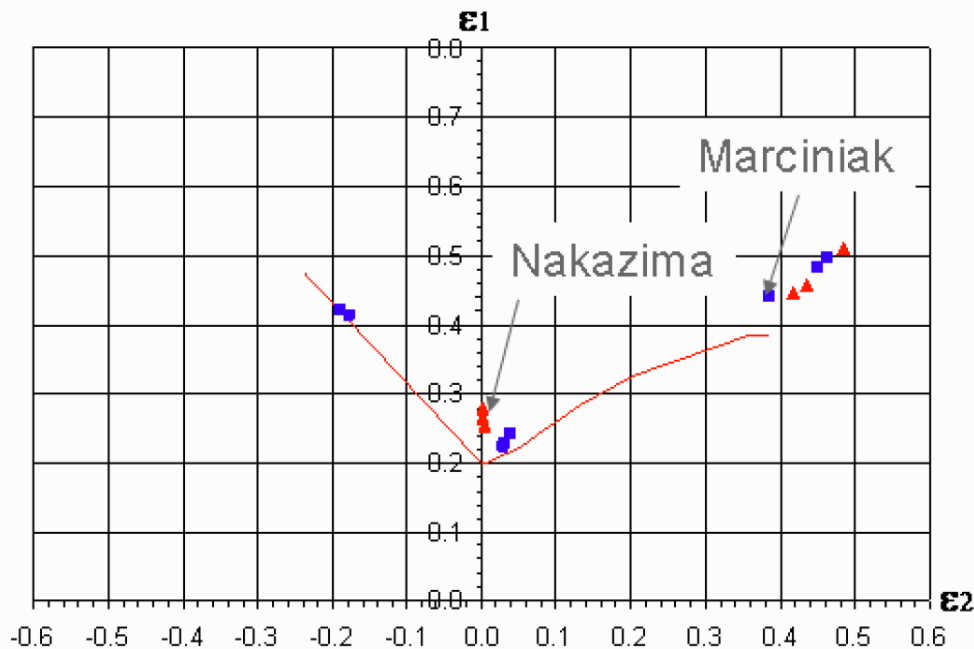


Figure 4-8: Comparison of necked points generated using Nakazima and Marciniak tooling for 1mm DP590. Image from Sriram et al. (2009).

The significant difference between the experimental and theoretical DP600 forming limits cannot be solely attributed to comparing the Keeler-Brazier theoretical curve against the ISO 12004-2 experimental strain analysis. Sriram et al. (2009) conducted experiments for a number of dual phase steels that confirmed the accuracy of the Keeler-Brazier (North American) theoretical curve relative to the Keeler tactile method. Similarly, Sriram et al. observed that the Arcelor-Mittal European theoretical curve is strongly supported by the forming limit curve determined by the ISO 12004-2 method. Although the ISO 12004-2 method is more conservative than the Keeler method, the maximum allowable difference is about 7% major engineering strain (Figure 4-9). The 20% major engineering strain difference observed in the plane strain region of the DP600 FLD is well beyond the acceptable variation between the Keeler-Brazier theoretical curve and the experimental curve obtained using the ISO 12004-2 strain analysis. The

significant difference between the experimental quasi-static formability results obtained using the ISO 12004-2 procedure and the Keeler-Brazier theoretical forming limit curve must be due to errors in the experimental FLC generation and/or a result of uncommonly poor material formability.

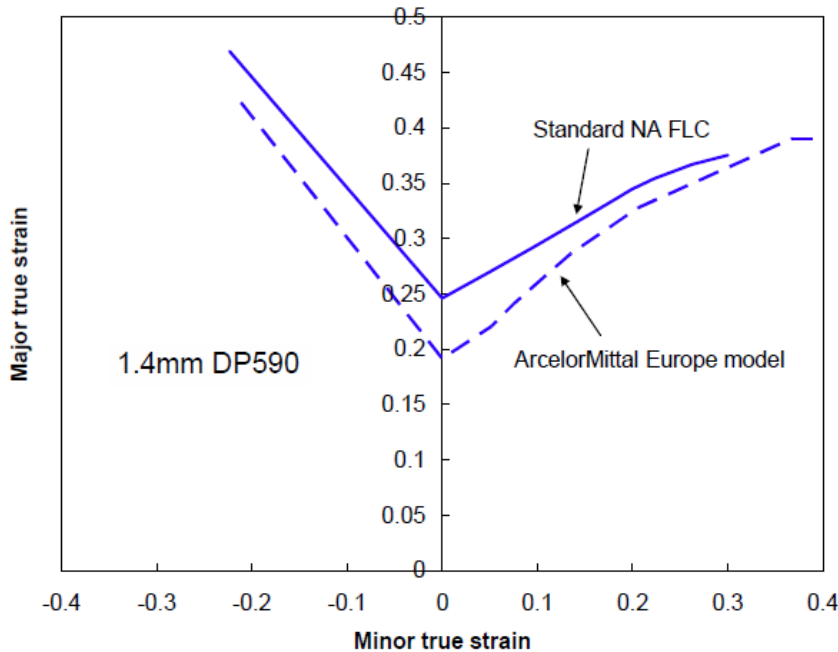


Figure 4-9: Comparison between standard North American and European theoretical models for 1.4mm DP590. Image from Sriram et al. (2009).

The experimental DP600 quasi-static FLC is unexpectedly much lower than the theoretical FLC, but the position of the experimental forming limit curve has been observed for the same grade of material by other researchers. The experimental quasi-static DP600 forming limit curve has a plane strain intercept value that is the same as the plane strain intercept for 1.4mm DP590, which was also generated using the Marciniak test method coupled with the ISO standard procedure by Sriram et al. (2009) (Figure 4-10). The FLC for the 1.5mm DP600 is slightly higher in the uniaxial and biaxial regions than the 1.4mm DP590 FLC. The material supplier was the same and the thickness of the material was virtually the same for both batches, indicating that it is very reasonable to compare the formability of these two materials. Despite the consistency, the strain hardening exponent of the 1.4mm DP600 was 0.135, which is significantly lower

than the 0.184 value measured for the 1.5mm DP600. The FLC of the 1.5mm DP600 should be significantly higher than the FLC for the 1.4mm material for all minor strain values because the height of the FLC is a function of the strain hardening exponent according to Keeler and Brazier (1977). The strain hardening exponent for the 1.5mm DP600 was confirmed by three independent testing facilities. The strain hardening exponent provided by Sriram et al. for the 1.4mm DP590 is likely accurate because the experimental data closely matches the theoretical forming limit curve, which generally indicates that the strain hardening exponent is correct. Raghavan et al. proposed a relationship for the theoretical forming limit curve that ignored the strain hardening exponent and instead varied with the total elongation. The total elongation of the 1.4mm DP590 reported by Sriram et al. was 22.4% and the total elongation of the 1.5mm DP600 was 29%. The Raghavan theoretical curve is identical to the Keeler curve for the 1.4mm DP600. In contrast, the Raghavan prediction for the 1.5mm material is 6% engineering strain lower than the Keeler curve, but still 14% engineering strain above the experimental FLC from the external research facility. Although the quasi-static formability of the 1.5mm DP600 sheet steel is very similar to the formability observed by Sriram et al., the properties of the 1.5mm DP600 indicate that the experimental FLC should be significantly higher than it is.

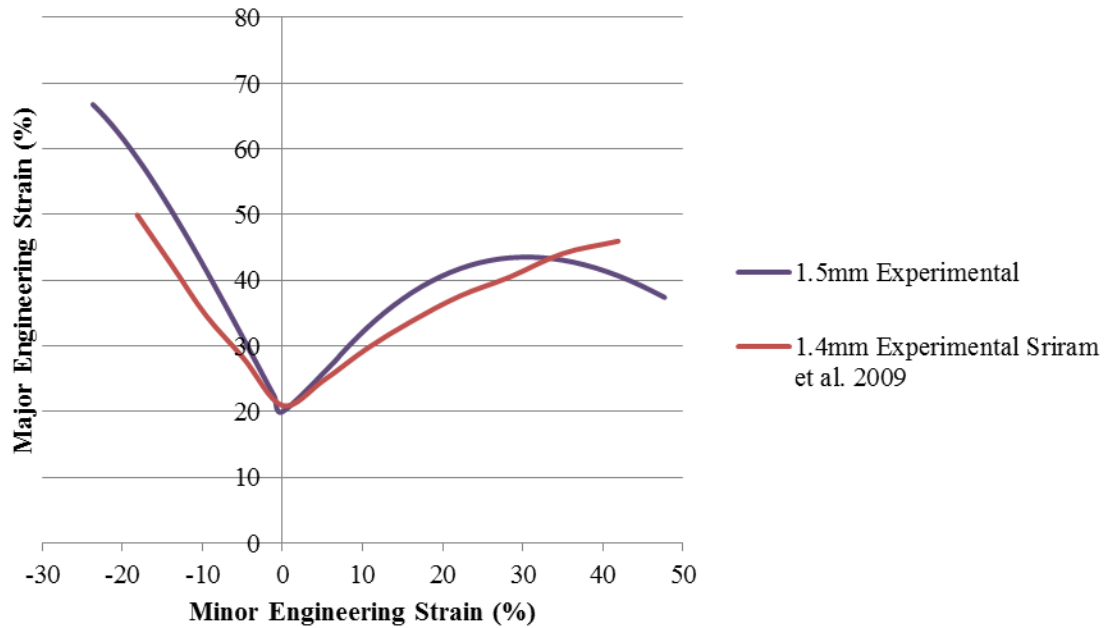


Figure 4-10: The experimental FLCs for 1.5mm DP600 and 1.4mm DP590.

The strain measurement methodologies and FLC generation techniques may account for the discrepancy between the formability measurements, but it is also possible that inaccurate data points were included in the analysis by the external research facility. Only the equation to fit the data points for the quasi-static forming limit was supplied, and the details of the experiments were withheld, so it is possible that quality issues such as splitting off-center, wrinkled or cracked drivers, improper calibration of measurement tools, and incorrect data manipulation occurred.

In addition to the conflicting quantitative formability data previously mentioned, there is qualitative evidence to suggest that the DP600 FLC is lower than the theoretical curve. As part of a separate industrial component of the research project, personnel at partnering manufacturers have been conducting full scale forming trials and the DP600 blanks tend to rupture during the quasi-static drawing process. One of the many potential causes for this unexpected rupturing is that the actual formability of the DP600 is less than the formability assigned to it during the virtual design of the drawing process. The drawing process was designed using the theoretical forming limit curve, so it is possible that the

ruptures are occurring because the actual formability of the steel is less than what is predicted using the Keeler-Brazier relation.

The quasi-static experimental DP600 forming limit curve generated using the Marciniak methodology coupled with the ISO standard procedure is much lower than expected. The differences in the test methodology and the forming limit curve generation methodology do not account for the large discrepancy in the plane strain region. An FLC obtained from the literature for a very similar batch of DP600 sheet steel gives further evidence as to the inaccuracy of the 1.5mm DP600 experimental curve. The theoretical FLC used by the steel supplier based on the material properties and the Nakazima experimental results suggest that the FLC should be significantly higher. The full scale forming trials indicate that the forming curve for this batch of DP600 steel could be lower than what is common for this grade of steel. The evidence is inconclusive as to the correct position of the quasi-static DP600 forming limit curve. By association, there is also uncertainty about the position of the AA5182-O experimental forming limit curve because it was created using the same procedure as the DP600 forming limit curve. Without an unquestionable quasi-static FLC for each material, the formability change achieved using EHFF cannot be indisputably evaluated.

### **4.3 Experimental EHFF**

The electrohydraulic free forming experiments were conducted primarily to determine the formability of DP600 and AA5182-O in high-velocity forming conditions. The mechanics of the EHF process can be analyzed by examining the energy delivered to the chamber and by quantifying the asymmetry of the process.

#### **4.3.1 Energy**

The input voltage required to form a specimen with a neck, the corresponding theoretical energy, and the experimental energy measured at the chamber, varied based on the specimen geometry and the material (Table 4-2 and Table 4-3). The amount of input

energy required generally increased as the size of the holes in the specimen increased. The plane strain and intermediate draw specimens required the least amount of energy. The uniaxial specimens required the most energy because they had the smallest gauge section which allowed the majority of the water to bypass the blank.

Table 4-2: DP600 input voltages to cause a neck.

<b>Specimen</b>	<b>Critical Voltage (kV)</b>	<b>Theoretical Energy (kJ)</b>	<b>Energy at Chamber (kJ)</b>
Biaxial	13.6	18.5	4.3
Plane Strain	10.1	10.2	2.8
Intermediate Draw	11.2	12.5	3.3
Uniaxial	15	22.5	5.0

Table 4-3: AA5182-O input voltages to cause a neck.

<b>Specimen</b>	<b>Critical Voltage (kV)</b>	<b>Theoretical Energy (kJ)</b>	<b>Energy at Chamber (kJ)</b>
Biaxial	6.6	4.4	1.3
Plane Strain	6.1	3.7	1.0
Intermediate Draw	6.4	4.1	1.2
Uniaxial	8.8	7.7	2.2

The biaxial specimens required a high input energy since more energy must be used to deform the blank. The chamber conditions for the biaxial specimens are quite different from the other specimens since the chamber is sealed because there are no holes in the biaxial specimens. Air cannot rush in to fill the void created by the displacement of water, so the density of the water in the chamber must decrease since the volume drastically increases as the blank deforms but the chamber is sealed. All of the other specimen geometries allow the exchange of air and water between the chamber volume and the environment through holes in the specimens.



The power trace, or rate of energy supply to the chamber, has a sinusoidal shape as determined from experimental measurements using Rogowski coils at both the Magnepress and the chamber (Figure 4-11). The discharge time was approximately constant at about 120 $\mu$ s across the range of input voltages. The experimental noise that occurred for about 4 $\mu$ s near time zero was removed from the energy calculation. Assuming a symmetrical energy history, the amount of energy that occurred in the timespan of the noise for a 6.3kV discharge was approximately 0.3kJ as measured at the chamber and 0.6kJ as measured at the Magnepress. Even with the addition of this initial assumed energy, the measured energy falls well below the theoretical value. The summation of the energy over time shows a linear increase in the energy of the discharge (Figure 4-12).

The shape and duration of the power trace are unique to the experimental configuration, and even different configurations on the same pulse unit could have different power traces. The power trace can be influenced by factors including the position, length, and material of the busbars, the electrode gap and use of a bridge wire, the resistivity of forming fluid, and the internal parameters of the pulse unit. The high sensitivity of the power trace to many factors is a strong indication that the variance in experimental configurations from lab to lab will cause significant differences in the duration and intensity of the pressure pulse that forms the blank. The characteristics of the pressure pulse are linked to the formability enhancement mechanisms that are activated and therefore the formability results observed. Although it is seldom the case, detailed energy measurements should always be published with experimental results because of importance of the power trace on the pressure pulse and consequently on the formability of the material.

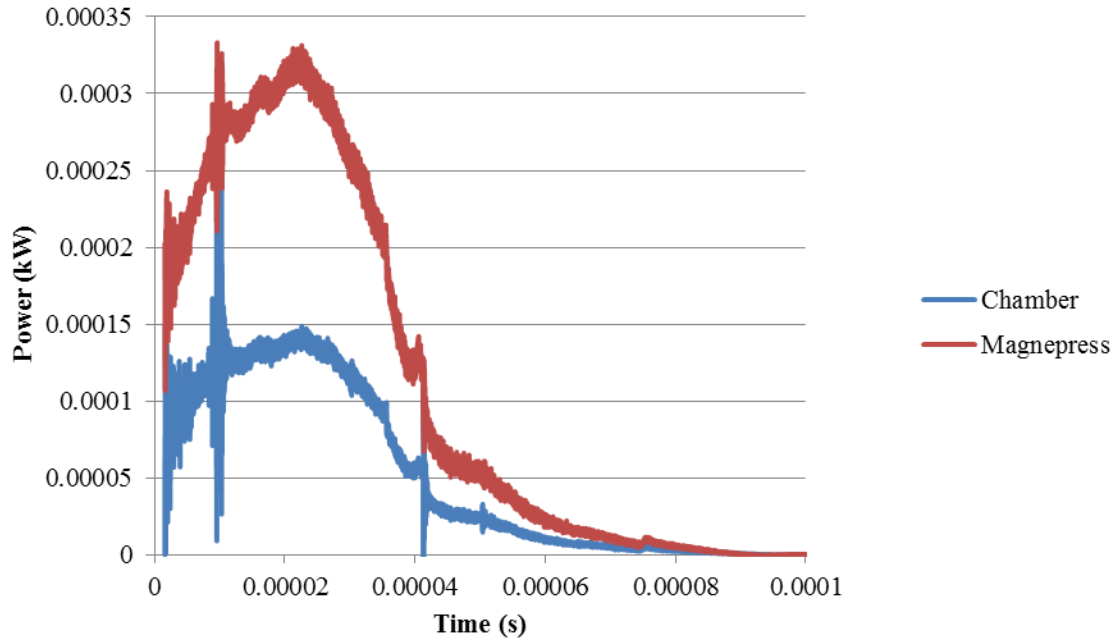


Figure 4-11: The power trace for a 6.3kV pulse as measured at the chamber and at the Magnepress.

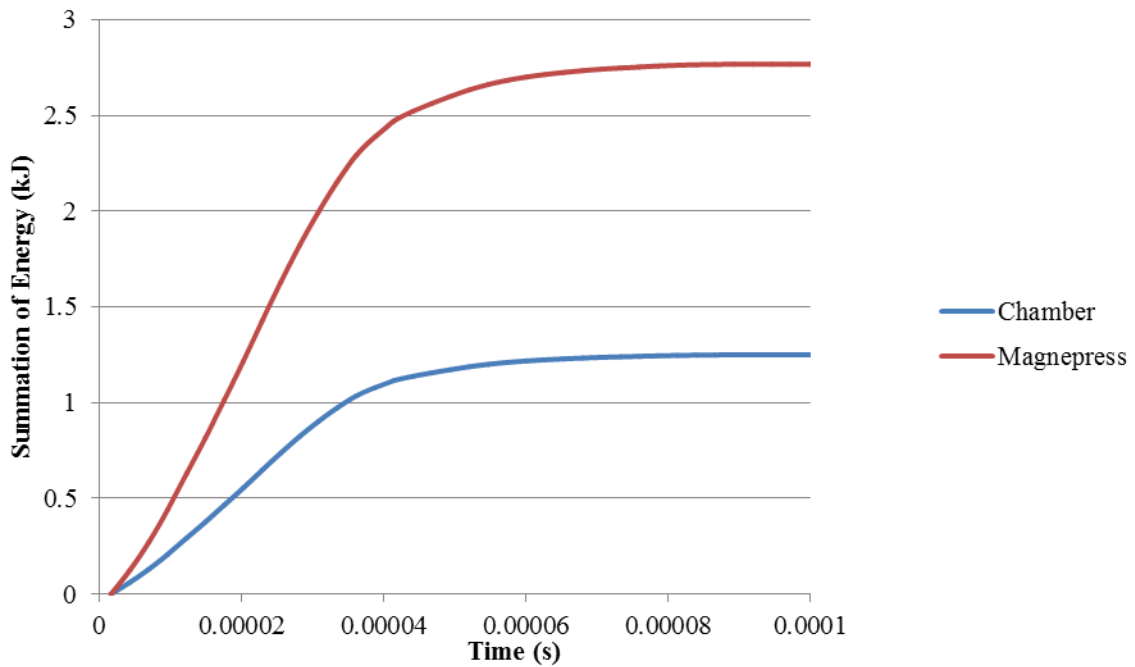


Figure 4-12: Summation of discharged energy over time for a 6.3kV pulse as measured at the chamber and at the Magnepress.

The amount of energy discharged by the Magnepress pulse unit is about two-thirds of the theoretical energy that can be stored in the capacitors (red square data points, Figure 4-13). There appears to be a significant energy loss between the Magnepress and the chamber, as less than half the energy measured at the Magnepress actually reached the chamber (blue diamond data points, Figure 4-13). The energy losses in the path to the chamber make the actual energy delivered to the chamber less than one third of the theoretical energy that can be stored in the capacitors (green triangle data points, Figure 4-13). The energy reduction between the Magnepress and chamber is particularly troublesome because there was insufficient energy to cause the uniaxial steel specimens to neck, which negatively affected the ability to determine the EHFF FLC for DP600.

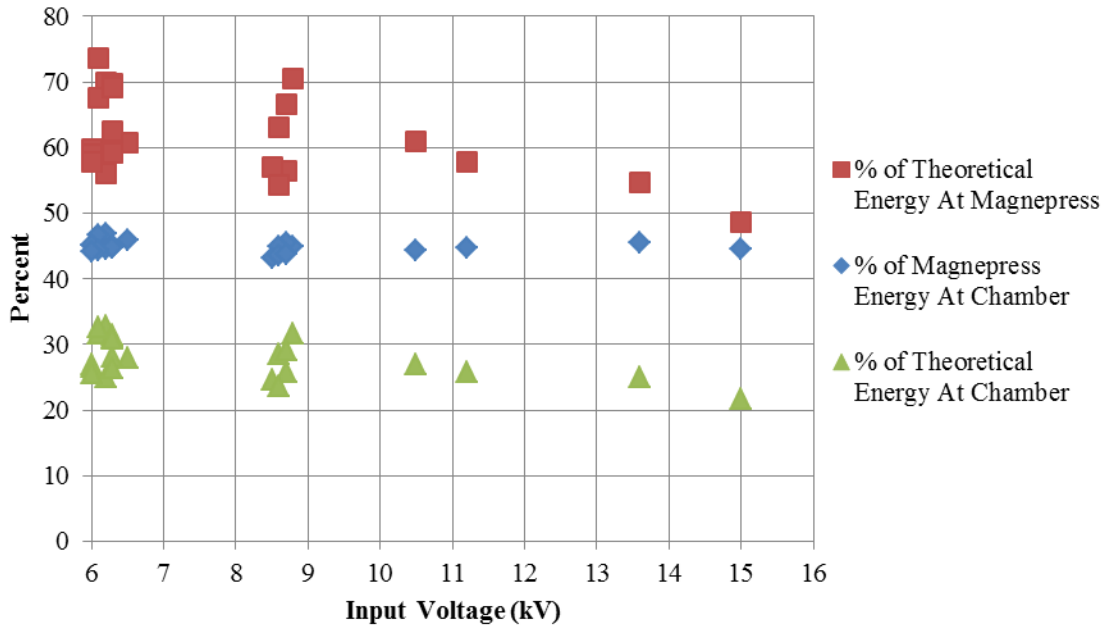


Figure 4-13: Comparison of theoretical energy and experimental energy measured at both the Magnepress and chamber over the range of input voltages.

### 4.3.2 Formability

A total of 268 specimens were formed to produce the electrohydraulic free forming FLCs for AA5182-O aluminum and DP600 steel, although only 34 necked FLC specimens

were formed over the entire series of experiments. The experiments were conducted over several months, and over that time changes in the forming conditions such as using a different pulse unit, the fabrication of a new chamber geometry, and damage to the pulse equipment occurred. The changes to the experimental set-up meant that only 132 blanks were formed in the final conditions, of which 23 (17%) were necked. Fifty two steel specimens were formed in the final forming conditions to achieve sixteen necked specimens (31%), of which fourteen gridded specimens were used to generate the steel FLC (Figure 4-14, Appendix C). Eighty aluminum specimens were formed in the final conditions to achieve seven necked specimens (9%), of which four gridded specimens were used to generate the FLC (Figure 4-15, Appendix C). The major and minor strains of only a few square grids per specimen, corresponding to the points identified as necked, were plotted on the FLD. The measured strains were plotted together along with the quasi-static FLC for each material.

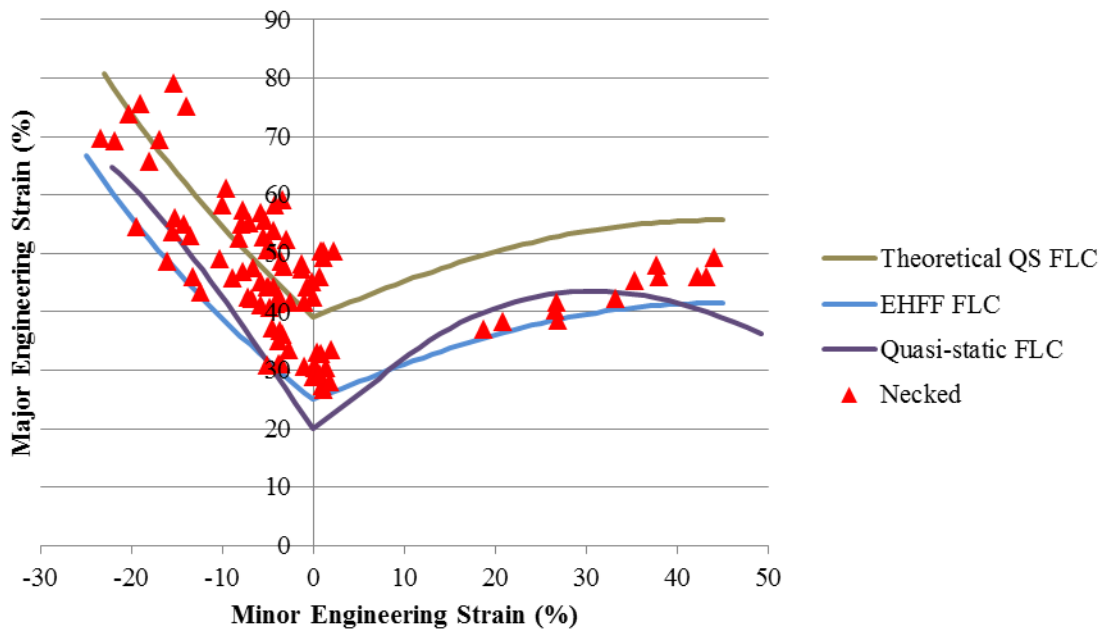


Figure 4-14: DP600 1.5mm thick EHFF necked strain measurements and the resulting EHFF FLC.

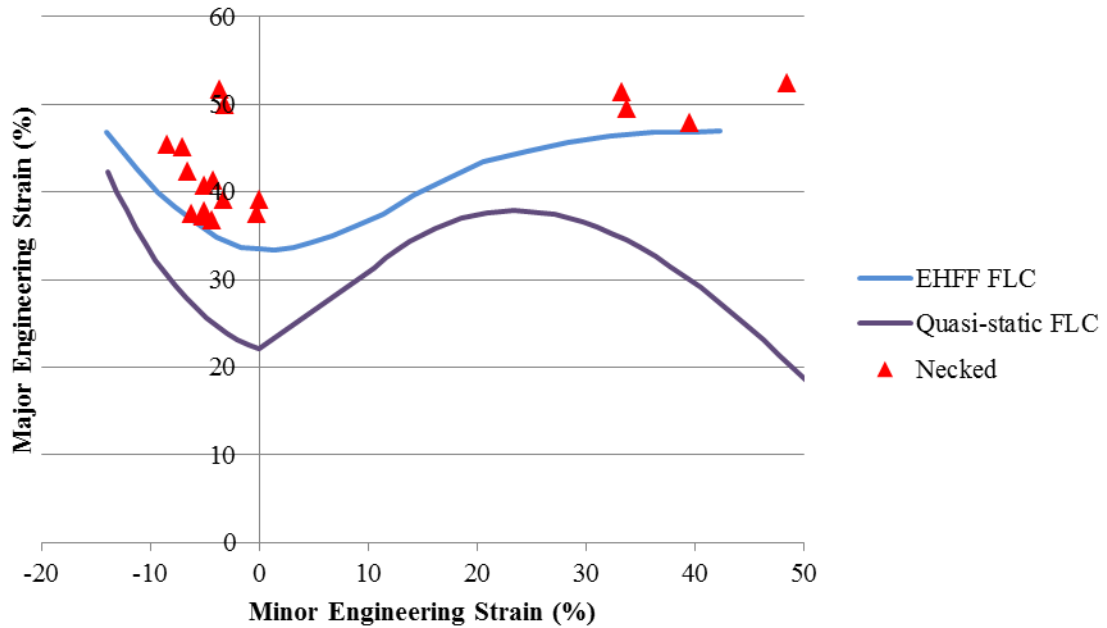


Figure 4-15: AA5182-O 1.5mm thick EHFF necked strain measurements and the resulting EHFF FLC.

The DP600 EHFF FLC (Figure 4-14) shows no formability improvement compared to the quasi-static experimental FLC. The small shape differences between the two curves can be attributed to the strain measurement and FLC generation procedures and is within the typical band of uncertainty associated with an FLC. At the plane strain intercept, the DP600 EHFF FLC is marginally higher by 6% engineering strain than the quasi-static experimental curve, but the exact opposite is observed at significant negative and positive minor strains. The EHFF FLC has a similar shape to the theoretical FLC, but is about 14% engineering strain below the theoretical curve at the plane strain intercept. It is interesting to note that there are many measured strains from necked grids which easily exceeded the theoretical forming limit curve, particularly in the negative and zero minor strain regions of the FLD.

The AA5182-O EHFF FLC (Figure 4-15) is 11% engineering strain above the quasi-static experimental curve at the plane strain intercept. The AA5182-O EHFF FLC indicates a significant formability improvement over the quasi-static FLC for the entire

range of forming conditions, and in particular, a remarkable formability improvement between -10% and 0% minor strain.

For DP600, the Keeler-Brazier relation with an  $FLC_0$  of 25% was used to fit the necked EHFF data. For AA5182-O, the shape of the 1.0mm quasi-static curve from Wu et al. (2003) fit the shape of the critical EHFF data points, and was used as a template to generate a forming limit curve for the necked EHFF data. In comparison to the 1.0mm FLC from Wu et al. (2003), the negative minor strain portion of the curve and the plane strain intercept were shifted up by 9% engineering strain, and the positive minor strain portion of the curve was shifted up 2.5% engineering strain. The two sides of the AA5182-O EHFF curve were matched by using a 4<sup>th</sup> order polynomial to fit the data between 0% and +10% engineering strain.

The EHFF FLCs were generated with extreme care and attention to detail. The large number of data points across key regions of the FLC means that there is no difficulty to interpolate between sets of data in order to draw the FLCs. There is some overlap between the majority of the points, especially on the negative minor strain side of the FLC, so the position and shape of the EHFF FLC for both materials was almost unambiguous. On the positive minor strain side of the FLD, it would have been beneficial to have an additional specimen geometry to fill the gap between balanced biaxial and plane strain. This region is of particular importance because the absolute minimum of the FLC is sometimes observed to lie in the region between 0% and 5% positive minor engineering strain.

To overcome the shortage of necked specimens to create the FLC, one aluminum biaxial specimen and one steel biaxial specimen that were formed with a different experimental configuration during the early experiments with a slightly different experimental configuration were included in the respective plots of necked points. The total number of necked specimens used to generate the FLC for each material is shown in Table 4-4. The additional biaxial specimens were required because of the combined effects of the low probability of capturing a necked specimen in EHFF and the difficulty to form a neck in the biaxial region due to shear fracture. Shear fracture can limit the formability of some

metals before the onset of localized necking, particularly in specimens with positive minor strain, as reported by Korhonen and Manninen (2008) and Kim et al. (2011).

Table 4-4: Total number of necked specimens used to generate the FLC.

<b>Material</b>	<b>AA5182-O</b>	<b>DP600</b>
Uniaxial	0	3
Intermediate Draw	2	4
Plane Strain	1	5
Biaxial	2	3

There were a large amount of blanks required for trial and error to find the optimum forming conditions and correct input voltage. To save time and resources, some specimens were formed without a grid during the trial and error process, and occasionally a specimen that necked was not gridded. Therefore, not all of the necked specimens could be used to plot necked points on the FLD (Table 4-5). It was possible to form a neck in the gauge section for each of the four specimen geometries for both steel and aluminum (Figure 4-16). The geometry of the modified specimen dominated any material anisotropy, as the neck or failure was always perpendicular to the gauge length. Despite initial concerns about the possibility of edge cracking, the blanks prepared by CNC milling were experimentally shown to neck in the center of the gauge section and no edge cracking was observed.

Table 4-5: Total number of necked specimens in the final forming conditions.

<b>Specimen</b>	<b>AA5182-O</b>	<b>DP600</b>
Biaxial	1	2
Plane Strain	1	6
Intermediate Draw	2	4
Uniaxial	3	4

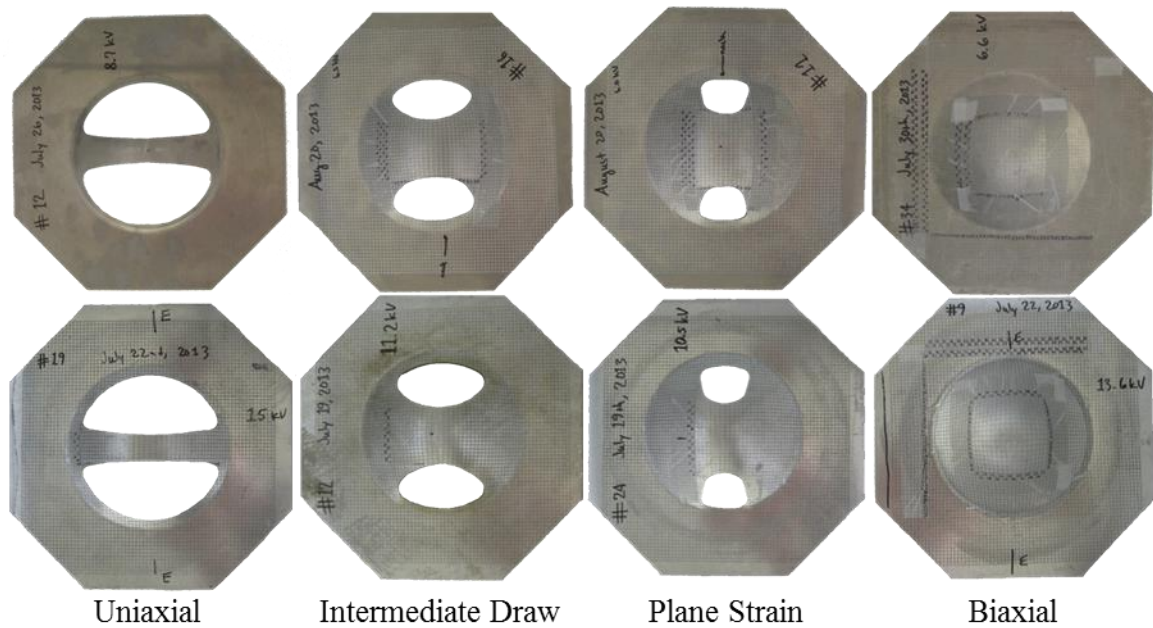


Figure 4-16: Necked specimens in each strain path for AA5182-O (top row) and DP600 (bottom row).

It is difficult to generate necked specimens in most materials with EHF because it is a dynamic process with significant process variability and accordingly the exact same conditions do not occur with each discharge. In addition, unlike quasi-static tests, there is no user control during the EHF process, and therefore no way to stop the process when a neck starts to develop. The difficulty to form a neck in a particular specimen geometry varied with the material and the strain path. For example, a specimen formed at the critical voltage for plane strain and intermediate draw geometries of DP600 routinely formed a neck, whereas for biaxial DP600, only two specimens formed with a voltage input of 13.6kV were necked by chance. For uniaxial DP600, the low capacitance of the Magnepress made the total energy that could be stored in the capacitors less than the energy required to form a necked specimen. The maximum input voltage of the pulse unit was barely sufficient to form three necked specimens by chance, with the majority of the uniaxial specimens being safe because of insufficient input energy.

Although the variability of the EHF process was overcome for DP600 by forming several specimens, it was especially difficult to capture a neck in AA5182-O specimens due to its limited post uniform elongation. The small strain window in which to capture a neck in



an AA5182-O specimen means that aluminum is especially sensitive to any changes in the process, and the inability of aluminum to compensate for variations in the EHF process accounts for the low frequency of necked aluminum specimens. An example for the challenge of capturing a neck in aluminum EHFF specimens is that three consecutive intermediate draw specimens formed at an input voltage of 6.3kV were safe, necked, and split, respectively (Figure 4-17).

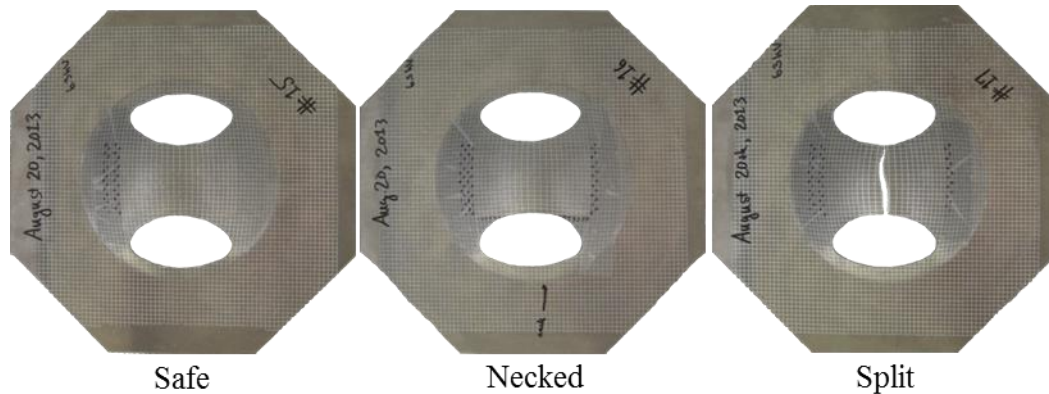


Figure 4-17: Three consecutive aluminum intermediate draw specimens formed at 6.3kV were safe, necked, and split.

The Magnepress is controlled in 100V increments, which is too large to form necked specimens for some specimen geometries, particularly in aluminum. As a result of the large increments of input voltage, very few AA5182 necked specimens were formed. However, several aluminum specimens were formed at approximately the same energy required to form a neck and happened to split. Strain values measured from grids that closely border a small split can provide some indication of the limit strain. Strain measurements from grids in close proximity to a small split were added to the AA5182-O FLD to increase the amount of data points and thus enhance the confidence in the EHFF FLC (Figure 4-18). In total, 15 AA5182-O specimens were used to generate data points (Table 4-6).

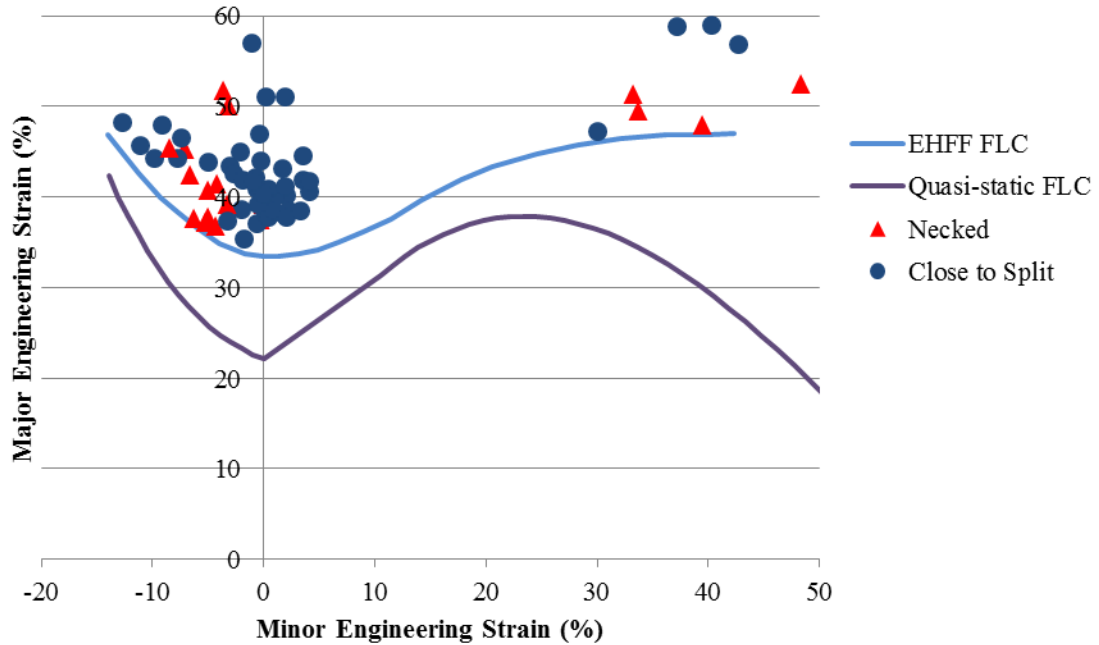


Figure 4-18: AA5182-O 1.5mm thick EHF necked and proximity to split strain measurements and the EHF FLC.

Table 4-6: Quantity of specimens used to generate AA5182-O data points.

Specimen	Necked	Close to Split
Biaxial	2	1
Plane Strain	1	4
Intermediate Draw	2	3
Uniaxial	0	2

The location of the steel and aluminum quasi-static experimental forming limit curves is about the same, even though the shapes of the curves are very different (Figure 4-6). In contrast, the shapes of the experimental EHF forming limit curves are very similar for the two materials, and the AA5182-O EHF forming limit curve is higher than the DP600 forming limit curve (Figure 4-19). The AA5182-O has greater formability in EHF than the DP600 for zero and positive minor strains, while the two materials have approximately the same formability in EHF at minor strains that are less than -10% engineering strain.

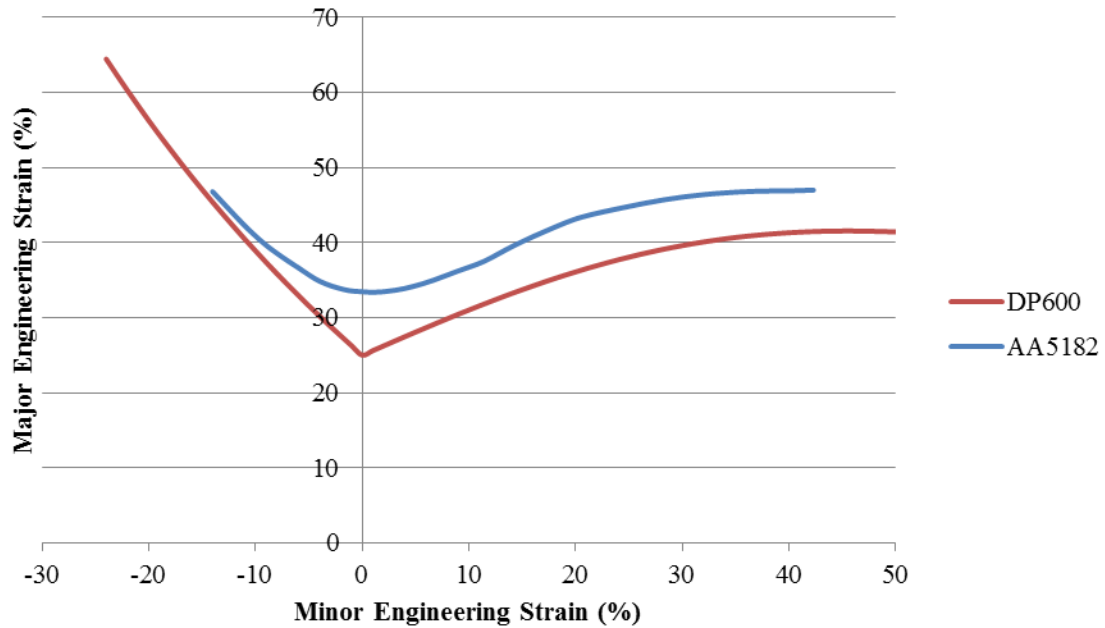


Figure 4-19: Comparison of the experimental EHFF FLCs for DP600 and AA5182-O.

The average height for necked specimens was recorded from the experimental EHFF specimens for each material and for each strain path (Table 4-7). The height of the necked specimens was used as a reference to set the amount of space between the blank and die in the mini-die experiments.

Table 4-7: Average height of necked specimens (mm).

<b>Specimen</b>	<b>AA5182-O</b>	<b>DP600</b>
Biaxial	29.6	33.3
Plane Strain	23.5	22.2
Intermediate Draw	24.7	23.6
Uniaxial	31.4	26.3

The surface profiles (the final height of the specimen based on the deformed distance from the apex) of the DP600 and AA5182-O specimens were very similar for all strain paths. The shape of all specimens for both materials was convex, which is quite different than is observed in EMF experiments. The intermediate draw and plane strain specimens formed to approximately the same height for both materials and had very similar height

distributions. The aluminum uniaxial specimens formed to greater height than the DP600 uniaxial specimens, while the opposite was true for biaxial specimens (Figure 4-20, Appendix C).

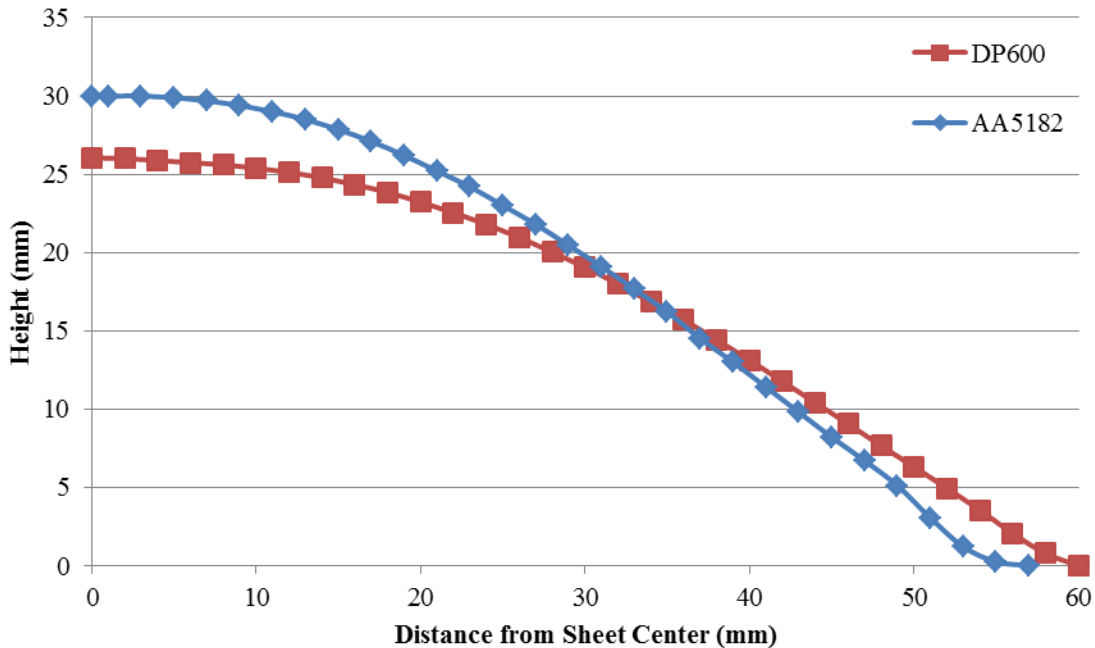


Figure 4-20: Final displacement of the sheet measured radially from the sheet center for necked DP600 and AA5182-O uniaxial specimens.

The strain profiles from the center to the edge of the sheet (based on the undeformed distance from the sheet center) were very similar for each of the specimen geometries for both the DP600 and AA5182-O materials (Figure 4-21, Figure 4-22, Appendix C). In general, even though necked specimens from each material had similar heights, the DP600 had a uniform strain distribution, while the strains of the AA5182-O specimens were comparatively more concentrated near the apex. The vastly different input energies required to cause a neck likely changed the profile of the pressure pulse on the surface of the blank, and therefore the amount of stretch in different regions of the blank is expected to be different.

For the same loading path, the ratio of the strain in the major or minor direction is indicated by the r-value, which varies slightly from material to material. Even though DP600 and AA5182-O specimens necked at about the same height, the aluminum

specimens generally had more major strain and less minor strain (Figure 4-21, Figure 4-22, Appendix C). Compared to DP600, AA5182-O has a higher quasi-static r-value in the rolling direction, so for the same amount of major strain, the quasi-static r-value in the rolling direction indicates that the AA5182-O should have a lower minor strain. However, r-value may change with strain rate and reference direction, and the quasi-static r-value is not necessarily indicative of the r-value in other conditions. For DP600, the r-value increases slightly with strain rate in all three reference directions, while the r-value is much more consistent for AA5182-O (Rahmaan et al., 2014). The DP600 high rate r-value is higher than the high rate r-value for AA5182-O, so the observed pattern of the aluminum specimens having more major strain and less minor strain is expected.

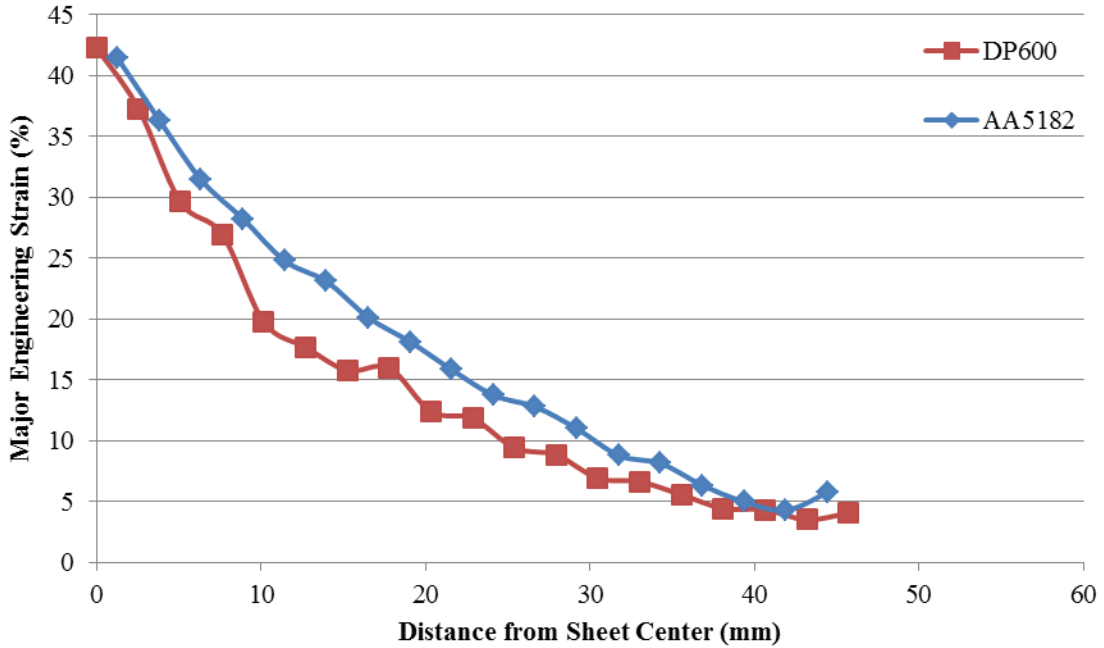


Figure 4-21: Major strain distribution measured radially from the sheet center for safe DP600 and AA5182-O uniaxial specimens.

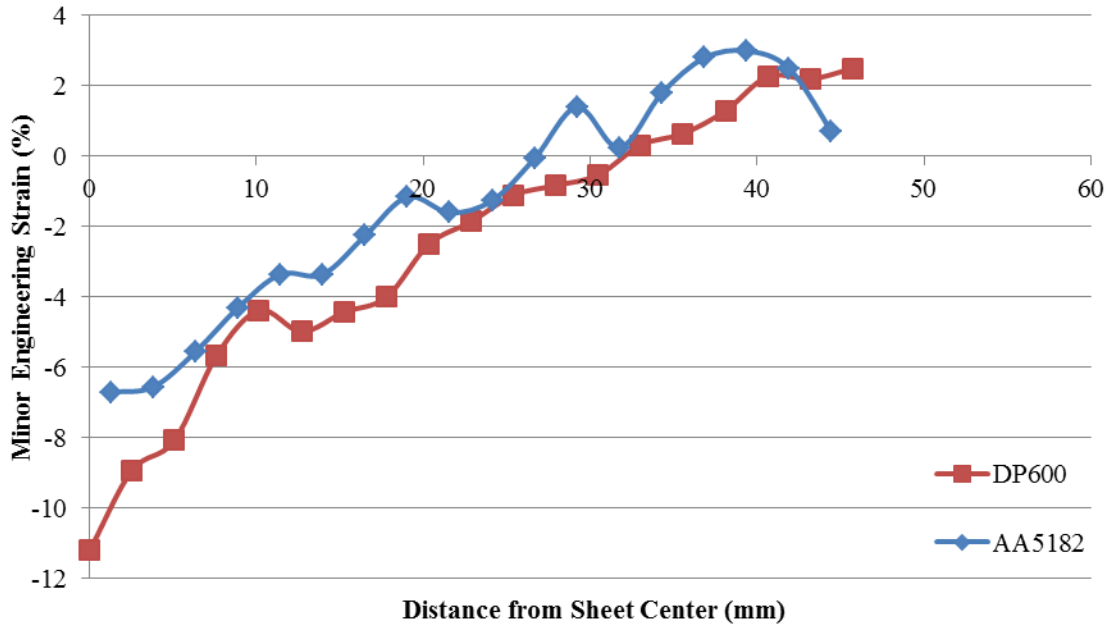


Figure 4-22: Minor strain distribution measured radially from the sheet center for safe DP600 and AA5182-O uniaxial specimens.

### 4.3.3 Anisotropy and Asymmetry

The simulation of EHFF assumed the forming pressure on the blank was axisymmetric and employed classical elasticity and plasticity theories which assume that the metal deforms in a uniform and isotropic manner. However, these simplifications are easily debunked because both AA5182-O and DP600 are somewhat anisotropic materials over the entire spectrum of EHFF strain rates and the EHF discharge and the resulting pressure pulse may not be axisymmetric. The strain distribution in the EHFF biaxial specimens can be used to evaluate if there is significant asymmetry in the process as a whole, but cannot differentiate between the two possible causes. The other geometries cannot show material anisotropy because the strain distribution is controlled by the geometry of the blank and causes the sheet to neck in a specified direction regardless of material orientation.

Several biaxial specimens of each material were analyzed to establish trends in the data relative to anisotropy. The major strain distributions were measured from the center to the edge of the sheet on each side of the apex, so there are two measurements for each sheet direction. The strain values from a safe biaxial AA5182-O specimen are similar for both the rolling and transverse directions, and the measurements from both sides of the apex in the rolling direction are nearly identical (Figure 4-23). The minor strain shows similar trends and there is no significant anisotropy observed in the strain distribution for the aluminum biaxial specimens, indicating that the material can be assumed as isotropic and that the process can be assumed axisymmetric.

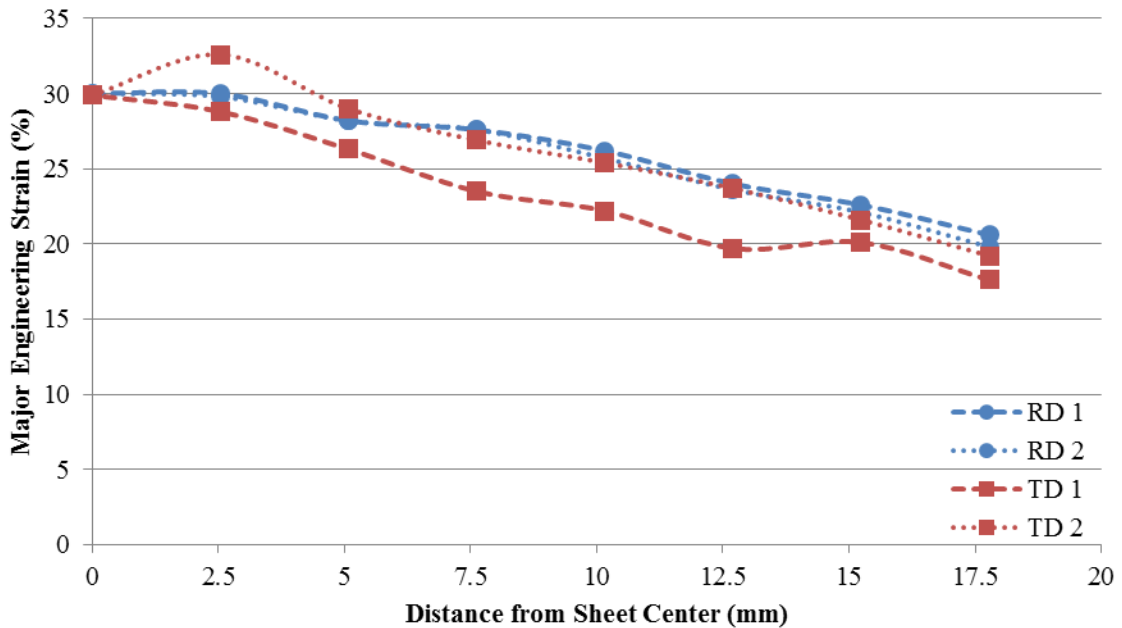


Figure 4-23: Major strain measurements from a safe biaxial AA5182-O specimen in the rolling and transverse directions.

The major strain distribution from a safe biaxial DP600 steel specimen shows that the rolling direction strains are very similar to the transverse direction strains in the region of the apex, but away from the apex the difference between the two sides is not negligible and may indicate some anisotropy (Figure 4-24). The strains were measured up to 23mm away from the apex to allow for a thorough analysis over the majority of the specimen. The strains were measured on each side of the apex, so there are two measurements for

each sheet direction. The minor strain shows similar trends and there is no significant anisotropy observed in the strain distribution for the steel biaxial specimens, indicating that the material can be assumed as isotropic and confirming that the process can be assumed axisymmetric.

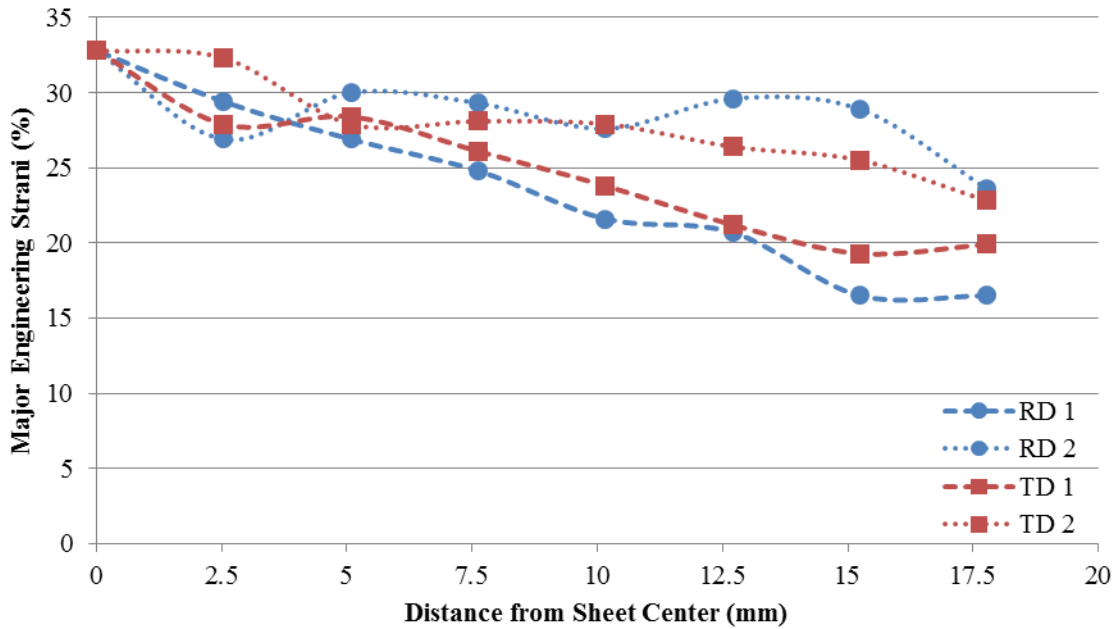


Figure 4-24: Major strain measurements from a safe biaxial DP600 specimen in the rolling and transverse directions.

The splitting direction in biaxial specimens, formed with a small amount of excess energy to avoid catastrophic failure, can also be used to assess the material anisotropy. Splitting originated parallel to the rolling direction for both DP600 and AA5182-O, regardless of the orientation with respect to the electrodes. The grain morphology caused by the rolling process had more influence on the failure direction than any asymmetry in the pressure distribution. For DP600, cracks always extended in a direction parallel to the sheet rolling direction, indicating that the tensile force which caused the crack was perpendicular to the rolling direction (Figure 4-25). The preferential cracking direction of DP600 shows that material anisotropy is non-negligible. For AA5182, some cracks were parallel to the rolling direction, and some extended in more than one direction, indicating that the material anisotropy is not as strong as it is for DP600 (Figure 4-26). It is probable that the



input energy required to cause a neck and the associated height of a necked specimen would be less if the gauge sections of the specimens were running parallel to the transverse direction since the major strains would be acting perpendicular to the preferential failure direction.



Figure 4-25: Splitting in biaxial DP600 specimens.

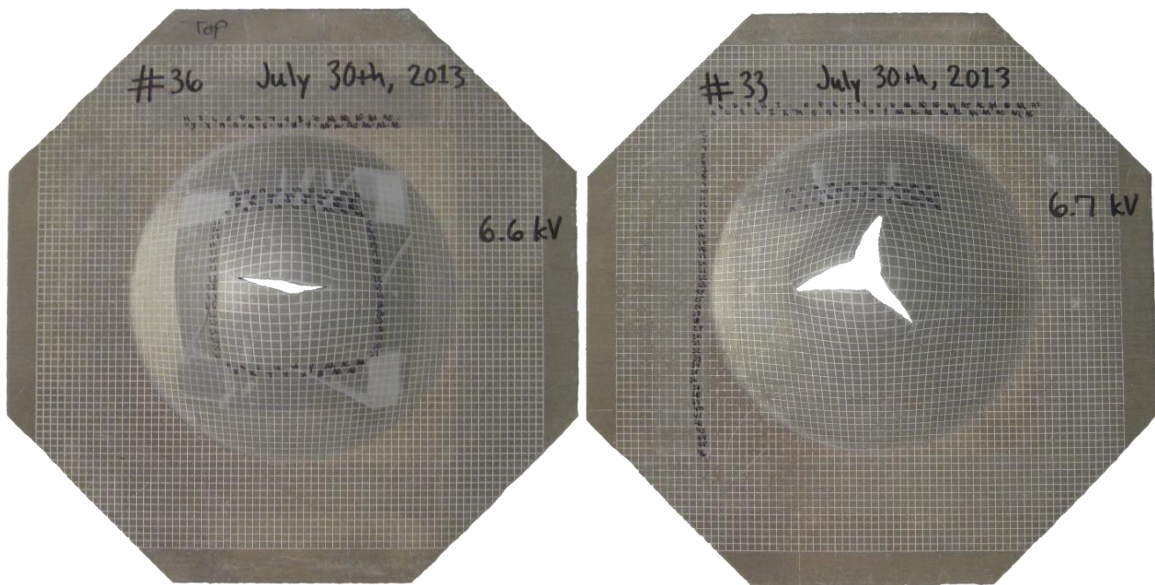


Figure 4-26: Splitting in biaxial AA5182-O specimens.

For both materials, there is evidence of some planar anisotropy reported from the uniaxial tensile test data at a range of strain rates (Rahmaan et al., 2014) and from the direction of failure propagation in EHFF biaxial specimens. However, the anisotropy observed in the measured strain distribution was not significant for these materials. For the specimens with machined cut-outs (uniaxial, intermediate draw, and plane strain), it was possible to align the gauge section either parallel or perpendicular to the rolling direction of the material; but for all of these specimens, the gauge section was aligned with the rolling direction for the sake of consistency.

#### 4.4 Numerical Simulation of EHFF

The complex physics involved with the discharge of electrons through water and the resulting plasma channel were omitted from the numerical simulation to reduce the complexity and computational cost. The simulation began by applying nodal acceleration to the water, which is analogous to the propagation of a fully developed shockwave. The unit nodal acceleration curve was scaled by an acceleration multiplier value to correlate the height of the numerical and experimental specimens. The magnitude of acceleration was adjusted for each material and geometry so that the final dome height of the numerical specimens matched the average height of the associated necked experimental specimens (Table 4-8).

Table 4-8: Numerical simulation acceleration multiplier ( $\text{mm/s}^2$ ) for AA5182-O and DP600.

<b>Specimen</b>	<b>AA5182-O</b>	<b>DP600</b>
Biaxial	1.0E+08	2.2E+8
Plane Strain	1.5E+08	2.2E+8
Intermediate Draw	2.6E+08	4.6E+8
Uniaxial	5.4E+08	6.6E+8

Three locations along the centerline of the specimens, at a radial distance of 0mm, 15mm, and 30mm from the sheet center, were selected to provide insight into how certain

parameters varied within the blank (Figure 4-27). The time history of several parameters was measured at the three locations to quantify the gradient of the selected parameters from the apex of the sheet to the outer radius.

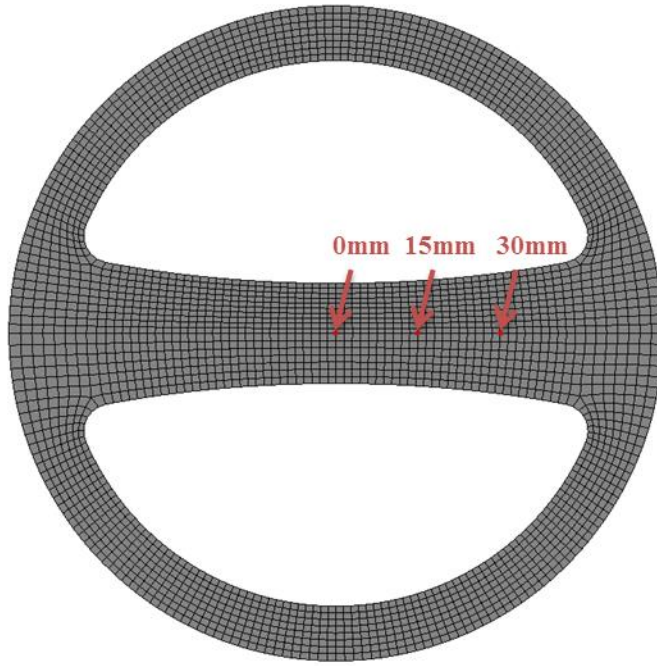


Figure 4-27: Radial distance from the sheet center to locations for measurements on uniaxial specimens.

The duration, distribution, and intensity of the acceleration applied to the water nodes in the numerical simulation were calibrated by comparing the numerical specimen profiles to the experimental profiles. The final shape of the experimental specimens for all specimen geometries and both materials were convex (Figure 4-28, Appendix D). The acceleration profile was refined until the numerical specimens matched the curvature of the experimental specimens to within less than 1.5mm.

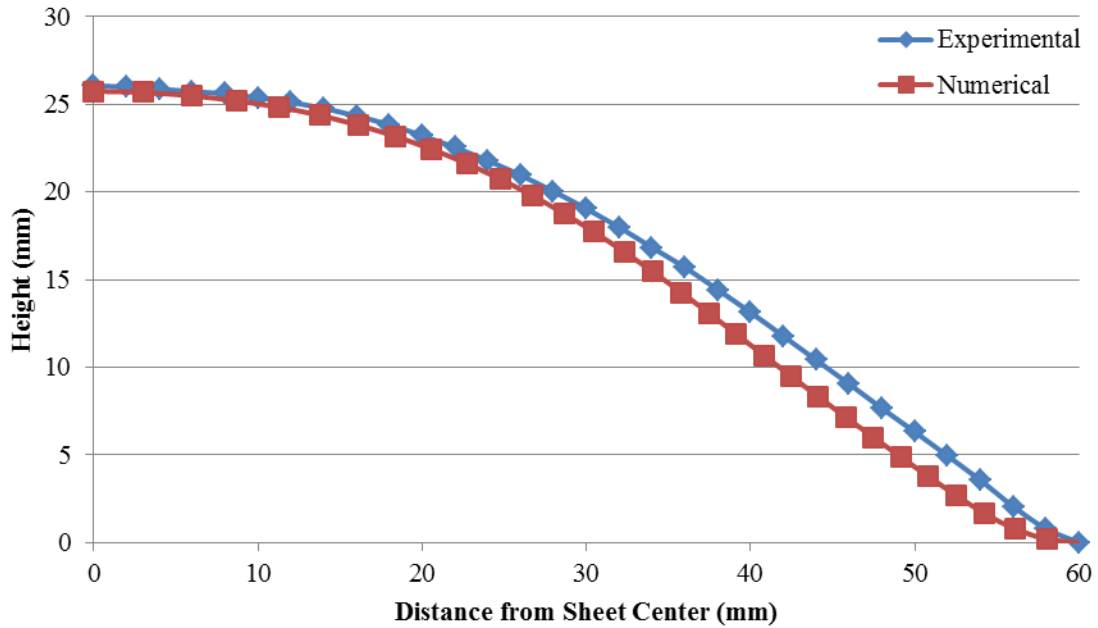


Figure 4-28: Final displacement of the sheet measured radially from the sheet center for experimental and numerical DP600 uniaxial specimens.

The evolution of the sheet profile was generated at 100 $\mu$ s intervals (Figure 4-29, Appendix D). Similar to the simulation work of Hassannejadasl et al. (2014) and Golovashchenko et al. (2013) the displacement of the apex lags behind the displacement of the outer edge early in the process. Conversely, the experiments of Rohatgi et al. (2011) using a similarly shaped chamber (152mm diameter compared to 120mm here) and a pulse unit with significantly more capacitance (720 $\mu$ F compared to 200 $\mu$ F here) did not show a delay in the central region of the sheet. Rohatgi et al. may not have observed the lag due to the forming process being less dynamic as a result of a pulse machine that delivers a longer energy pulse than the equipment used in these experiments.

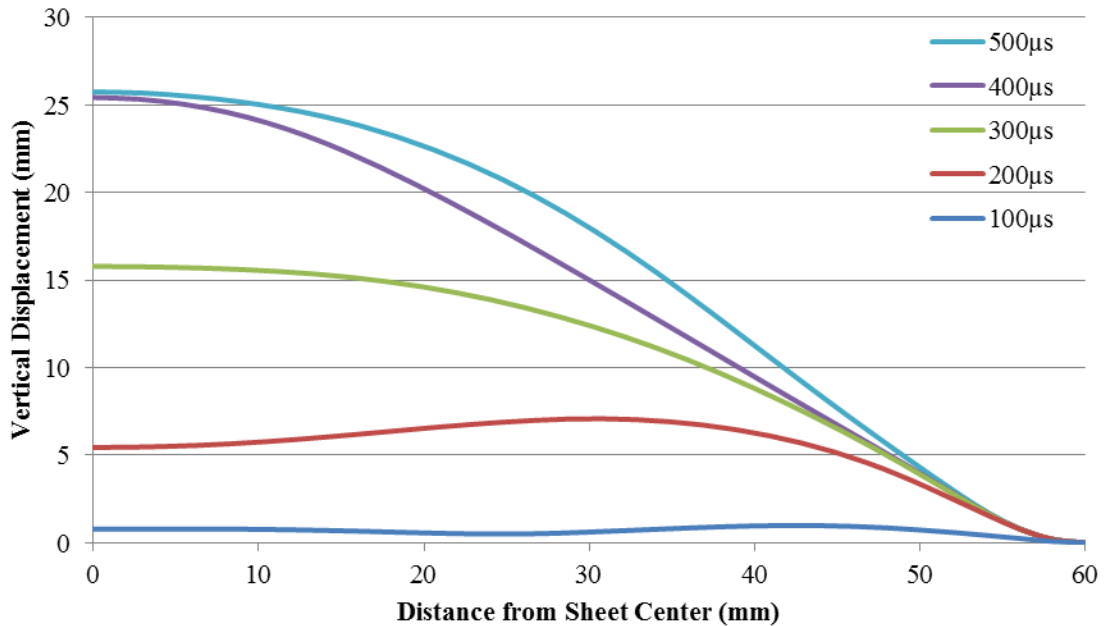


Figure 4-29: Evolution of the sheet displacement measured radially from the sheet center for DP600 uniaxial specimens.

The velocity time history shows that each area of the sheet experiences a similar velocity profile, with the maximum velocity occurring at the apex (Figure 4-30, Appendix D). The peak velocity occurs concurrently for all three reported locations in EHFF, which confirms that the blank is not formed sequentially as reported by Hassannejadasl et al. (2014) and Golovashchenko et al. (2013). The peak velocity at the apex was approximately 120m/s for uniaxial DP600 specimens, but varied between 75m/s and 170m/s based on strain path and material for other specimens. The simulations were able to capture the double peak behaviour of the velocity at the apex that was experimentally observed by Rohatgi et al. (2011). The predicted maximum velocities for the EHFF specimens are on the order of the EHFF biaxial specimen results reported by Rohatgi et al. (2011).

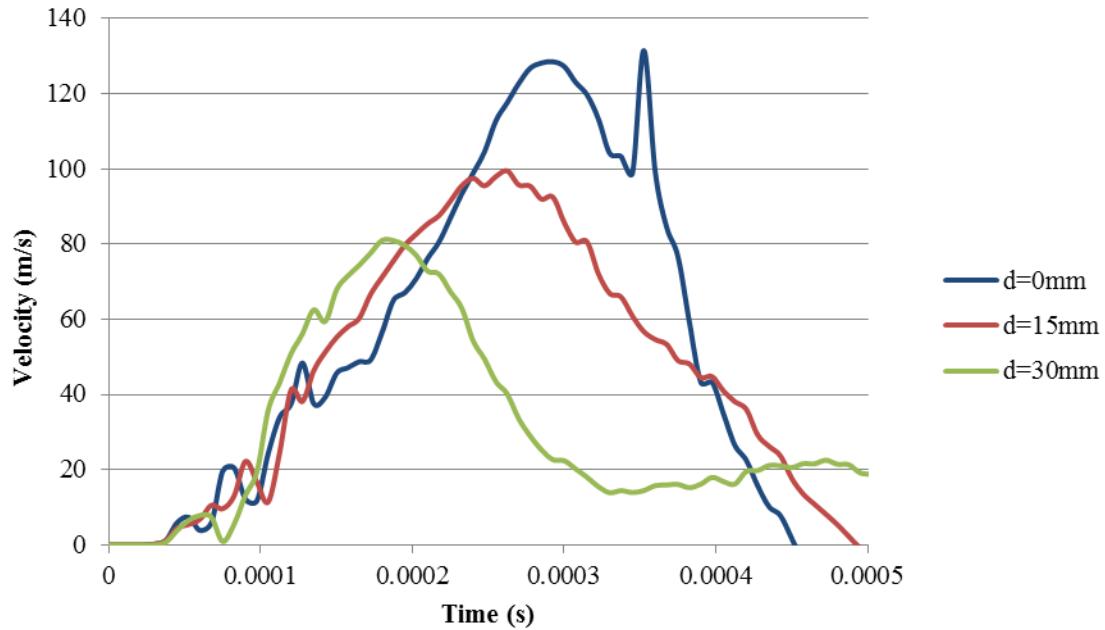


Figure 4-30: Velocity at distances of 0, 15, and 30mm from the specimen center for DP600 uniaxial specimens.

The major strain time history shows that all three locations accumulate strain concurrently (Figure 4-31, Appendix D), as observed by the experiments of Rohatgi et al. (2011). The simulations predict the duration of the forming was on the order of 1000 $\mu$ s, and varied from 500 $\mu$ s to 1500 $\mu$ s depending on the geometry and material. It is important to also consider that the duration of nodal acceleration used in these simulations was consistent, even though the magnitude of acceleration was scaled to achieve a different forming height. The predicted duration of forming is about two times longer than reported in the simulation work of Golovashchenko et al. (2013), possibly due to a number of factors including the chamber geometry, the electrode position, the forming tool, and the method used to model the pressure pulse. The predicted forming time is on the order of the forming time reported in the experimental work of Rohatgi et al. (2011). It is possible that both Golovashchenko et al. and Rohatgi et al. are reporting the correct forming time for their particular configuration of experimental equipment, since the shape and duration of the discharge is affected by a number of parameters including the electrical system and the chamber geometry.

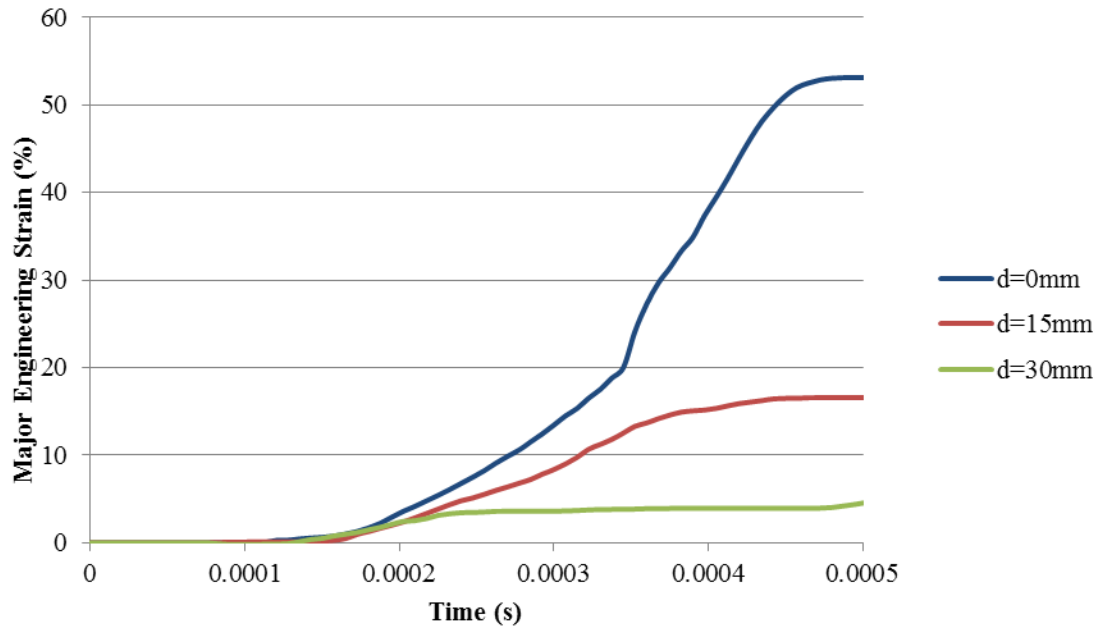


Figure 4-31: Major strain at distances of 0, 15, and 30mm from the specimen center for DP600 uniaxial specimens.

The predicted strain paths for all four specimen geometries were recorded at three locations along the radius for both DP600 and AA5182-O (Figure 4-32 and Figure 4-33). The strain paths were identical between the two materials, with the only difference being the final strains. The strain paths for both the uniaxial and biaxial geometries were consistent from the center to the outer regions of the sheet. The strain paths for both intermediate draw and plane strain geometries varied along the radial distance; the desired strain path was observed at the center of the sheet and the strain shifted more toward the stretching side of the FLD as the distance from the center increased. The minor strain tends to become more positive as the distance from the sheet center increases in these two geometries since far away from the apex there is more material to transfer the hoop stress, thus inducing positive minor strains.

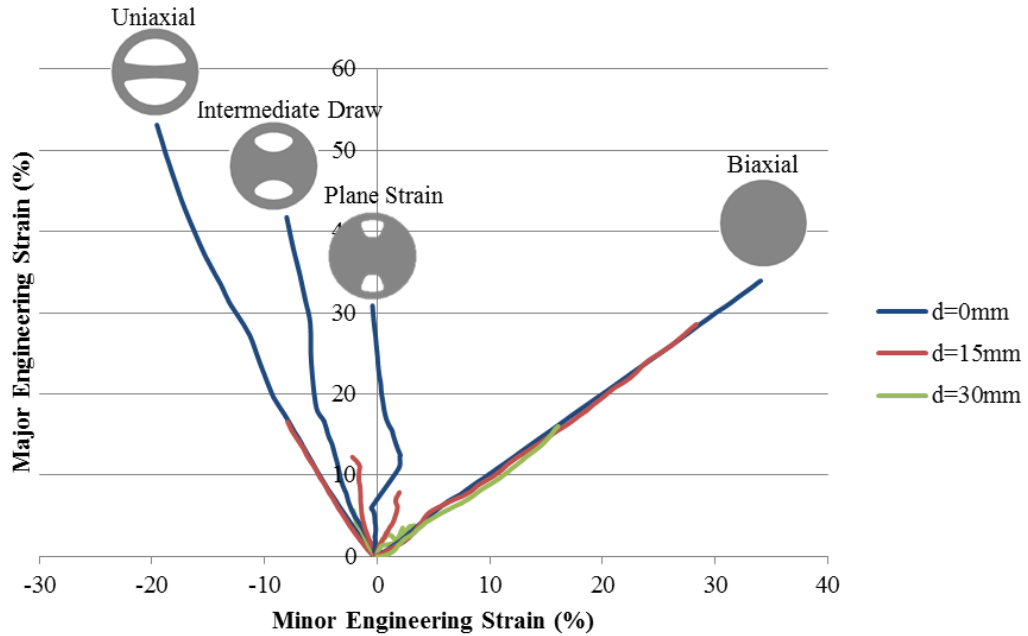


Figure 4-32: Predicted strain path at distances of 0, 15, and 30mm from the specimen center for each specimen geometry for DP600.

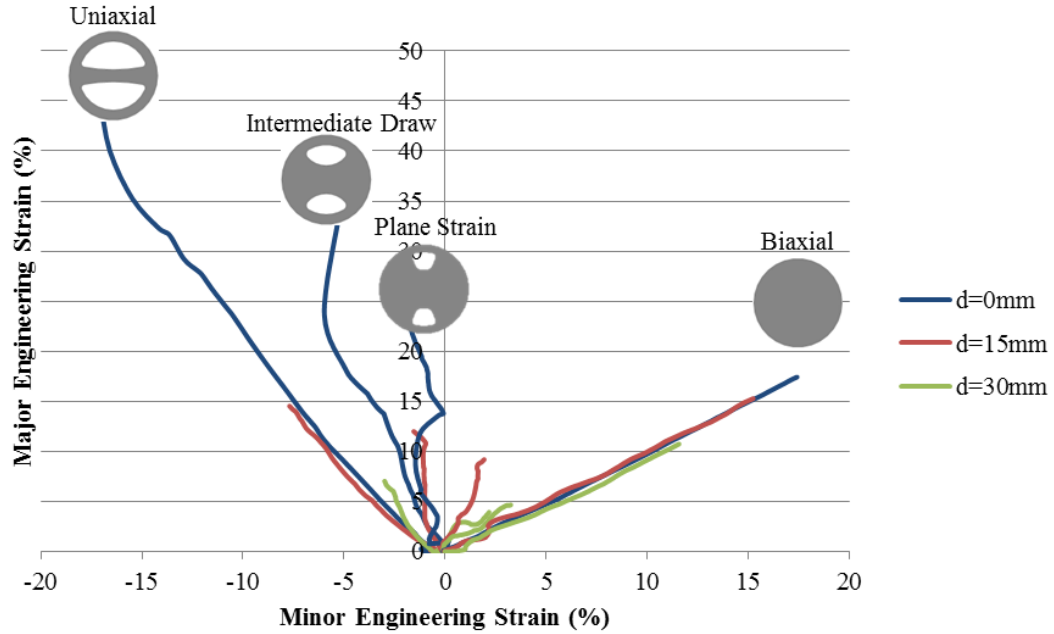


Figure 4-33: Predicted strain path at distances of 0, 15, and 30mm from the specimen center for each specimen geometry for AA5182-O.



The equivalent strain rate history shows the apex experiences a peak strain rate of approximately  $6000\text{s}^{-1}$  for uniaxial DP600 (Figure 4-34, Appendix D). There is a significant decrease in strain rate as the distance from the apex increases. The maximum strain rate at the apex varied from  $2500$  to  $10,000\text{s}^{-1}$  depending on the material and the specimen geometry. It should be noted that the peak strain rate is very sensitive to mesh size and to the method used to model the electrohydraulic discharge, and thus is not a very effective means for comparison. The predicted peak strain rates in EHFF are about the same as predicted for the partial filling of a conical die by Golovashchenko et al. (2013). As expected, the free forming peak strain rates are significantly lower than the peak strain rates in EHDF that were predicted by Golovashchenko et al. (2013) to be  $20,000\text{s}^{-1}$ . However, the predicted peak strain rates for EHFF are about ten times greater than the strain rates observed by Rohatgi et al. (2011), which may be a result of using different experimental set-ups, or may indicate that there was an error with the strain rate measurement reported by Rohatgi et al. (2011). Rather than the very short peak strain rate, the average strain rate at each location can be used to make more reliable comparison. The high frequency oscillation of the strain rate curves makes them difficult to evaluate, and the very large spikes in strain rate for very short durations in a very small region of the blank may not have a substantial contribution to formability improvement. The strain rate varies with time and position, so the average strain rate over the entire forming process may have more influence on the formability of the material than the absolute maximum strain rate. The average values at all three locations for each specimen geometry and for both materials were on the order of  $200$  to  $1600\text{s}^{-1}$  depending on the material and the specimen geometry, indicating that the strain rates throughout the entire specimen are substantially higher than in quasi-static forming (Figure 4-34, Appendix D).

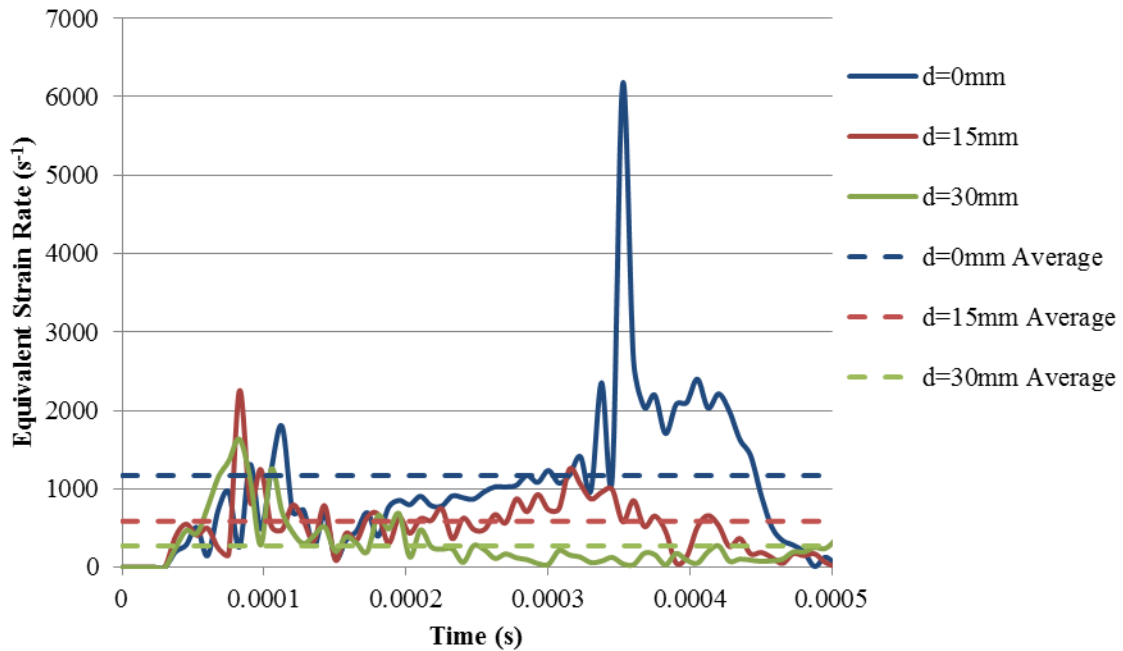


Figure 4-34: Equivalent strain rate and the average equivalent strain rate at distances of 0, 15, and 30mm from the specimen center for DP600 uniaxial specimens.

It should be mentioned that the peak strain rate is defined by a large number of data points and that the time step was very small; therefore the predicted peak strain rates are a reliable estimate of the actual peak strain rates in the EHFF process.

#### 4.5 Comparison of Experimental and Numerical Results

One of the greatest benefits of EHFF is the potential to correlate the input loading of a numerical model with the experimental energy. In the experiments, the significant energy losses of the EHF process make it impossible to quantify the amount of energy used to form the blank, thus energy measurements from the experiments cannot be directly input into a numerical model. The numerical loading is often estimated by correlating the experimental and numerical results since the experimental energy cannot be quantified. The main concern with estimating the numerical loading by correlating the results is that, in EHDF, the upper bound of numerical input energy is not well defined. It is possible to determine if insufficient loading is applied to an EHDF model because the blank will not

completely fill the die; but it is very difficult to determine if too much energy is applied because the deformation of the blank is limited by the shape of the die. In contrast, the shape and height of the blank are strongly correlated to the input loading in EHFF. Thus, the correlation between experimental energy and numerical loading should first be conducted for EHFF, and the findings can then be applied to EHDF.

The nodal acceleration applied to the numerical simulations was calibrated such that the maximum height of the numerical specimens was the same height as the experimental specimens that contained a neck. Based on the results, it is clear that the amount of nodal acceleration applied to the numerical model to represent a particular input energy is different for the two materials (Figure 4-35). The biaxial specimen results are outliers for both materials, so they were omitted from the trendlines. Even with the biaxial results omitted, the EHFF results do not provide a universal expression for converting the experimental energy to nodal acceleration for the numerical model used here. However, the similarity of the ratio of the experimental energy to the nodal acceleration for both materials shows that a different conversion factor may exist for each specimen geometry (Table 4-9).

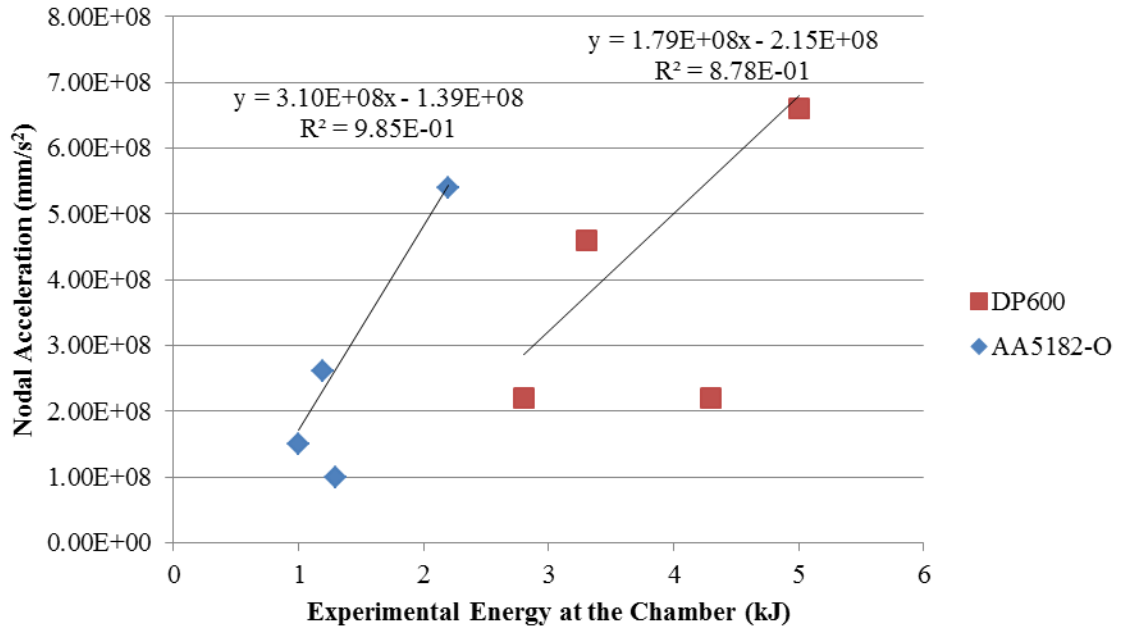


Figure 4-35: Comparison of experimental energy measured at the chamber (kJ) to the nodal acceleration applied in the simulation (mm/s<sup>2</sup>).

Table 4-9: Ratio of experimental energy measured at the chamber (kJ) to the nodal acceleration applied in the simulation (mm/s<sup>2</sup>).

Specimen	AA5182-O	DP600
Biaxial	1.30E-08	1.95E-08
Plane Strain	6.67E-09	1.27E-08
Intermediate Draw	4.62E-09	7.17E-09
Uniaxial	4.07E-09	7.58E-09

In general, the predicted strain values agreed quite well with the experimentally measured strains (Figure 4-36, Appendix D). The predicted strain at the apex is somewhat greater than experimentally measured for uniaxial, plane strain and intermediate draw specimen geometries of both materials. In the simulation, the strain at the apex of these specimens was very sensitive to the height that the specimens formed to. Beyond a certain height, a very small increase in specimen height (on the order of 3mm) could result in a

disproportionally large increase in the strain very close to the apex (on the order of 75% engineering strain) due to instability in the numerical model. The simulation did not use a damage model, and thus material softening could not be captured.

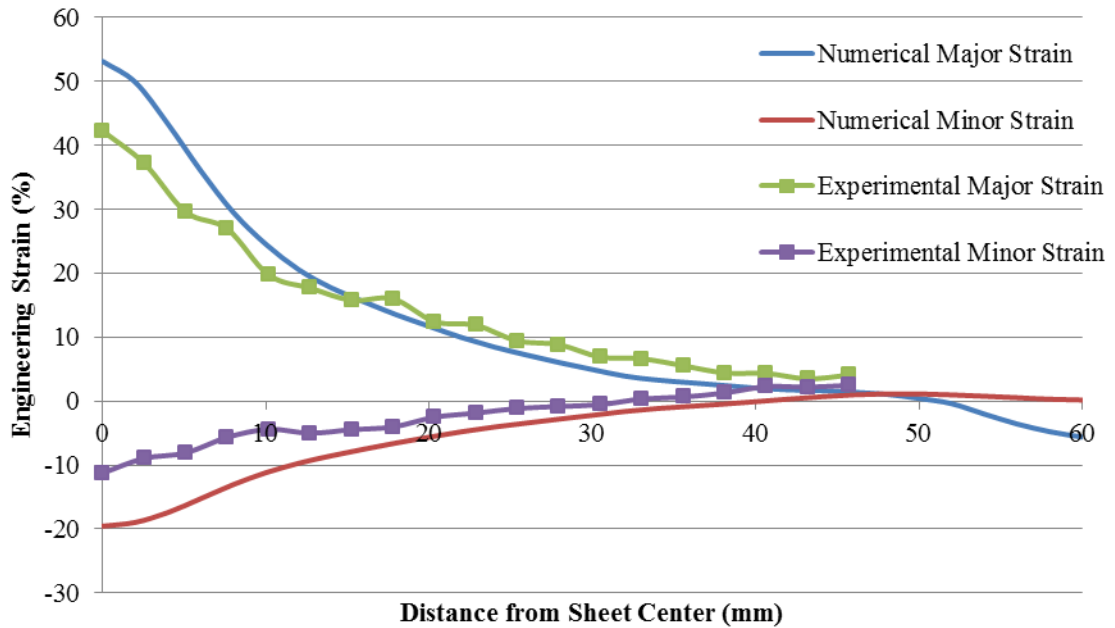


Figure 4-36: Comparison of experimental and predicted major and minor strains measured radially from the center of the DP600 uniaxial specimens.

The numerically predicted strain paths of the apex element were compared to the strains measured from grids in the gauge section for all geometries of steel and aluminum specimens. Safe strains in necked specimens were compared to the predicted strain paths for DP600 (Figure 4-37). Safe strains in safe specimens were compared to the predicted strain paths for AA5182-O (Figure 4-38). Both materials show agreement between the experimental strain data and the predicted strain paths. However, the measured minor strain values for the uniaxial and intermediate draw specimens are less negative than predicted. In general, the experimental strains fall in the regions that they were numerically designed to for both DP600 and AA5182-O.

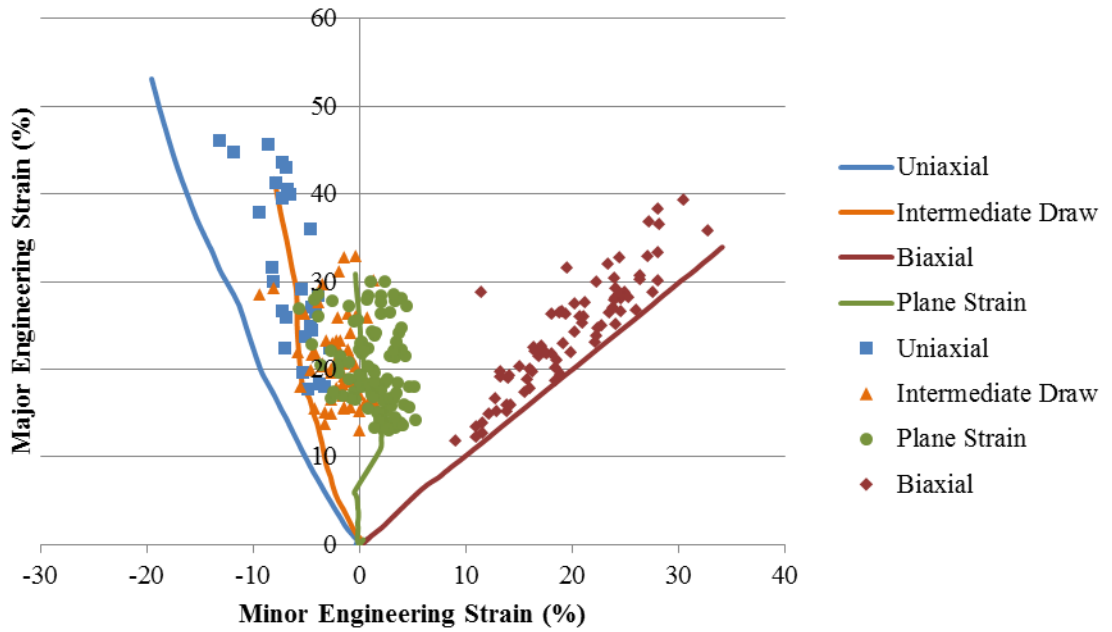


Figure 4-37: Predicted strain paths and experimental safe strain distributions in necked DP600 specimens.

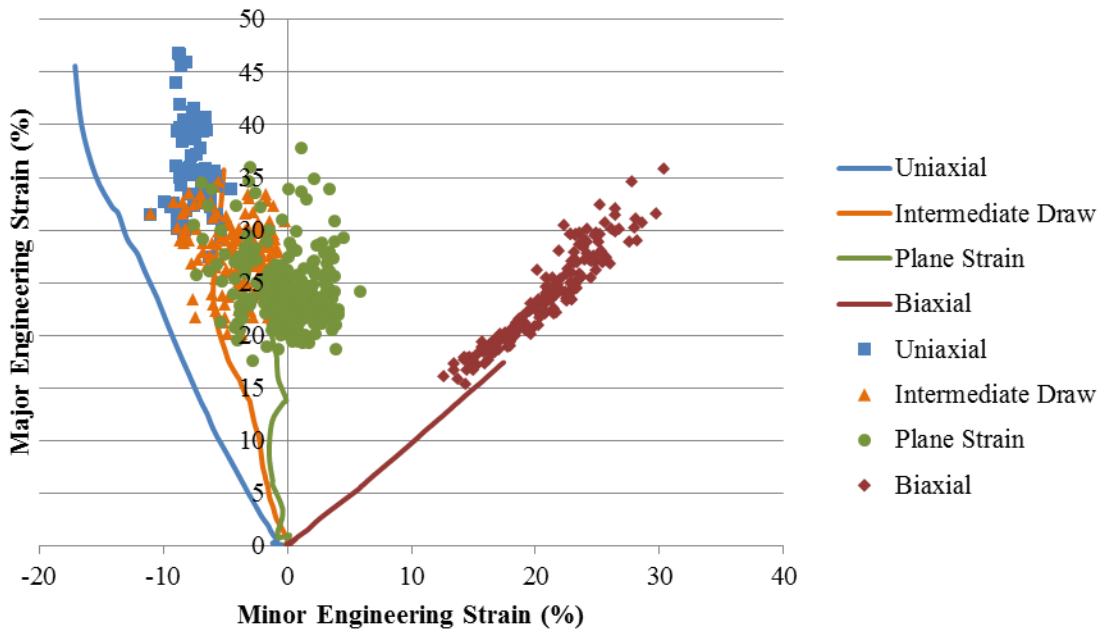


Figure 4-38: Predicted strain paths and experimental safe strain distributions in safe AA5182-O specimens.

The specimens behaved exactly as they were designed to due to the care taken during the initial design of the specimen geometries, even though the initial numerical simulations used to design the specimens were unrefined. As predicted, there was no splitting in the corner areas away from the gauge section. Necking originated from the center of the gauge section for each specimen and there was only one gauge section per specimen, which simplified the analysis of the peak strains in a specimen. Unlike the work of Davies (2012), the necks developed in the direction predicted by numerical simulation (Figure 4-39).

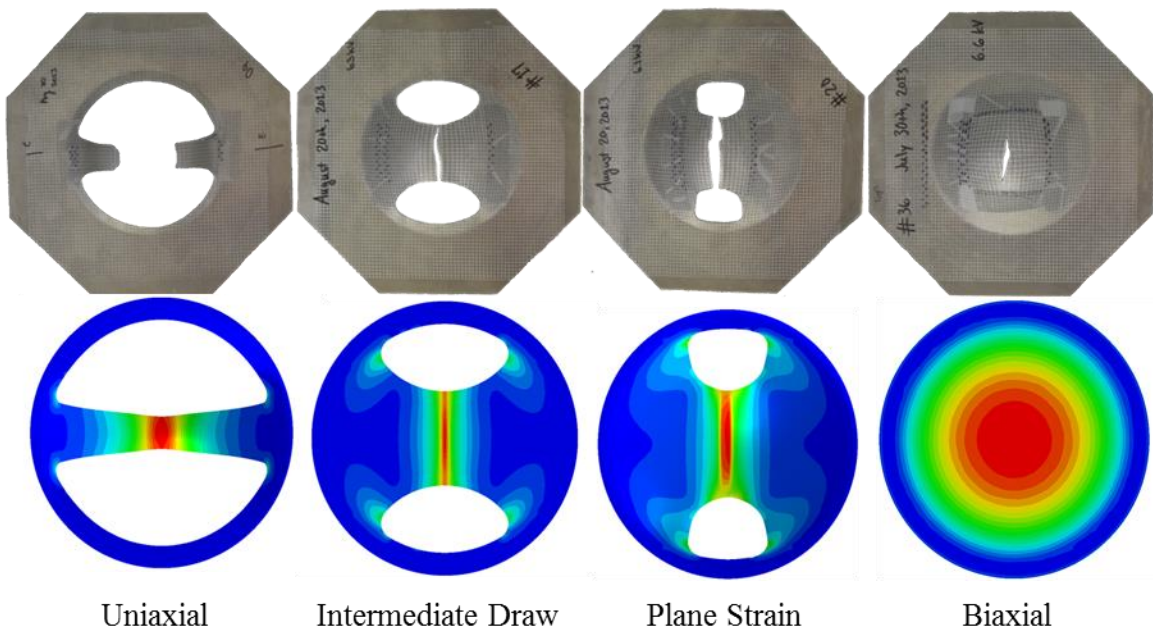


Figure 4-39: Comparison of experimental and numerical specimens showing that actual failures occurred from the center of the gauge as predicted by the strain distribution.

#### 4.6 Mini-die Forming Experiments

A new type of die forming, with the die offset from the gauge section, was designed. To validate the procedure, preliminary experiments were conducted. The DP600 sheet steel was chosen as the material because it was easier to form a necked specimen than with the AA5182-O. The procedure only had to be validated for one specimen geometry, so the intermediate draw specimen was selected. The uniaxial and biaxial DP600 free forming

experiments required almost all of the electrical energy available from the Magnepress, and mini-die forming experiments typically require more energy than free forming experiments, thus mini-die forming experiments could not be conducted for uniaxial and biaxial DP600 specimens.

In order to establish a baseline for comparing the EHDF results, an EHFF specimen that was very close to failure was selected. An EHFF specimen formed safely to a height of 21.9mm with an input voltage of 11.3kV was selected as the baseline (Figure 4-40), since it shows a very typical strain distribution as confirmed by two other similar specimens. For comparison, the critical free forming height for DP600 intermediate draw specimens was 23.7mm at an input voltage of 11.2kV. Some of the strains in the free formed specimen substantially exceeded the EHFF FLC because the specimen was accelerated with an input voltage close to the critical value and reached a height close to the critical height (Figure 4-41). The strains in excess of the FLC are not too surprising because it is not uncommon for the strain measured on safe specimens formed close to the critical height (at any strain rate) to be equivalent to or exceed the FLC (for that particular strain rate). The radial distribution of major and minor strains in the free formed specimen provides a baseline for comparison to the effects of die contact (Figure 4-42).



Figure 4-40: Side view of a safe EHFF specimen.



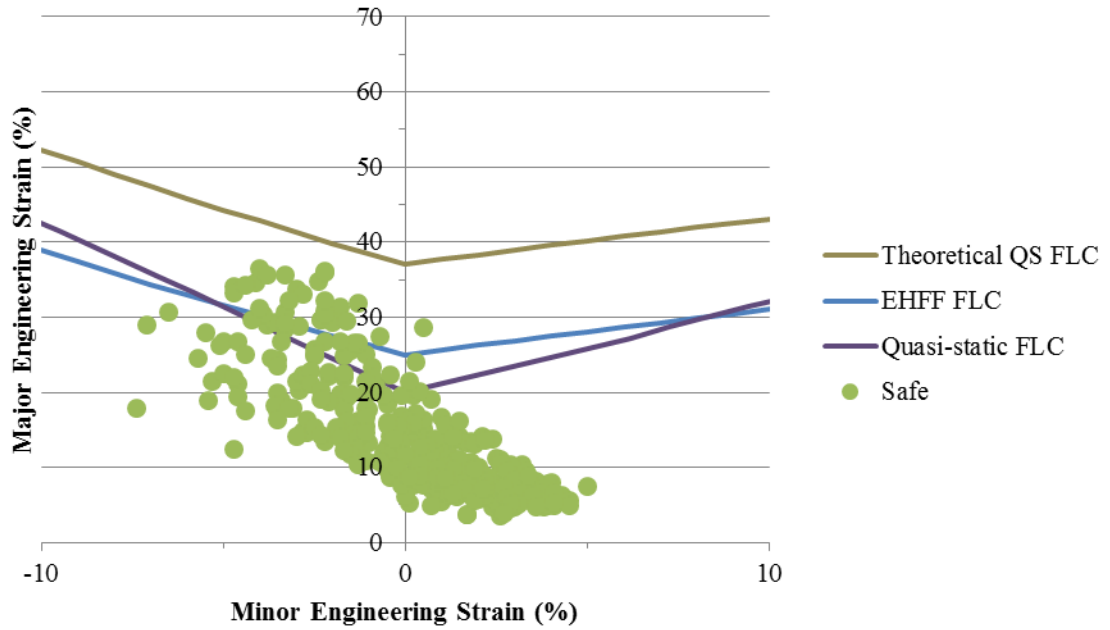


Figure 4-41: Strain measurements from one safe specimen in free forming with input voltage equivalent to the critical voltage.

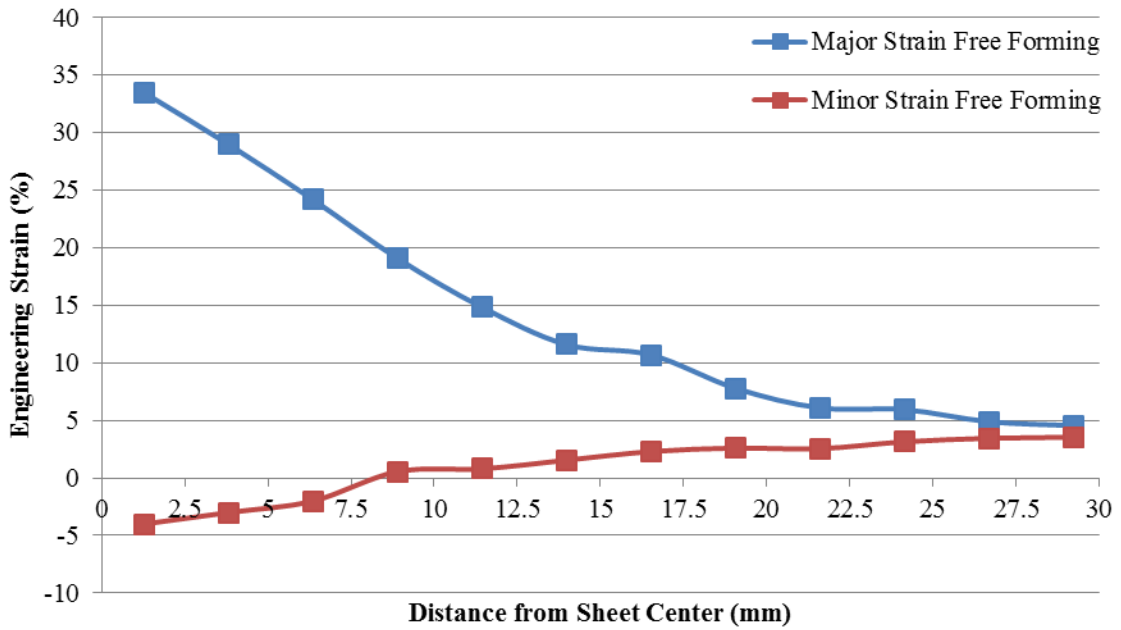


Figure 4-42: Major and minor strains measured radially from the center of one specimen formed in EHFF with input voltage equivalent to the critical voltage.

In mini-die forming, there are two options when deciding how far away to place the die from the blank. The first option is to put the die lower than the free forming height of the specimen to ensure sufficient tool-sheet interaction. The gap between the blank and die was set 3.7mm below the critical free forming height of DP600 intermediate draw specimens to create a 20mm gap between the blank and the die. The input voltage was moderately increased from the critical value of 11.2kV to 12.5kV for a specimen. The result of the lowered forming height and the increased voltage was that the gauge section of the specimen contacted the die and the specimen was safe (Figure 4-43). The maximum strains were mostly below the EHFF FLC (Figure 4-44). The strains in the center of the sheet were actually below the strains measured in the baseline free formed specimen, indicating there was no formability improvement observed in this method of die forming because the die surface was too low (Figure 4-45). The major strain at the apex of the mini-die formed specimen was lower than the free formed specimen because the die impeded the stretching of the material. However, the strain at the perimeter of the die contact was higher than the strain measured in that region of the free formed specimen because the momentum of the blank caused this region to continue stretching when the apex of the specimen could no longer travel upward.



Figure 4-43: Side profile of a mini-die forming specimen with the die lower than the free forming height.

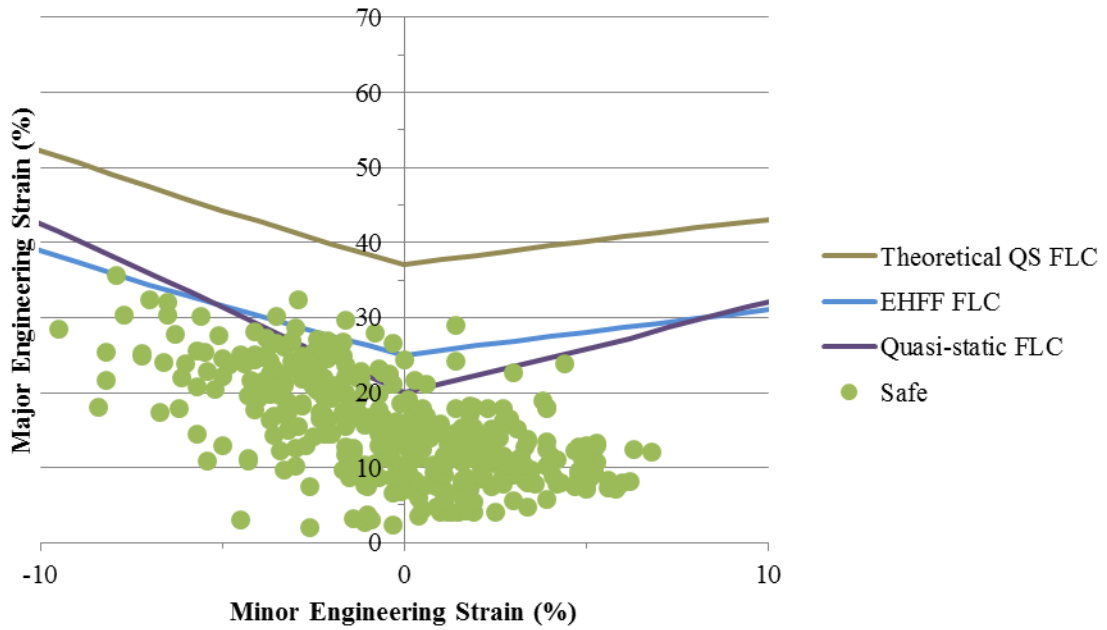


Figure 4-44: Strain measurements from one specimen in mini-die forming with the die lower than the free forming height.

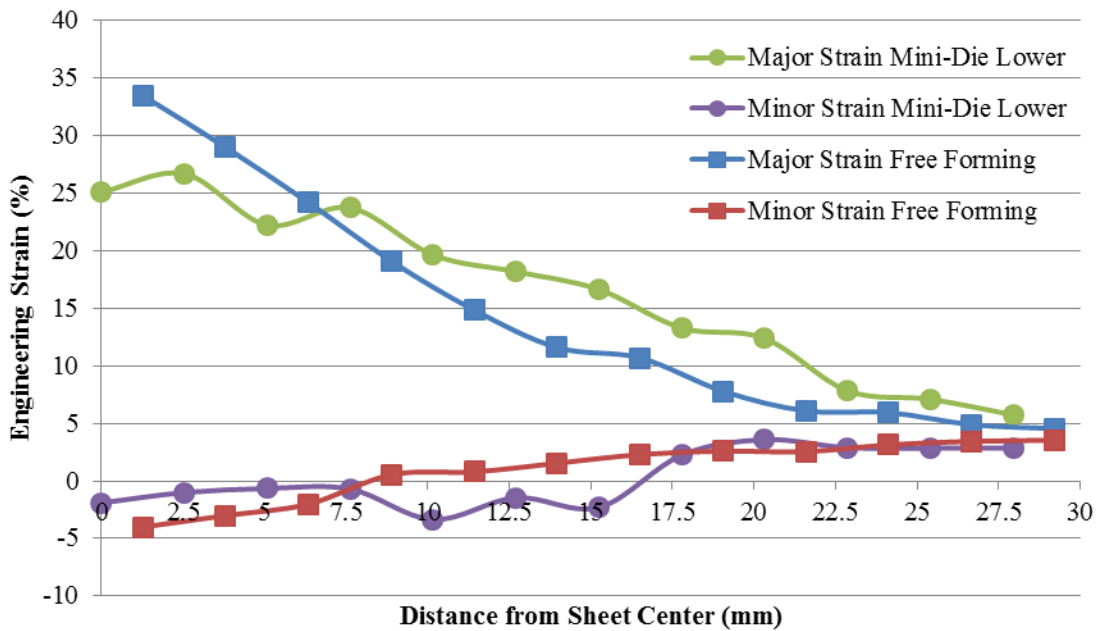


Figure 4-45: Comparison of the major and minor strains measured radially from the centers of an EHFF specimen and one specimen formed in electrohydraulic mini-die forming with the die lower than the free forming height.

The second option for the height of a mini die is to set the die higher than the free forming height for that specimen geometry. The gap between the blank and the die was set 6.3mm above the critical free forming height of DP600 intermediate draw specimens to create a 30mm gap between the blank and the die. The input voltage was set to its maximum level of 15kV to supply a specimen with sufficient energy to reach the die. The gauge section of the specimen contacted the die, but splitting still occurred (Figure 4-46). The marks on the surface of the blank suggest that the specimen likely split before impacting the die, so perhaps the die height should have been lower than 6.3mm above the free forming height. Several strain measurements on this specimen exceeded the EHFF FLC and the free forming data points (Figure 4-47). The high strain values indicate significant formability improvement is possible in mini-die forming when the distance between the blank and the mini-die surface is greater than the critical free forming height. However, because the specimen split, it is unclear if the significant formability improvement can be observed on safe or necked specimens if the die is positioned at a lower height that is also in excess of the free forming height. Compared to the typical radial strain distribution, a large increase in the major strain within 5mm of the apex was observed in the mini-die formed specimen (Figure 4-48).



Figure 4-46: Side profile of a mini-die forming specimen with the die higher than the free forming height.

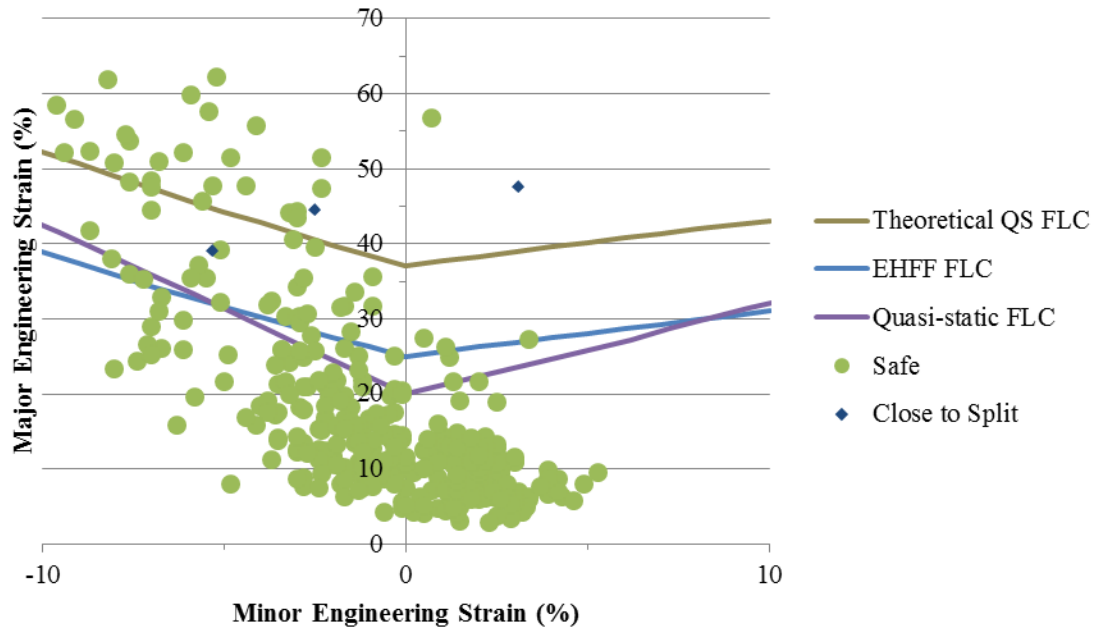


Figure 4-47: Strain measurements in mini-die forming with increased die height.

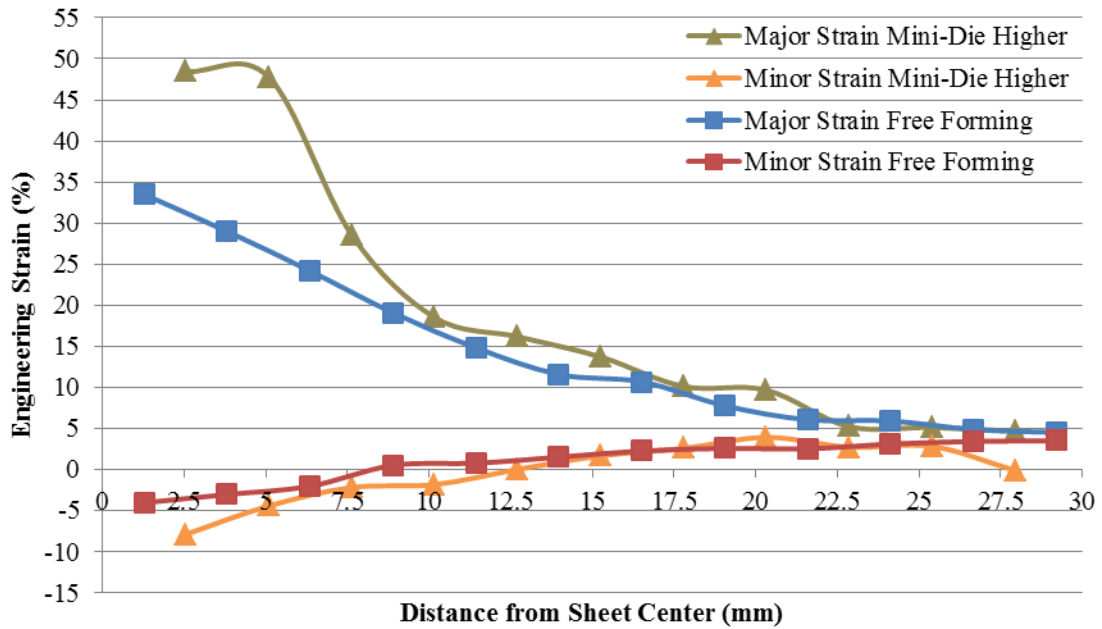


Figure 4-48: Comparison of the major and minor strains measured radially from the centers of an EHFF specimen and one specimen formed in electrohydraulic mini-die forming with the die higher than the free forming height.

Another DP600 intermediate draw specimen was formed at the same die surface offset of 6.3mm above the critical free forming height with the input voltage reduced to 14kV to try to avoid fracture. However that specimen also split, so it remains unclear if it is possible to obtain safe or necked specimens above the critical free forming height by simultaneously adjusting the input voltage and the gap between the blank and the mini-die.

In all mini-die and traditional die forming experiments the velocity of the blank, the strain rate, and the hydrostatic pressure at the contact zone between the blank and the die are directly correlated to the energy discharged. A more powerful pressure pulse activates the formability enhancement mechanisms with greater intensity, thus contributing to an increase of the maximum strain before fracture. From this perspective, it is obvious that a single FLC cannot be created for high strain rate die forming processes. Although it is not a good indication of the forming limit because even safe strains measured on free formed specimens can exceed the FLC, the best way to demonstrate the enhanced formability of die forming is to evaluate how much the measured strains exceed quasi-static and free forming FLCs. By examining the case with the die lower than the free forming height and the case with the die above the free forming height, it is clear that significantly higher strains can be observed with the gap between the blank and die larger than the critical free forming height. Although mini-die forming is not able to solve the intrinsic non-singularity of the die forming FLC, mini-die forming provides the first experimental approach to achieve strains on the negative minor strain side of the FLD. In addition, mini-die forming allows specimens that have negative, near zero, and positive minor strains to be formed in a single experimental set-up, which solves the consistency issues attributed to the experimental procedures previously employed by other researchers.

## 5 Discussion

The significant formability improvement in high rate die forming processes is attributed to phenomena that result from the impact of the blank against the die, such as void growth suppression, through-thickness compression and shear deformation, and bending-unbending in the area of contact between the blank and the die. In addition, the high strain rates in both die forming and free forming high-velocity forming processes cause material constitutive behaviour changes that may contribute to formability increases. The peak strain rates achieved in EHDF are on the order of  $20,000\text{s}^{-1}$ , while the peak strain rates in EHFF are between 2500 to  $10,000\text{s}^{-1}$ . Although the strain rates achieved in EHFF are significantly greater than in quasi-static forming processes, it is unclear if the strain rates are sufficient to cause moderate formability improvements attributed to inertia in the plastic flow instability, as described by Drucker (1959).

Electromagnetic forming experiments on aluminum alloys by Imbert et al. (2005), Oliveira et al. (2005), and Golovashchenko (2007) showed no formability improvement in free forming but significant die forming formability improvement. These works, although they were limited to the electromagnetic forming of aluminum alloys, are the basis for many claims that the strain rates in free forming are insufficient to cause formability improvement. However, the pressure distribution and resulting sheet deformation profile in EMF cause the deformation mechanisms to be different than in EHF and EF. For example, the free formed biaxial specimens in EMF reported a circumferential failure mode due to the initial lag of the center part of the blank (Imbert et al., 2005), while radial failures were observed in EHF (Golovashchenko et al., 2013) and EF (Dariani et al., 2009). In addition to the aluminum EMF results that report no formability increase in high-velocity free forming, Golovashchenko et al. (2013) reported no formability increase in radially split biaxial DP590 blanks that failed to fill the die in EHF. In contrast, Dariani et al. (2009) showed moderate formability improvement in both AISI 1045 steel and AA6061 aluminum using drop hammer (lower rate) and explosive free forming tests (higher rate), especially on the positive minor strain side of the FLC. Although the works of many researchers showed that it was not possible to observe a

large formability improvement using high-velocity free forming, Dariani et al. showed that the formability of free forming operations can exceed quasi-static levels.

Many researchers claim that the limited formability improvement in free forming compared to die forming is more than the result of a lack of die interaction and significantly reduced peak strain rate. The failure observed in free forming is often classified as a quasi-static failure mode because the pattern and formability levels are similar to quasi-static results. Free forming has largely been grouped with quasi-static deformation because as the blank decelerates the final stage of deformation occurs in quasi-static forming conditions. However, the bulk of the plastic strain occurs at high strain rates, so the high rate mechanisms that delay damage initiation are active for a majority of the forming process. For example, simulation results (Figure 5-1) and the experimental results of Rohatgi et al. (2011) show the strain rate is significantly above quasi-static strain rates for the majority of the strain history at both the apex and at a location 15mm away from the apex. In addition, only about 2% engineering strain occurs at the low strain rates as the specimen is decelerating. However, it is plausible that the neck itself occurs at low strain rates since there is a very small strain window between safe forming and splitting in which a neck can be formed. Although the plastic strain which causes necking may occur at quasi-static strain rates, significant inertial effects that are active throughout the majority of the forming process allow the formability of the sheet to exceed quasi-static limits.



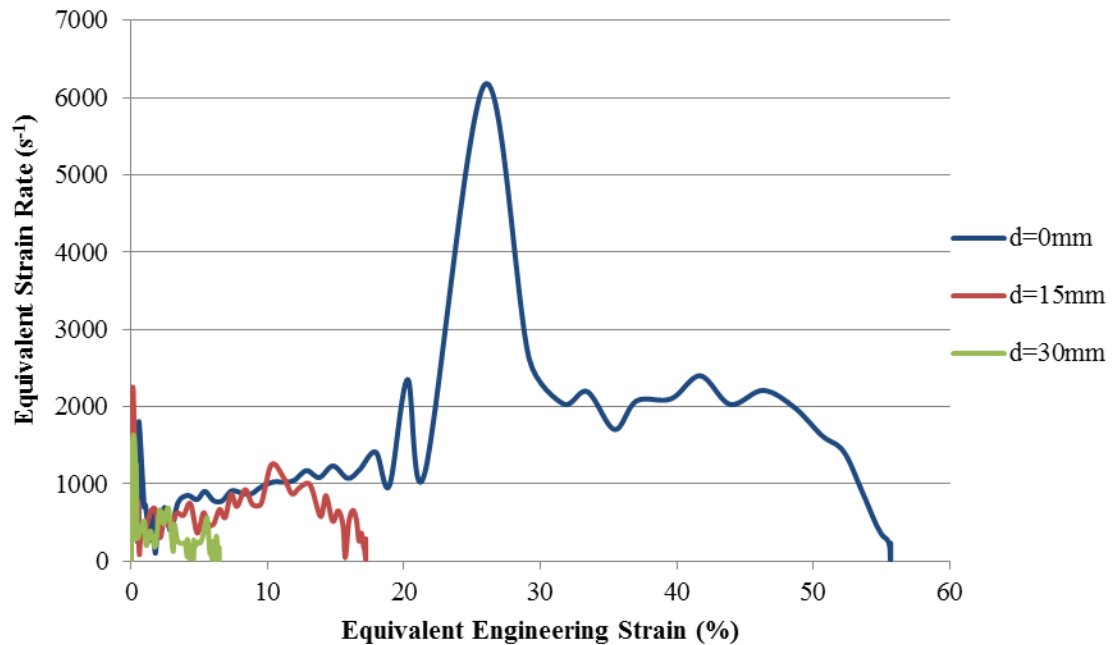


Figure 5-1: The equivalent strain rate versus equivalent strain for DP600 uniaxial specimens.

High-velocity free forming has largely been disregarded because the formability improvement is substantially less than the improvement observed in pulsed die forming. As such, the EHFF formability and failure mode have traditionally been attributed to the quasi-static failure mode. Prior to this work, the free forming formability had only been quantified in the biaxial stretching condition because a rigorous methodology to achieve any different strain state had not been established. The biggest obstacle to determining the forming limits at negative and near zero minor strains has been a lack of experimental specimens that can achieve the appropriate minor strains. The quasi-static Marciniak and Nakazima specimens cannot be used with pulsed forming processes because they could damage the clamping tool and are susceptible to cracking in the radii when used with EHF. Davies (2012) created modified specimens for use with EHF, but the specimens failed to produce necked data points due to poor design which caused stress localizations and eventually failure in the radii of the cutouts. Dariani et al. (2009) explosively formed some original modified specimens, but with limited success because the specimens had two gauge sections and were susceptible to cracking in the radii of the cutouts. Banabic et al. (2013) generated data points for the quasi-static forming limit curve by hydraulically

bulging five original specimen geometries using carrier blanks. Although they were developed simultaneously without knowledge of one another, the deformation process and the concept for the specimen geometries used by Banabic et al. are somewhat similar to the process and geometries described here. The modified EHF specimen geometries were significantly different from the quasi-static Marciniak or Nakazima punch forming specimens, the modified EHF specimens used by Davies (2012), and the modified EF specimens used by Dariani et al. (2009). The modified specimen geometries used for the EHFF experiments were original designs that used three different ellipse sizes to achieve different strain paths. The specimens were optimized to cause the maximum strain to occur at the apex, avoid cracking in the radii of the cutouts, and to be used without a sheet driver for the EHF process. The cutouts of the specimens were optimized by adjusting the width of the gauge section and the radii of the ellipses to avoid cracking in the radii. The water passing through the holes in the blank was handled via tooling modifications to prevent rebounding of the water and to alleviate safety concerns. The blanks achieved necks without any twisting or distortion, including in the gauge section. Although it was of initial concern, especially for the narrow uniaxial specimens, there was no shearing of the gauge section from the outer ring. Necking originated from the middle for all four geometries without edge cracking.

The importance of capturing a neck in the EHFF specimens, and the significant amount of effort that was expended to form only a few necks, should not be understated. Many authors fail to generate the forming limit curve in appropriate ways, which leads to exaggerated formability improvement claims. The most common presumption is that a safe grid in excess of the forming limit curve indicates a formability improvement. It is quite difficult to form a necked specimen in die forming, so safe grids are routinely measured on split specimens, but a safe distance away from the split, and the results are used to indicate a formability improvement. However, safe grids do not clearly represent formability improvement, as shown by the many safe grids on split EHFF specimens that are significantly beyond the EHFF FLC (Figure 5-2). The evidence from the EHFF specimens supports the requirement of the Keeler method of plotting the strains from necked grids to establish the forming limit curve since it is not uncommon to have safe strains 10% engineering strain above the FLC (Green and Black, 2003).

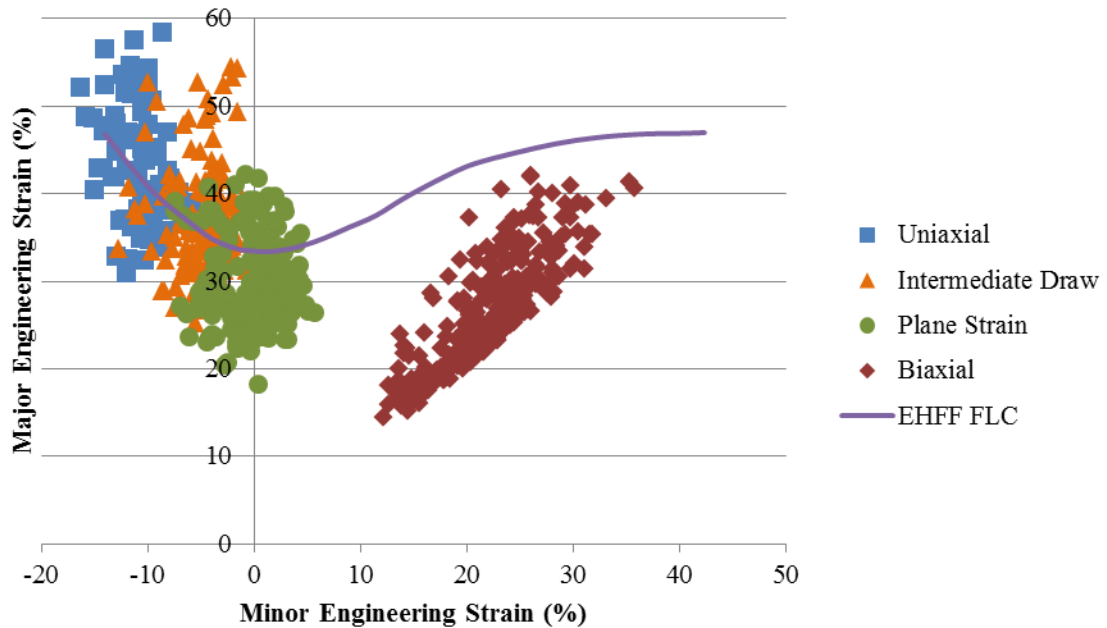


Figure 5-2: Safe grids measured on split EHFF aluminum specimens in comparison to the EHFF FLC.

The effects of non-linear strain paths in die forming operations should also be considered when interpreting the remarkable formability improvement reported by other researchers. High velocity free forming and incomplete die forming processes tend to have linear strain paths, while significant contact forces between the blank and die can change the strain path in complete die forming (Figure 5-3). The strain based forming limit curve shifts and changes shape depending on the nature and magnitude of the pre-strain, and is therefore strictly valid only when the strain path is linear throughout the deformation process (Stoughton, 2001). The strain results for non-linear high rate die forming operations are often compared to quasi-static forming limit curves that have been developed using linear strain paths. The die forming formability improvement may not be as substantial as reported because the forming limit curve may be higher than the original forming limit curve once it is adjusted to account for changes in strain path.

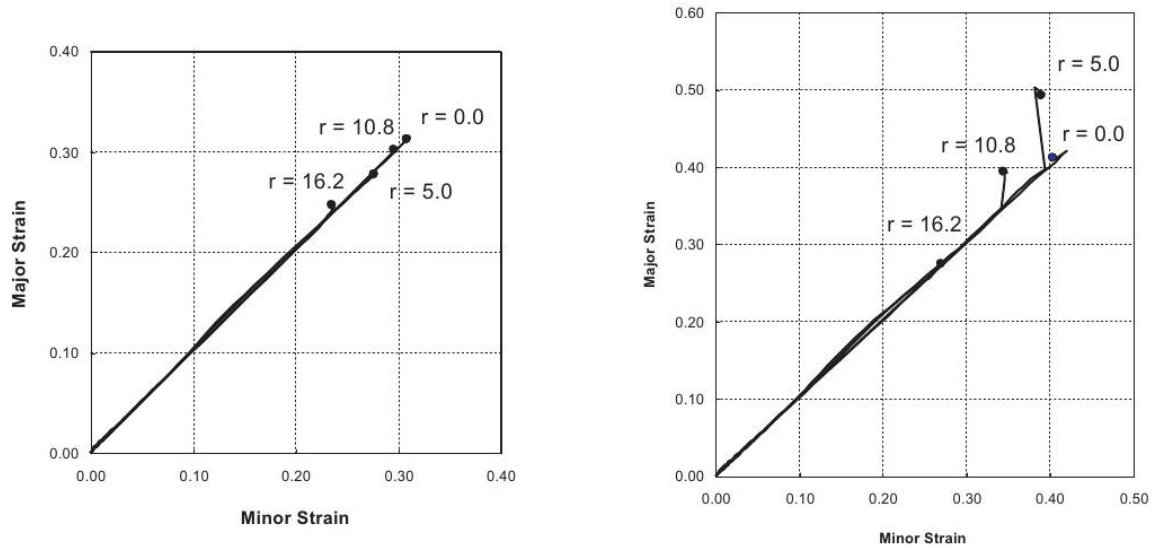


Figure 5-3: Strain path from biaxial specimens in incomplete die forming (left) and complete die forming (right). Image from Golovashchenko et al. (2013).

Many researchers also make the inadvisable comparison of strain data which has been generated with completely different experimental set-ups for different strain paths. Pulsed metal forming is dynamic and the duration, amplitude, and profile of energy delivered to the blank affects which formability enhancement mechanisms become active. The different pulse characteristics, volume of water, blank size, sheet deformation profile, and forming time between different experimental set-ups could have an effect on the formability that is observed. The formability results of two different processes used to generate different strain paths should not be displayed on the same diagram because it implies consistency between the two data sets, while the dynamics of the forming process used to achieve the results are assuredly very different.

Laboratory scale EHDF experiments report significant formability improvements because the full benefits of the EHF process become realized when the sheet metal blank approaches its final shape at very high strain rates and impacts the die surface with high contact forces. However, the high contact forces in lab-scale die forming generate significant tool wear and damage that would be unacceptable in a production environment (Ibrahim et al., 2012). In production, the contact forces would need to be significantly reduced in order to limit tool wear, and accordingly the significant

formability improvement observed in the lab would not be observed in production. In applications where die impact forces are limited, strain rate sensitivity and inertial effects would be active in moderately improving the formability of the material. Therefore, the application of EHF technology to automotive production would more closely match the lab-scale EHFF conditions. Accordingly, the method presented in this thesis for experimentally determining the FLC at high rates is the best method to assess the formability of a material for practical pulsed metal forming processes.

This work builds on the successes and failures of previous researchers to provide the first true assessment of the pulsed forming FLC across the entire spectrum of minor strains. The methodology and the results outlined in this work are a framework for identifying which materials are capable of achieving the greatest formability improvement when used in lab-scale EHFF processes.

## 6 Summary and Conclusions

The high strength-to-weight ratio of high strength and low density materials such as DP600 steel and AA5182-O aluminum can be used in automotive applications to reduce fuel consumption and greenhouse gas emissions. Pulsed forming processes, such as EHF, can increase the formability of some sheet materials to overcome the poor quasi-static formability that limits the number of applications where these materials can be used. Previous attempts to quantify high-velocity formability have been unsuccessful in reliably determining the high-velocity forming across the entire minor strain spectrum for a number of reasons. In this work, substantial progress has been made in the ability to quantify the forming limits of materials in high-velocity forming:

- A systematic and reliable procedure to experimentally determine the forming limit curve in EHFF was developed.
- The forming limit curves were determined for AA5182-O and DP600 sheets formed in EHFF.
- The EHFF formability was compared to the quasi-static formability for both materials.
  - Compared to its quasi-static forming limit, there is no formability change in EHFF for DP600 steel.
  - Compared to its quasi-static forming limit, there is a moderate formability increase in for AA5182-O aluminum. In the plane strain region the EHFF FLC was 11% major engineering strain greater than the quasi-static FLC.
- A numerical model of EHFF was created to determine the in-process parameters.
  - The peak strain rates in each of the four specimen geometries occurred at the center of the specimens and were between 2500 and 10,000 s<sup>-1</sup>.

The experimental procedure for determining the FLC was established on the basis of four specimen geometries, which were designed to cover the entire spectrum of minor strains. Experiments were conducted on 268 specimens, with a total of 34 necked specimens. Necked specimens made from DP600 steel and AA5182-O aluminum sheets were used to construct the experimental EHFF forming limit curves. The EHFF FLCs were compared to the quasi-static FLCs to assess the change in formability that occurs from the EHF

process. The different results of DP600 and AA5182-O show that the quasi-static FLC may or may not be indicative of the EHFF forming limit, depending on the material. A numerical model was calibrated based on the experimental results. Based on the results of the numerical model, EHFF should not be considered a quasi-static forming process because:

- The maximum strain rate at the apex varied from 2500 to 10,000s<sup>-1</sup> depending on the material and the specimen geometry.
- The average strain rates within 30mm of the specimen center were on the order of 200 to 1600s<sup>-1</sup> depending on the material and the specimen geometry.
- Only about 2% engineering strain occurs at low strain rates as the specimens decelerate.

The developed experimental procedure, and the corresponding EHFF FLCs for DP600 and AA5182-O that were obtained, represent major advancements in the ability to properly select parts and lightweight materials for future EHF applications. The experimental EHFF results make a substantial contribution to the fundamental understanding of the forming conditions in which the benefits of EHF technology can be fully utilized. The experimental forming limit curves are clear assessments of the benefits of EHF technology in forming conditions which had not been adequately explored and documented.

The methodology for rigorous determination of the FLC in EHFF using unique specimen geometries and tooling modifications provides the best procedure for future high rate formability assessment. In addition to free forming, the unique specimen geometries can also be used with the framework and tooling established to conduct mini-die forming experiments to assess the effects of die impact on the high-velocity FLC.

## Bibliography

- ASTM International. "Standard test method for determining forming limit curves." *ASTM E2218*, 2008: 1-15.
- ASTM International. "Standard test method for tensile strain-hardening exponents (n-values) of metallic sheet materials." *ASTM E646*, 2007: 1-8.
- ASTM International. "Standard test methods for tension testing of metallic materials." *ASTM E8*, 2011: 1-28.
- Avitzur, B. *Handbook of metal forming processes*. New York: John Wiley & Sons, 1983.
- Balanethiram, V.S., and G.S. Daehn. "Enhanced formability of interstitial free iron at high strain rates." *Scripta Metallurgica et Materialia*, 1992: 1783-1788.
- Balanethiram, V.S., and G.S. Daehn. "Hyperplasticity: Increased forming limits at high workpiece velocity." *Scripta Metallurgica et Materialia*, 1994: 515-520.
- Banabic, D., L. Lazarescu, L. Paraianu, I. Ciobanu, I. Nicodim, and D.S. Comsa. "Development of a new procedure for the experimental determination of the Forming Limit Curves." *CIRP Annals - Manufacturing Technology*, 2013: 1-4.
- Bruno, E.J. *High velocity forming of metals*. Dearborn, Michigan: American Society of Tool and Manufacturing Engineers, 1968.
- Chachin, V., J. Sharin, G. Zdor, V. Shaduya, and A. Zhuravsky. Electrohydraulic treatment of structural materials. United States Patent US4068514. January 17, 1978.
- Cheah, L., and J. Heywood. "Meeting U.S. passenger vehicle fuel economy standards in 2016 and beyond." *Energy Policy*, 2011: 454-466.
- Clark, D.S., and D.S. Wood. "The tensile impact properties of some metals and alloys." *Transactions of ASM v. 42*. 1950. 45.
- Dariani, B.M., G.H. Liaghat, and M. Gerdooei. "Experimental investigation of sheet metal formability under various strain rates." *Proceedings of the Institution of*



*Mechanical Engineers, Vol.223, part B: Journal of Engineering Manufacture*, 2009: 703-712.

Dassault Systèmes. *Abaqus Analysis User's Manual*. Providence, Rhode Island, USA: Dassault Systèmes Simulia Corp, 2010.

Davies, R., and E.R. Austin. *Developments in high speed metal forming*. New York, USA: Industrial Press, 1970.

Davies, R.W. *Pulse-pressure forming (PPF) of lightweight materials*. Richland, Washington: Pacific Northwest National Laboratory, 2012.

Drucker, D.C. "A definition of stable inelastic material." *Journal of Applied Mechanics*, 1959: 101-106.

FMTI Systems Inc. *FMTI technical application notes: Effect of FMTI grid analyzer position on error*. 2008. <http://www.fmtisystems.com/technotes.htm> (accessed November 14, 2012).

Golovashchenko, S.F. "Material formability and coil design in electromagnetic forming." *Journal of Materials Engineering and Performance*, 2007: 314-320.

Golovashchenko, S.F. "Numerical and experimental results on pulsed tubes calibration." *Proceedings of the 1999 TMS Symposium, Sheet Metal Forming Technology*. San Diego, California: The Minerals, Metals & Materials Society, 1999. 117-127.

Golovashchenko, S.F., A.J. Gillard, and A. Mamutov. "Formability of dual phase steels in electrohydraulic forming." *Journal of Materials Processing Technology*, 2013: 1191-1212.

Goodwin, G.M. "Application of strain analysis to sheet metal forming problems in the press shop." *SAE Technical Paper No. 680093*, 1968: 767-774.

Green, D.E., and K.C. Black. "A visual technique to determine the forming limit for sheet materials." *SAE Transactions: Journal of Materials & Manufacturing*, 2003: 624-634.

- Hassannejadasl, A., D.E. Green, and S. F. Golovashchenko. "Electrohydraulic forming of dual phase steels; Numerical and experimental work." *The 9th International Conference and Workshop on Numerical Simulation of 3D Sheet Metal Forming Processes*. Melbourne, Australia: Numisheet, 2014. 1115-1118.
- Hecker, S.S. "A simple forming limit curve technique and results on aluminum alloys." *Proceedings of the 7th Biennial Congress of the IDDRG*. Amsterdam, Netherlands: International Deep Drawing Research Group, 1972.
- Hecker, S.S. "Technique for determining forming limit curves." *Sheet Metal Industries* 52, no. 11 (1975): 671-676.
- Hu, X., and G.S. Daehn. "Effect of velocity flow localization in tension." *Acta Materialia*, 1996: 1021-1033.
- Ibrahim, R., S.F. Golovashchenko, A. Mamutov, J. Bonnen, A.J. Gillard, and L. Smith. "Analysis of contact stresses in high speed sheet metal forming processes." *Proceedings of the International Conference on High Speed Forming*. Dortmund, Germany, 2012. 93-102.
- Imbert, J.M., S.L. Winkler, M.J. Worswick, and S.F. Golovashchenko. "Formability and damage in electromagnetically formed AA5754 and AA6111." *1st International Conference on High Speed Forming*. Dortmund, Germany: University of Dortmund, 2004. 202-210.
- Imbert, J.M., S.L. Winkler, M.J. Worswick, D.A. Oliveira, and S.F. Golovashchenko. "The effect of tool-sheet interaction on damage evolution in electro-magnetic forming of aluminum alloy sheet." *Journal of Materials and Technology*, 2005: 146-155.
- International Organization for Standardization. "Metallic materials - Sheet and strip - Determination of forming-limit curves - Part 2: Determination of forming-limit curves in the laboratory." *ISO 12004-2*, 2008: 1-27.

- Johnson, G.R., and W.H. Cook. "A constitutive model and data for metals subjected to large strains, high strain rates and high temperatures." *Proceedings of the 7th International Symposium on Ballistics*. 1983. 541-547.
- Keeler S.P., Backofen W.A. "Plastic instability and fracture in sheets stretched over rigid punches." *Transactions of A.S.M.*, Vol. 56, 1963: 25-48.
- Keeler, S.P. "Circular grid system - a valuable aid for evaluating sheet metal formability." *SAE Technical Paper No. 680092*, 1968.
- Keeler, S.P., and W.G. Brazier. "Relationship between laboratory material characterization and press shop formability." *Microalloying 75*. New York, 1977. 517-530.
- Kim, S.B., H. Huh, H.H. Bok, and M.B. Moon. "Forming limit diagram of auto-body steel sheets for high-speed metal forming." *Journal of Materials Processing Technology*, 2011: 851-862.
- Korhonen, A.S., and T. Manninen. "Forming and fracture limits of austenitic stainless steel sheets." *Materials Science and Engineering: A*, 2008: 157-166.
- Lane, T. *Description of an Electrometer invented by Mr. Lane; with an account of some experiments made by him with it: in a letter to Benjamin Franklin*. Vol. 57. London, United Kingdom: Philosophical Transactions of the Royal Society of London, 1767.
- Leu, D. "The limiting drawing ratio for plastic instability of the cup-drawing process." *Journal of Materials Processing Technology*, 1999: 168-176.
- Li, J., J.E. Carsley, T.B. Stoughton, L.G. Hector Jr., and S.J. Hugh. "Forming limit analysis for two-stage forming of 5182-0 aluminum sheet with intermediate annealing." *International Journal of Plasticity*, 2013: 21-43.
- Marciniak, Z., K. Kuczynski, and T. Pokora. "Influence of the plastic properties of a material on the forming limit diagram for sheet metal in tension." *International Journal of Mechanical Sciences*, Vol 15, 1973: 789-800.

- Mynors, D.J., and B. Zhang. "Applications and capabilities of explosive forming." *Journal of Materials Processing Technology*, 2002: 1-25.
- Nakazima, K., T. Kikuma, and K. Hasuka. "Study on the formability of steel sheets." *Technical Report No. 264, Yawata Iron and Steel Co.*, 1968: 141.
- National Highway Traffic Safety Administration (NHTSA). "Fuel Economy." *National Highway Traffic Safety Administration*. April 1, 2010.  
<http://www.nhtsa.gov/PR/DOT-56-10> (accessed November 14, 2012).
- Oliveira, D.A., M.J. Worswick, M. Finn, and D. Newman. "Electromagnetic forming of aluminum alloy sheet: Free-form and cavity fill experiments and model." *Journal of Materials Processing Technology*, 2005: 350-362.
- Priestly, J. *Experiments on the lateral force of electrical explosions*. London, United Kingdom: Philosophical Transactions of the Royal Society of London, 1769.
- Psyk, V., D. Risch, B.L. Kinsey, A.E. Tekkaya, and M. Kleiner. "Electromagnetic forming - a review." *Journal of Materials Processing Technology*, 2011: 787-829.
- Raghavan, K.S., R.C. van Kuren, and H. Darlington. "Recent progress in the development of forming limit curves for automotive steel sheets." *SAE Technical Paper No. 920437*, 1992.
- Rahmaan, T., A. Bardelcik, J.M. Imbert, S. Kim, and M.J. Worswick. "Strain rate sensitivity and anisotropy of TRIP 780, DP600, and AA5182-O sheet metal alloys." *ICILLS Conference*. South Africa, 2014. 1-4.
- Rohatgi, A., E.V. Stephens, R.W. Davies, M.T. Smith, A. Soulami, and S. Ahzi. "Electro-hydraulic forming of sheet metals: Free-forming vs. conical-die forming." *Journal of Materials Processing Technology*, 2012: 1070-1079.
- Rohatgi, A.h, E.V. Stephens, A. Soulami, R.W. Davies, and M.T. Smith. "Experimental characterization of sheet metal deformation during electro-hydraulic forming." *Journal of Materials Processing Technology*, 2011: 1824-1833.

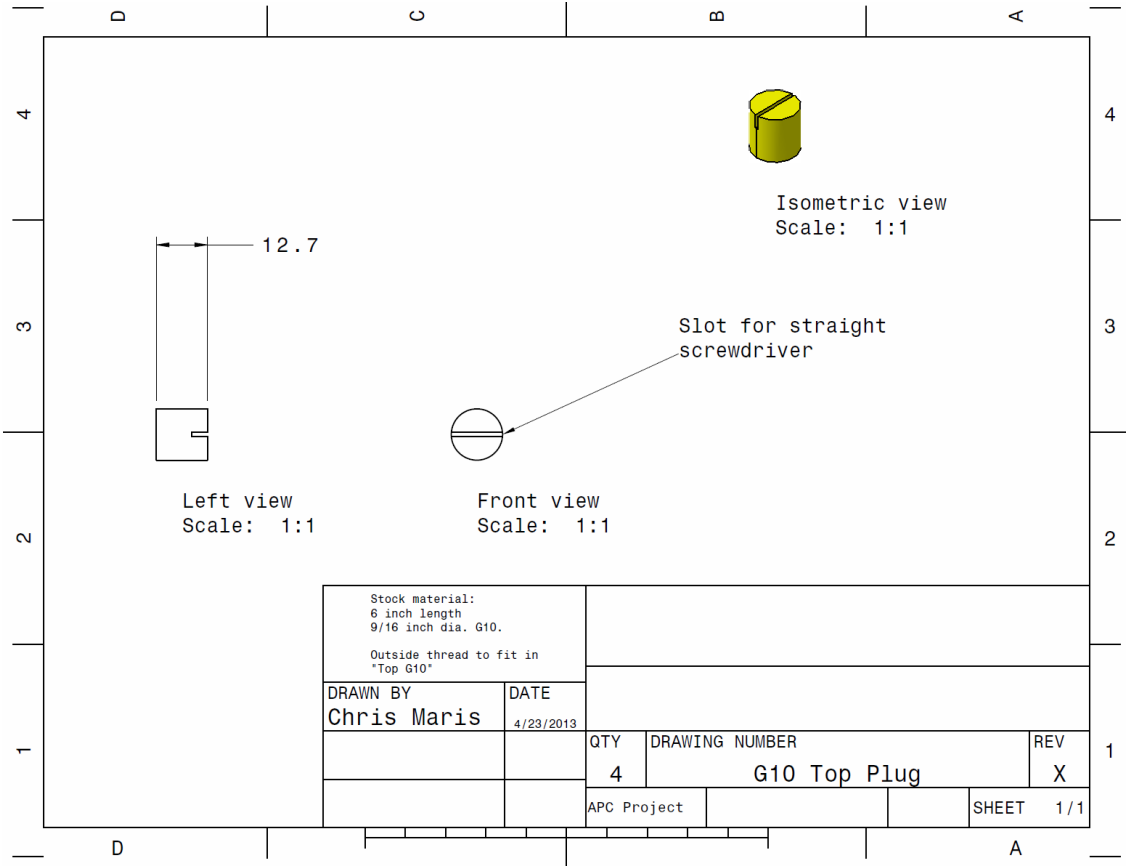
- Samei, J., D.E. Green, and S.F. Golovashchenko. "Metallurgical investigations on hyperplasticity in dual phase steels." *Journal of Manufacturing and Science in Engineering*, 2014: in press.
- Seth, M., V.J. Vohnout, and G.S. Daehn. "Formability of steel sheet in high velocity impact." *Journal of Materials Processing Technology*, 2005: 390-400.
- Sklad, M.P., and J.D. Verhaeghe. "Forming limit curve based on shear under tension failure criterion." *Proceedings of the IDDRG 2010 Int. Conference*. Graz, Austria: International Deep Drawing Research Group, 2010. 1-10.
- Sriram, S., G. Huang, B. Yan, and J-L Geoffroy. "Comparison of forming limit curves for advanced high strength steels using different techniques." *SAE International Journal Materials and Manufacturing*, 2009: 472-481.
- Stoughton, T.B. "Stress-based forming limits in sheet-metal forming." *Journal of Engineering Materials Technology*, 2001: 417-422.
- Woodward, S., C. Weddeling, G.S. Daehn, V. Psyk, B. Carson, and A.E. Tekkaya. "Production of low-volume aviation components using disposable electromagnetic actuators." *Journal of Materials Processing Technology*, 2011: 886-895.
- Wu, P.D., M. Jain, J. Savoie, S.R. MacEwen, P. Tugcu, and K.W. Neale. "Evaluation of anisotropic yield functions for aluminum sheets." *International Journal of Plasticity*, 2003: 121-138.

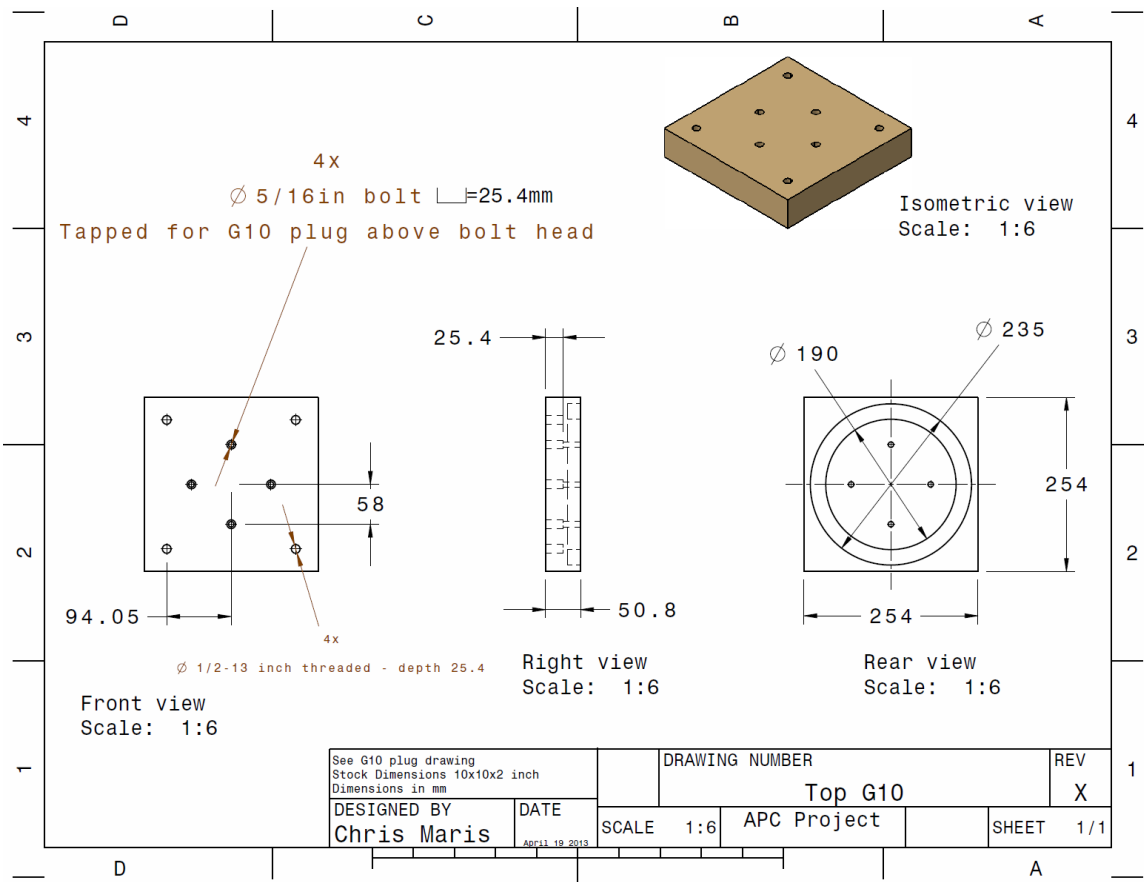
# Appendices

## Appendix A: Engineering Drawings of Custom Tooling

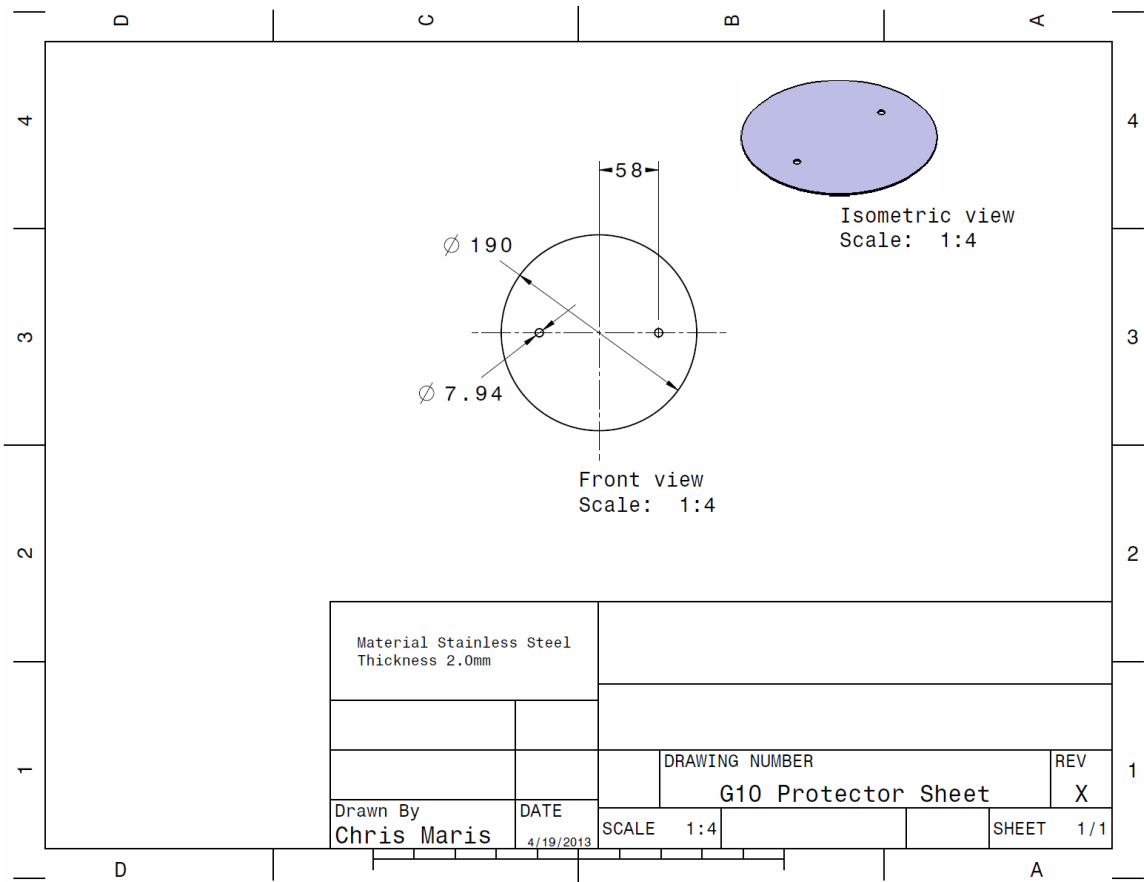
Engineering drawings for each piece of custom manufactured tooling are shown in the following pages. The drawings are in the order of the assembled parts from the ram of the press toward the table of the press.

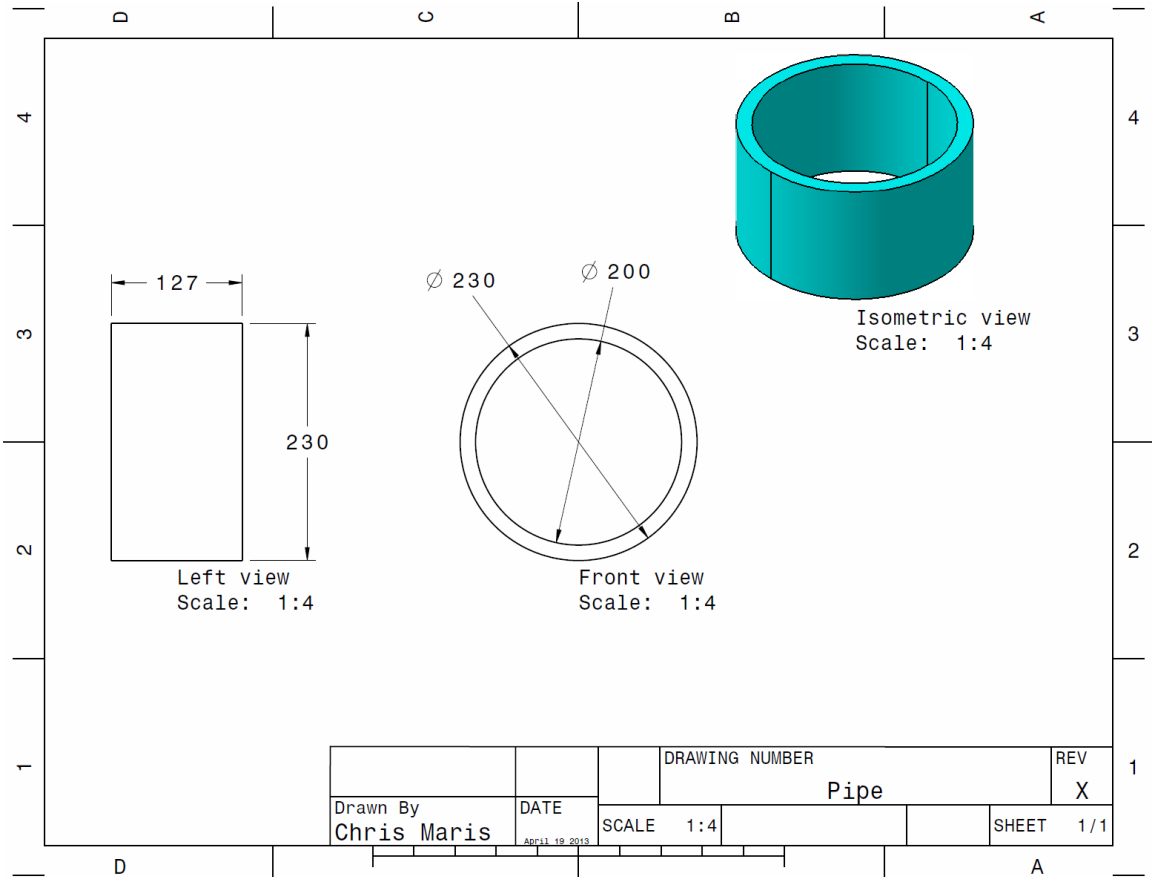
G10 Top Plug.....	143
Top G10 .....	144
G10 Protector Sheet .....	145
Pipe .....	146
Die Adapter.....	147
Adapter Ring.....	148
Mini-die Spacer.....	149
Narrow Flat Mini-die .....	150
Wide Flat Mini-die.....	151
Chamber.....	152
Chamber Section Cuts.....	153
L Bracket.....	154
Bottom G10.....	155
CNC Mill Fixture for EHF Specimens .....	156

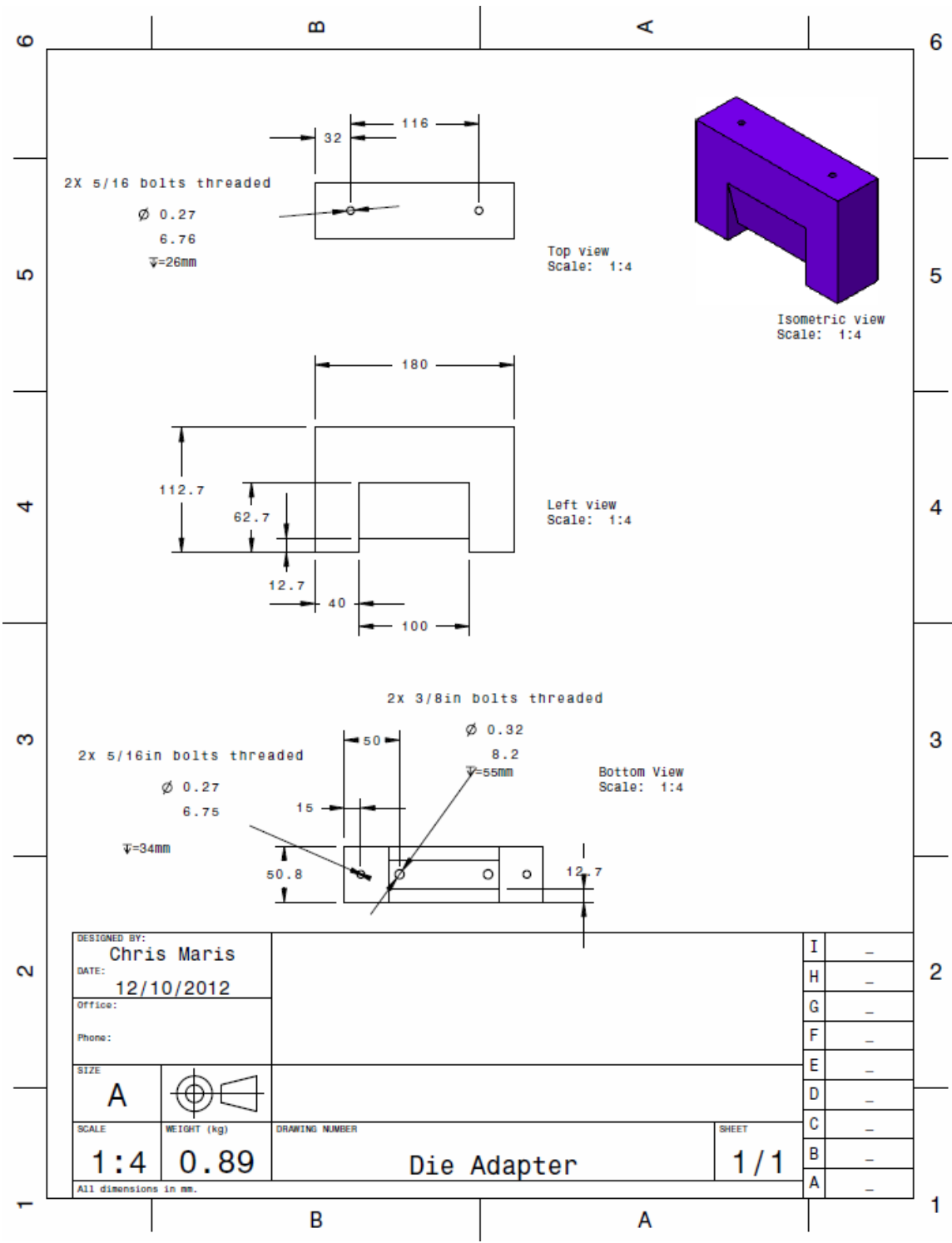


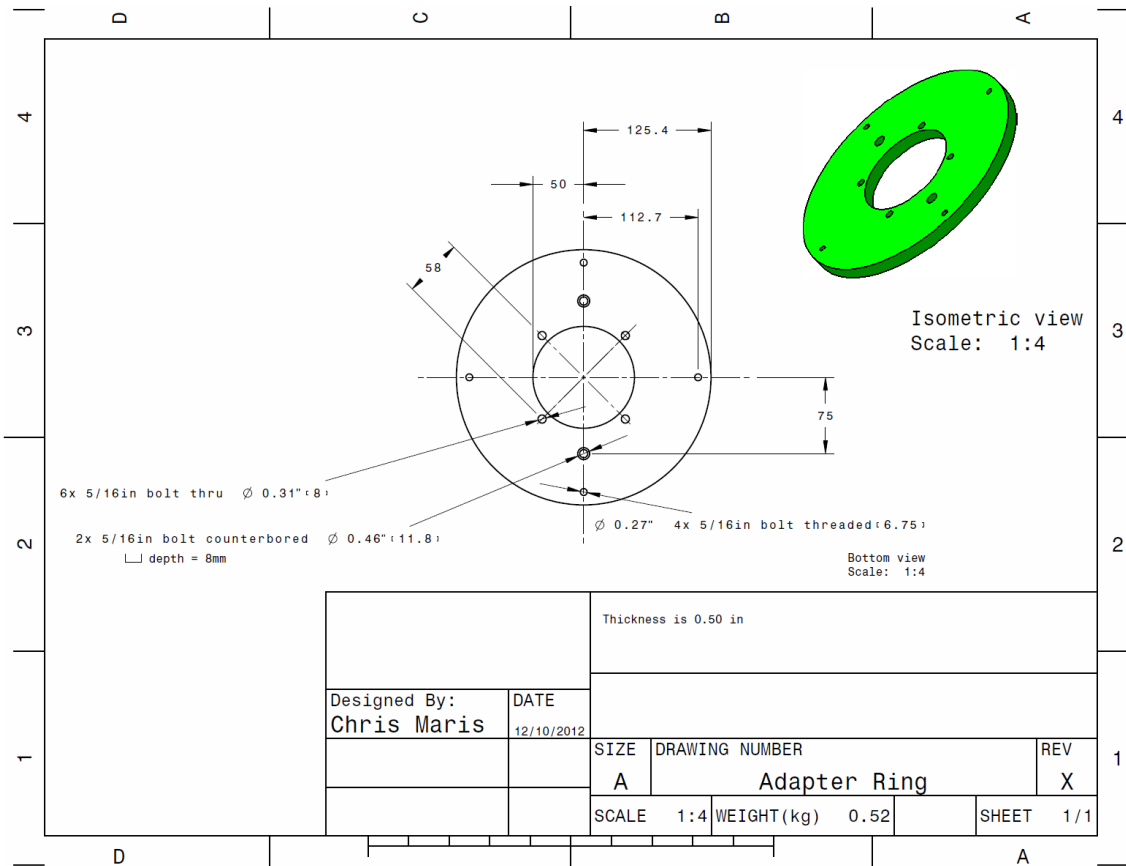


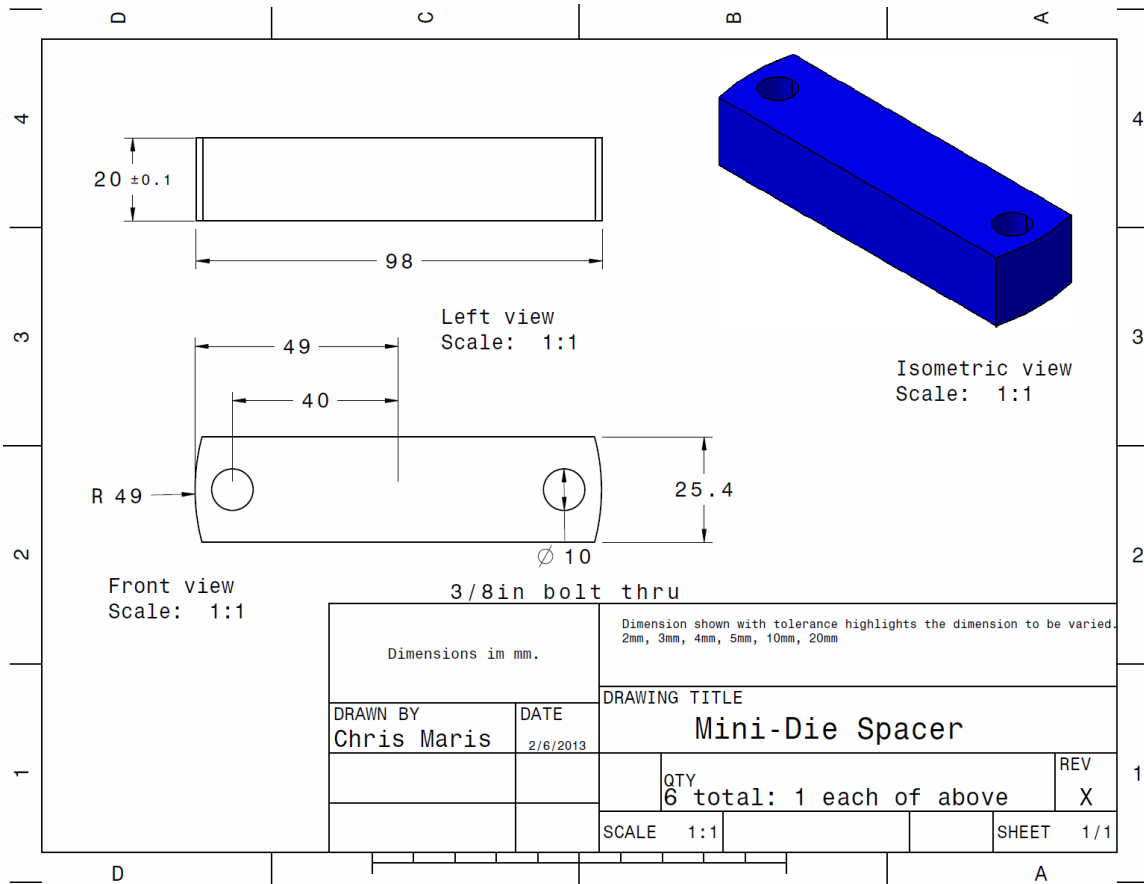


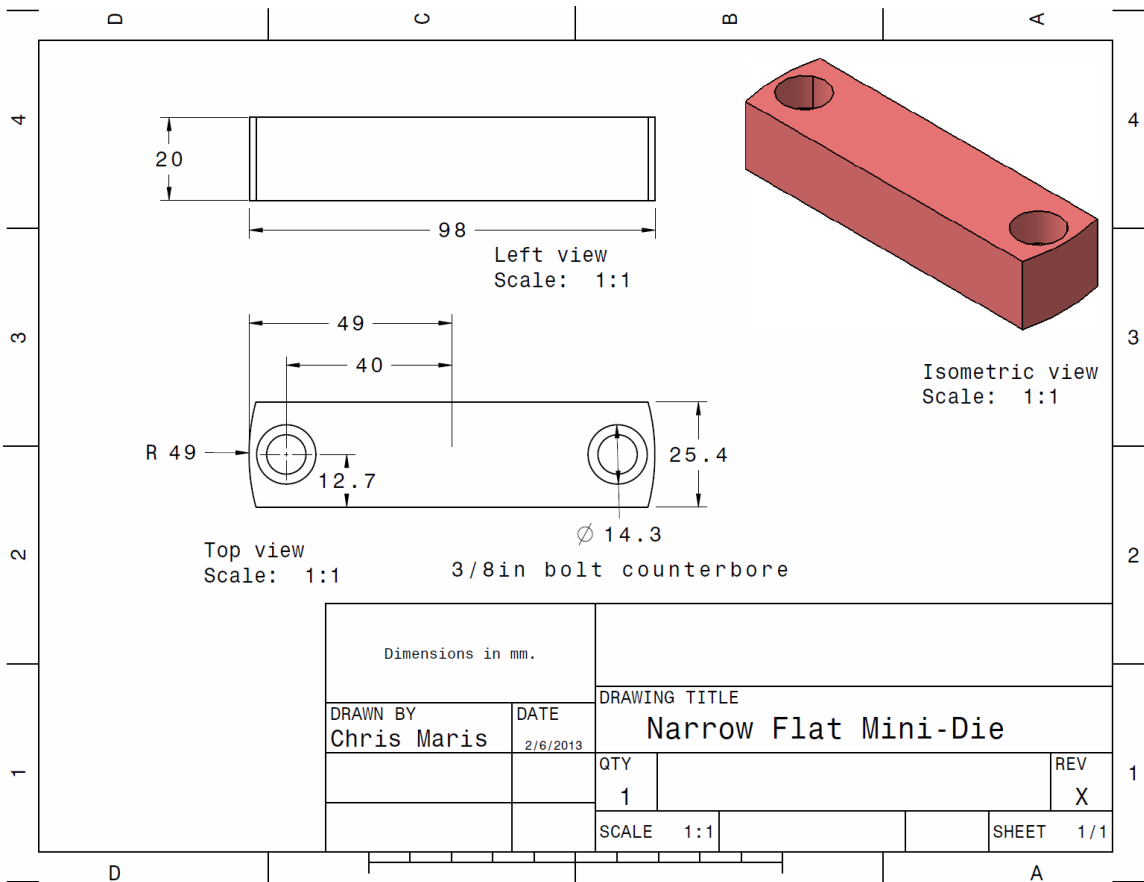


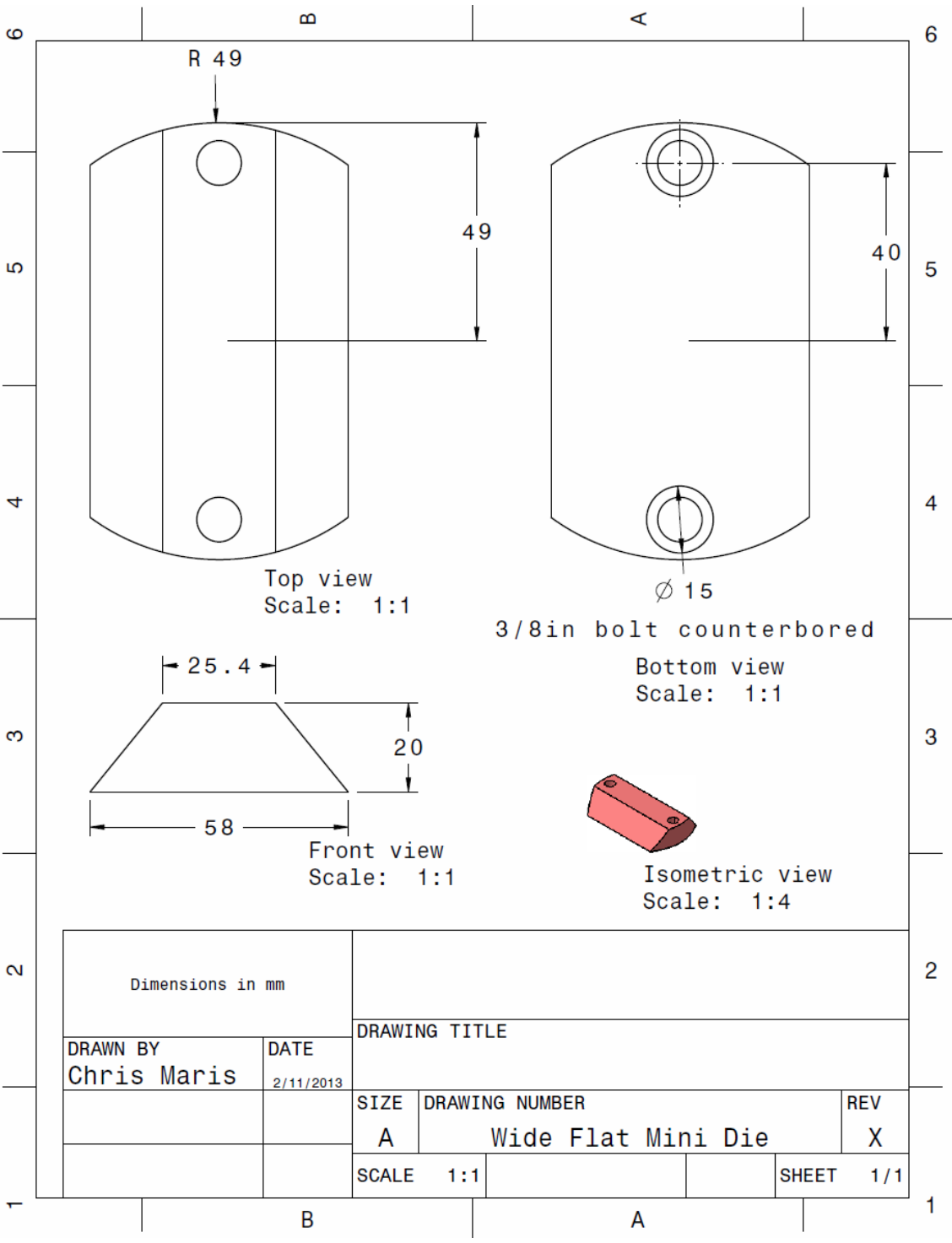


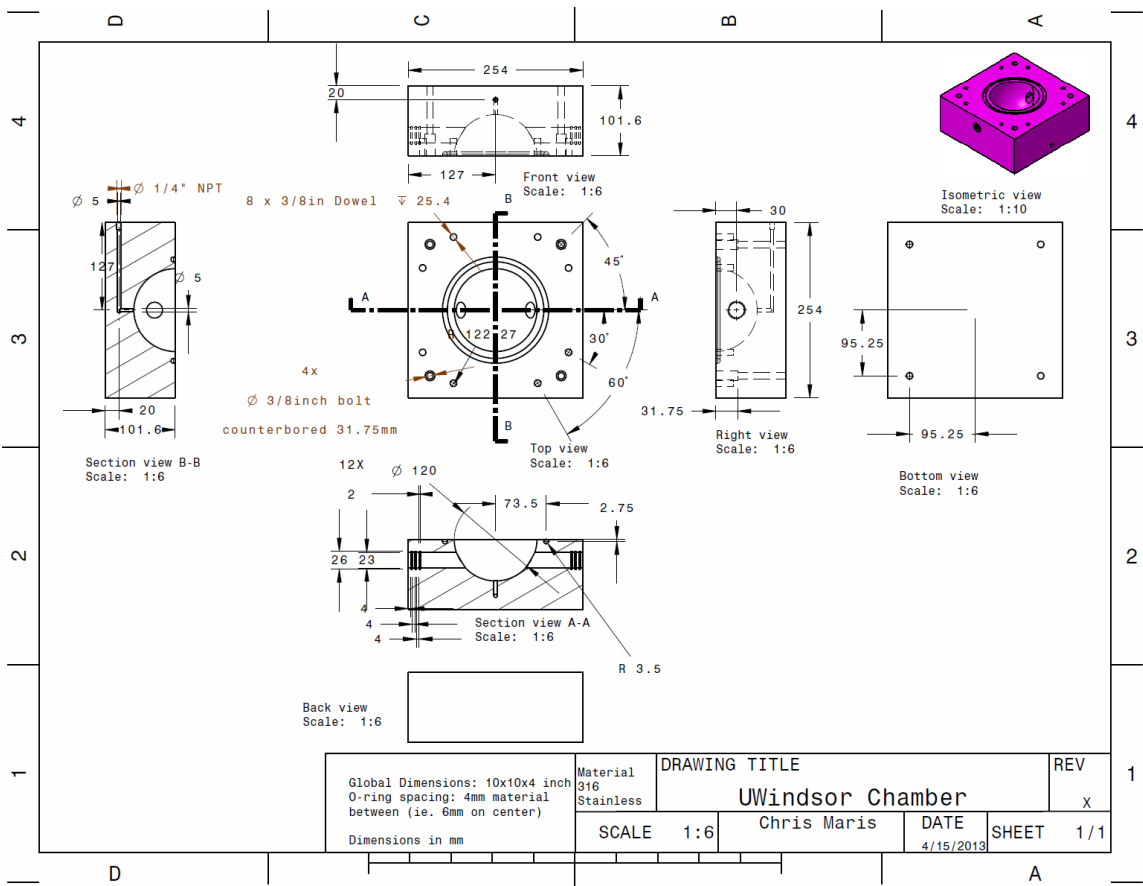




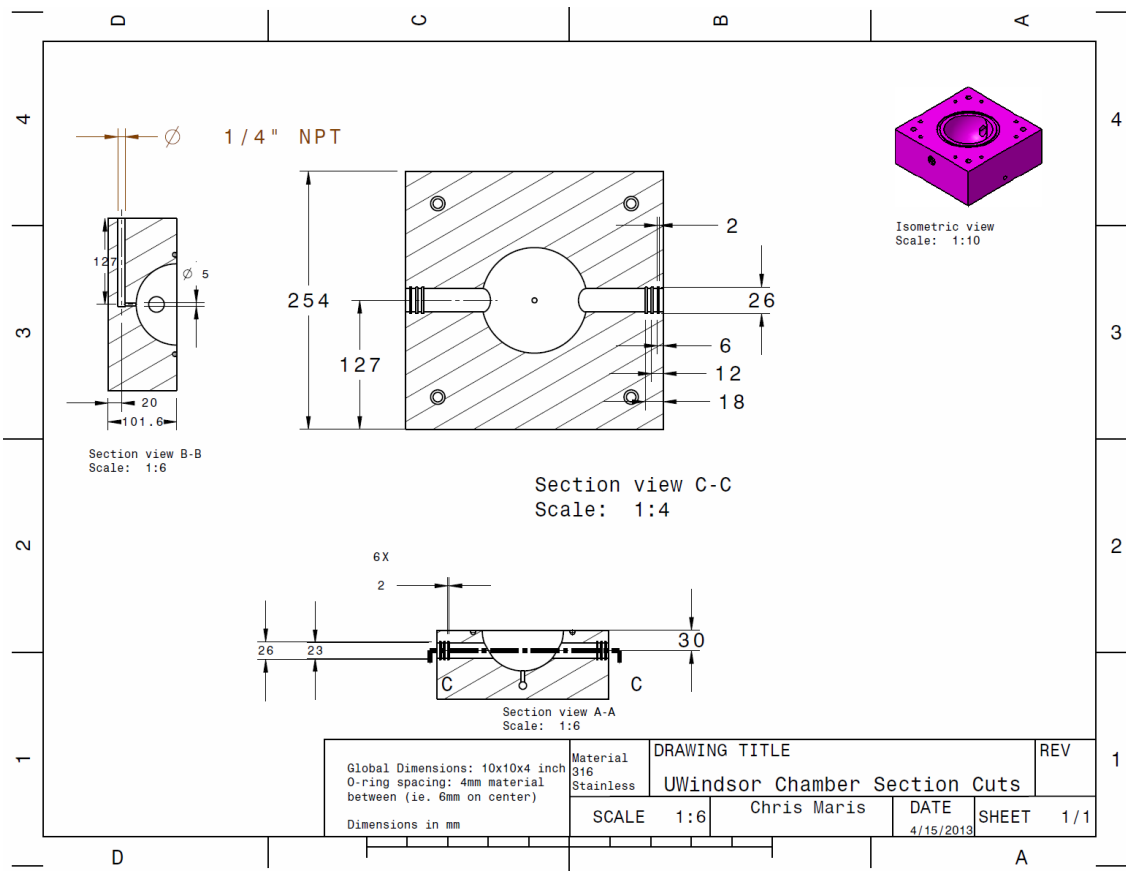


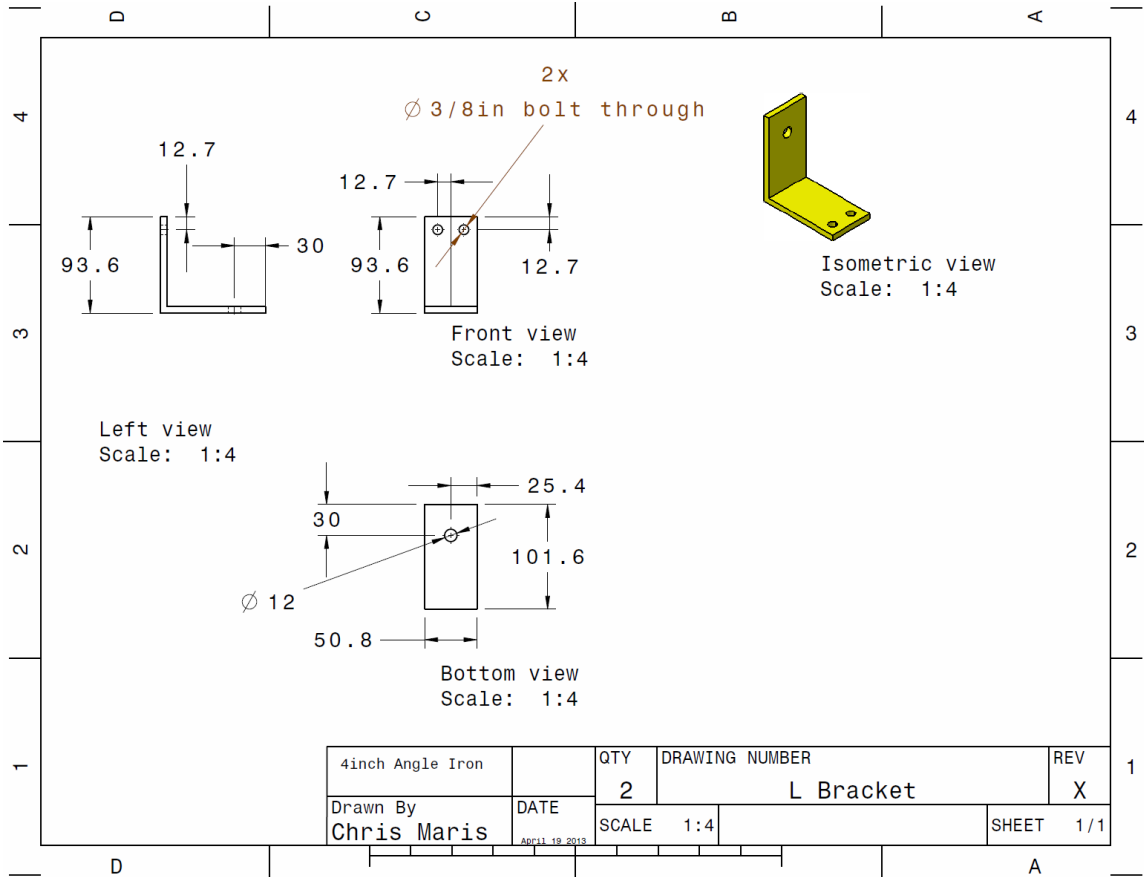


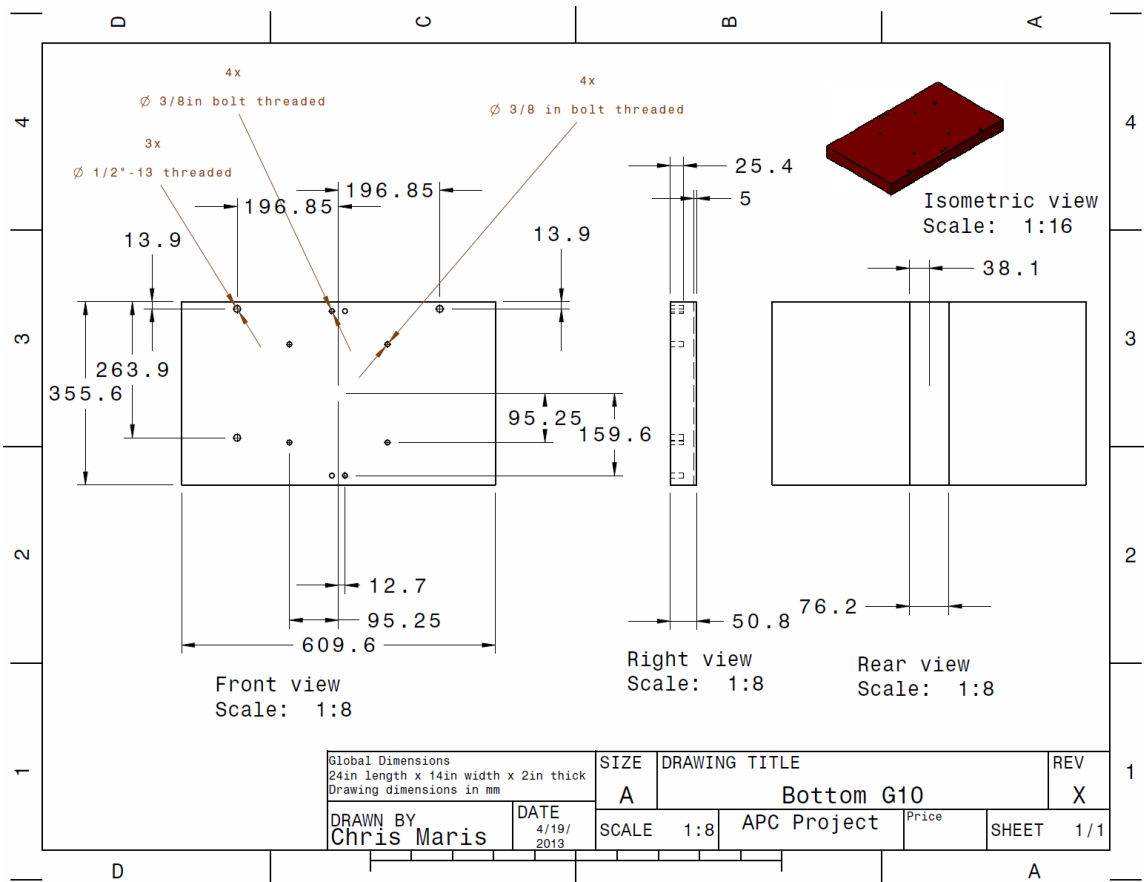


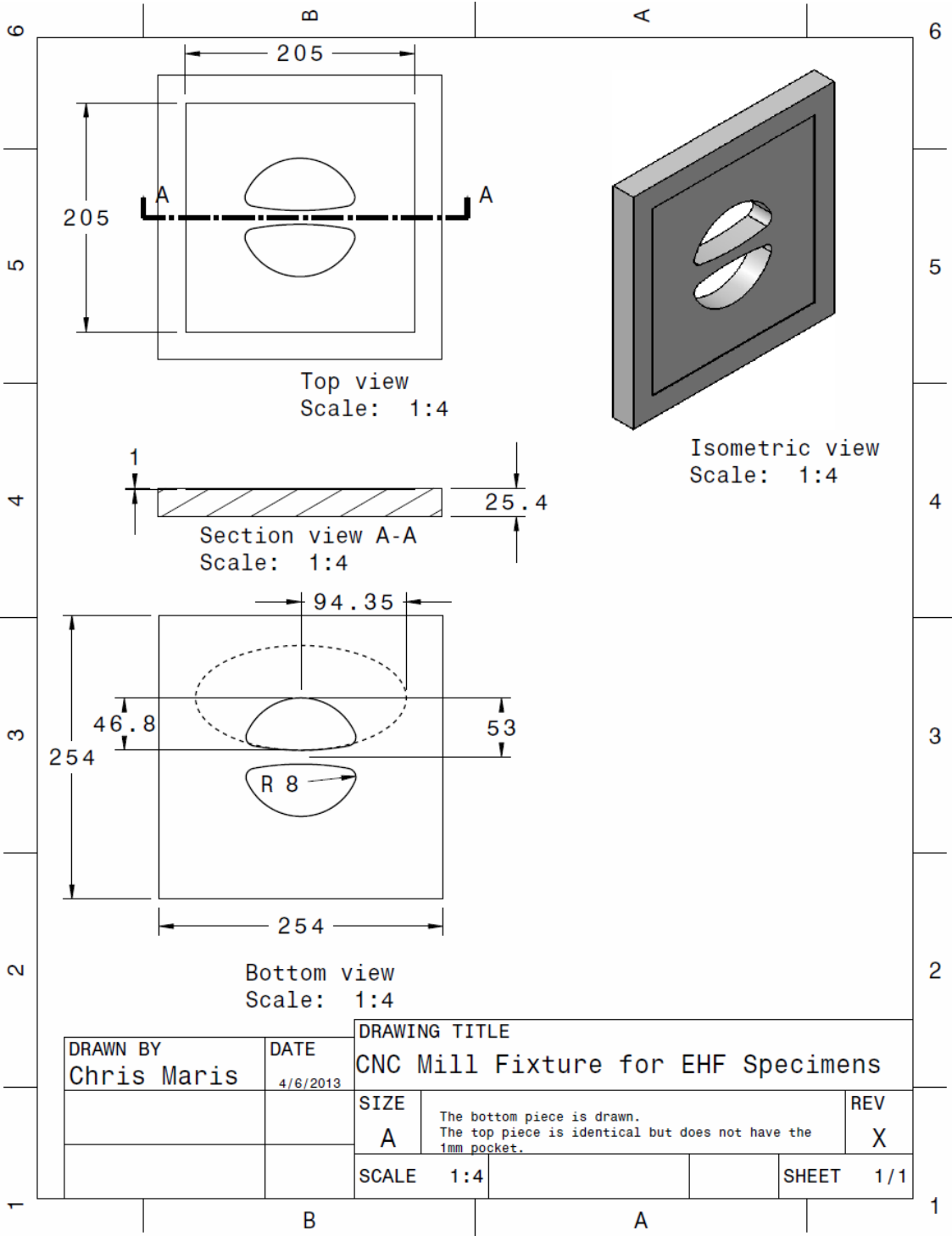








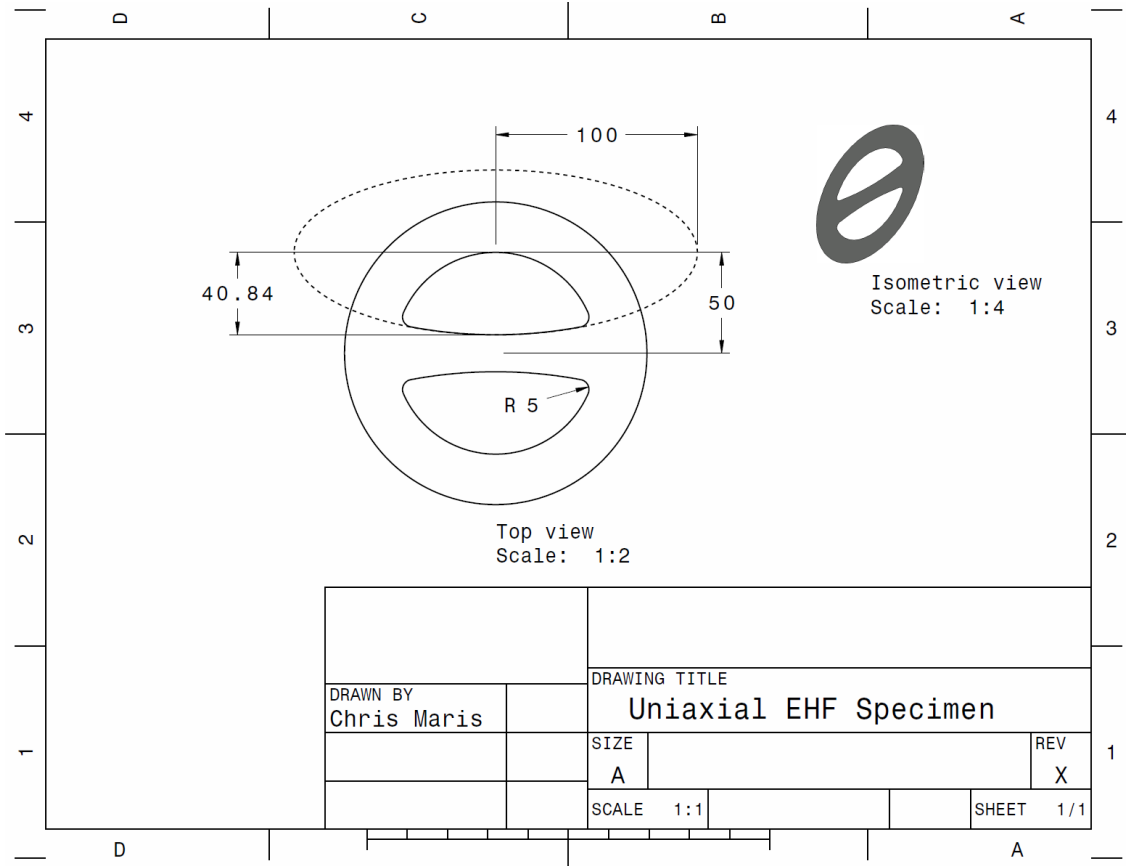




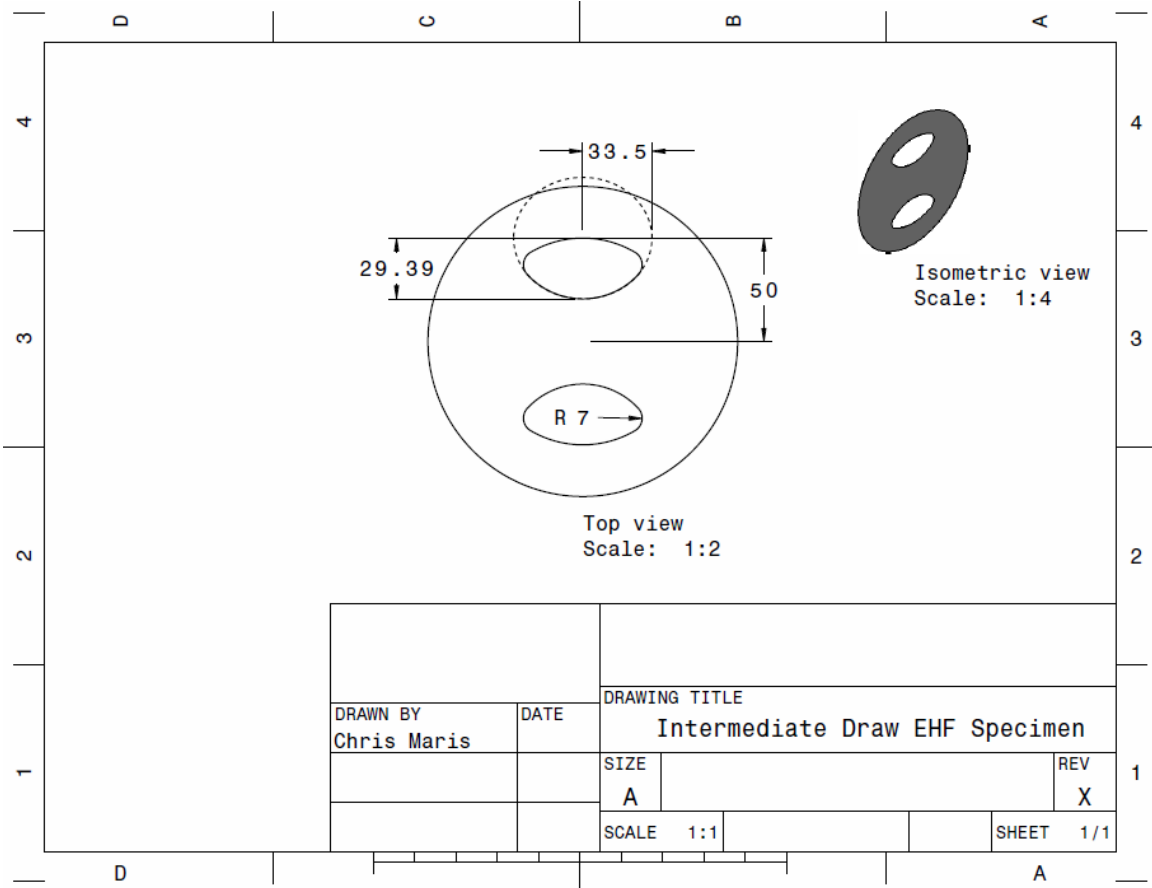
## **Appendix B: Engineering Drawings of Modified EHF Specimens**

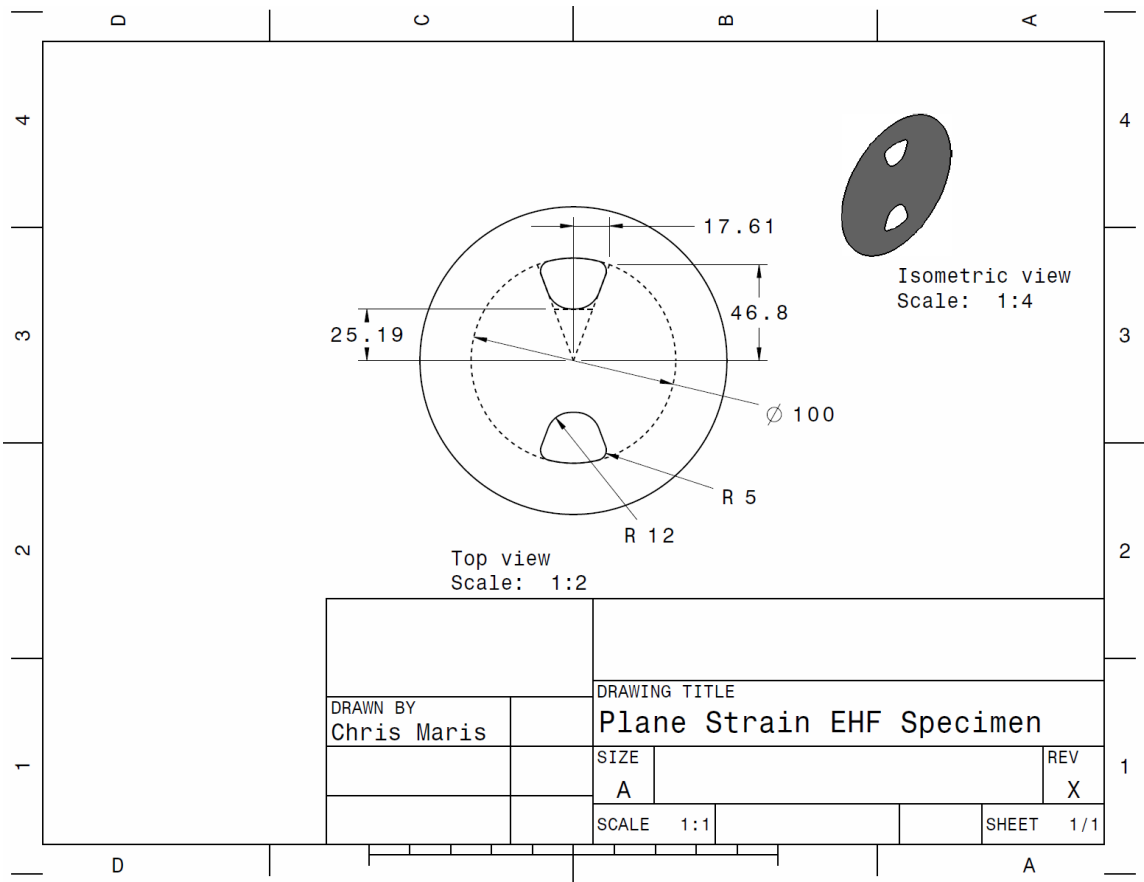
The engineering drawings for the novel EHF specimens are included in this appendix.

Uniaxial.....	158
Intermediate Draw .....	159
Plane Strain.....	160
Biaxial.....	161



		DRAWING TITLE	
DRAWN BY Chris Maris		Uniaxial EHF Specimen	
	SIZE A	REV X	
	SCALE 1:1	SHEET 1/1	



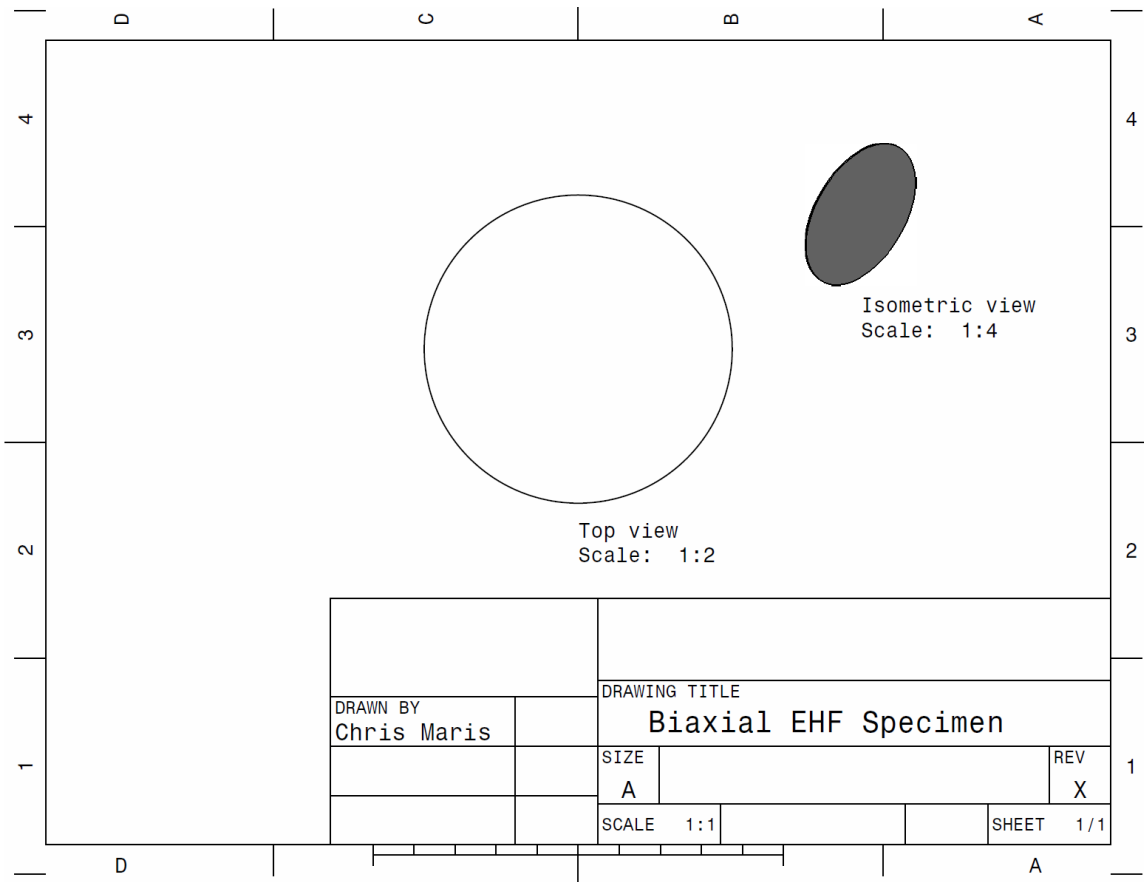


Top view  
Scale: 1:2

Isometric view  
Scale: 1:4

DRAWN BY Chris Maris		DRAWING TITLE Plane Strain EHF Specimen		
		SIZE A	REV X	1
		SCALE 1:1	SHEET 1/1	





## Appendix C: Experimental EHFF Results

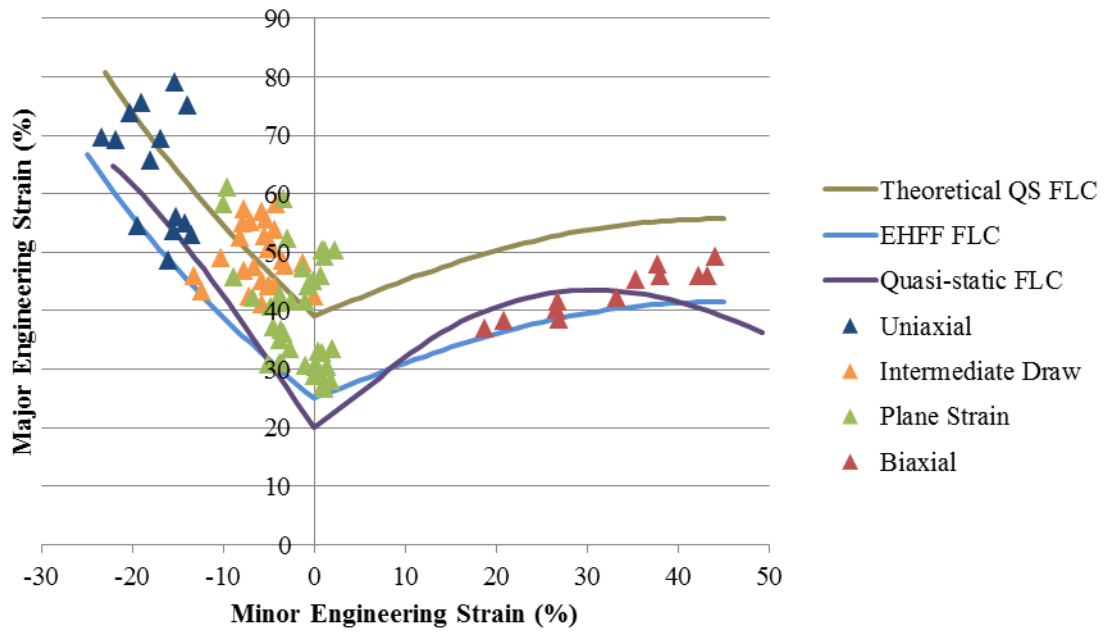
This appendix contains the experimental EHFF results.

The EHFF FLC experimental data points for DP600 and AA5182-O .....	163
The DP600 EHFF FLC with necked strain measurements sorted by specimen geometry .....	164
The AA5182-O EHFF FLC with necked strain measurements sorted by specimen geometry .....	165
The AA5182-O EHFF FLC with necked strain measurements and strain measurements from close to the split sorted by specimen geometry.....	166
Final displacement of the sheet measured radially from the sheet center for necked DP600 and AA5182-O specimens.....	167
Major strain distribution measured radially from the sheet center for safe DP600 and AA5182-O specimens.....	168
Minor strain distribution measured radially from the sheet center for safe DP600 and AA5182-O specimens.....	169

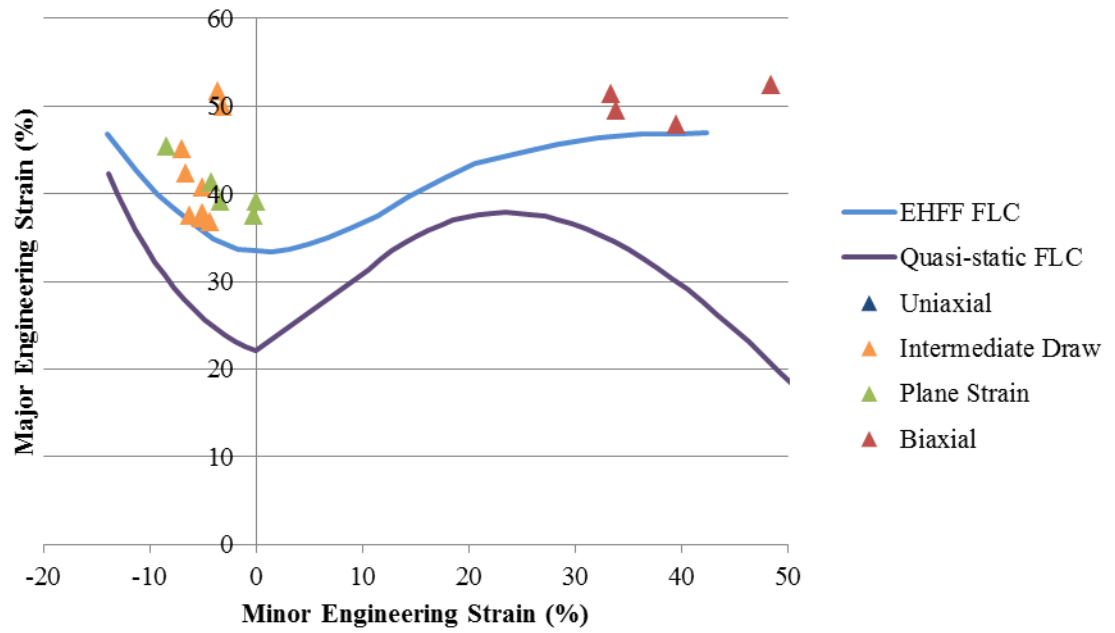
**The EHFF FLC experimental data points for DP600 and AA5182-O.**

<b>DP600</b>		<b>AA5182</b>	
Major strain	Minor strain	Major strain	Minor strain
64.47	-24.00	46.80	-14.03
60.26	-22.00	42.57	-11.23
56.25	-20.00	39.98	-9.29
52.44	-18.00	38.37	-7.80
48.81	-16.00	36.59	-5.93
45.35	-14.00	34.84	-3.97
42.05	-12.00	33.74	-1.69
38.89	-10.00	33.46	0.03
35.87	-8.00	33.40	1.35
32.98	-6.00	33.67	3.13
30.21	-4.00	34.19	4.84
27.55	-2.00	35.00	6.69
25.00	0.00	36.20	8.93
26.24	2.00	37.50	11.39
27.47	4.00	39.62	14.23
28.69	6.00	41.90	17.77
29.87	8.00	43.40	20.57
31.03	10.00	44.70	24.57
32.15	12.00	45.71	28.30
33.22	14.00	46.42	32.13
34.24	16.00	46.82	36.22
35.20	18.00	46.90	39.83
36.10	20.00	46.99	42.28
36.94	22.00		
37.72	24.00		
38.42	26.00		
39.05	28.00		
39.61	30.00		
40.10	32.00		
40.51	34.00		
40.85	36.00		
41.12	38.00		
41.32	40.00		
41.46	42.00		
41.53	44.00		

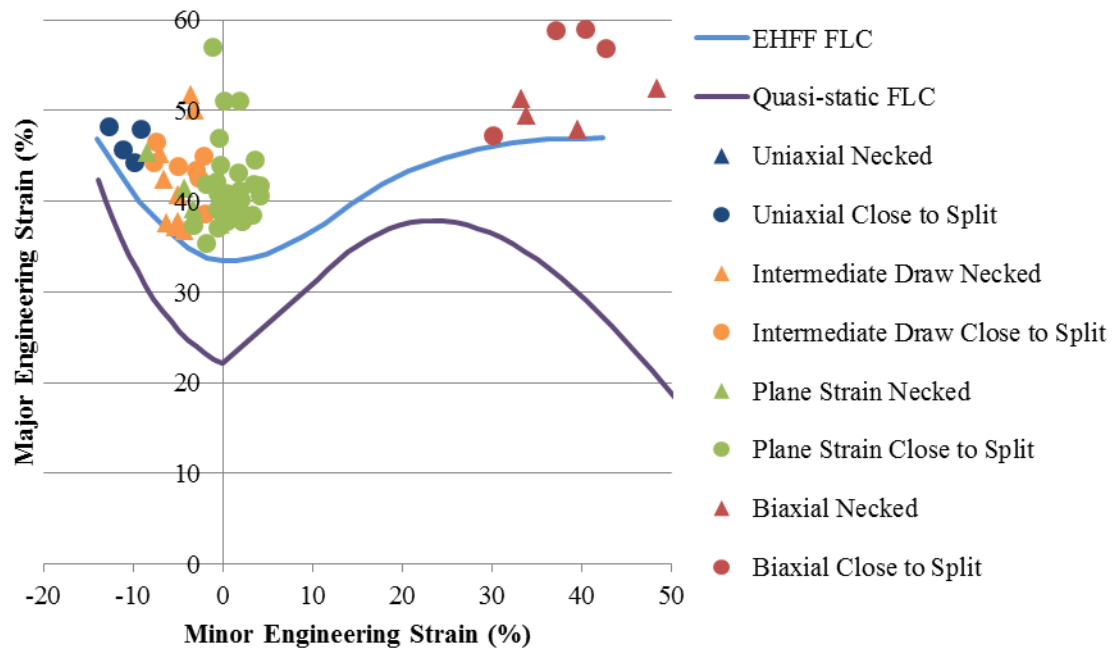
The DP600 EHFF FLC with necked strain measurements sorted by specimen geometry.



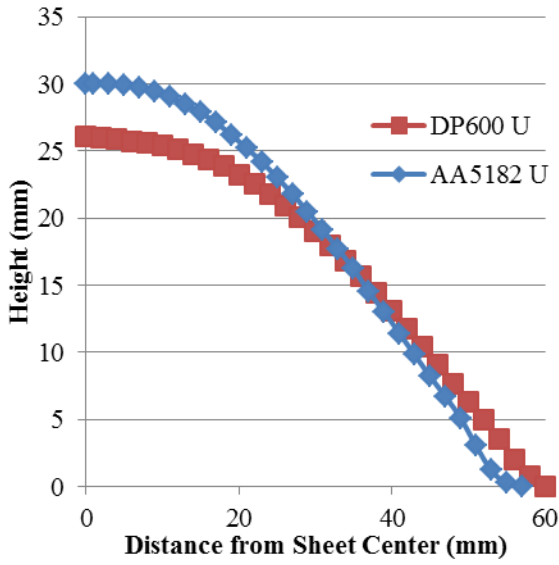
The AA5182-O EHFF FLC with necked strain measurements sorted by specimen geometry.



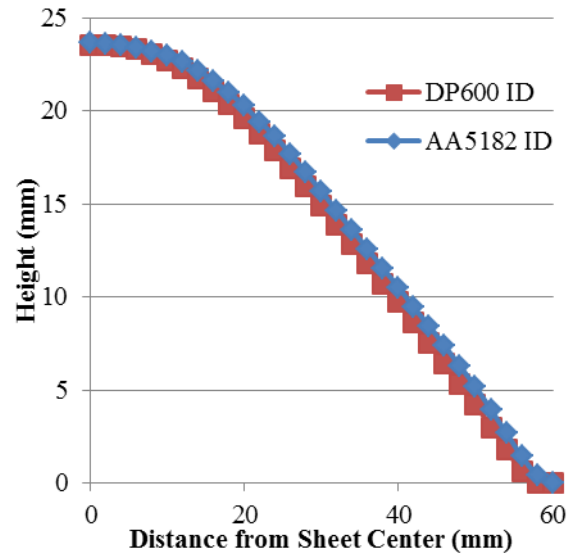
The AA5182-O EHFF FLC with necked strain measurements and strain measurements from close to the split sorted by specimen geometry.



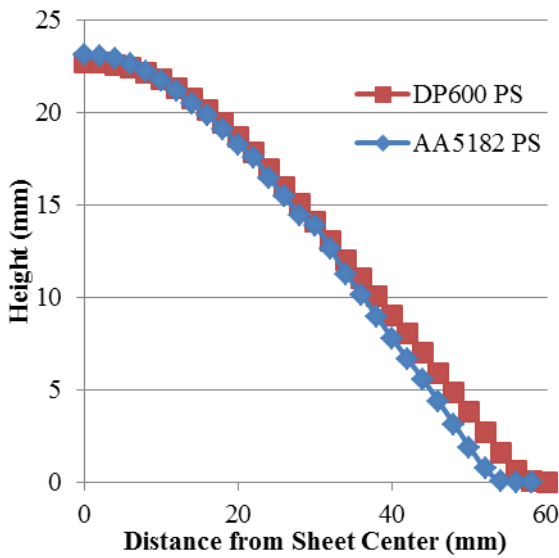
**Final displacement of the sheet measured radially from the sheet center for necked DP600 and AA5182-O specimens.**



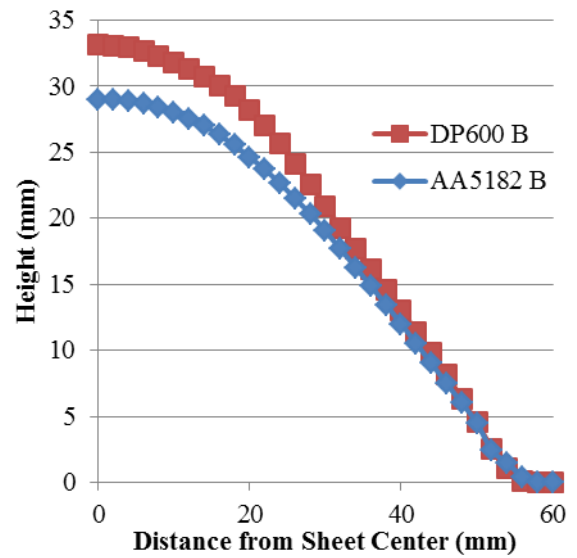
Uniaxial



Intermediate Draw

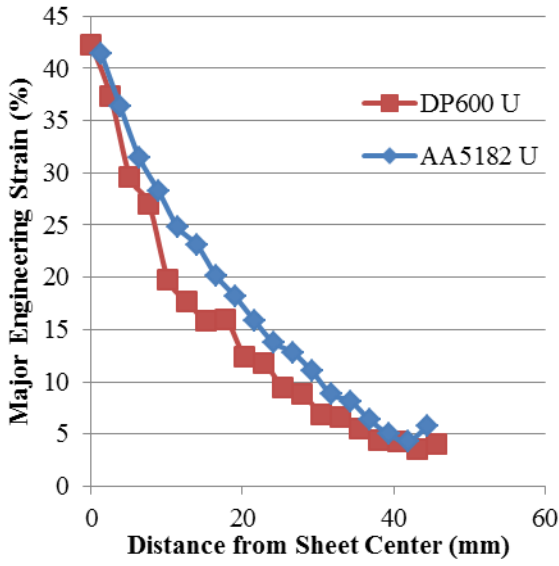


Plane Strain

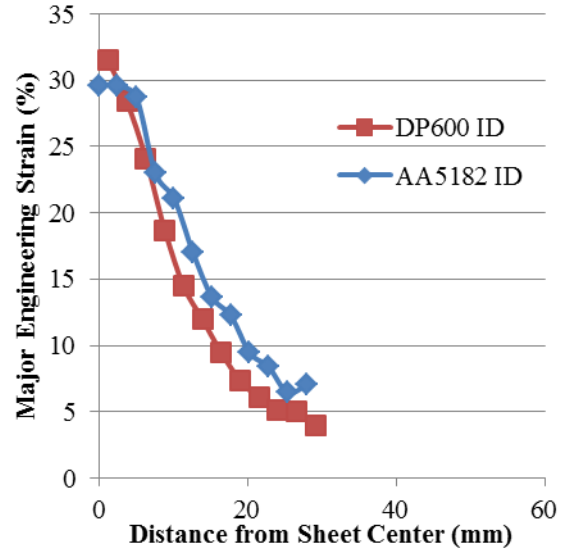


Biaxial

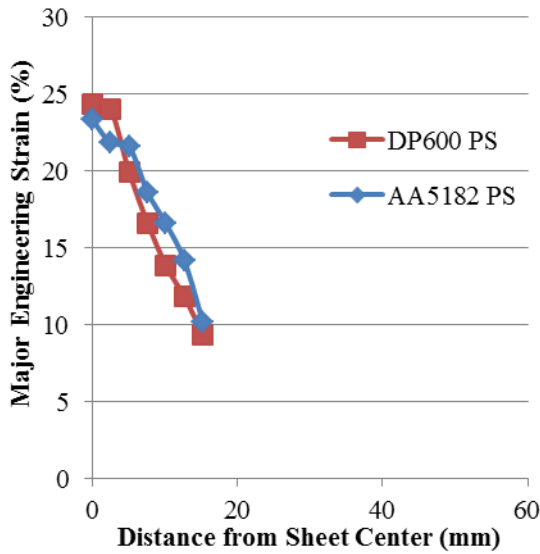
**Major strain distribution measured radially from the sheet center for safe DP600 and AA5182-O specimens.**



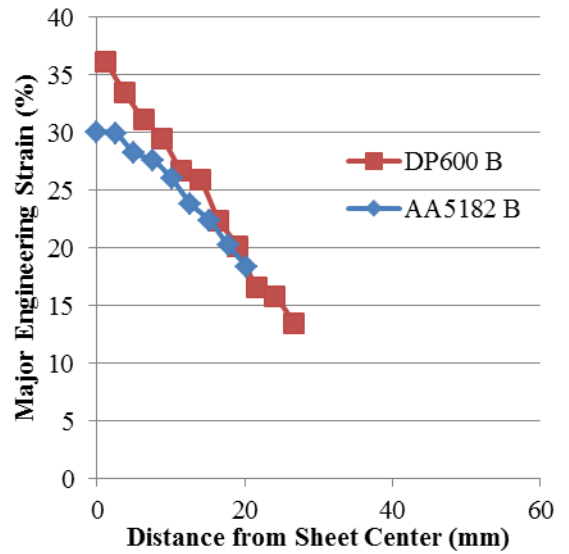
Uniaxial



Intermediate Draw



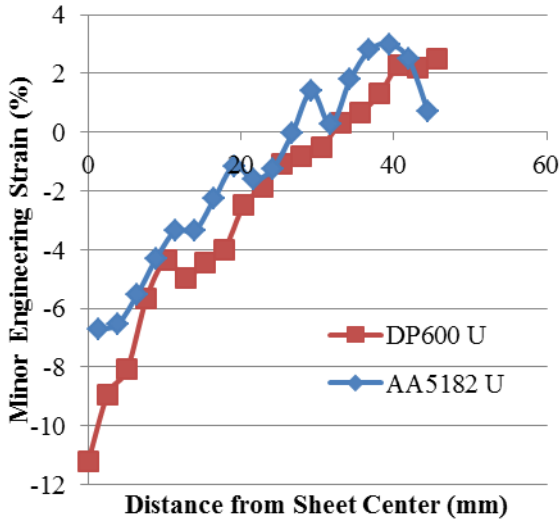
Plane Strain



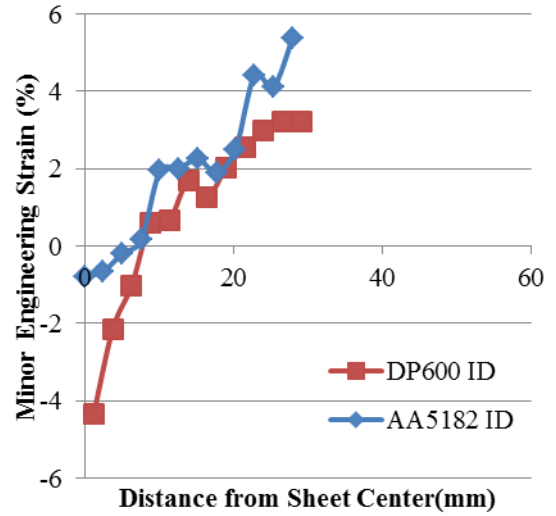
Biaxial



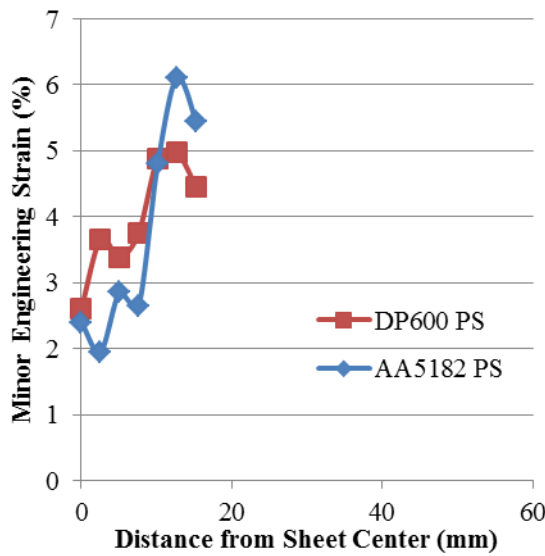
Minor strain distribution measured radially from the sheet center for safe DP600 and AA5182-O specimens.



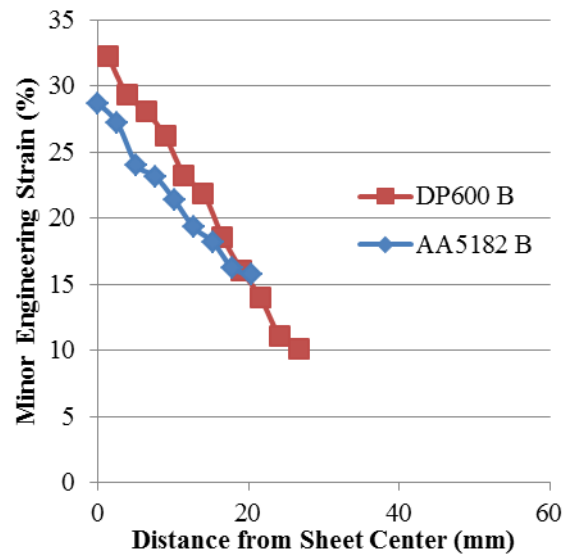
Uniaxial



Intermediate Draw



Plane Strain



Biaxial

## Appendix D: Numerical Simulation of EHFF Results by Strain Path

This appendix contains the numerical EHFF results.

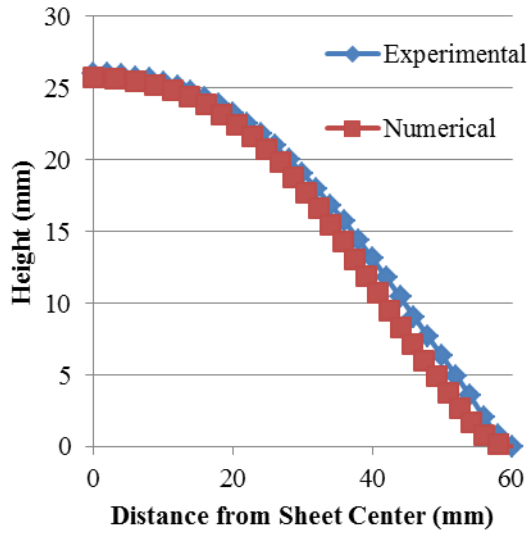
Final displacement of the sheet measured radially from the sheet center for experimental and numerical DP600 specimens. ....	172
Final displacement of the sheet measured radially from the sheet center for experimental and numerical AA5182-O specimens. ....	173
Evolution of the sheet displacement measured radially from the sheet center for DP600 specimens. ....	174
Evolution of the sheet displacement measured radially from the sheet center for AA5182-O specimens. ....	175
Velocity at distances of 0, 15, and 30mm from the specimen center for DP600 specimens. ....	176
Velocity at distances of 0, 15, and 30mm from the specimen center for AA5182-O specimens. ....	177
Major strain at distances of 0, 15, and 30mm from the specimen center for DP600 specimens. ....	178
Major strain at distances of 0, 15, and 30mm from the specimen center for AA5182-O specimens. ....	179
Equivalent strain rate and the average equivalent strain rate at distances of 0, 15, and 30mm from the specimen center for DP600 specimens. ....	180
Equivalent strain rate and the average equivalent strain rate at distances of 0, 15, and 30mm from the specimen center for AA5182-O specimens. ....	181
Comparison of experimental and predicted major and minor strains measured radially from the center of the DP600 specimens. ....	182

Comparison of experimental and predicted major and minor strains measured  
radially from the center of the AA5182-O specimens .....183

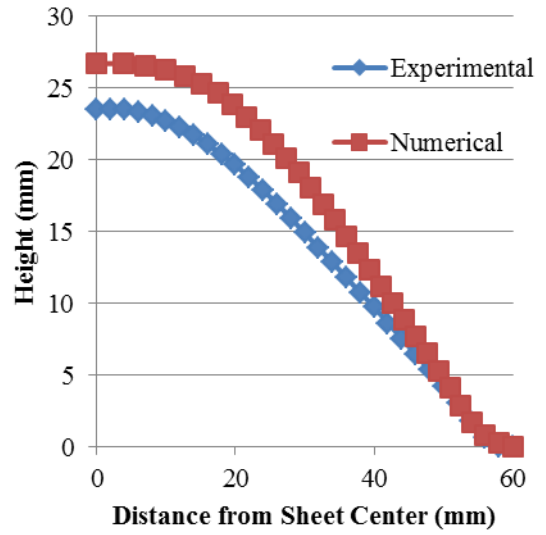
Equivalent strain rate vs. equivalent strain for DP600 specimens.....184

Equivalent strain rate vs. equivalent strain for AA5182-O specimens.....185

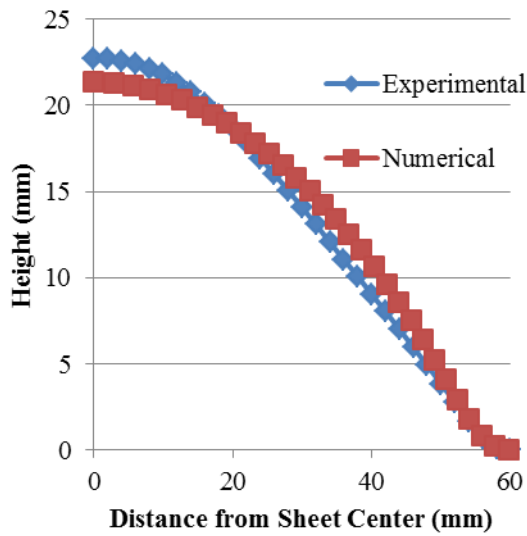
**Final displacement of the sheet measured radially from the sheet center for experimental and numerical DP600 specimens.**



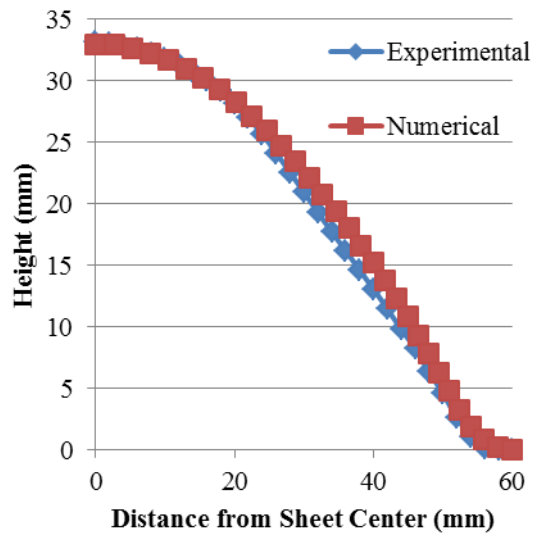
Uniaxial



Intermediate Draw

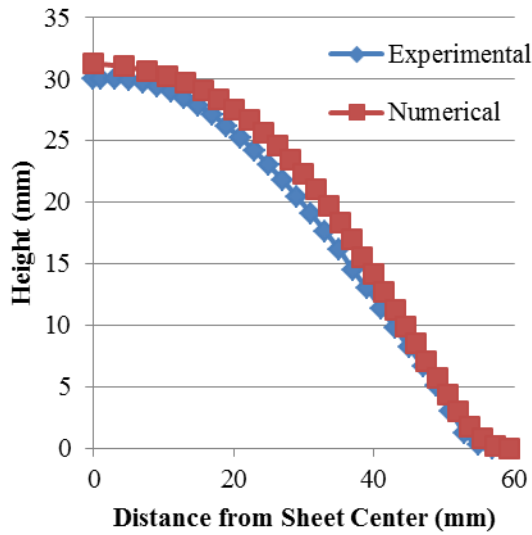


Plane Strain

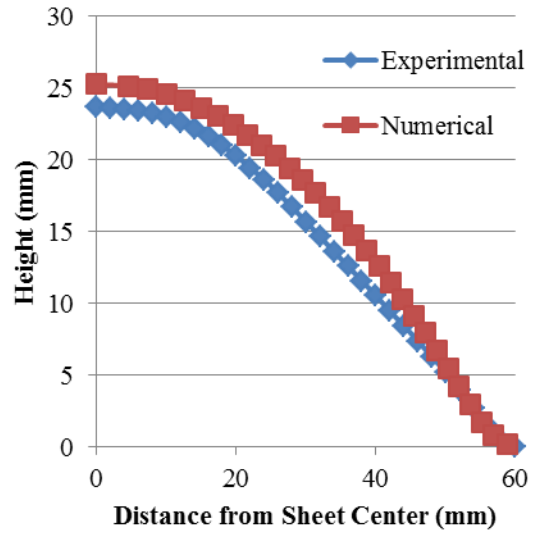


Biaxial

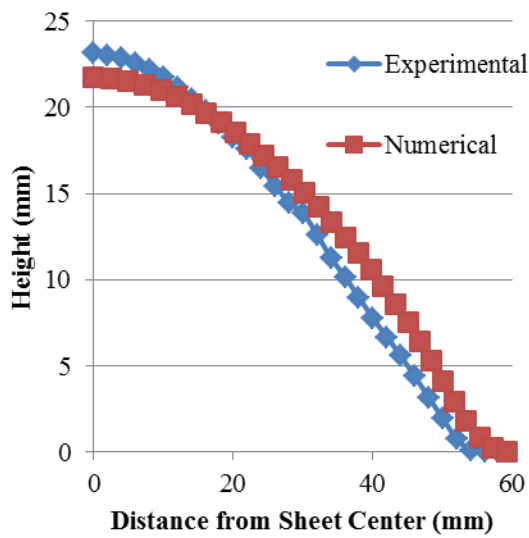
**Final displacement of the sheet measured radially from the sheet center for experimental and numerical DP600 specimens.**



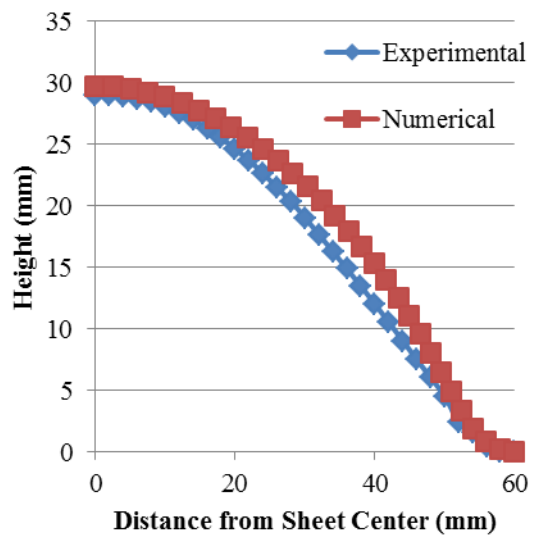
Uniaxial



Intermediate Draw

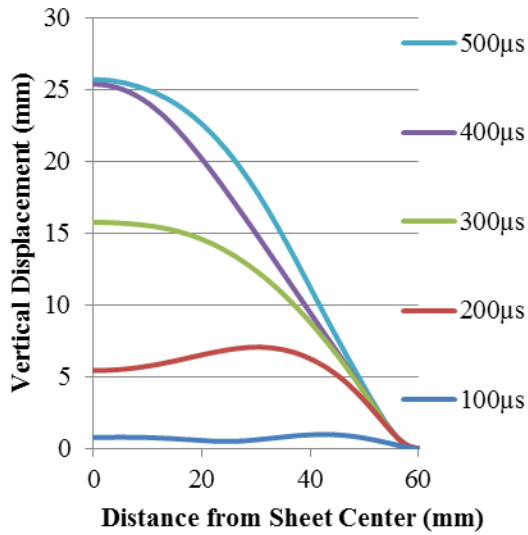


Plane Strain

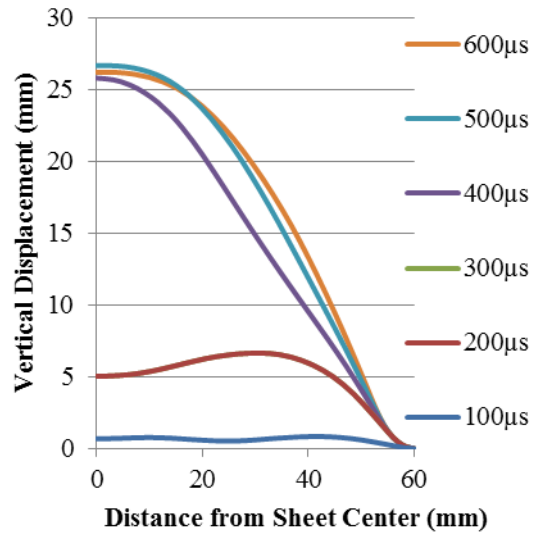


Biaxial

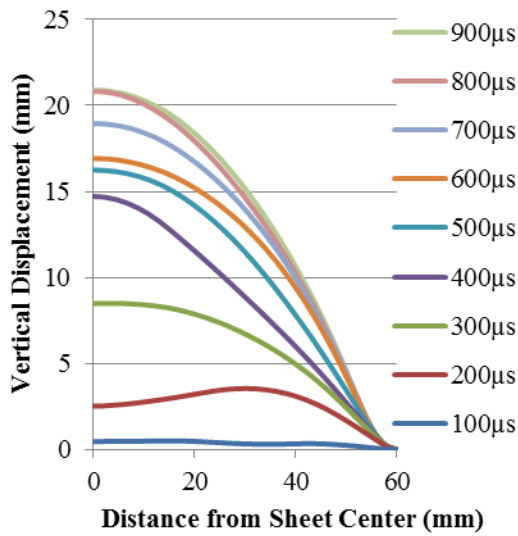
**Evolution of the sheet displacement measured radially from the sheet center for DP600 specimens.**



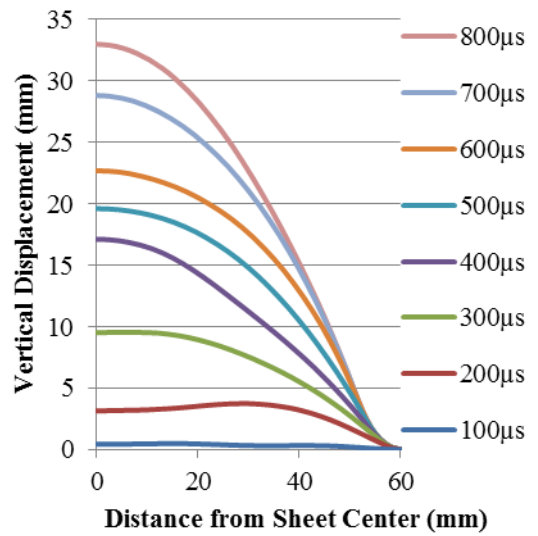
Uniaxial



Intermediate Draw

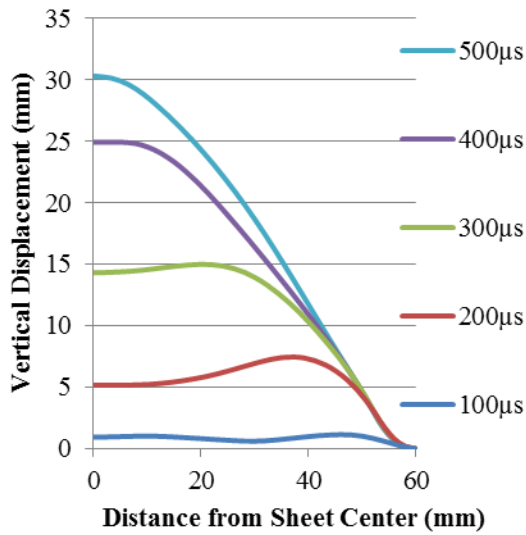


Plane Strain

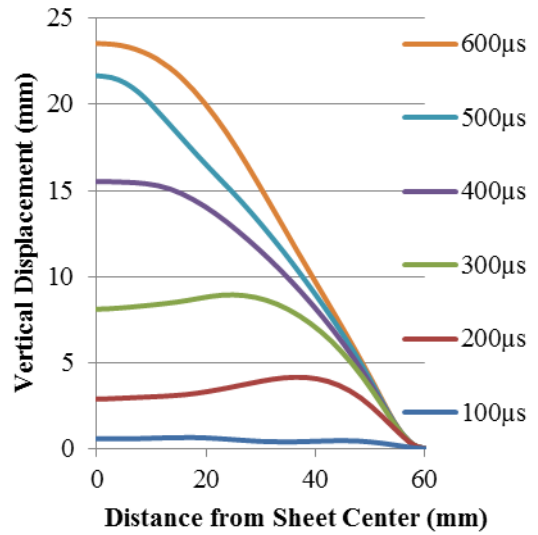


Biaxial

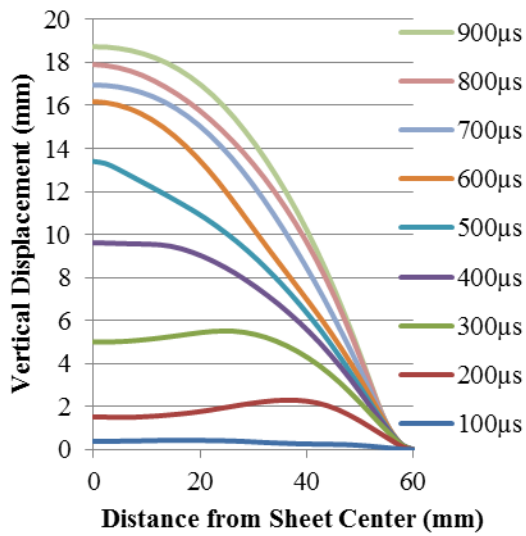
**Evolution of the sheet displacement measured radially from the sheet center for AA5182-O specimens.**



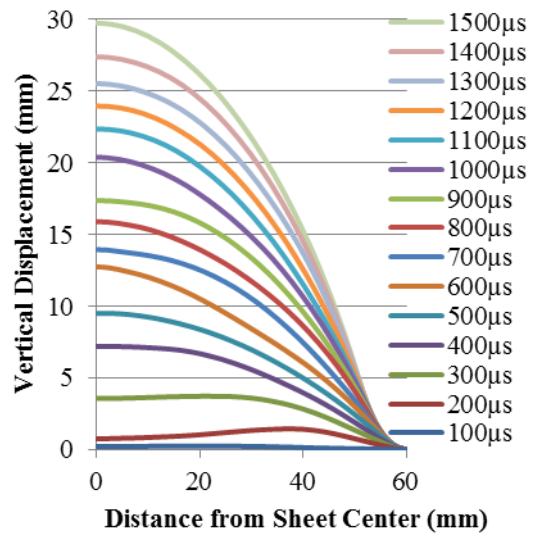
Uniaxial



Intermediate Draw

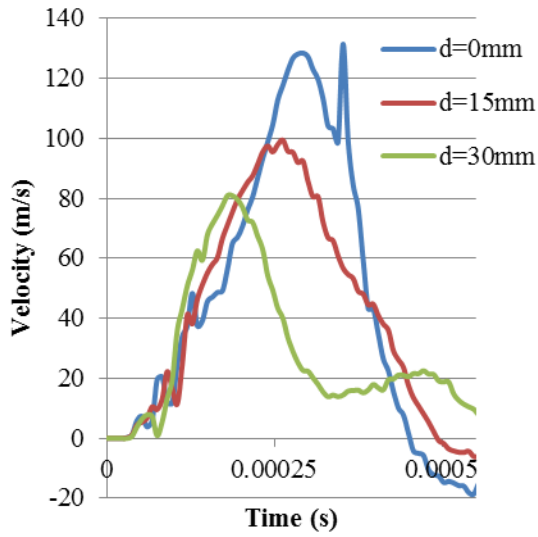


Plane Strain

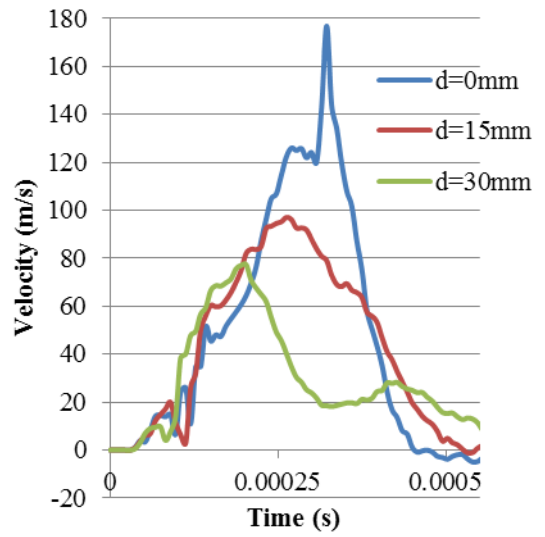


Biaxial

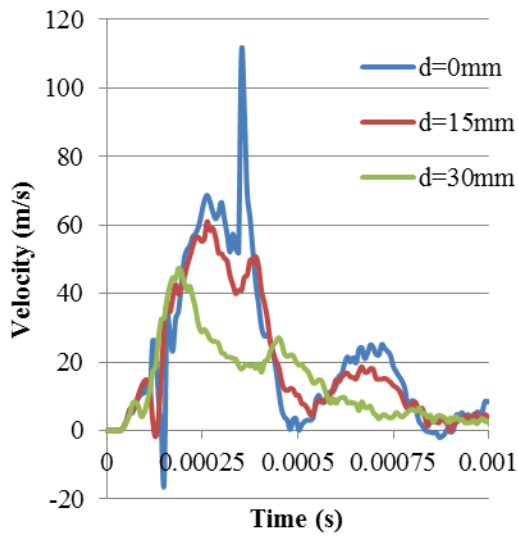
**Velocity at distances of 0, 15, and 30mm from the specimen center for DP600 specimens.**



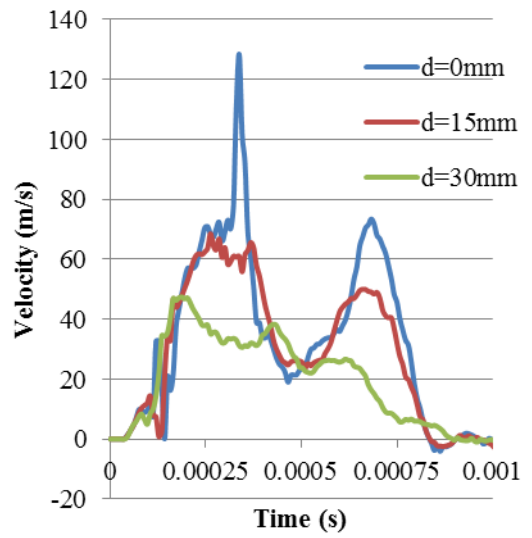
Uniaxial



Intermediate Draw



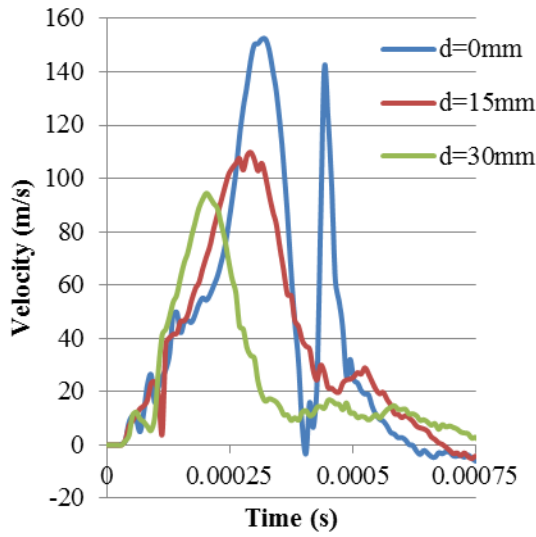
Plane Strain



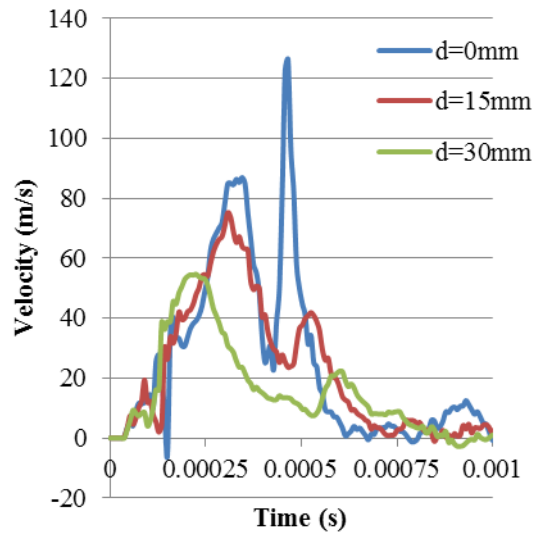
Biaxial



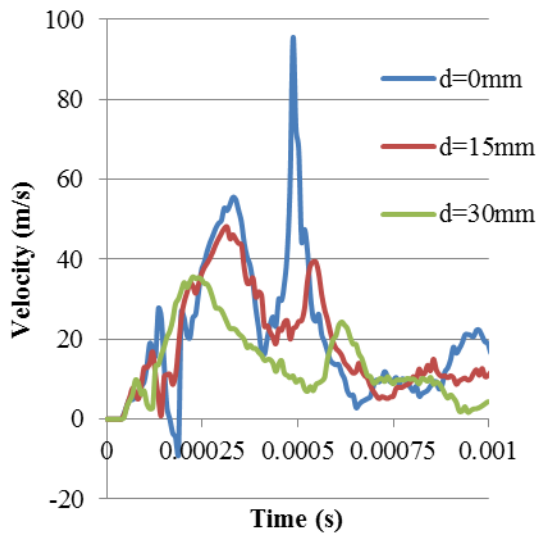
**Velocity at distances of 0, 15, and 30mm from the specimen center for AA5182-O specimens.**



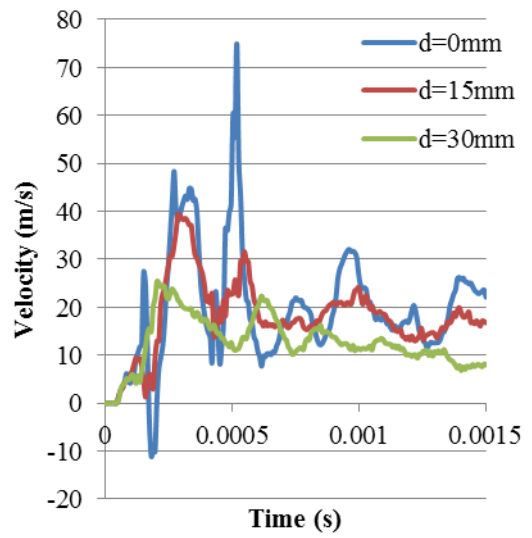
Uniaxial



Intermediate Draw

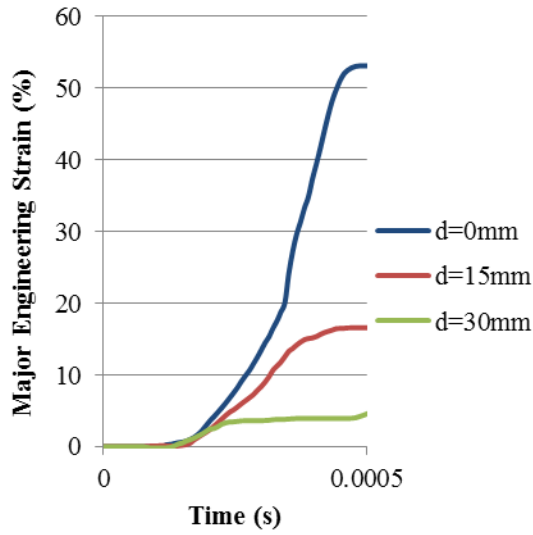


Plane Strain

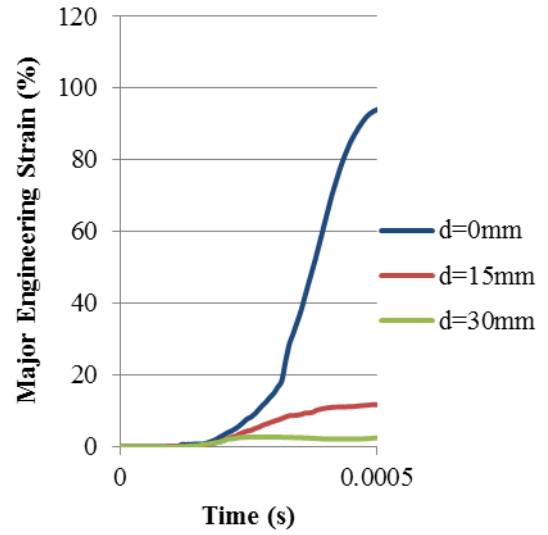


Biaxial

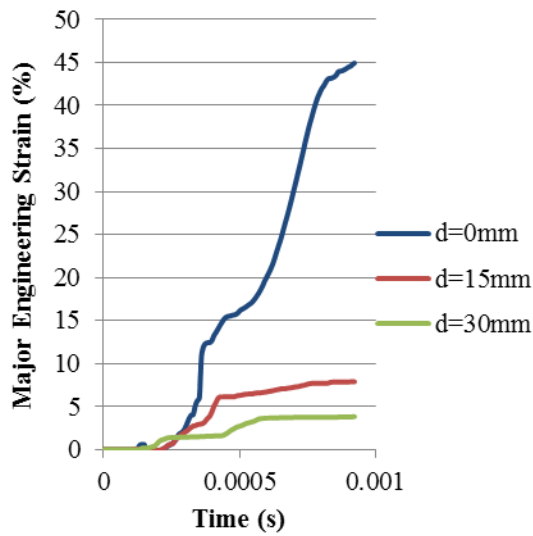
Major strain at distances of 0, 15, and 30mm from the specimen center for DP600 specimens.



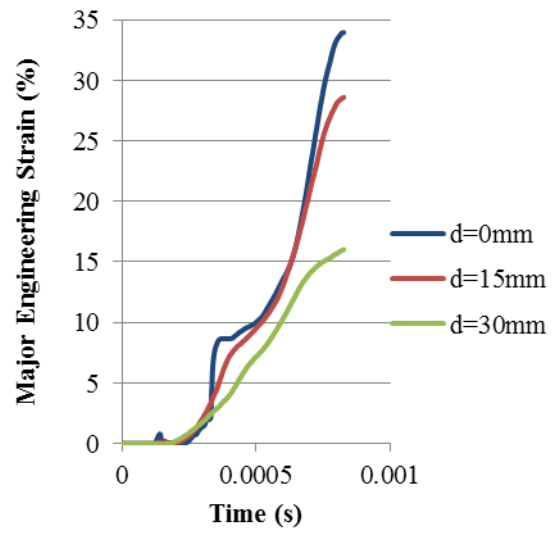
Uniaxial



Intermediate Draw

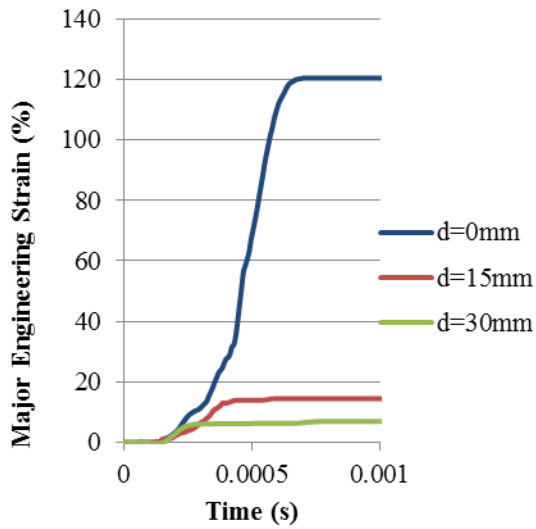


Plane Strain

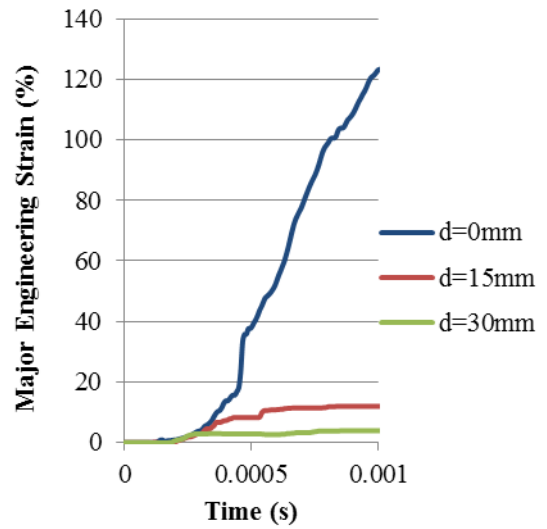


Biaxial

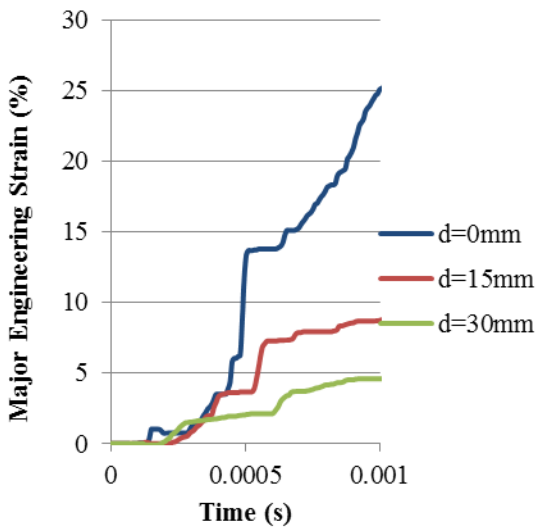
**Major strain at distances of 0, 15, and 30mm from the specimen center for AA5182-O specimens.**



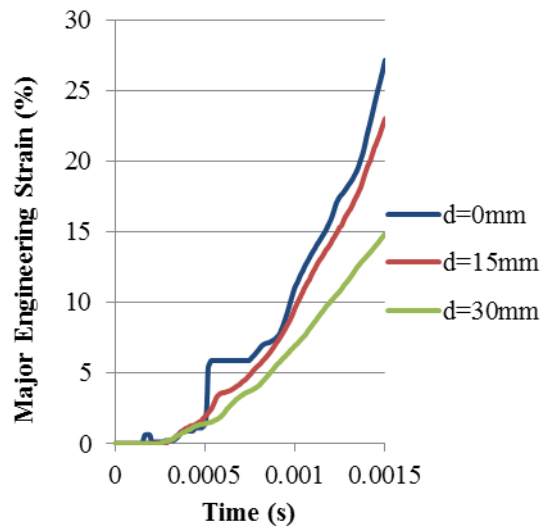
Uniaxial



Intermediate Draw

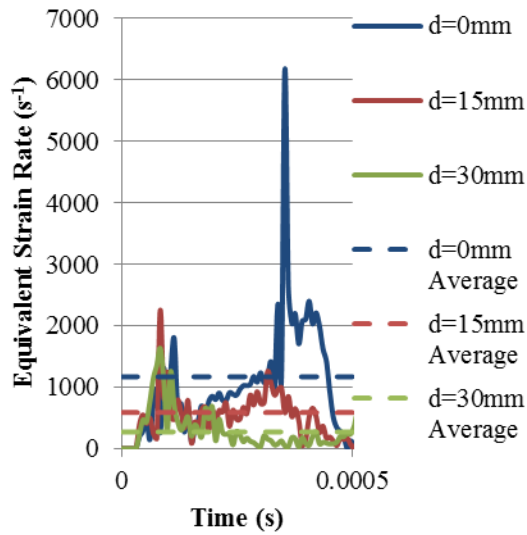


Plane Strain

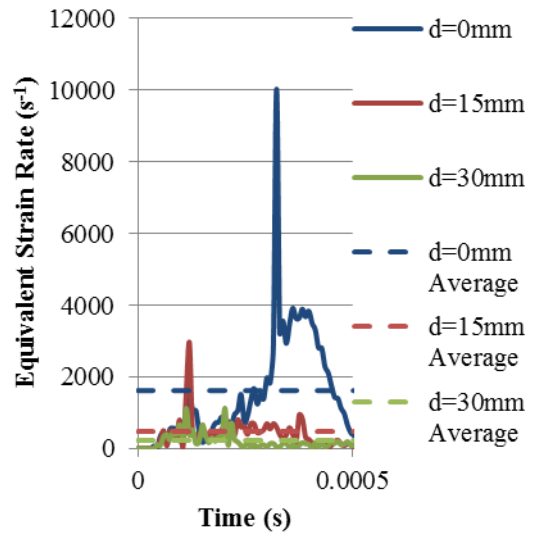


Biaxial

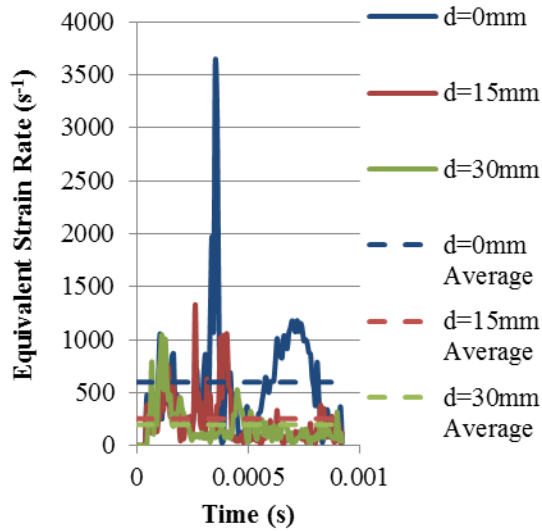
**Equivalent strain rate and the average equivalent strain rate at distances of 0, 15, and 30mm from the specimen center for DP600 specimens.**



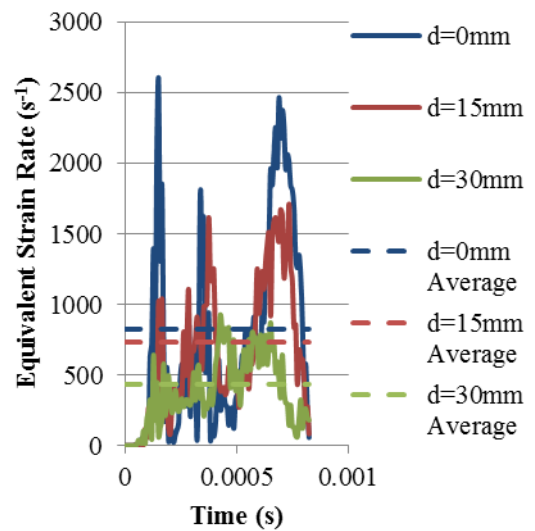
Uniaxial



Intermediate Draw

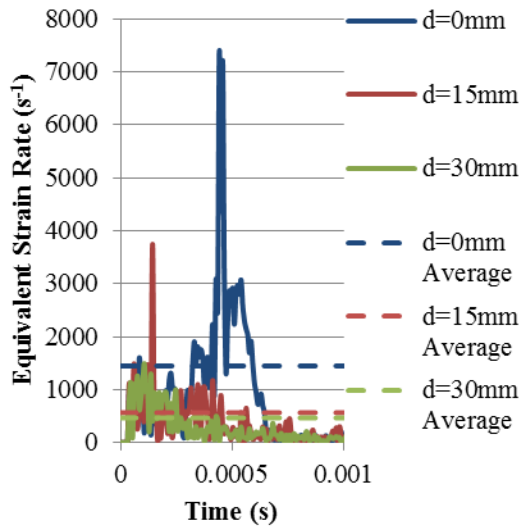


Plane Strain

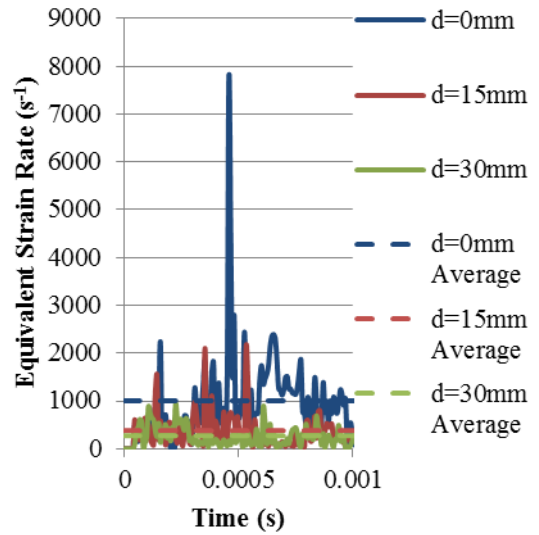


Biaxial

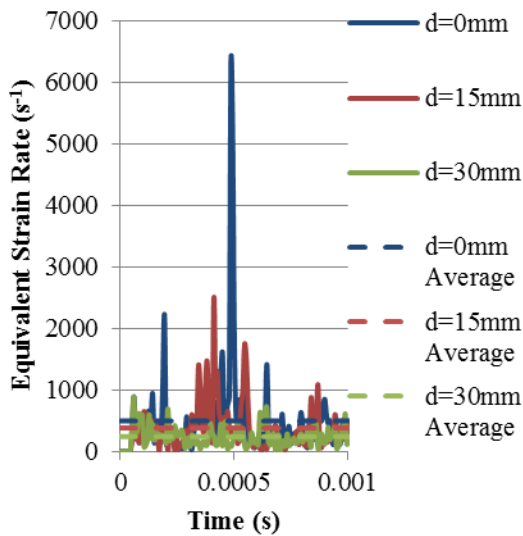
**Equivalent strain rate and the average equivalent strain rate at distances of 0, 15, and 30mm from the specimen center for AA5182-O specimens.**



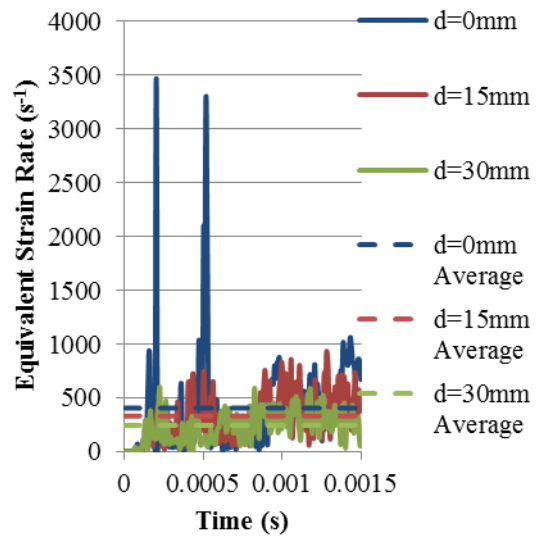
Uniaxial



Intermediate Draw

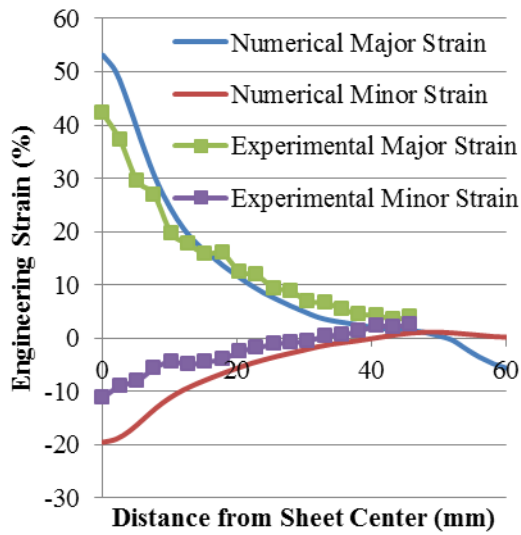


Plane Strain

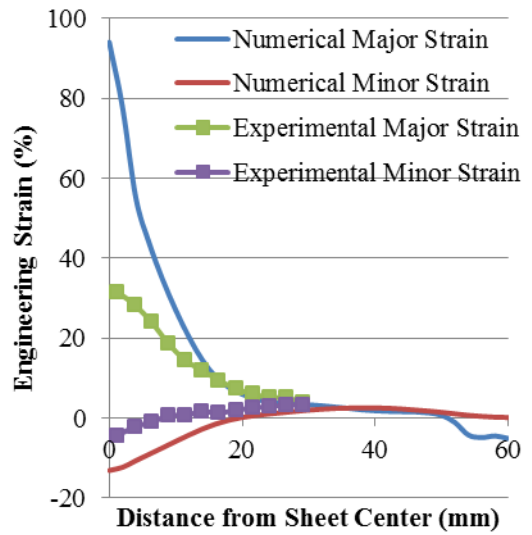


Biaxial

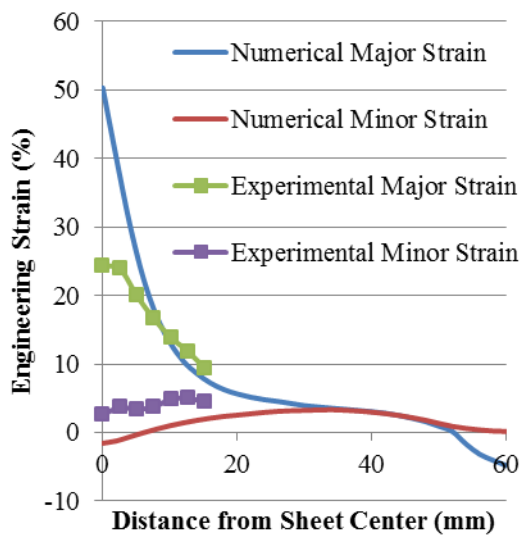
**Comparison of experimental and predicted major and minor strains measured radially from the center of the DP600 specimens.**



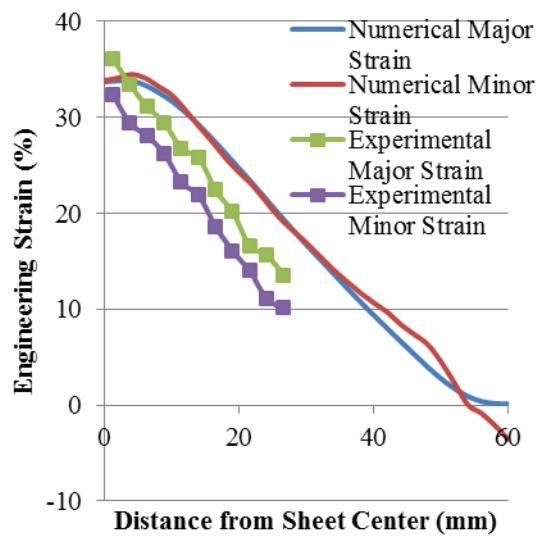
Uniaxial



Intermediate Draw

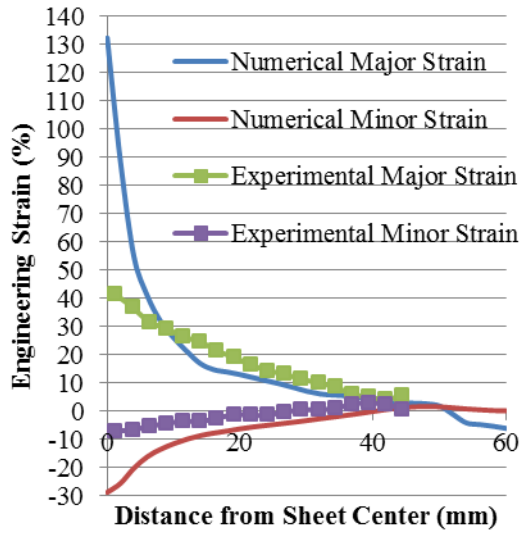


Plane Strain

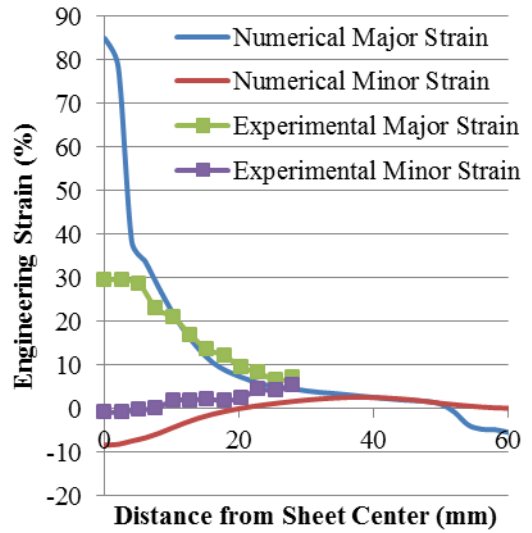


Biaxial

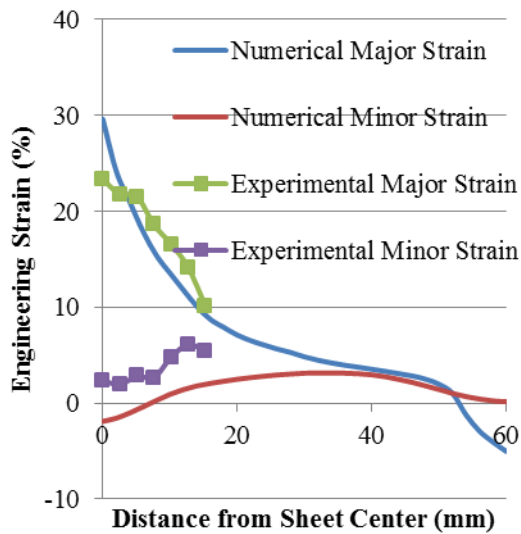
**Comparison of experimental and predicted major and minor strains measured radially from the center of the AA5182-O specimens.**



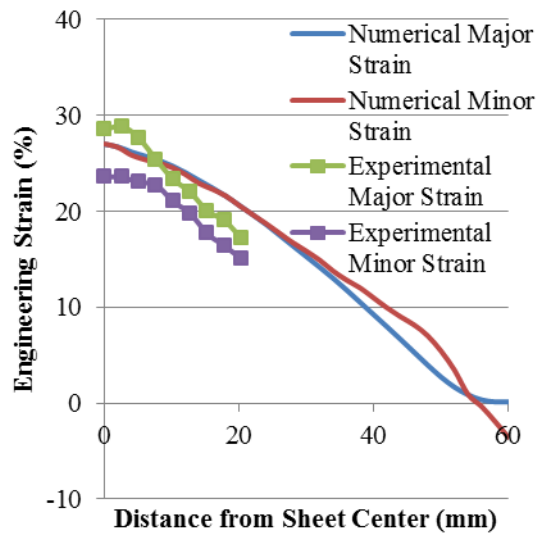
Uniaxial



Intermediate Draw

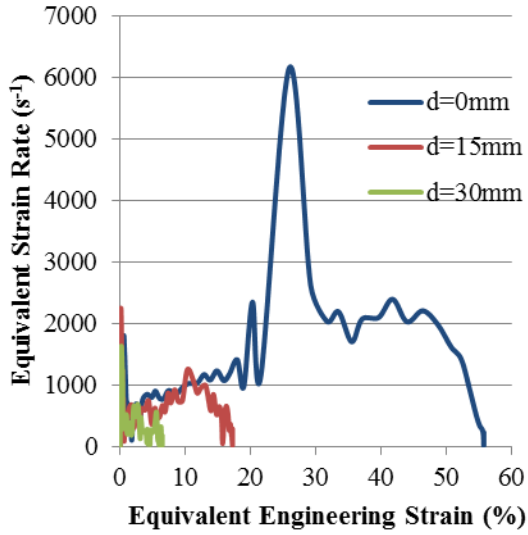


Plane Strain

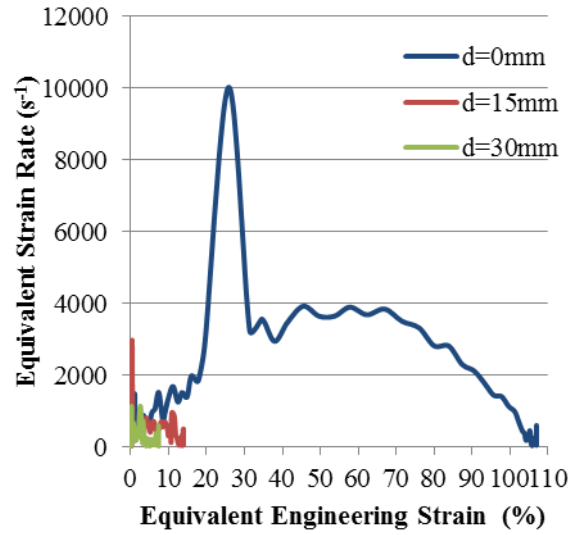


Biaxial

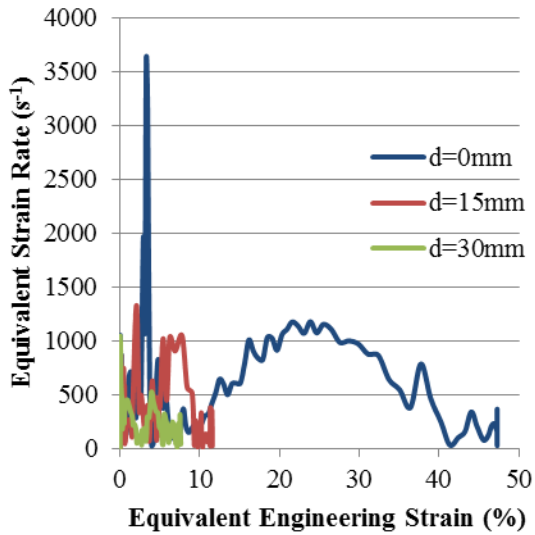
**Equivalent strain rate vs. equivalent strain for DP600 specimens.**



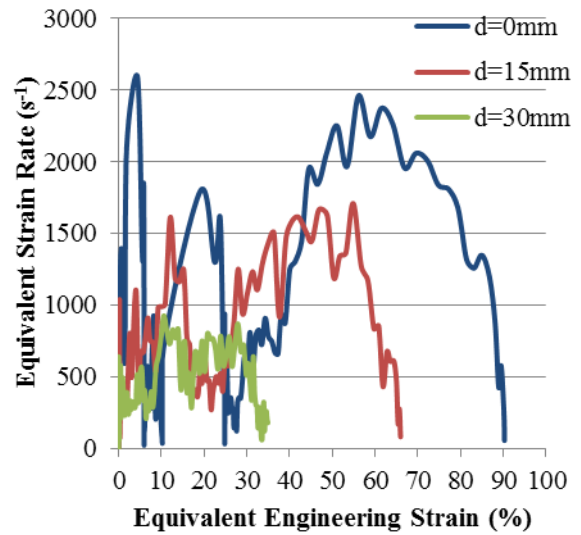
Uniaxial



Intermediate Draw



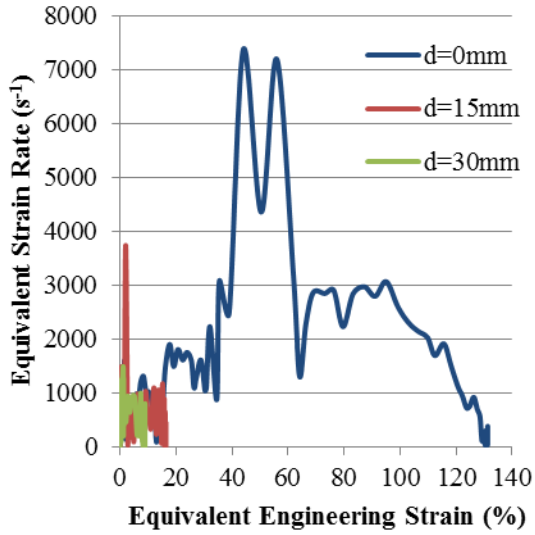
Plane Strain



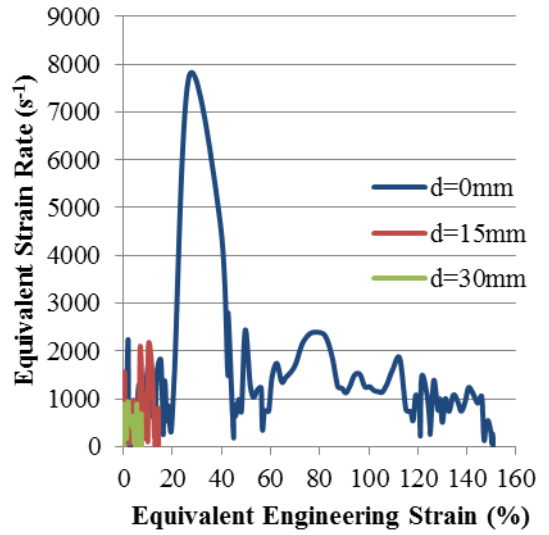
Biaxial



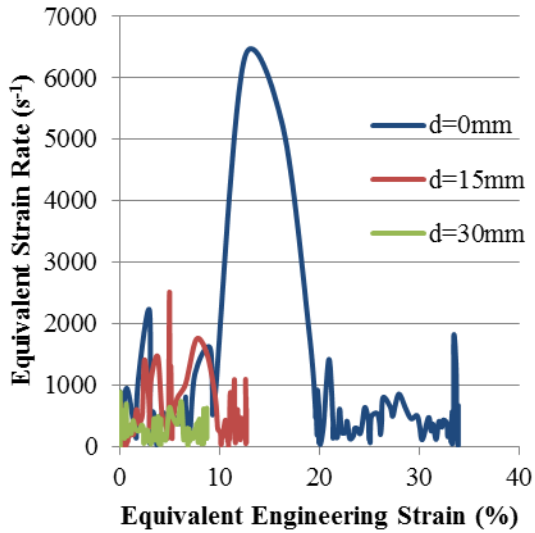
**Equivalent strain rate vs. equivalent strain for AA5182-O specimens.**



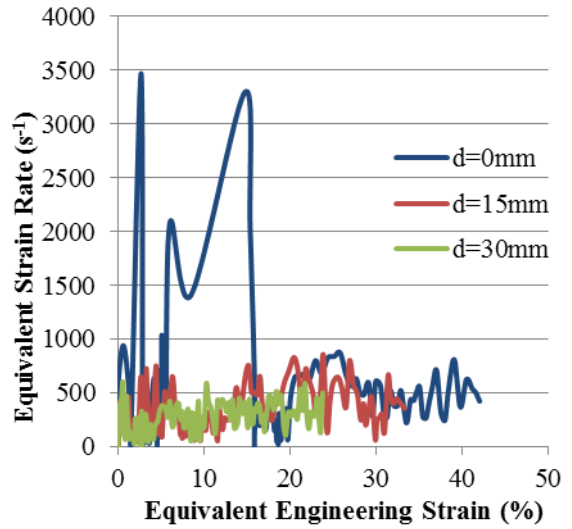
Uniaxial



Intermediate Draw



Plane Strain



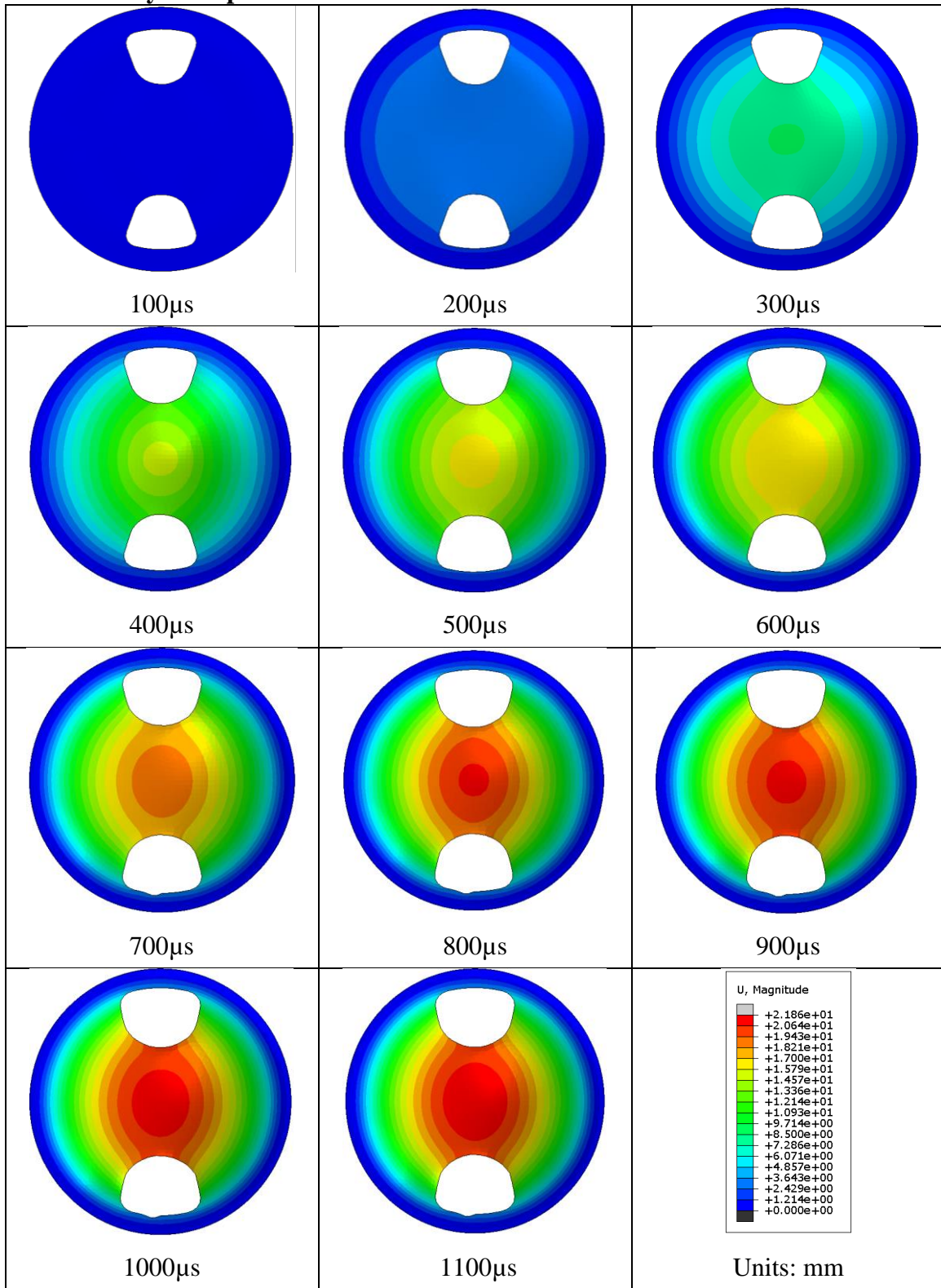
Biaxial

## **Appendix E: Numerical Simulation of EHFF Time History**

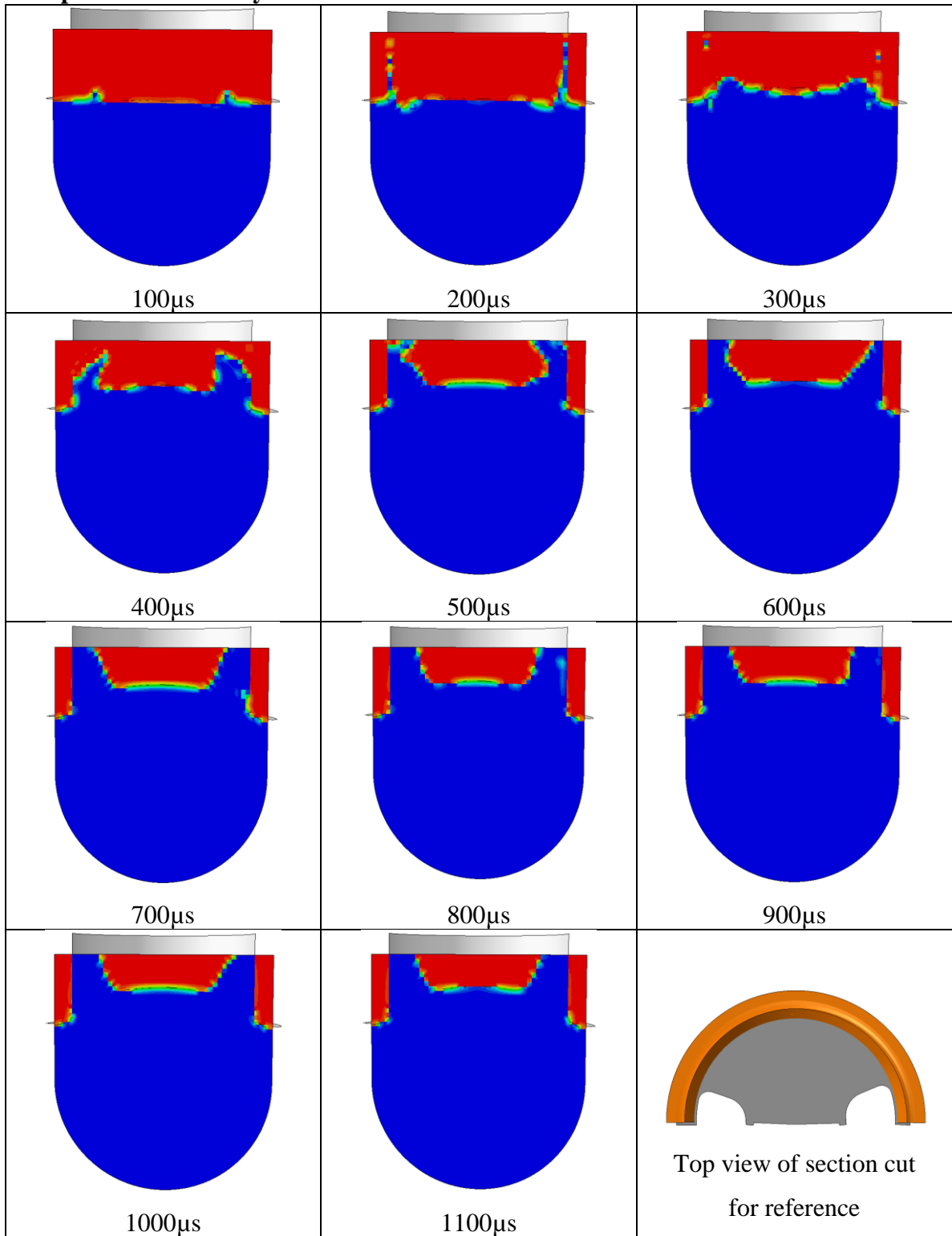
This appendix contains graphical results from the EHFF simulation of a DP600 plane strain specimen.

Time history of displacement.....	187
Graphical time history.....	188

**Time history of displacement.**



**Graphical time history.** Red is the air and blue is water.



## **Vita Auctoris**

NAME: Christopher J.L. Maris

PLACE OF BIRTH: Chatham, ON

YEAR OF BIRTH: 1989

EDUCATION: Blenheim District High School, Blenheim, ON, 2007

University of Windsor, B.A.Sc., Windsor, ON, 2011

University of Windsor, M.A.Sc., Windsor, ON, 2014